LPV Lateral Control of Autonomous and Automated Vehicles

Ariel Medero Borrell

To cite this version:

Ariel Medero Borrell. LPV Lateral Control of Autonomous and Automated Vehicles. Other. Université Grenoble Alpes [2020-..]; Universitat politècnica de Catalunya - BarcelonaTech, 2023. English. NNT : 2023GRALT067 . tel-04842226

HAL Id: tel-04842226
https://theses.hal.science/tel-04842226v1

Submitted on 17 Dec 2024

THÈSE

Pour obtenir le grade de

DOCTEUR DE L'UNIVERSITÉ GRENOBLE ALPES
et de l'UNIVERSITAT POLITÈCNICA DE CATALUNYA

École doctorale : EEATS
Spécialité : Automatique - Productique
Unité de recherche : GIPSA-Lab / SAFE Team

Titre de la thèse en français : Contrôle Latéral LPV des Véhicules Autonomes et Automatisés

Titre de la thèse en anglais : LPV Lateral Control of Autonomous and Automated Vehicles

Présentée par :

MEDERO BORRELL, Ariel

Direction de thèse :

Olivier SENAME Professeur des Universités, UGA	Directeur de thèse
Vicenç PUIG Full Professor, UPC	Co-Directeur de thèse

Rapporteurs :

Michel BASSET
Professeur des Universités, ENSISA-IRIMAS Université de Haute-Alsace
Chouki SENTOUH
Maitre de Conférences HDR, INSA Hauts-de-France

Thèse soutenue publiquement le **28/09/23**, devant le jury composé de :

Michel BASSET Professeur des Universités, ENSISA-IRIMAS Université de Haute-Alsace	Rapporteur
Chouki SENTOUH Maitre de Conférences HDR, INSA Hauts-de-France	Rapporteur
John J. MARTINEZ Professeur des Universités, Grenoble-INP	Président de Jury
Fatiha NEJJARI Associate Professor, UPC	Examinatrice
Olivier Sename Professeur des Universités, UGA	Directeur de Thèse
Vicenç Puig Full Professor, UPC	Co-Directeur de Thèse

Acknowledgements

I would like to express my heartfelt gratitude to my thesis supervisors. Their guidance and support throughout this research journey have been invaluable. Attending international conferences and witnessing the recognition and admiration they receive from the academic community has filled me with pride. Working with them has been a privilege, and I am grateful for the opportunity to learn from such esteemed persons.

Vicenç has played a pivotal role in my academic journey. As my professor during my master's studies and later as my mentor for my master's thesis, he ignited my passion for control theory and has been a constant source of encouragement. Without his support, I may never have considered pursuing a PhD in the first place. Despite the physical distance throughout most of my thesis, I always felt confident that I could rely on him whenever needed.

Meanwhile, Olivier has been an incredible source of inspiration throughout these three years. His unwavering commitment to scientific rigor and his insatiable curiosity have pushed me to continually improve and seek better solutions. Moreover, his kindness and genuine care for those around him have made the experience of working with him truly delightful. I am also immensely grateful for his patience in helping me refine my scientific writing skills.

I would like to extend my gratitude to Marcelo, Hussam, Gian Marco and Andreu for their close collaboration throughout this journey and for being always there to bounce ideas off each other. I hope that we will have the chance to continue working together in some ways in the future. I also want to give a special recognition to the incredible group of *stagieres* I had the privilege of working with: Wissam, Hasan, Hachem, Ana, Zaman, and Hassanein. The level of work and dedication you all demonstrated in such short projects is truly impressive. I have no doubt that each of you has a bright future ahead, and I am confident that you will achieve great things.

I would like to express my sincere appreciation to the exceptional engineers of the SAFE team, Pierre, Amaury, and Jonathan. Their hard work, skills, and dedication have been instrumental in the success of this thesis. The experimental side of my research work would simply not have been possible without their invaluable contributions and without being able to count on them each time something was off with the platforms.

It cannot miss a huge hug to my close colleagues at IRI and specially at GIPSA. You are too many to name, and I fear missing someone given my bad memory. I feel an immense gratitude for the family ambience in the lab and for making me feel at home in Grenoble, this three years would not have been at all the same without you guys.

My family and their support have helped me through this years a lot. I cannot thank them enough for all that they have done for me. I know that after three years my parents still do not know what I am working on, they even think I am a simple university student, I still love them.

Finally, I have no word big enough to thank my pillar and support. *Mon Amour.* 我爱你

Yo soy de donde crece la palma.
Yo vengo de todas partes
y hacia todas partes voy.

José Martí

Abstract — It is expected that automated driving will enhance road safety, increase highway capacity, reduce carbon emissions, and make transportation more accessible to disabled and older people. However, fully automated systems are not expected to be widely available until the 2040 decade. Due to this reason, human drivers will still be behind the wheel for the imminent future. On the other hand, Advanced Driver Assistance Systems (ADAS) are becoming increasingly more advance and are a feature of most modern cars. This drive towards increased automated driving and the effects of human-automation interaction pose interesting challenges from a control theory perspectives. In this context, this thesis proposes the use of LPV/$\mathcal{H}_\infty$ approaches that allow the synthesis of controllers capable to adapting to variations on the vehicle speed and to mitigate the effect of saturation on the steering actuator. In the human-automation interaction context, the thesis proposes an integrated lateral control ADAS strategy tasked with helping the human driver during critical scenarios. The criticality of the situation is estimated based on fault detection techniques that monitor the driver's performance. This estimation is then used to activate the LPV/$\mathcal{H}_\infty$ lateral ADAS controller if required, or to deactivate it otherwise. Both the autonomous driving and ADAS control strategies proposed in this thesis have been experimentally validated on a reduced scale vehicle platform present at GIPSA-Lab.

Keywords: Linear Parameter Varying, Autonomous Vehicles, ADAS, Fault Tolerant Control, Integrated Control.

Résumé — La conduite automatisée devrait améliorer la sécurité routière, augmenter la capacité des autoroutes, réduire les émissions de carbone et rendre les transports plus accessibles aux personnes handicapées et âgées. Toutefois, les systèmes entièrement automatisés ne devraient pas être largement disponibles avant la décennie 2040. C'est pourquoi les conducteurs humains resteront au volant dans un avenir proche. D'autre part, les systèmes avancés d'aide à la conduite (ADAS) sont de plus en plus perfectionnés et font partie de la plupart des voitures modernes. Cette évolution vers une automatisation accrue de la conduite et les effets de l'interaction entre l'homme et l'automatisation posent des défis intéressants du point de vue de la théorie du contrôle. Dans ce contexte, cette thèse propose l'utilisation d'approches LPV/$\mathcal{H}_\infty$ qui permettent la synthèse de contrôleurs capables de s'adapter aux variations de la vitesse du véhicule et d'atténuer l'effet de la saturation sur l'actionneur de direction. Dans le contexte de l'interaction homme-automatisation, la thèse propose une stratégie ADAS de contrôle latéral intégrée chargée d'aider le conducteur humain dans les scénarios critiques. La criticité de la situation est estimée sur la base de techniques de détection des pannes qui surveillent les performances du conducteur. Cette estimation est ensuite utilisée pour activer le contrôleur ADAS latéral LPV/$\mathcal{H}_\infty$ si nécessaire, ou pour le désactiver dans le cas contraire. Les stratégies de conduite autonome et de contrôle ADAS proposées dans cette thèse ont été validées expérimentalement sur une plateforme de véhicule à échelle réduite présente au GIPSA-Lab.

Mots clés : Systèmes Linéaires à Paramètres Variables, Véhicules Autonomes, ADAS, Contrôle Tolérant aux Pannes, Contrôle Intégré.

Resumen — Se espera que la conducción automatizada mejore la seguridad vial, aumente la capacidad de las autopistas, reduzca las emisiones de carbono y haga el transporte más accesible para discapacitados y personas mayores. Sin embargo, no se espera que los sistemas totalmente automatizados estén ampliamente disponibles hasta la década de 2040. Por este motivo, los conductores humanos seguirán al volante en un futuro inminente. Por otro lado, los Sistemas Avanzados de Asistencia al Conductor (ADAS) son cada vez más avanzados y forman parte de la mayoría de los coches modernos. Este impulso hacia una conducción cada vez más automatizada y los efectos de la interacción hombre-automatización plantean retos interesantes desde el punto de vista de la teoría de control. En este contexto, esta tesis propone el uso de técnicas LPV/$\mathcal{H}_\infty$ que permiten sintetizar controladores capaces de adaptarse a variaciones en la velocidad del vehículo y de mitigar el efecto de saturación en el actuador de dirección. En el contexto de la interacción hombre-automatización, la tesis propone una estrategia ADAS de control lateral integrado encargada de ayudar al conductor humano durante escenarios críticos. La criticidad de la situación se estima a partir de técnicas de detección de fallos que monitorizan la actuación del conductor. Esta estimación se utiliza entonces para activar el controlador ADAS lateral LPV/$\mathcal{H}_\infty$ si es necesario, o para desactivarlo en caso contrario. Tanto la conducción autónoma como las estrategias de control ADAS propuestas en esta tesis han sido validadas experimentalmente en una plataforma de vehículo a escala reducida presente en GIPSA-Lab.

Palabras claves: Sistemas Lineares con Parámetros Variables, Vehículos Autónomos, ADAS, Control Tolerante a Fallos, Control Integrado.

Resum — S'espera que la conducció automatitzada millori la seguretat viària, augmenti la capacitat de les autopistes, redueixi les emissions de carboni i faci el transport més accessible per a discapacitats i persones majors. No obstant això, no s'espera que els sistemes totalment automatitzats estiguin àmpliament disponibles fins a la dècada de 2040. Per aquest motiu, els conductors humans seguiran al volant en un futur imminent. D'altra banda, els Sistemes Avançats d'Assistència al Conductor (ADAS) són cada vegada més avançats i formen part de la majoria dels cotxes moderns. Aquest impuls cap a una conducció cada vegada més automatitzada i els efectes de la interacció home-automatització plantegen reptes interessants des del punt de vista de la teoria de control. En aquest context, aquesta tesi proposa l'ús de tècniques LPV/$\mathcal{H}_\infty$ que permeten sintetitzar controladors capaços d'adaptar-se a variacions en la velocitat del vehicle i de mitigar l'efecte de saturació en l'actuador de direcció. En el context de la interacció home-automatització, la tesi proposa una estratègia ADAS de control lateral integrat encarregada d'ajudar al conductor humà durant escenaris crítics. La criticitat de la situació s'estima a partir de tècniques de detecció de fallades que monitoren l'actuació del conductor. Aquesta estimació s'utilitza llavors per a activar el controlador ADAS lateral LPV/$\mathcal{H}_\infty$ si és necessari, o per a desactivar-ho en cas contrari. Tant la conducció

autònoma com les estratègies de control ADAS proposades en aquesta tesi han estat validades experimentalment en una plataforma de vehicle a escala reduïda present en GIPSA-Lab.
Paraules Clau: Sistemes Linears amb Paràmetres Variables, Vehicles Autònoms, ADAS, Control Tolerant a Fallades, Control Integrat.

GIPSA-Lab, 11 rue des Mathématiques Grenoble Campus
Grenoble, France

Institut de Robòtica i Informàtica Industrial, C/ Llorens i Artigas 4-6
Barcelona, Spain

Résumé Étendu en Français — La conduite automatisée devrait améliorer la sécurité routière, augmenter la capacité des autoroutes, réduire les émissions de carbone et rendre les transports plus accessibles aux personnes handicapées et âgées. Toutefois, les systèmes entièrement automatisés ne devraient pas être largement disponibles avant la décennie 2040. Les niveaux de conduite automatisée peuvent être classés du niveau 0, où le système ne fournit au conducteur que des signaux d'avertissement, au niveau 5, où le système peut conduire la voiture dans toutes les conditions.

Au moment de la rédaction de ce manuscrit de thèse, certains modèles de la marque Mercedes Benz sont les seuls cas, pour l'ensemble de l'industrie des transports, de véhicules autorisés à conduire légalement au niveau 3 d'autonomie. Cependant, ce système automatisé n'est autorisé que sur les autoroutes d'Allemagne et dans certaines régions des États-Unis. Dans les deux cas, à une vitesse maximale de 60km/h. De plus, l'investissement dans les entreprises technologiques de conduite entièrement autonome a ralenti de 60%. Les trois années qui se sont écoulées depuis le début de la thèse ont été marquées, dans le domaine des véhicules autonomes, par un déclin de l'intérêt pour la technologie sans conducteur et par une réorientation de l'industrie vers le développement de systèmes avancés d'aide à la conduite (ADAS) automatisés de niveau 2 et de niveau 3.

Il ne fait aucun doute que cette évolution est marqué par des défis technologiques majeurs pour la conduite automatisée aux niveaux 4 et 5. Du point de vue de la théorie du contrôle, ces défis soulèvent des questions importantes :

- *Comment le contrôleur peut-il être adapté pour tenir compte des différentes situations de conduite et traiter les dysfonctionnements potentiels du véhicule?* La dynamique d'un véhicule diffère considérablement entre la conduite à basse vitesse et la conduite à vitesse de croisière sur autoroute. L'interaction entre les pneus et la route change considérablement en fonction du revêtement et de l'état de la route. Certains actionneurs du véhicule peuvent connaître des défaillances partielles ou atteindre des points de saturation, ce qui peut avoir un impact négatif sur les performances du contrôleur conçu dans des conditions nominales.
- *Comment pouvons-nous gérer efficacement la coordination entre les différents actionneurs qui travaillent ensemble pour atteindre un objectif commun?* Actuellement, les véhicules sont déjà équipés de plusieurs actionneurs tels que le système de direction motorisé, le système de freinage antiblocage (ABS) et d'autres. Toutefois, leur utilisation combinée est limitée par la capacité restreinte des conducteurs humains à gérer simultanément plusieurs commandes. La mise en œuvre de systèmes automatisés offre la possibilité de tirer parti de la redondance présente dans les commandes des véhicules.

En outre, comme la conduite entièrement autonome de niveau 5 est plus éloignée que prévu il y a quelques années, les conducteurs humains seront toujours derrière le volant. D'autre part, les systèmes ADAS sont de plus en plus perfectionnés et font partie de la plupart des voitures modernes. En fait, à partir de juillet 2024, une série de fonctions ADAS seront obligatoires dans tous les nouveaux véhicules vendus au sein de l'Union européenne. La question suivante se pose alors :

- *Comment prendre en compte l'interaction entre le conducteur et les systèmes ADAS automatisés?* Des nombreux accidents sont dus au fait que les conducteurs prennent des mesures incompatibles avec la situation rencontrée, ce qui peut entraîner des réactions indésirables du véhicule, voire une instabilité, et le système ADAS pourrait apporter une aide dans ces cas-là. Cependant, un système ADAS qui semble invasif peut conduire de nombreux conducteurs à désactiver ces aides, ce qui va à l'encontre de l'objectif premier du système.

La principale motivation de cette thèse est d'étudier si la théorie LPV, et en particulier si les contrôleurs adaptatifs LPV, peuvent apporter une réponse efficace aux questions soulevées précédemment.

Objectifs de la thèse

Les objectifs de recherche de cette thèse sont de développer des approches de contrôle tolérantes aux fautes, pour les applications de véhicules automatisés. Les objectifs fixés pour atteindre ce but sont les suivants :

- Proposer des approches de synthèse pour les observateurs et les contrôleurs robustes dans le cadre LPV.
- Étudier l'intégration de la détection des pannes basée sur un modèle et des contrôleurs adaptatifs utilisant les approches LPV.
- Concevoir des contrôleurs LPV reconfigurables pour les véhicules autonomes, robustes aux dysfonctionnements des actionneurs, tels que la saturation des actionneurs.
- Étudier les approches permettant d'intégrer le comportement du conducteur dans la conception d'une commande basée sur un modèle. Ces modèles de comportement du conducteur devraient être utilisés pour détecter les erreurs du conducteur humain et pour développer un contrôleur ADAS latéral afin d'améliorer la sécurité du véhicule.
- Mettre en œuvre et valider les algorithmes développés dans des expériences en temps réel.

Contributions de la thèse

Les contributions faites dans la thèse peuvent être classées dans les catégories suivantes : contributions aux contrôles de la conduite automatisée utilisant les techniques LPV, contributions à la théorie du contrôle et contributions aux contrôles LPV d'un point de vue de la mise en œuvre. Les sous-sections suivantes détaillent ces contributions.

Contributions à la théorie du contrôle

- ***Proposition d'un cadre LPV basé sur une grille à temps discret***. Les approches LPV pour les systèmes à temps discret (DT) ont été principalement explorées dans les cadres LPV polytopiques ou de transformation fractionnaire linéaire (LFT). L'approche LPV basée sur la grille offre des avantages notables par rapport à l'approche polytopique, qui est l'approche LPV la plus répandue dans la littérature. Ces avantages incluent la possibilité de prendre en compte les taux de variation des paramètres et d'éviter les problèmes d'overbounding dans l'espace des paramètres. Cependant, l'approche LPV basée sur la grille n'a été développée que pour les systèmes à temps continu.

  Cette thèse introduit un nouveau cadre spécialement conçu pour les approches en grille à temps discret, appelé ici : *grid and local variation bound framework*. Ce cadre permet la reformulation des conditions LMI, telles que les conditions de stabilité et les conditions pour le calcul de la norme L_2 induite des systèmes DT-LPV, en utilisant des fonctions de Lyapunov dépendantes des paramètres comme un problème d'optimisation LMI fini. La thèse présente de nouveaux théorèmes et propositions illustrant la synthèse de contrôleurs et d'observateurs DT-LPV dans ce nouveau *grid and local variation bound framework*.

  Le cadre de la grille et de la limite de variation locale est présenté au Chapitre 4. Ensuite, le Chapitre 4 et Chapitre 5 introduisent les conditions de synthèse par retour d'état qui sont utilisées pour la plupart des problèmes de synthèse de contrôleur dans la thèse. Le cadre DT basé sur la grille est également utilisé dans le Chapitre 7 pour la conception de l'observateur LPV.

- ***Des conditions LMI pour le contrôle des systèmes M^3D.*** Les systèmes multi-modes multi-dimensionnels (M^3D) ont été introduits pour la première fois par E. Verriest dans [Ver06]. Les systèmes M^3D sont des systèmes de commutation pour lesquels chacun des modes du système peut avoir un nombre différent d'états. Le fait que le nombre d'états soit différent pour plusieurs modes signifie que les résultats bien connus pour l'étude des systèmes à commutation [GC06a]; [GC06b] ne peuvent pas être directement appliqués à ces systèmes.

  L'intérêt d'étudier de tels systèmes dans le cadre de cette thèse apparaît lors de l'étude des propriétés de stabilité des transitions de *handover* et *takeover*. Ces transitions se produisent lors du passage du mode de contrôle des véhicules automatisés de la commande autonome à la commande manuelle assistée et vice-versa. Comme nous le verrons dans cette thèse, le nombre d'états considérés dans la conception du contrôle pour ces modes peut être différent.

  Notez que les résultats de ce travail ne sont pas présentés en tant que chapitres principaux dans ce manuscrit de thèse car l'étude des transitions LPV M^3D Autonomous-ADAS est encore en cours. Il a été décidé de mettre l'accent dans ce manuscrit sur les approches LPV avec des résultats bien vérifiés dans l'application de la conduite automatisée. Le contenu de l'article déjà publié sur le contrôle des systèmes M^3D est présenté en annexe B.

Contributions aux aspects de la mise en œuvre des approches de contrôle de la LPV

- ***Parameter-Dependent State-Feedback (PDSF) et Static Output-Feedback Controllers.*** Ce nouveau type de contrôleurs est basé sur une approche de synthèse en deux étapes utilisant le lemme de projection et les approches LPV basées sur la grille. L'approche de synthèse en deux étapes permet d'appliquer directement aux conditions LMI une structure de contrôleur fixe avec des gains de contrôleur constants. Les gains du contrôleur sont affines sur une fonction de base, avec une dépendance sur les paramètres variables, ce qui permet au contrôleur global de s'auto-planifier sans nécessité d'étape d'interpolation. Du point de vue de la mise en œuvre, cela conduit à une mise en œuvre directe de la loi de commande en temps réel.

  Cette approche de synthèse de contrôle est appliquée dans le Chapitre 4 pour le problème de contrôle de la direction autonome et dans le Chapitre 7 pour le contrôle ADAS latéral. En outre, l'approche duale est utilisée dans le chapitre 7 pour la synthèse du gain de l'observateur.

- ***MPC basé sur l'ordonnancement des paramètres variables liés à la conception.*** Il a été proposé un schéma de réglage optimal en ligne pour les paramètres d'ordonnancement liés à la conception des systèmes de contrôle adaptatifs LPV. Plus précisément, la méthode est conçue dans le cadre du *Model Predictive Control* (MPC). Le principal avantage de la solution proposée est qu'elle détermine automatiquement en ligne l'ordonnancement LPV des paramètres variables liés à la conception. Cela évite au concepteur d'avoir à développer une fonction d'ordonnancement (ce qui est souvent une tâche répétitive et obscure).

  Il est à noter que les résultats de ce travail ne sont pas présentés dans ce manuscrit de thèse car il a été choisi de se concentrer sur les travaux basés sur les approches LPV/$\mathcal{H}_\infty$, qui sont au cœur du travail de thèse.

Contributions aux approches LPV pour la conduite automatisée

- ***Contrôleur PDSF (Parameter-Dependent State-Feedback) pour la conduite autonome.*** L'approche de contrôle PDSF a été mise en œuvre pour la direction autonome dans une application de suivi de trajectoire sur le plateforme expérimentale *Scaled Automated Vehicles*, présentée dans le Chapitre 4. Il est remarquable que, bien que la conception DT basée sur la grille comprenne plus de 150 points de grille, le contrôleur résultant ne nécessite que quatre matrices à gain constant. Cela met en évidence la réduction significative de l'effort de mise en œuvre obtenue grâce à l'utilisation de contrôleurs PDSF.

- ***Contrôleur LPV Gain-Scheduled basé sur une grille avec un comportement anti-windup.*** Dans la conception de la commande de direction autonome, des paramètres variables liés à la conception ont été introduits et combinés à l'approche DT basée sur la grille. Cela a permis de développer un contrôleur LPV qui émule le comportement d'un mécanisme anti-Windup. En utilisant le paramètre variable lié à la conception, le contrôleur module l'amplitude maximale de la direction. La programmation en ligne de ce paramètre permet d'éviter les effets d'enroulement lorsque l'actionneur de direction atteint son point de saturation. L'efficacité de cette conception a été validée par des expériences en temps réel menées sur une plate-forme expérimentale. Le contenu du Chapitre 5 décrit cette contribution.

- ***Détection des erreurs du conducteur à l'aide d'approches de détection des défauts***. La thèse propose plusieurs méthodes de détection des fautes pour évaluer l'ampleur des erreurs du conducteur par rapport au comportement de conduite attendu, en utilisant des modèles nominaux du conducteur et des informations sur la planification de la trajectoire du système de conduite automatisée. Initialement, dans le Chapitre 6, une approche de l'espace de parité est suggérée pour les cas impliquant un modèle de conducteur linéaire invariant dans le temps (LTI). Cependant, des approches plus avancées pour la détection des erreurs du conducteur sont présentées, employant un observateur PI dans le Chapitre 8 et un observateur PI LPV dans le Chapitre 7. Ces méthodes avancées peuvent identifier les erreurs du conducteur dans des intervalles de fréquences spécifiques et de prendre en compte les modèles de conducteur LPV qui s'adaptent aux différentes vitesses du véhicule. La validation en temps réel confirme l'efficacité de cette proposition pour détecter rapidement les situations dangereuses.

- ***Contrôle ADAS latéral***. En utilisant des approches LPV/$\mathcal{H}_\infty$ et des paramètres variables liés à la conception, la conception proposée pour le contrôleur ADAS latéral permet une transition sûre du mode d'assistance inactif au mode d'assistance actif. Lorsqu'il est actif, il aide le conducteur à maintenir la stabilité du véhicule dans les situations critiques. Plusieurs variantes de conception ont été proposées, y compris des configurations à un ou plusieurs actionneurs. La principale caractéristique de cette conception est de fournir une assistance au conducteur tout en minimisant les niveaux d'intrusion. Le contenu de la partie III de la thèse décrit cette contribution.

- ***Validation expérimentale sur la plateforme SAV (Scaled Automated Vehicle)***. Un temps important a été consacré au développement de la plateforme SAV au GIPSA-Lab. En particulier pour la transition de la version originale de la plateforme, utilisant une carte PX4 programmée en C embarqué, à sa version actuelle programmée dans l'environnement ROS2 et le langage Python, qui est beaucoup plus conviviale et permet une vitesse d'itération de développement rapide. Les détails sur la plate-forme ainsi que l'effort d'identification du système pour modéliser la dynamique de la voiture SAV sont présentés dans le Chapitre 2.

  Les contributions faites dans cette thèse ont été largement testées et validées sur la plateforme SAV. Les résultats expérimentaux pour les contrôleurs de direction autonomes dans la Partie II ont été testés sur la plateforme SAV. En outre, la plateforme a également été utilisée pour valider la stratégie ADAS proposée dans la thèse, les résultats expérimentaux obtenus étant donnés dans le Chapitre 8 et dans l'Annexe A.

Perspectives futures

Cette thèse a fourni quelques contributions qui pourraient ouvrir des pistes de travail intéressantes pour des études futures :

- **Conditions LMI de la synthèse en temps discret** : Il sera utile d'étendre les conditions LMI présentées dans cette thèse pour les structures dépendantes des paramètres et les contrôleurs LPV à gain programmé basés sur la grille au-delà de la synthèse par retour d'état (SF). Certains travaux préliminaires ont été réalisés en ce qui concerne la synthèse de contrôleurs à rétroaction de sortie statique (SOF), cependant, la synthèse de contrôle à rétroaction de sortie dynamique (DOF) sur le cadre de temps discret basé sur la grille reste un défi ouvert.
- **Planification optimale des paramètres variables liés à la conception** : L'utilisation de méthodes basées sur les MPC pour planifier en ligne les paramètres variables liés à la conception est une approche prometteuse. Les résultats préliminaires développés au cours de la thèse pourraient être étendus en intégrant l'étape de planification avec ce problème d'ordonnancement optimal comme un problème optimal conjoint. Cela ouvre la possibilité d'augmenter l'interconnexion entre les étapes de planification et de contrôle, ce qui peut conduire à de meilleures performances.
- **Commande robuste de transition Handover/Takeover avec la théorie M^3D** : L'étude des propriétés de stabilité et de robustesse des transitions entre le *handover* et le *takeover* dans les systèmes automatisés est bien adaptée à l'approche de contrôle M^3D. Si les contrôleurs latéraux autonomes et ADAS proposés dans cette thèse sont pris comme modèles de base, cela impliquera la nécessité d'étendre les résultats du contrôle M^3D à la théorie LPV.
- **Validation expérimentale supplémentaire de l'ADAS** : La validation expérimentale effectuée sur la plateforme SAV de la stratégie ADAS intégrée a montré un grand potentiel. Toutefois, il convient de reconnaître les limites de la plateforme SAV pour l'application ADAS. La validation expérimentale future de la stratégie proposée pourrait être effectuée en améliorant la plateforme, par exemple en installant une caméra frontale pour donner au conducteur une vue à la première personne et en utilisant un volant comme dispositif d'entrée pour le conducteur. En outre, la stratégie pourrait être testée dans des simulateurs ADAS spécialisés ou même dans des véhicules à taille réelle.

Contents

List of Figures

List of Tables

Acronyms

ADAS	Advanced Driver Assistance Systems
BM	Bycicle Model
BRL	Bounded Real Lemma
CT	Continuous-Time
DT	Discrete-Time
DLC	Double Lance Change
DM	Driver Model
HEDM	Heading Error Driver Model
LEDM	Lateral Error Driver Model
LFT	Linear Fractional Transformation
LMI	Linear Matrix Inequality
LTI	Linear Time Invariant
LPV	Linear Varying Parameter
MIMO	Multiple-Input Multiple-Output
MPC	Model Predictive Control
PDLF	Parameter-Dependent Lyapunov Function
PDLM	Parameter-Dependent Lyapunov Matrix
PDSF	Parameter-Dependent State-Feedback
PI	Proportional-Integral
RMS	Root Mean Square
SAV	Scaled Automated Vehicle
SDP	Semi-Definite Programming
SF	State-Feedback
SS	State-Space
ROS	Robot Operating System

Introduction

Context of the Thesis

This thesis was developed as a part of the project SARAH (SAfe and Robust Autonomous veHicles) from October 2020 to September 2023, carried out as an international joint thesis (*cotutelle*) collaboration by Universtitat Politécnica de Catalunya (UPC) and Université Grenoble Alpes (UGA). The research work has been done at the Gipsa-Lab laboratory at UGA and the Institut de Robòtica i Informàtica Industrial (IRI) at UPC.

The research was jointly supervised by Prof. Olivier Sename and Prof. Vicenç Puig, and was supported by the French National Research Agency (CNRS, "Investissements d'Avenir", ANR-15-IDEX-02) and has been partially supported by ROBOTEX 2.0 (Grants ROBOTEX ANR-10-EQPX-44-01 and TIRREX ANR-21-ESRE-0015) funded by the French program Investissements d'avenir. It has also been partially funded by the Spanish State Research Agency (AEI) and the European Regional Development Fund (ERFD) through the project SaCoAV (ref. MINECO PID2020-114244RB-I00) and by FPI UPC grant 2020FPI-UPC-008. The supports are gratefully acknowledged.

Motivations of the Thesis

It is expected that automated driving will enhance road safety, increase highway capacity, reduce carbon emission, and make transportation more accessible to disabled and older people. However, fully automated systems are not expected to be widely available until the 2040 decade. The levels of automated driving can be categorized from Level 0, where the system provide the driver only with warning signals, to Level 5, where the system can drive the car under all conditions. See Fig. 1 for an overview of the different autonomy levels according to SAE International.

At the moment of writing this thesis manuscript, some models of the Mercedes Benz brand are the only cases for the whole transportation industry of vehicles allowed to drive legally at a Level 3 of autonomy. Still, this automated system is only allowed in highways of Germany and in certain regions of the United States. In both cases, at a maximum speed of $60km/h$. Moreover, investment in full self-driving tech companies has slow down by 60%[1]. These three years since the thesis started have been marked in the autonomous vehicle field by a decline of interests in driverless technology and an industry shift towards the development of Level 2 and Level 3 automated Advanced Driving Assistance Systems (ADAS).

Without a doubt this shift is marked by major technological challenges for automated

---

[1] https://www.theverge.com/2023/5/5/23711586/autonomous-vehicle-investment-toyota-nvidia

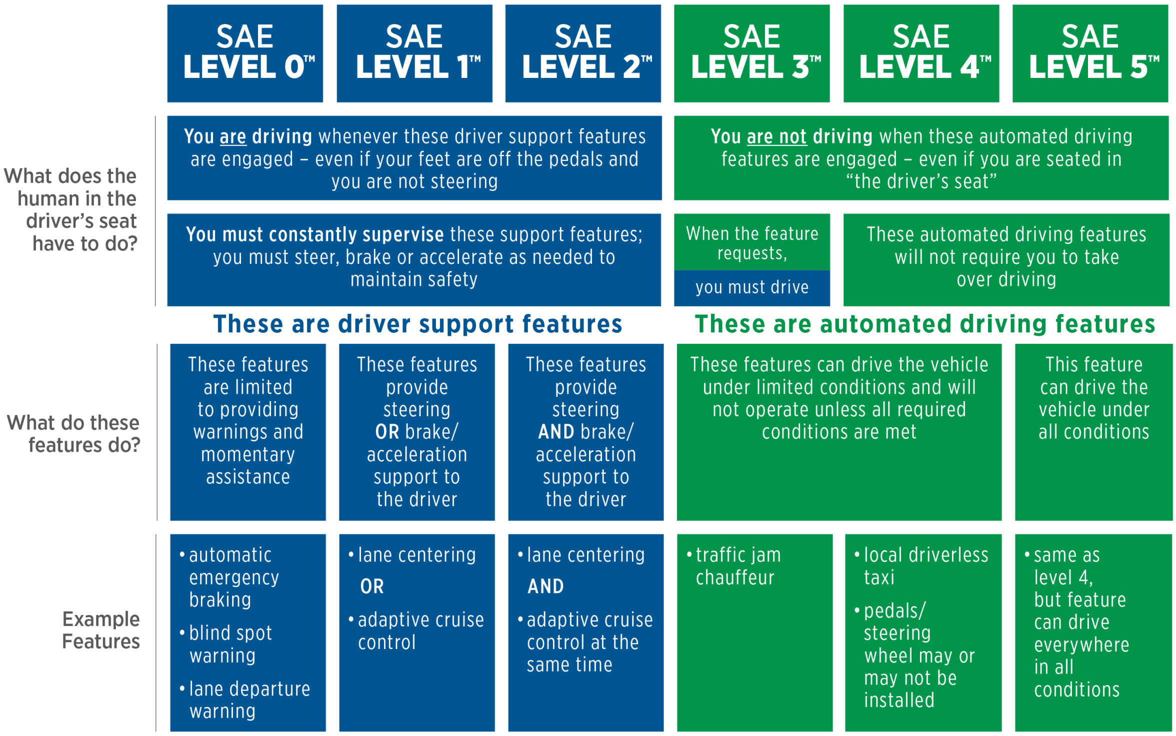

	SAE LEVEL 0™	SAE LEVEL 1™	SAE LEVEL 2™	SAE LEVEL 3™	SAE LEVEL 4™	SAE LEVEL 5™
What does the human in the driver's seat have to do?	**You are driving** whenever these driver support features are engaged – even if your feet are off the pedals and you are not steering			**You are not driving** when these automated driving features are engaged – even if you are seated in "the driver's seat"		
	You must constantly supervise these support features; you must steer, brake or accelerate as needed to maintain safety			When the feature requests, you must drive	These automated driving features will not require you to take over driving	
	These are driver support features			**These are automated driving features**		
What do these features do?	These features are limited to providing warnings and momentary assistance	These features provide steering **OR** brake/ acceleration support to the driver	These features provide steering **AND** brake/ acceleration support to the driver	These features can drive the vehicle under limited conditions and will not operate unless all required conditions are met		This feature can drive the vehicle under all conditions
Example Features	• automatic emergency braking • blind spot warning • lane departure warning	• lane centering **OR** • adaptive cruise control	• lane centering **AND** • adaptive cruise control at the same time	• traffic jam chauffeur	• local driverless taxi • pedals/ steering wheel may or may not be installed	• same as level 4, but feature can drive everywhere in all conditions

Figure 1: Different levels of automated driving. Source: www.SAE.org

driving at Level 4 and Level 5. These challenges from the control theory point of view present important questions:

- *How can the controller be adapted to accommodate varying driving situations and address potential vehicle malfunctions?* The dynamics of a vehicle differ significantly between low-speed driving and cruising at highway speeds. The tire road interaction changes dramatically depending on road surface and condition. Certain vehicle actuators may experience partial failures or reach saturation points, which can negatively impact the performance of the controller designed under nominal conditions.

- *How can we effectively manage the coordination among various actuators that work together towards a shared objective?* Currently, vehicles already have multiple actuators such as the motorized steering system, Anti-Locking Brake System (ABS), and others. However, their combined utilization is restricted by the limited capacity of human drivers to handle multiple inputs simultaneously. The implementation of automated systems opens up opportunities to leverage the redundancy present in vehicle controls.

Moreover, as Level 5 full autonomous driving is further away than expected some years ago, human drivers will still be behind the wheel. On the other hand, ADAS systems are becoming increasingly more advanced and are a feature of most modern cars. In fact, starting from July 2024 a series of ADAS features will be mandatory in all new sold vehicles within the European Union[2]. Then, the following question arises:

- *How to take into account the interaction between the driver and the automated ADAS systems?* Many accidents are caused by drivers generating actions inconsistent with the situation encountered, which may lead to undesired vehicle responses or even instability, and the ADAS system could provide support in these cases. However, an ADAS system that feels invasive may lead many drivers to disable such aids, which defeats the purpose of the system in first place.

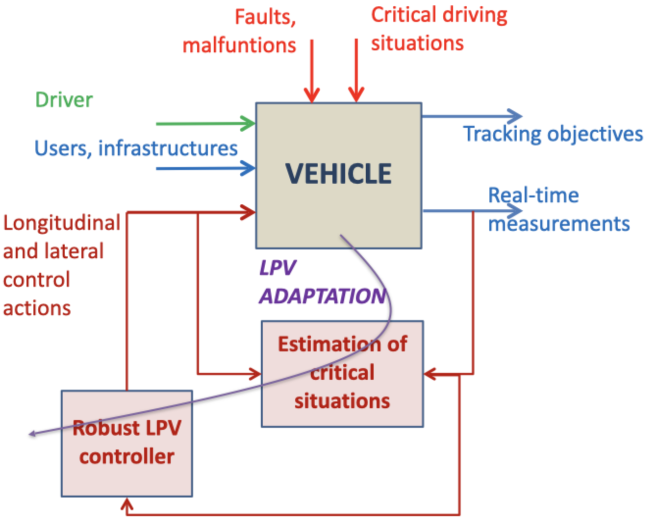

Figure 2: Desired control system, with LPV adaptation as a tool to accommodate faults and driver errors in the vehicle control loop. SARAH (SAfe and Robust Autonomous veHicles) project UGA-UPC.

The main motivation of this thesis is to study whether the LPV theory and in particular whether LPV adaptive controllers can provide an efficient answer to the questions raised before according to the above scheme.

Objectives of the Thesis

The research objectives of this thesis are to develop fault tolerant control approaches (as shown in Fig 2), for automated vehicles applications. The objectives set to achieve this goal are the following:

- to propose synthesis approaches for robust observer and controllers in the LPV framework.

---

[2] https://ec.europa.eu/commission/presscorner/detail/en/ip_22_4312

- to study the integration of model-based fault detection and adaptive controllers employing LPV approaches.
- to design reconfigurable LPV controllers for autonomous vehicles robust to actuator malfunctions, such as actuator saturation.
- to study approaches to integrate the driver's behaviour to be used in a model based control design. These models of driver's behaviour should be used for detecting human driver errors and to develop lateral ADAS controller to enhance the safety of the vehicle.
- to implement and validate the developed algorithms in real-time experiments.

Contributions of the Thesis

The contributions made in the thesis can be categorized into the following categories: contributions to automated driving controls using LPV techniques, contributions to control theory and contributions to LPV controls from an implementation point of view. The following subsections detail those contributions.

Contributions to Control Theory

- ***Proposition of a Discrete-Time Grid-Based LPV framework***. LPV approaches for Discrete-Time (DT) systems have primarily been explored within the Polytopic or Linear Fractional Transformation (LFT) LPV frameworks. The Grid-Based LPV approach offers notable advantages over the Polytopic approach, which is the most prevalent LPV approach in the literature. These advantages include the ability to account for parameter variation rates and avoid overbounding issues in the parameter space. However, the Grid-Based LPV approach has only been developed for Continuous-Time systems.

  This thesis introduces a new framework specifically designed for Discrete-Time Grid-Based approaches referred here as: grid and local variation bound framework. This framework enables the reformulation of LMI conditions, such as stability conditions and conditions for the computation of the induced L_2-norm of DT-LPV systems, using parameter-dependent Lyapunov functions as a finite LMI optimization problem. The thesis presents new theorems and propositions illustrating the synthesis of DT-LPV controllers and observers within this novel grid and local variation bound framework.

  The grid and local variation bound framework is presented in Chapter 4. Then, Chapter 4 and Chapter 5 introduce State-Feedback synthesis conditions which used for most of the controller synthesis problems in the thesis. The DT Grid-Based framework is also used in Chapter 7 for LPV observer design.

- ***LMI conditions for control of Multi-Mode Multi-Dimensional Systems***. Multi-Mode Multi-Dimensional Systems (M^3D) were first introduced by E. Verriest in [Ver06].

M^3D systems are switching systems for which each of the modes of the system can have a different number of states. The fact that the number of states is different for multiple modes means that well known results for the study of switched systems [GC06a]; [GC06b] cannot be directly applied for these systems.

The interest of studying such systems within the scope of this thesis arises when studying the stability properties of handover and takeover transitions. These transitions occur when switching the control mode of automated vehicles from autonomous control to manual assisted control and vice-versa. As will be seen in this thesis, the number of states considered in the control design for these modes can be different.

Note that the results from this work are not presented as main chapters in this thesis manuscript as the study of LPV M^3D Autonomous-ADAS transitions are still a work in progress. It was decided to rather put the focus of this manuscript in LPV approaches with well verified results in the application of automated driving. The contents of the already published paper on the control of M^3D systems is presented in Appendix B.

Contributions to Implementation Aspects of LPV Control Approaches

- ***Parameter-Dependent State-Feedback (PDSF) and Static Output-Feedback Controllers***. This novel type of controllers are based on a two-steps synthesis approach making use of the Projection Lemma and Grid-Based LPV approaches. The two-steps synthesis approach allows to enforce directly onto LMI conditions a fixed controller structure with constant controller gains. The controller gains are affine on some basis function, with dependency on the varying parameters, which allows the overall controller to self-schedule without requiring any interpolation step. From an implementation point of view, this leads to an straightforward real-time control law implementation.

  This control synthesis approach is applied in Chapter 4 for the autonomous steering control problem and in Chapter 7 for lateral ADAS control. Moreover, the dual approach is used in Chapter 7 for observer gain synthesis.

- ***MPC based scheduling of design-related varying-parameters***. It was proposed an optimal online tuning scheme for design-related scheduling parameters of adaptive Linear Parameter Varying (LPV) control systems. Specifically, the method is conceived within the Model Predictive Control (MPC) framework. The major advantage of the proposed solution is that it automatically determines the LPV scheduling of design-related varying-parameters online. Avoiding that the designer has to develop any scheduling function (which is often a repetitive and obscure task).

  Note that the results from this work are not presented in this thesis manuscript as it was chosen to focus on the works based on LPV/$\mathcal{H}_\infty$ approaches, which are the core of the thesis work.

Contributions to LPV Approaches for Automated Driving

- ***Parameter-Dependent State-Feedback (PDSF) controller for autonomous steering***. The PDSF control approach was implemented for autonomous steering in a path tracking application on an experimental platform, presented in Chapter 4. Remarkably, despite the DT Grid-Based design consisting of over 150 grid-points, the resulting controller only required four constant gain matrices. This highlights the significant reduction in implementation effort achieved through the use of PDSF controllers.

- ***Gain-Scheduled Grid-Based LPV controller with Anti-Windup behaviour***. In the design of autonomous steering control, design-related varying parameters were introduced and combined with the DT Grid-Based approach. This resulted in the development of an LPV controller that emulates the behavior of an Anti-Windup mechanism. By utilizing the design-related varying parameter, the controller modulates the maximum steering magnitude. Online scheduling of this parameter enables the prevention of windup effects when the steering actuator reaches its saturation point. The effectiveness of this design was validated through real-time experiments conducted on an experimental platform. The contents of Chapter 5 describe this contribution.

- ***Detection of driver errors using fault detection approaches***. The thesis proposes several fault-detection methods to assess the extent of driver errors compared to expected driving behavior, utilizing nominal driver models and path planning information from the automated driving system. Initially, in Chapter 6 a Parity Space approach is suggested for cases involving a Linear Time-Invariant (LTI) driver model. However, more advanced approaches for driver error detection are presented, employing PI Observer in Chapter 8 and an LPV PI Observers in Chapter 7. These advanced methods can identify driver errors within specific frequency ranges and accommodate LPV driver models that adjust to varying vehicle speeds. Real-time validation confirms the effectiveness of this proposition in promptly detecting hazardous situations.

- ***Lateral ADAS Control***. Employing LPV/$\mathcal{H}_\infty$ approaches and design-related varying parameters the proposed design for lateral ADAS controller enables the safe transition from inactive to active assistance mode. When active, it assists the driver in maintaining vehicle stability during critical situations. Various design variants have been proposed, including both single-actuator and multi-actuator configurations. The main feature of this design is on providing driver assistance while minimizing intrusiveness levels. The contents of Part III of the thesis describe this contribution.

- ***Integrated ADAS Strategy***. The driver detection algorithm and the lateral ADAS controller are integrated into a cohesive strategy. This integration allows the level of assistance to be determined based on the magnitude of estimated driver errors. The effectiveness of this strategy has been experimentally validated and tested with multiple drivers, demonstrating its efficacy. The contents of Part III of the thesis describe this contribution.

- ***Experimental Validation on the Scaled Automated Vehicle (SAV) Platform***. An important amount of time has been dedicated to the development of the SAV platform at GIPSA-Lab. In particular for the transition from the original version of the platform, using a PX4 board programmed in embedded C, to its current version powered by the ROS2 environment and the Python language, which is much more user friendly and enables fast development iteration speed. Details on the platform as well as the system identification effort to model the SAV car dynamics are presented in Chapter 2.

The contributions made in this thesis have been extensively tested and validated on the SAV platform. The experimental results for the autonomous steering controllers in Part II were tested on the SAV platform. In addition, the platform was also used to validate the ADAS strategy proposed in the thesis, the experimental results obtained given in Chapter 8 and in Appendix A.

Thesis Outline

The thesis manuscript is split into three parts plus a chapter providing concluding remarks:

- Part I: This part is dedicated for the required background in control theory and the derivation of dynamical models for the vehicle dynamics and driver steering models.
    - Chapter 1: Presents some notions on control theory useful to develop control synthesis techniques for Linear Parameter Varying (LPV) systems.
    - Chapter 2: Covers the longitudinal and lateral vehicle dynamics and the derivation of the so-called bicycle model.
    - Chapter 3: Provides a literature review of driver models for the human steering behaviour and introduces the driver models that will be used for the design of the integrated ADAS strategy.
- Part II: Here new LPV approaches are developed to the control of fully autonomous vehicle steering.
    - Chapter 4: Introduces synthesis conditions for the Parameter-Dependent State-Feedback control approach. Then, this control approach is used to develop an autonomous steering controller. Finally, the controller is implemented on a real scaled vehicle platform.
    - Chapter 5: Introduces synthesis conditions for Gain-Scheduled Grid-Based DT SF LPV controllers. Using this approach the steering controller introduced in Chapter 4 is augmented with the addition of a design-related varying parameter that modifies the allowed control authority to emulate an Anti-Windup mechanism. Experimental results are presented to validate the approach.
- Part III: This part is focused on presenting different variants that have been proposed in this thesis of an integrated ADAS strategy for lateral vehicle control.
    - Chapter 6: Serves as an introduction to the integrated ADAS strategy. The fault detection approach for detecting driver errors based on fault detection techniques

  is introduced. Then, it is presented the combined driver-vehicle model that will be used for ADAS controller design and the lateral controller synthesis carried out in the LPV/$\mathcal{H}_\infty$ framework.
  - Chapter 7: Expands the integrated ADAS strategy by incorporating the vehicle's longitudinal velocity as a varying parameter. The chapter also present improvements to the fault-detection algorithm by using an LPV PI observer for detecting driver errors. The ADAS controller design is extended including braking actions in addition to steering commands as controller outputs, with each actuator control authority managed by a dedicated design-related varying parameter.
  - Chapter 8: In this chapter the lateral ADAS controller and the PI Observer strategy are adapted for implementation on an scaled automated vehicle. In this platform, the integrated strategy has been validated experimentally with multiple Test Drivers.
- Conclusions: Provide some concluding remarks on the results achieved in this thesis and comments on possible future works.

Thesis Notation

General Notation

The vector and matrix notation is standard. $\mathbb{R}$ represents the set of all real numbers while $\mathbb{R}^+$ represents the set of positive real numbers. x^T represents the transpose of x, X^{-1} represents the inverse of X and X^{-T} represents the transpose inverse of X. $\mathcal{X} = ker(X)$ represents that $\mathcal{X}$ is a base of the null space of X. $\|x\|_2$ represents the L_2-norm of the vector x.

Sampling instance k dependency for Discrete-Time systems will be dropped, e.g. $x := x(k)$, unless it is required for clarification or to emphasize real-time implementations. Superscript $+$ indicates that a sampling instance dependent vector $x(k)$ is being evaluated at sampling instance $k+1$, e.g. $x^+ := x(k+1)$.

$\mathcal{Z}$ is employed as a discretization operator. $\mathcal{Z}_T$ specifies that the discretization is carried out with the Tustin discretization approach. $\mathcal{Z}_{ZOH}$ specifies that the discretization is carried out with the complete zero order hold discretization approach.

Unless otherwise specified, all units in this thesis are given in S.I..

LMI Related Notation

Matrix $X(\geq) > 0$ represents that X is symmetric positive (semi-)definite. Matrix $X(\leq) < 0$ represents that X is symmetric negative (semi-)definite. To simplify notation the following abreviation is made He(X)= $X + X^T$. The symbol $\star$ in an LMI represents a symmetric element transposed. In LMI conditions, bold letters $\mathbf{X}$ are used to identify the matrix X as an optimization variables in the LMI optimization problem.

LPV Related Notation

Considering a vector of varying parameters ρ, subscript i indicates that it is being referred to an individual element ρ_i of the vector ρ. Subscript p will represent that a parameter dependent vector $x(\rho)$ is evaluated at a frozen point value g_p, e.g. $x_p := x(g_p)$. When considering a polytope centered around a frozen point value g_p, the superscript v indicates that a parameter vector $x(\rho)$ is evaluated at a vertex g_p^v of such polytope, e.g. $x_p^v := x(g_p^v)$.

Publication List

International Journal Papers

Title: LMI Conditions for Stability and State-Feedback $\mathcal{H}_\infty$ Control of Discrete-Time Multimode Multidimensional Systems
Authors: A. M. Borrell, O. Sename and V. Puig
Status: Published in in IEEE Control Systems Letters, vol. 6, pp. 2876-2881, 2022, doi: 10.1109/LCSYS.2022.3179941.
Reference: *A. M. Borrell, O. Sename and V. Puig, "LMI Conditions for Stability and State-Feedback $\mathcal{H}_\infty$ Control of Discrete-Time Multimode Multidimensional Systems," in IEEE Control Systems Letters, vol. 6, pp. 2876-2881, 2022, doi: 10.1109/LCSYS.2022.3179941.*

Title: Fixed-Structure Parameter-Dependent State Feedback Controller: an Scaled Autonomous Vehicle Path-Tracking Application
Authors: A. M. Borrell, O. Sename and V. Puig
Status: Under Review in Control Engineering Practice, Submitted 2023

International Conference Papers

Title: Control Reconfiguration of Lateral ADAS Steering Control in the Presence of Driver Errors Using Combined Parity Space / LPV Approaches
Authors: A. M. Borrell, O. Sename and V. Puig
Conference: 5th International Conference on Control and Fault-Tolerant Systems
Place: Saint-Raphael, France **Date:** September 29th - October 1st, 2021

Title: LPV Lateral Control for ADAS Based on Driver Performance Monitoring
Authors: A. M. Borrell, O. Sename and V. Puig
Conference: 11th IFAC Symposium on Fault Detection, Supervision and Safety for Technical Processes SAFEPROCESS 2022
Place: Pafos, Cyprus **Date:** June 8th - 10th, 2022
Award: Best Student Paper

Title: MPC-based optimal parameter scheduling of LPV controllers: Application to Lateral ADAS Control
Authors: Ariel M. Borrell, M. M. Morato, V. Puig and O. Sename

Conference: 30th Mediterranean Conference on Control and Automation (MED) 2022
Place: Vouliagmeni, Grece **Date:** June 28th - July 10st, 2022

Title: State-Feedback and Static-Output-Feedback Parametric Controllers Based on a Discrete-Time LPV Grid Based Approach
Authors: Ariel M. Borrell, V. Puig and O. Sename
Conference: 5th IFAC Workshop on Linear Parameter Varying Systems LPVS 2022
Place: Montreal, Canada **Date:** September 27th - 30th, 2022

Title: Design and Experimental Validation of an $\mathcal{H}_\infty$ Adaptive Cruise Control for a Scaled Car
Authors: Sayssouk, W., Atoui, H., Medero, A., Sename, O.
Conference: 10th International Conference on Mechatronics and Control Engineering ICMCE 2021.
Place: Lisbon, Portugal **Date:** July 26th - 28, 2021

Part I

Control and Modeling Background

Part I: Introduction

Part I serves as an introduction for key and required recurring concepts used in this thesis:

- Chapter 1: Provides definitions for dynamical systems and LMI conditions that will be widely used for the developments of the controller synthesis results presented in later chapters.
- Chapter 2: Describes the vehicle dynamics and the derivation of the control oriented Bicycle Model of the vehicle lateral dynamics. Here it is also presented the characteristics and parameters of the two vehicles considered for the development of results in later chapters: the high-fidelity simulation model of a Renault Megane car and the Scaled Automated Vehicle (SAV) platform developed in GIPSA-Lab.
- Chapter 3: Presents literature works which developed dynamical models to describe the steering behaviour of human drivers. Taking inspiration from these works, Chapter 3 presents two driver models which will be used for the developments of the results in the proposed ADAS strategy in this thesis. Furthermore, a system identification validation of these driver models is given, showing that indeed such models can capture the human driving characteristics.

CHAPTER 1

Background on LPV Systems and LMI Analysis

Contents

1.1 Introduction

This chapter presents some notions on control theory useful to develop control synthesis techniques for Linear Parameter Varying (LPV) systems. The theory background content presented in the following is not a deep survey of the vast literature on LPV control, rather, only topics which are essential to the concepts developed in remaining chapters of this thesis are here introduced. In this spirit, as the control tools used for controller synthesis on this thesis relate to Discrete-Time (DT) approaches rather than continuous ones, the definitions and concepts introduced in this chapter will focus only on DT systems. Moreover, in this chapter it is only presented already well-known results from the literature and general theorems related to stability and $\mathcal{H}_\infty$ norm computation of LPV systems. Contributions regarding control synthesis in these topics are presented in this thesis, however, they will be introduced in later chapters in the context for which those contributions were required.

To fully grasp the topics on this chapter, readers are expected to have some prior knowledge on Dynamical Systems Control as well as use of Optimization Techniques and specially Linear Matrix Inequalities (LMI) in control. The references listed below provide an introductory entry point to these topics.

- System norms: [Boy+94]; [PV08]; [WS94]
- Discrete-Time systems: [Oga95]; [Rob07]
- Robust control based on $\mathcal{H}_\infty$ theory: [ZD98]; [SP07]
- Use of LMI and convex optimization in control: [Boy+94]; [PV08]; [WS94]
- LPV systems: [AG95]; [Wu+96]; [AGB95]; [AA98]; [PV08]; [Tót10]; [Fer14]; [Bri14]

1.1.1 Chapter Structure

The structure of the chapter is as follows. First, in Sec. 1.2 definitions for DT dynamical systems are introduced. Then Sec. 1.3 presents some useful lemmas to manipulate Linear Matrix Inequalities (LMI) followed by LMI conditions that can be used to asses the stability and induced L_2-norm performance of an LPV system

1.2 Discrete-Time Dynamical Systems

1.2.1 Nonlinear Discrete-Time Systems

The dynamical behaviour of systems can be captured in the form of a system of nonlinear (NL) equations. Generally obtained from physics and first principles or from some identification method based on available sequential data of the system. Nonlinear dynamical systems can be defined as follows.

Definition 1.1 (Discrete-Time Nonlinear Representation)
Given the nonlinear set of first order difference equations $f(x, w) \in \mathbb{R}^{n_x}$ and the nonlinear set of zero order difference equations $h(x, w) \in \mathbb{R}^{n_z}$ the nonlinear dynamics of a system Ξ are given as follows:

$$\Xi = \begin{cases} x^+ = f(x, w) \\ z = h(x, w) \end{cases} \tag{1.1}$$

where $x \in \mathbb{R}^{n_x}$ is the state-vector, $w \in \mathbb{R}^{n_w}$ is the vector of exogenous inputs and $z \in \mathbb{R}^{n_z}$ is the vector of performance outputs. The time difference elapsed in the transition from state x to x^+ is given by a constant sampling time T_s.

In Definition 1.1, the vector of exogenous inputs w refers to all possible inputs that can affect the system, such as disturbances, sensor noises or even the reference signals used for tracking. On the other hand, the vector of performance outputs z refers to signals which are of interest to understand the behaviour of the system of study. Some examples of output signals of interest could be the measurements of some of the state variables, tracking errors or the controller action.

1.2.2 Discrete-Time Linear Systems

By means of Taylor expansion of the nonlinear systems dynamics given in Definition 1.1 around some equilibrium point (x_0, w_0), e.g. $f(x_0, w_0) = 0$, it is always possible to obtain a linear representation of the system dynamics. Such that the system matrices that define the linear dynamics around the equilibrium point are given as:

$$\begin{array}{ll} \mathcal{A} = \left.\frac{\partial f(x,w)}{\partial x}\right|_{x=x_0,w=w_0} & \mathcal{B} = \left.\frac{\partial f(x,w)}{\partial w}\right|_{x=x_0,w=w_0} \\ \mathcal{C} = \left.\frac{\partial g(x,w)}{\partial x}\right|_{x=x_0,w=w_0} & \mathcal{D} = \left.\frac{\partial g(x,w)}{\partial w}\right|_{x=x_0,w=w_0} \end{array} \tag{1.2}$$

More general, Linear Time Invariant (LTI) systems State-Space (SS) models for Discrete-Time (DT) systems are defined as follows.

Definition 1.2 (Discrete-Time State-Space Representation of Linear Time Invariant Systems) *Given matrices* $\mathcal{A} \in \mathbb{R}^{n_x \times n_x}$, $\mathcal{B} \in \mathbb{R}^{n_x \times n_w}$, $\mathcal{C} \in \mathbb{R}^{n_z \times n_x}$ *and* $\mathcal{D} \in \mathbb{R}^{n_z \times n_w}$, *the DT dynamics of an LTI system* Ξ *are given as follows:*

$$\Xi = \begin{cases} x^+ = \mathcal{A}x + \mathcal{B}w \\ z = \mathcal{C}x + \mathcal{D}w \end{cases} \tag{1.3}$$

where $x \in \mathbb{R}^{n_x}$ *is the state-vector,* $w \in \mathbb{R}^{n_w}$ *is the vector of exogenous inputs and* $z \in \mathbb{R}^{n_z}$ *is the vector of performance outputs. The time difference elapsed in the transition from state* x *to* x^+ *is given by a constant sampling time* T_s.

The success of the LTI SS representation comes from the fact that models of a dynamical system Ξ given by Eq. (1.3) allow to study in a systematic and straightforward formulation complex systems such as Multiple-Inputs Multiple-Outputs (MIMO) systems or systems made of the interconnection of many subsystems. Moreover, the fact that systems expressed as in Eq. (1.3) can be studied with the use of Linear Algebra techniques, represents a great benefit and makes the tools developed for SS systems easily transferable across many engineering domains in which control engineering may be involved. One example of such a powerful tool that emanates from the ability to use linear algebra to treat SS models is the use of Linear Matrix Inequalities (LMI) [Boy+94], which provide a flexible control and analysis solution for dynamical systems in the form of optimization problems which can be efficiently solved with Semi-Definite Programming (SDP) solvers.

1.2.3 Discrete-Time LPV Systems

Instead of linearizing the NL system in Eq. 1.1 around an equilibrium point, doing this around a trajectory, then it is obtained a Linear Parameter-Varying (LPV) system. Alternatively, one could also use the so-called *linear embedding* approach [Sha12] to obtain a pseudo-linear representation of the NL dynamics in Eq. 1.1 as an LPV representation.

The LPV systems are characterized by having a SS representation as in Definition 1.2. However, in contrast to LTI SS models, the system matrices of LPV model present parameters that evolve over time. Combining the set of varying parameters in a vector $\rho \in \mathbb{R}^m$, in this thesis the following assumptions are made.

Assumption 1.1
Each varying parameter value $\rho_i(k)$ *is known and is bounded by extremal values* $\underline{\rho}_i$ *and* $\overline{\rho}_i$ *such that* $\underline{\rho}_i \leq \rho_i(k) \leq \overline{\rho}_i$, $\forall k$. *The joint set of bounds on* ρ_i, $i = 1, \ldots, m$, *then form the varying parameter admissible space* $\Omega \in \mathbb{R}^m$, *such that* $\rho(k) \in \Omega$, $\forall k$.

Assumption 1.2
The rate of variation $\nu_i(k)$ *for each varying parameter* ρ_i *between two consecutive sampling times* k *and* $k+1$ *is bounded by* $\underline{\nu}_i$ *and* $\overline{\nu}_i$ *such that* $\underline{\nu}_i \leq \nu_i(k) \leq \overline{\nu}_i$, $\forall k$.

The SS representations of LPV systems can then be defined as follows:

Definition 1.3 (Discrete-Time State-Space Representation of Linear Parameter Varying Systems)
Given a vector of time-varying parameters $\rho \in \mathbb{R}^m$ *and matrices* $\mathcal{A}(\rho) \in \mathbb{R}^{n_x \times n_x}$, $\mathcal{B}(\rho) \in \mathbb{R}^{n_x \times n_w}$, $\mathcal{C}(\rho) \in \mathbb{R}^{n_z \times n_x}$ *and* $\mathcal{D}(\rho) \in \mathbb{R}^{n_z \times n_w}$, *the DT dynamics of an LPV system* $\Xi(\rho)$ *are given as follows:*

$$\Xi(\rho) = \begin{cases} x^+ = \mathcal{A}(\rho)x + \mathcal{B}(\rho)w \\ z = \mathcal{C}(\rho)x + \mathcal{D}(\rho)w \end{cases} \tag{1.4}$$

where $x \in \mathbb{R}^{n_x}$ *is the state-vector,* $w \in \mathbb{R}^{n_w}$ *is the vector of exogenous inputs and* $z \in \mathbb{R}^{n_z}$ *is the vector of performance outputs. The time difference elapsed in the transition from state* x *to* x^+ *is given by a constant sampling time* T_s.

In this thesis it is considered LPV systems whose system matrices are defined as affine on some basis function with dependency on the varying parameter vector as follows:

Definition 1.4 (Affine LPV Description)
Given an LPV system as in Definition 1.3, it is said to be affine in a basis function $\theta(\rho)$ *if the system matrices of the LPV system are defined as follows:*

$$\begin{array}{ll} \mathcal{A}(\rho) = \mathcal{A}_0 + \sum_{n=1}^{N} \theta_n(\rho)\mathcal{A}_n \ , & \mathcal{B}(\rho) = \mathcal{B}_0 + \sum_{n=1}^{N} \theta_n(\rho)\mathcal{B}_n \\ \mathcal{C}(\rho) = \mathcal{C}_0 + \sum_{n=1}^{N} \theta_n(\rho)\mathcal{C}_n \ , & \mathcal{D}(\rho) = \mathcal{D}_0 + \sum_{n=1}^{N} \theta_n(\rho)\mathcal{D}_n \end{array} \tag{1.5}$$

where $\mathcal{A}_0, \ldots, \mathcal{A}_n$, $\mathcal{B}_0, \ldots, \mathcal{B}_n$, $\mathcal{C}_0, \ldots, \mathcal{C}_n$ *and* $\mathcal{D}_0, \ldots, \mathcal{D}_n$ *are constant matrices. The vector*

$\theta(\rho) = (1, \theta_1(\rho), \ldots, \theta_N(\rho))$ *forms the parameter dependent basis function, with* $\theta_n(\rho) \in \mathbb{R}$ *a scalar function.*

Note that the affine description in Eq. (1.5) of the system matrices of the LPV system in Eq. (1.4) does not represent a loss of generality. This is so as both the choice of the scheduling scalar functions $\theta_n(\rho)$ and the amount N of them are arbitrary and allow for general parameter dependency. To exemplify this point, let us consider the following system:

$$\begin{bmatrix} \dot{v}_y \\ \ddot{\psi} \end{bmatrix} = \begin{bmatrix} -\frac{C_{\alpha f}+C_{\alpha r}}{m v_x} & -v_x - \frac{C_{\alpha f} l_f - C_{\alpha r} l_r}{m v_x} \\ -\frac{C_{\alpha f} l_f - C_{\alpha r} l_r}{I_z v_x} & -\frac{C_{\alpha f} l_f^2 + C_{\alpha r} l_r^2}{I_z v_x} \end{bmatrix} \begin{bmatrix} v_y \\ \dot{\psi} \end{bmatrix} + \begin{bmatrix} \frac{C_{\alpha f}}{m} \\ \frac{C_{\alpha f} l_f}{I_z} \end{bmatrix} \delta \tag{1.6}$$

As will be seen in Chapter 2, this is the so-called Bicycle Model of the vehicle lateral dynamics. The parameter v_x in Eq. (1.6) represents the vehicle longitudinal velocity which is time varying. This makes the system in Eq. (1.6) an LPV system. It is then possible to obtain an LPV representation of Eq. (1.6) according to Definition 1.3 and Definition 1.4 with basis function $\theta(v_x) = (1, v_x, \frac{1}{v_x})$ and where

$$\mathcal{A}(v_x) = \begin{bmatrix} 0 & 0 \\ 0 & 0 \end{bmatrix} + v_x \cdot \begin{bmatrix} 0 & -1 \\ 0 & 0 \end{bmatrix} + \frac{1}{v_x} \cdot \begin{bmatrix} -\frac{C_{\alpha f}+C_{\alpha r}}{m} & -\frac{C_{\alpha f} l_f - C_{\alpha r} l_r}{m} \\ -\frac{C_{\alpha f} l_f - C_{\alpha r} l_r}{I_z} & -\frac{C_{\alpha f} l_f^2 + C_{\alpha r} l_r^2}{I_z} \end{bmatrix} \tag{1.7}$$

and

$$\mathcal{B} = \begin{bmatrix} \frac{C_{\alpha f}}{m} \\ \frac{C_{\alpha f} l_f}{I_z} \end{bmatrix} \tag{1.8}$$

Interest in LPV systems come from the flexibility of the LPV modeling approach to capture time varying and non-linear behaviours in a linear-like model. Once an LPV model of the system of study have been obtained, one can extend the techniques that have been developed for LTI systems to these more complex cases. The most important extension being, without a doubt, the ability to extend LMI techniques for study and synthesis of closed-loop control systems, beyond the scope of LTI systems.

1.3 LMI Analysis of LPV Systems

1.3.1 Useful Literature Results

Before defining LMI conditions to study important properties of LPV systems, in this subsection we collect some existing results and lemmas from the literature which are used for the development of the results presented on this thesis. These conditions are well-known, however they play a key role in the development of LMI conditions in this and later chapter of this thesis, for a more exhaustive list of useful LMI conditions see [CF19].

1.3.1.1 Schur Complement

The well known Schur Complement lemma allows to transform a nonlinear matrix inequality into an equivalent LMI.

Lemma 1.1 (Schur Complement Lemma)
Given symmetric matrices Q and R, with $R \geq 0$, and a matrix S, the two following statements are equivalent:

- $\begin{bmatrix} Q & S \\ S^T & R \end{bmatrix} > 0$
- $\begin{bmatrix} R & S^T \\ S & Q \end{bmatrix} > 0$
- $Q - SR^{-1}S^T > 0$

1.3.1.2 Projection Lemma

The following lemma, known as the Projection Lemma or Elimination Lemma in the literature, allows to eliminate some variable from the matrix inequality condition. Then, this could be used to transform a Bilinear Matrix Inequality into a set of equivalent LMI, which can be efficiently solved.

Lemma 1.2 (Projection Lemma)
Given a symmetric matrix $\Psi \in \mathbb{R}^n$ and two matrices N, M of column dimension n, consider the problem of finding some matrix Θ of compatible dimensions such that

$$\Psi + N^T\Theta^T M + M^T\Theta N > 0. \tag{1.9}$$

Denote $\mathcal{N}_M$, $\mathcal{N}_N$ any matrices whose columns form bases of the null spaces of M and N respectively. Then (1.9) *is solvable for Θ if and only if*

$$\begin{cases} \mathcal{N}_M^T\Psi\mathcal{N}_M > 0 \\ \mathcal{N}_N^T\Psi\mathcal{N}_N > 0 \end{cases} \tag{1.10}$$

1.3.1.3 Simplified Young's Relation

This lemma was first used for the study of the stability of DT LTI systems in [DOBG99]. The interest of this lemma is that it allows to introduce a slack variable G in the LMI problem, such that the Lyapunov matrix gets decoupled from extra constraints that are required for the linearization of the matrix inequalities in the synthesis problem. This approach for DT then became known as G-shaping paradigm [OGB02].

Lemma 1.3 (Simplified Young's Relation [OGB02]; [CF19])
For all matrices $G \in \mathbb{R}^{n \times n}$ *and* $P > 0 \in \mathbb{R}^{n \times n}$*,*

$$G^T P G \geq G + G^T - P^{-1} \tag{1.11}$$

holds.

1.3.2 Stability of LPV Systems

Stability is one of the main important properties concerning dynamical systems. The following concerns with the Robust Stability of LPV systems in a Lyapunov sense, for more details on LPV and systems stability the reader is referenced to [Bri14]. Now, consider the LPV system from Definition 1.3 restricted to its autonomous dynamics:

$$x^+ = \mathcal{A}(\rho)x, \tag{1.12}$$

Let us consider a Parameter-Dependent Lyapunov Function (PDLF)

$$V(x, \rho) = x^T X(\rho) x \ , \tag{1.13}$$

where $X(\rho) \in \mathbb{R}^{n_x \times n_x}$ is a symmetric Positive Definite matrix referred to as Parameter-Dependent Lyapunov Matrix (PDLM). According to Lyapunov theory, if the derivation of the PDLF in Eq. (1.13) fulfills the following condition

$$V(x^+, \rho^+) - V(x, \rho) < 0 \ , \tag{1.14}$$

then, the autonomous system Eq. (1.12) is stable. Substituting Eq. (1.12) and Eq. (1.13) in Eq. (1.14) the following condition is obtained:

$$x^T[\mathcal{A}(\rho)^T X(\rho^+)\mathcal{A}(\rho) - X(\rho)]x < 0 \tag{1.15}$$

From this condition then it is obtained the following LMI which allows to prove the stability of LPV the autonomous system Eq. (1.12).

$$\mathcal{A}(\rho)^T X(\rho^+)\mathcal{A}(\rho) - X(\rho) < 0 \tag{1.16}$$

Although this condition is adequate to test the stability of LPV systems, it can not be employed for the task of controller design. For this reason it is most often modified using Schur's Complement Lemma 1.1. A key modification to the stability condition in Eq. (1.12) was introduced in [dBG99], such that it is augmented with a new slack variable. See [dBG99]; [OGB02] for more details on the benefits of this slack variable for LTI systems and [DB01b] for the case of systems with varying parameters.

The following theorem provides a extended sufficient stability condition for LPV systems making use of this extended variable.

Theorem 1.1 ([DB01b])
Consider an autonomous DT-LPV $\Xi(\rho)$ system as in Eq. (1.12)*. If, $\forall \rho \in \Omega$, there exist a symmetric matrix $X(\rho) \geq 0 \in \mathbb{R}^{n_x \times n_x}$ and a matrix $G(\rho) \in \mathbb{R}^{n_x \times n_x}$ such that the following condition holds*

$$\begin{bmatrix} G(\rho)^T + G(\rho) - X(\rho^+) & G(\rho)^T \mathcal{A}(\rho) \\ \star & X(\rho) \end{bmatrix} > 0 \ , \tag{1.17}$$

then, the DT-LPV system $\Xi(\rho)$ is robustly stable.

Proof. According to Lemma 1.3, condition Eq. (1.17) is equivalent to:

$$\begin{bmatrix} G(\rho)^T X(\rho^+)^{-1} G(\rho) & G(\rho)^T \mathcal{A}(\rho) \\ \star & X(\rho) \end{bmatrix} > 0 \tag{1.18}$$

Multiplying Eq. (1.18) on the left by $diag(\begin{bmatrix} G(\rho)^{-T} & I \end{bmatrix})$ and on the right by its transpose, then the following condition is obtained:

$$\begin{bmatrix} X(\rho^+)^{-1} & \mathcal{A}(\rho) \\ \star & X(\rho) \end{bmatrix} > 0 \tag{1.19}$$

Finally, applying Schur's Lemma 1.1 around $X(\rho^+)^{-1}$ on this last condition recovers the sufficient stability condition Eq. (1.16). This concludes the proof. ☐

1.3.3 Induced L_2-norm of LPV Systems

Dynamical systems are not only subject to their internal dynamics but also to external exogenous inputs, as seen in the DT-LPV system $\Xi(\rho)$ from Definition 1.3. For this reason it is important to quantify the robustness and sensitivity of a system to external actions. The effects that exogenous inputs w have on the performance outputs z of a system can be quantified with its induced L_2-norm.

Definition 1.5 (Induced L_2-norm [Boy+94])
The induced L_2-norm of the system $\Xi(\rho)$ as in Definition 1.3 is the quantity

$$\sup_{\|w\|_2 \neq 0} \frac{\|z\|_2}{\|w\|_2} \ , \tag{1.20}$$

where the L_2-norm of u is $\|u\|_2^2 = \int_0^\infty u^T u dt$.

Remark 1.1
Note that for an LTI system its L_2 gain equals its $\mathcal{H}_\infty$ norm [Boy+94].

Introducing the scalar value γ_∞ as an upper bound of the induced L_2-norm of a system $\Xi(\rho)$, such that

$$\frac{\|z\|_2}{\|w\|_2} \leq \gamma_\infty \ , \tag{1.21}$$

the following theorem allows to compute this value through the use of the Bounded Real Lemma LMI making use of the additional slack variable introduced in [dBG99].

Theorem 1.2 ([SBN06]; [DC+10])
Consider a DT-LPV $\Xi(\rho)$ *system as in Eq.* (1.4) *and a given scalar* γ_∞*. If,* $\forall \rho \in \Omega$*, there exist a symmetric matrix* $X(\rho) \geq 0 \in \mathbb{R}^{n_x \times n_x}$ *and a matrix* $G(\rho) \in \mathbb{R}^{n_x \times n_x}$ *such that the following condition holds*

$$\begin{bmatrix} G^T(\rho) + G(\rho) - X(\rho^+) & G^T(\rho)\mathcal{A}(\rho) & G^T(\rho)\mathcal{B}(\rho) & 0 \\ \star & X(\rho) & 0 & \mathcal{C}(\rho)^T \\ \star & \star & \gamma_\infty I & \mathcal{D}(\rho)^T \\ \star & \star & \star & \gamma_\infty I \end{bmatrix} > 0 \tag{1.22}$$

then, the DT-LPV system $\Xi(\rho)$ *is robustly stable with* $\frac{\|z\|_2}{\|w\|_2} < \gamma_\infty$.

Proof. Eq. (1.21) is equivalent to the following inequality condition

$$\frac{1}{\gamma_\infty} z^T z \leq \gamma_\infty w^T w \tag{1.23}$$

As such, if the following condition holds

$$V(x^+, \rho^+) - V(x, \rho) + \frac{1}{\gamma_\infty} z^T z - \gamma_\infty w^T w < 0 \ , \tag{1.24}$$

then, the LPV system $\Xi(\rho)$ is stable with γ_∞ as an upper bound on its induced L_2 gain. Employing a PDLF

$$V(x, \rho) = x^T X(\rho) x \tag{1.25}$$

and substituting Eq. (1.4) into Eq. (1.24) the following condition is obtained:

$$\begin{bmatrix} x \\ w \end{bmatrix}^T \begin{bmatrix} \mathcal{A}^T X^+ \mathcal{A} - X + \frac{1}{\gamma_\infty}\mathcal{C}^T\mathcal{C} & \mathcal{A}^T X^+ \mathcal{B} + \frac{1}{\gamma_\infty}\mathcal{C}^T\mathcal{D} \\ \star & \mathcal{B}^T X^+ \mathcal{B} + \frac{1}{\gamma_\infty}\mathcal{D}^T\mathcal{D} - \gamma_\infty I \end{bmatrix} \begin{bmatrix} x \\ w \end{bmatrix} < 0, \tag{1.26}$$

Note that in Eq. (1.26) the dependency on ρ of the state matrices of the DT-LPV system $\Xi(\rho)$ and the PDLM $X(\rho)$ have been omitted for the sake of brevity. Applying consecutive Schur Complements Lemma 1.1 in Eq. (1.26) around X^+ and $\frac{1}{\gamma_\infty} I$ followed by a congruence transformation by $diag(\begin{bmatrix} G(\rho)^T & I & I & I \end{bmatrix})$, the following equivalent condition is obtained:

$$\begin{bmatrix} G^T(\rho) X(\rho^+)^{-1} G(\rho) & G^T(\rho)\mathcal{A}(\rho) & G^T(\rho)\mathcal{B}(\rho) & 0 \\ \star & X(\rho) & 0 & \mathcal{C}(\rho)^T \\ \star & \star & \gamma_\infty I & \mathcal{D}(\rho)^T \\ \star & \star & \star & \gamma_\infty I \end{bmatrix} > 0 \tag{1.27}$$

Finally, applying the Simplified Young's Relation 1.3 recovers Eq. (1.22) from Theorem 1.2 as a sufficient condition of Eq. (1.24). This concludes the proof. □

Due to the addition of the slack variable G, condition Eq.(1.22) is known in the literature as Extended Bounded Real Lemma. This condition and variations of it have been well studied in the literature, see [DB01a]; [SBN06]; [DC+10]; [Hil+14]; [PO19] and references therein. The main objective with the introduction of the slack variable G is to reduce the conservatism of the LMI. This is obviously achieved as the new variable introduces new degrees of freedom that the SDP solver can exploit. But more importantly, as will be seen in later chapters, this slack variable allows to decouple the Lyapunov Matrix X from the controller synthesis task, instead the variable G is employed for this. It can be seen in [OGB02] a comparison of synthesis problems for DT LTI systems with and without this slack variable, with the case in which G was employed obtaining much less conservative in terms of upper bounds for γ_∞.

As seen in Remark 1.1, for an LTI system its L_2 gain equals its $\mathcal{H}_\infty$ norm. For this reason it is often extrapolated to LPV systems the term $\mathcal{H}_\infty$ control. However, strictly speaking induced L_2-norm is the most correct terminology when working with LPV systems. In any case, the fact that bounds on the induced L_2-norm of LPV systems can be computed efficiently through LMI techniques shows the main advantages of LPV systems. This is, the extension to LPV systems powerful LMI approaches from the LTI literature. As will be seen in the remaining of this thesis, one could use derivations of Theorem 1.2 to extend the $\mathcal{H}_\infty$ control theory [ZD98] to LPV systems.

1.3.4 Dual Theorems for Stability and Induced L_2-norm of LPV Systems

Depending on the intended purpose, it may be more interesting to consider the dual version of the conditions presented in Theorem 1.1 and Theorem 1.2. This can be simply done by using the controllability-observability duality of SS models, e.g. the relation between a SS system and its dual is

$$\begin{array}{ll} \mathcal{A} \to \mathcal{A}^T & \mathcal{B} \to \mathcal{C}^T \\ \mathcal{C} \to \mathcal{B}^T & \mathcal{D} \to \mathcal{D}^T \end{array} \tag{1.28}$$

Using the duality relation seen in Eq. (1.28), the following theorem provides a sufficient condition to test the stability of a DT-LPV system.

Theorem 1.3
Consider an autonomous DT-LPV $\Xi(\rho)$ system as in Eq. (1.12). If, $\forall \rho \in \Omega$, there exist a symmetric matrix $X(\rho) \geq 0 \in \mathbb{R}^{n_x \times n_x}$ and a matrix $G(\rho) \in \mathbb{R}^{n_x \times n_x}$ such that the following condition holds

$$\begin{bmatrix} G(\rho)^T + G(\rho) - X(\rho^+) & G(\rho)^T \mathcal{A}(\rho)^T \\ \star & X(\rho) \end{bmatrix} > 0 \ , \tag{1.29}$$

then, the DT-LPV system $\Xi(\rho)$ is robustly stable.

Analogously, the following theorem provides a sufficient condition to compute and upper bound γ_∞ on the induced L_2-norm of a system DT-LPV system.

Theorem 1.4
Consider a DT-LPV $\Xi(\rho)$ system as in Eq. (1.4) and a given scalar γ_∞. If, $\forall \rho \in \Omega$, there exist a symmetric matrix $X(\rho) \geq 0 \in \mathbb{R}^{n_x \times n_x}$ and a matrix $G(\rho) \in \mathbb{R}^{n_x \times n_x}$ such that the following

condition holds

$$\begin{bmatrix} G^T(\rho)+G(\rho)-X(\rho^+) & G^T(\rho)\mathcal{A}(\rho)^T & G^T(\rho)\mathcal{C}(\rho)^T & 0 \\ \star & X(\rho) & 0 & \mathcal{B}(\rho) \\ \star & \star & \gamma_\infty I & \mathcal{D}(\rho) \\ \star & \star & \star & \gamma_\infty I \end{bmatrix} > 0 \qquad (1.30)$$

then, the DT-LPV system $\Xi(\rho)$ *is robustly stable with* $\frac{\|z\|_2}{\|w\|_2} < \gamma_\infty$.

The proofs of both of these theorems are straightforward. Given the proven sufficient conditions Eq. (1.17) and Eq. (1.22) replace the system matrices $\mathcal{A}$, $\mathcal{B}$, $\mathcal{C}$ and $\mathcal{D}$ by their dual according to Eq. (1.28) to obtain the conditions in Eq. (1.29) and Eq. (1.30) respectively.

1.4 Conclusions

In this chapter it has been introduced the concept of DT-LPV systems based on an SS representation, which enables arbitrary parameter dependency through an affine description of the LPV system using basis functions. Despite its ability to capture nonlinear behavior, the SS representation of LPV systems facilitates the use of LMI-based techniques to prove important system characteristics. In this chapter, LMI conditions have been provided to demonstrate the LPV system robust stability and determine its induced L_2-norm. The LMI conditions and lemmas presented in this chapter will be extensively utilized throughout the remainder of this thesis to calculate robust and reconfigurable LPV controllers.

CHAPTER 2

Vehicle Dynamics: Modeling and Identification

Contents

2.1 Introduction

In this chapter we cover the basics of longitudinal and lateral vehicle dynamics and the derivation of the so called bicycle model, commonly used for the design task of vehicle lateral controls [Raj11]; [Gá+17]; [Cor+21]; [Ato+22b]. In this thesis two different vehicles have been considered. Firstly, a high fidelity model of a Renault Megane car, developed and presented in a former thesis [Fer14], was available as a Simulink model. This model will be used for preliminary validation and development of the results presented in this thesis. The second vehicle was a Scaled Automated Vehicle (SAV) developed recently in GIPSA-Lab, which will be employed for experimental validation of some of the thesis works.

The dynamical models developed in this chapter are based on first principles physical laws. As such, they are developed as a set of Continuous-Time (CT) differential equations, which can be eventually simplified into pure CT-LPV models. On the other hand, most of the synthesis techniques employed in this thesis use Discrete-Time approaches. However, direct discretization approaches for LPV systems are not straightforward [Tót10]. Therefore, this chapter will deal only with CT models derived from first principles. In futures chapters, the discretization method of the models here presented will be detailed when required for control design.

2.1.1 Chapter Structure

The organization of the chapter is as follows. Sect. 2.2 covers the nonlinear vehicle dynamics considering both longitudinal and lateral couplings, then with some assumptions it is presented the so-called bicycle model employed for control design of the lateral dynamics. Following this, Sec. 2.3 introduces some aspects of the Renault Megane simulation model and its parameters. Then, Sec. 2.4 presents an overview of the test platform for the Scaled Automated Vehicle, the identification process carried to determine the model parameters and finally the control-oriented bicycle model representation of its lateral dynamics is introduced.

2.2 Vehicle Dynamics

2.2.1 Nonlinear Dynamics

Modern road vehicles are very complex systems, which makes the control of vehicle dynamics a hard but interesting problem. They present deep couplings between the multiple subsystems that govern its lateral, longitudinal and vertical dynamics. Moreover, at high speeds the vehicle is affected by larger aerodynamic effects which can change dramatically the vehicles behaviour. In addition, the forces at the tires (responsible for all vehicle motions) are highly non-linear and depend on the surface in which the vehicle is moving.

In this work, for the derivation of control oriented models, it is assumed that the lateral and longitudinal components of the vehicle's acceleration are such that no vehicle lateral drift or wheel slipping occur. Under this assumption most of the vehicle dynamics complexities can be ignored or simplified. Specifically, the small accelerations assumption allows to decouple the lateral dynamics from the rest and guarantees that the tire forces remain within its linear operating region. The interested reader in more detailed descriptions of the full dynamics involved is referenced to [MMM95]; [KN00]; [Jaz08]; [Raj11].

As seen from Fig. 2.1, assuming an orthogonal coordinate frame fixed at the vehicle's Center of Mass (CoM), the coupled lateral and longitudinal dynamics of a vehicle is governed by three state variables. These variables are the longitudinal velocity v_x, the lateral velocity v_y and the vehicle's angular speed in its z axis or yaw rate $\dot{\psi}$, all defined at the vehicle

CoM. The derivation of the governing equations for the vehicle state variables are made in the following assuming a vehicle architecture such that the longitudinal active forces of the vehicle are applied in both rear wheels. Note that this is possible in modern cars thanks to traction control systems or in-wheel electric motors.

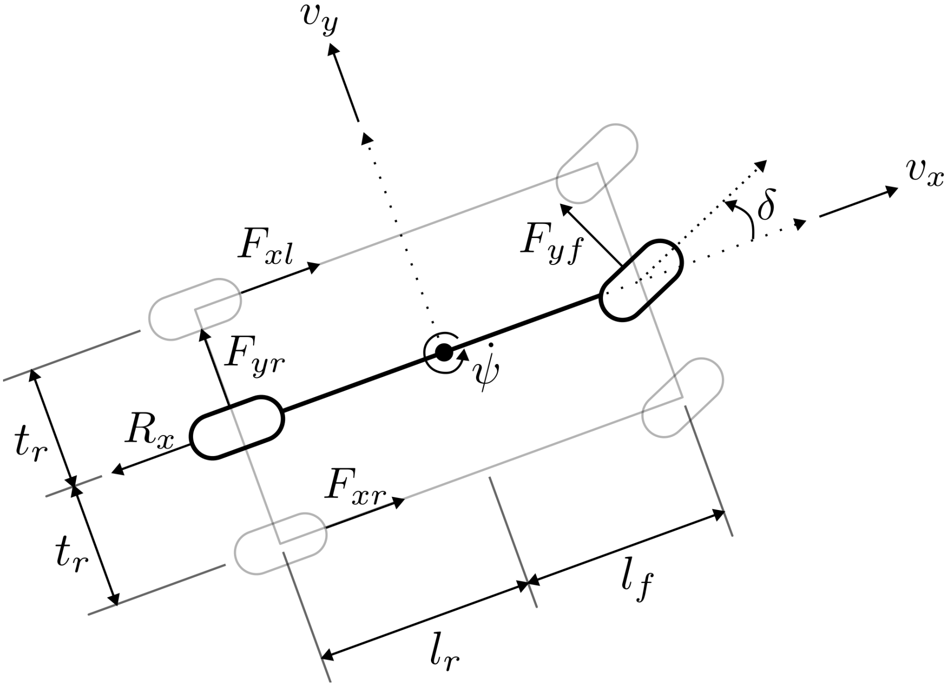

Figure 2.1: Vehicle force diagram at local coordinate frame.

Neglecting longitudinal traction forces, the forces acting on the vehicle are compressed into a single track (hence the name *bicycle* model). The lateral forces provided by the rear and front tires are F_{yr} and F_{yf}, respectively. Note that the lateral force of the front wheel is given with respect a front-wheel-fixed frame of reference. The front-wheel-fixed frame is rotated on the z axis with respect the vehicle's reference frame by an angle δ, which correspond with the angle of the front steering wheels. The friction forces are denoted by R_x, and are assumed to be opposite to the vehicle's longitudinal velocity.

For the vehicle architecture depicted in Fig. 2.1, F_{xl} and F_{xr} represent the longitudinal force applied at the rear left and rear right wheels, respectively. These forces can be either used to accelerate the vehicle or as braking forces. Note that in the case were $F_{xl} \neq F_{xr}$, this would result in an induced moment of force on the z axis of the vehicle, for this reason it is important to account for the traction forces F_{xi} in their actual point of application.

Based on Fig. 2.1 and according to Newton's law and a balance of moments of force at the CoM on the z axis, the equations of motions that dominate the vehicle dynamics are the following:

$$m(\dot{v}_x - \dot{\psi} v_y) = F_{xl} + F_{xr} - F_{yf} \sin\delta - R_x \tag{2.1a}$$

$$m(\dot{v}_y + \dot{\psi} v_x) = F_{yf} \cos\delta + F_{yr} \tag{2.1b}$$

$$I_z \ddot{\psi} = l_f F_{yf} \cos\delta - l_r F_{yr} + t_r F_{xr} - t_r F_{xl} \tag{2.1c}$$

The description of the forces appearing in Eq. (2.1) depend on the tire model employed. The following description of the tire forces are based on simplified small slip models [Raj11]. The longitudinal tire forces can be modeled as:

$$\begin{aligned} F_{xl} &= C_\sigma \sigma_l \\ F_{xr} &= C_\sigma \sigma_r \end{aligned} \tag{2.2}$$

The coefficient C_σ is called the longitudinal tire stiffness parameter, here it is assumed equal for both left and right rear wheels. The longitudinal slip ratio for the left rear wheel σ_l is defined as

$$\begin{aligned} \sigma_l &= \frac{r\omega_l - v_{xl}}{v_{xl}}, \text{ during braking} \\ \sigma_l &= \frac{r\omega_l - v_{xl}}{r\omega_l}, \text{ during acceleration} \end{aligned} \tag{2.3}$$

with r the effective wheel radius, ω_l the angular speed of the left rear wheel and v_{xl} the longitudinal speed at the left rear wheel center. The longitudinal slip ratio for the right rear wheel σ_r is similarly defined as

$$\begin{aligned} \sigma_r &= \frac{r\omega_r - v_{xr}}{v_{xr}}, \text{ during braking} \\ \sigma_r &= \frac{r\omega_r - v_{xr}}{r\omega_r}, \text{ during acceleration} \end{aligned} \tag{2.4}$$

with ω_r the angular speed of the right rear wheel and v_{xr} the longitudinal speed at the right rear wheel center.

The lateral forces applied to the front and rear wheels are modeled as

$$\begin{aligned} F_{yf} &= C_{\alpha f} \alpha_f \\ F_{yr} &= C_{\alpha r} \alpha_r \end{aligned} \tag{2.5}$$

where $C_{\alpha f}$ and $C_{\alpha r}$ are the front and rear cornering stiffness coefficients respectively. The front wheels side slip angle is defined as

$$\alpha_f = \delta - \arctan\left(\frac{v_y + l_f \dot{\psi}}{v_x}\right) \tag{2.6}$$

On the other hand, the rear wheels side slip angle is defined as

$$\alpha_r = -\arctan\left(\frac{v_y - l_r \dot{\psi}}{v_x}\right) \tag{2.7}$$

Note that the model for the tire forces in Eq. (2.2) and Eq. (2.5) are linear on the stiffness parameters C_σ and $C_{\alpha i}$. This is only true as long as the wheels side slip angles and slip ratios are small. In the case where the tires present high slip ratios or the vehicle presents high lateral accelerations, then these simple models would misrepresent the real tire forces. In order to obtain tire force models valid for a large range of scenarios one would then need to resort to empirical nonlinear tire models such as the so-called Magic Formula model by Pacejka [Pac12].

Finally, the friction forces are modeled according to the following model taken from [Jaz08]

$$R_x = mg(\mu_0 + \mu_1 v_x^4) \tag{2.8}$$

where μ_0 and μ_1 are friction coefficients. From the different models presented in [Jaz08], this model was chosen as it is the one that gave the best results during the identification of the SAV dynamics, which is the topic of Sec. 2.4.2.

2.2.2 Bicycle Model for the Lateral Dynamics

From the balance of forces and moments in Eq. (2.1), focusing on the states that drive the vehicle lateral dynamics, e.g. the lateral velocity v_y and the yaw rate $\dot\psi$, the following assumptions allow one to simplify the coupled nonlinear vehicle model into a control-oriented model of the vehicle lateral dynamics.

Assumption 2.1
The vehicle is submitted to small or moderate lateral accelerations, such that the coupling effect between the lateral dynamics and longitudinal dynamics can be discarded.

Assumption 2.2
The steering angle δ remains sufficiently small such that the small angle approximations $\sin\delta \approx \delta$ and $\cos\delta \approx 1$ holds.

Assumption 2.3
The tire slip ratio and wheel side slip angles are sufficiently small such that the tire forces remain within its linear behaviour zone. Then, the tire forces are given by Eq. (2.2) and Eq. (2.5). Moreover, in Eq. (2.6) and Eq. (2.7) the small angle approximation $\arctan x \approx x$ holds.

Then, the following control oriented model can be employed for the task of controller synthesis.

Definition 2.1 (Bicycle Model [Raj11])
The lateral vehicle dynamics is given by the following state-space model

$$\begin{bmatrix} \dot v_y \\ \ddot\psi \end{bmatrix} = \begin{bmatrix} -\frac{C_{\alpha f}+C_{\alpha r}}{m v_x} & -v_x - \frac{C_{\alpha f} l_f - C_{\alpha r} l_r}{m v_x} \\ -\frac{C_{\alpha f} l_f - C_{\alpha r} l_r}{I_z v_x} & -\frac{C_{\alpha f} l_f^2 + C_{\alpha r} l_r^2}{I_z v_x} \end{bmatrix} \begin{bmatrix} v_y \\ \dot\psi \end{bmatrix} + \begin{bmatrix} \frac{C_{\alpha f}}{m} \\ \frac{C_{\alpha f} l_f}{I_z} \end{bmatrix} \delta \tag{2.9}$$

Note that the Bicycle Model in Eq. (2.9) depends on the longitudinal velocity v_x of the vehicle. As the velocity is a varying variable of the vehicle, this makes the Bicycle Model a pure LPV system with v_x as its varying parameter.

2.2.3 Relation between the Vehicle and a Desired Trajectory

So far, the vehicle has been defined based on its dynamic variables. However, for vehicle control, it is important to establish the relationship between the vehicle and a desired trajectory. Figure 2.2 provides an illustration of the error signals used for this purpose.

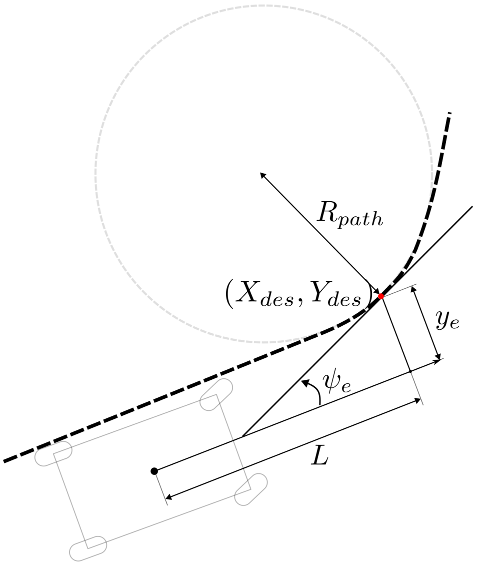

Figure 2.2: Vehicle heading and lateral error at look-ahead point.

First of all, note that the error signals are not defined at the vehicle CoM but at a distance L. This distance is called the look-ahead distance and it is defined in this thesis as

$$L = t_p v_x \ , \tag{2.10}$$

where t_p is a constant preview time in seconds. At the look-ahead distance, y_e then defines the lateral error of the vehicle to the orthogonal point on the desired trajectory. This orthogonal point is the desired tracking point (X_{des}, Y_{des}), marked in red in Fig. 2.2. The angle formed by the vehicle longitudinal velocity and the tangent line at the trajectory point (X_{des}, Y_{des}) defines the heading error angle ψ_e.

Note that the trajectory at the point (X_{des}, Y_{des}) is defined by an equivalent radius R_{path}. Using this equivalent radius, the road curvature is then defined as

$$k_{path} = \frac{1}{R_{path}} \tag{2.11}$$

2.3 Renault Megane Model and Parameters

For the purpose of validation and first design iterations of the results provided in this thesis it was first used a high-fidelity simulator of a real Renault Megane Coupé car for Simulink. Note that most of the model equations were first presented in [PV08] and later refined in [Fer14].

An interesting point about this simulator is that the model structure and parameters were identified and validated with real-data coming from real vehicle test experiments. Additionally, the model does not only cover the lateral and longitudinal dynamics of the vehicle but it also captures the behaviour of the suspension system. Thus capturing the vertical dynamics of the car as well as the load transfers due to changes in acceleration.

Moreover, the tire forces are not modeled using the small slip tire models as seen in Eq. (2.2) and Eq. (2.5). Instead the tire forces are modeled from an identified Magic Formula representation [Pac12]. The full set of model equations and model parameters for the Renault Megane Simulator model can be found in the thesis [Fer14]. From the accuracy of the identification results with regards the empirical data presented there, it can be said that the Simulink Renault Megane simulator exhibits a high level of fidelity.

2.3.1 Bicycle Model Parameters for the Renault Megane Car

For the task of lateral control design for the Renault Megane car it is used the Bicycle Model seen in Definition 2.1 with the following values for the model parameters:

Table 2.1: Renault Megane Bicycle Model Parameters

Parameter	Value
l_f	1.177
l_r	1.358
m	1400
I_z	1960
$C_{\alpha f}$	84085
$C_{\alpha r}$	87342

2.3.2 Augmented Bicycle Model for Differential Braking

Assuming that it is possible to use different amounts of braking forces on the right and left rear wheels. So, different values for F_{xl} and F_{xr} according to the vehicle architecture depicted in Fig. 2.1. Then, this differential braking can be used to induce a moment of force M_z on the z-axis of the vehicle. In order to make use of this effect as an additional control input for the Renault Megane model, the following extended version of the Bicycle Model [Dou+13] can be used for the task of controller synthesis.

Definition 2.2 (Extended Bicycle Model)
The lateral vehicle dynamics with additional induced moment of force on the z-axis is given by the following state-space model:

$$\begin{bmatrix} \dot{v}_y \\ \ddot{\psi} \end{bmatrix} = \begin{bmatrix} -\frac{C_{\alpha f}+C_{\alpha r}}{m v_x} & -v_x - \frac{C_{\alpha f} l_f - C_{\alpha r} l_r}{m v_x} \\ -\frac{C_{\alpha f} l_f - C_{\alpha r} l_r}{I_z v_x} & -\frac{C_{\alpha f} l_f^2 + C_{\alpha r} l_r^2}{I_z v_x} \end{bmatrix} \begin{bmatrix} v_y \\ \dot{\psi} \end{bmatrix} + \begin{bmatrix} \frac{C_{\alpha f}}{m} & 0 \\ \frac{C_{\alpha f} l_f}{I_z} & \frac{1}{I_z} \end{bmatrix} \begin{bmatrix} \delta \\ M_z \end{bmatrix} \tag{2.12}$$

For the Renault Megane model, the parameters of the Extended Bicycle Model are given in Table 2.1. Note that in the real-time implementation, for a given induced yaw moment of force M_z, computed by the controller, the braking torques that need to be applied on the left T_{brl} and right T_{brr} rear wheels can be assigned according to the following relations:

$$T_{brl} = \begin{cases} \frac{R \cdot M_z}{t_f}, & \text{if } M_z \geq 0 \\ 0, & \text{otherwise} \end{cases}, \quad T_{brr} = \begin{cases} \frac{-R \cdot M_z}{t_f}, & \text{if } M_z < 0 \\ 0, & \text{otherwise} \end{cases} \tag{2.13}$$

where $R = 0.3m$ is the radius of the wheel and $t_f = 0.7m$ is the distance from the wheel to the center-line of the car in the considered Renault Megane car.

Remark 2.1
It is considered to only apply the differential braking forces on the rear wheels in order to avoid coupling effects between braking and steering if the differential braking forces were to be applied on the front wheels.

2.4 Scaled Automated Vehicle

In this section an overview of the components of the Scaled Automated Vehicle platform as well as its communication architecture are presented. Then, we present the approach for parameter identification carried out for the SAV dynamics and finally control-oriented models that will be used in later chapter of this thesis for controller synthesis are introduced.

2.4.1 Platform Overview

The Scaled Automated Vehicle (SAV) Test Platform at GIPSA-Lab is a 1:12 scaled vehicle running in a Motion Capture room, see Fig. 2.3, designed to test control and planning algorithms for autonomous vehicles. The main components of the platform are the Motion Capture System, a remote desktop PC and the SAV RC Car. The Motion Capture system is an infrared Vicon Tracker system, capturing at a $100 H_z$ frequency the position and orientation of the SAV on the track. The SAV is a modified RC Car, equipped with two Brushless DC (BLDC) motors for longitudinal traction on the rear wheels and a Servo Motor as the front wheels steering actuator. Finally, the remote desktop PC runs the ROS2 software [Mac+22]

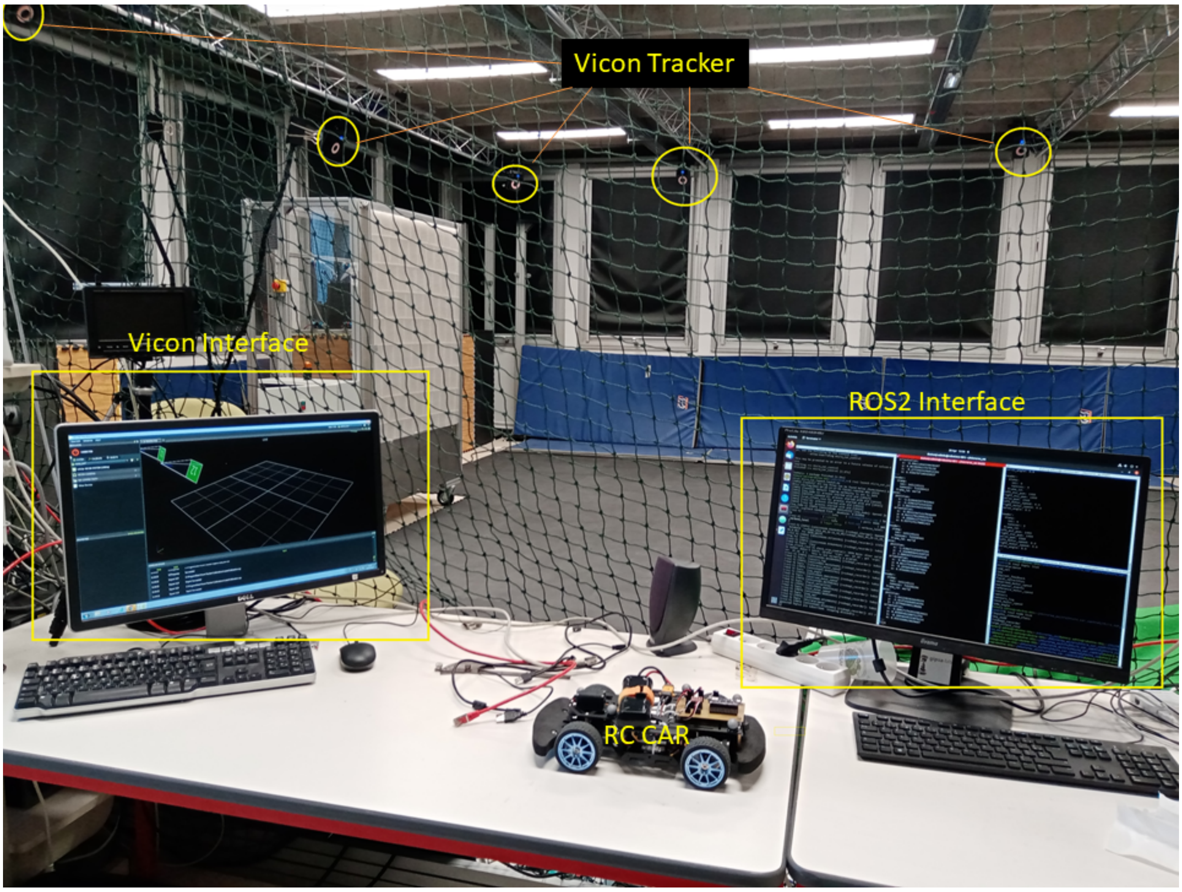

Figure 2.3: Scaled Automated Vehicle Test Platform.

to capture and process all the information from the Vicon Tracker system and car sensors. It also executes the control algorithms that are sent to the car via WiFi.

More details on the platform architecture and communications can be seen in Fig. 2.4. The SAV is controlled by an Arduino RP2040 microcontroller board. The RP2040 board runs microROS, which is used to both receive and send information with the remote PC. The information sent to the remote PC are the IMU measurements, angular speed readings from a dedicated hall-effect encoder for each BLDC motors and the voltage and current measurements from the battery. On the other hand, it receives the set-points commands for the BLDC motors angular speed and Servo Motor steering angle. It should be noted that the RP2040 board acts only as communication transmitter between the onboard sensors/actuators and the remote PC. Specifically, the lateral control law is processed remotely and only the communication with the Servo Motor is handled onboard the SAV.

The task of the remote PC is to handle and process all the data and information coming from the multiple sensors on the platform. The communication layer with the other platform components is handled by the ROS2 software tool by means of subscriptions to the multiple nodes and topics on the software. Importantly, there exist ROS2 libraries that allow to directly access the information from the Vicon mocap system. Whereas the WiFi communication protocol with the SAV is handled automatically by ROS2, the engineering task in this case reduces to subscribing and publishing the information on the ROS2 topics environment. The planning and control algorithm for the SAV are also programmed on the ROS2 environment at the remote PC using Python as the programming language. This is important as it means that the complexity of the algorithms will not be affected by the limited onboard memory and computing power on the SAV.

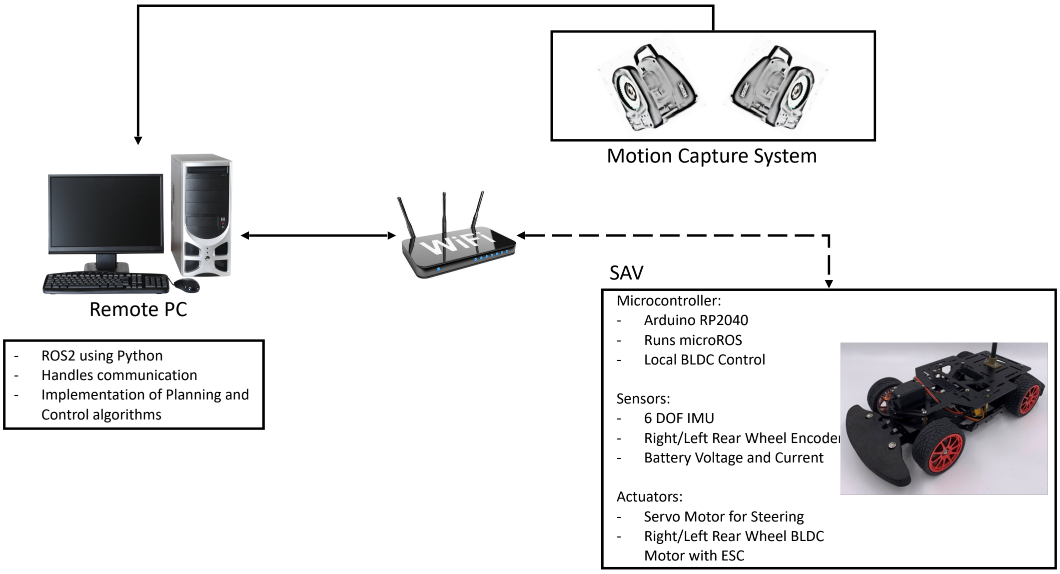

Figure 2.4: SAV Platform Architecture and Communications.

The Vicon Tracker connects to an interface PC, shown in Fig. 2.3 as Vicon Interface, which is itself connected with the remote ROS2 PC. The Vicon mocap system works by emitting infrared light, which is reflected by small balls made of infrared reflecting material and which are attached to the SAV. By using multiple infrared cameras, the Vicon system can then detect the position and orientation within the track of the SAV. The position detection by the Vicon system is done with a sub-millimeter accuracy at a frequency of $100H_z$. The precision and low noise from the position and orientation measurement obtained from the mocap system enables smooth and accurate derivation of these signals. As a result, the main signals used for vehicle control, e.g. yaw rate $\dot{\psi}$ and longitudinal v_x and lateral v_y velocities, are obtained from the derivative of the orientation and position signals from the Vicon system. Note that all of the signal processing is done remotely on the ROS2 PC.

2.4.2 SAV Parameter Identification

In the following the identification process to find suitable values for the model parameters that characterize the behaviour of the SAV dynamics is described. To identify these non measurable parameters a non-linear identification was performed, with the identification method consisting on a Prediction-Error Identification one solving the following non-linear optimization problem [THH12]

$$\min_{\Omega} \sum_{i=1}^{n_y} Q_i \cdot \mathrm{rms}(y_i - \hat{y}_i(\hat{x}, u)) \ , \ Q_i \in \mathbb{R}^+ \tag{2.14}$$

where $\Omega \in \mathbb{R}^{16}$ is the set of parameters to be identified and represents the optimization variables and Q_i is a positive scalar used to weight differently the estimation errors in the optimization. The list of all parameters in the set Ω can be found in Table 2.2. The vector y_i contains measured values for each of the SAV dynamics outputs such that $y \in \mathbb{R}^{n_y \times N}$, with $n_y = 3$ the number of measured signals and N the total amount of sampled measurements. For the SAV, the measured outputs are all three system state variables:

$$y = \begin{bmatrix} v_x & v_y & \dot{\psi} \end{bmatrix}^T \tag{2.15}$$

Meanwhile, $\hat{y}(\hat{x}, u)) \in \mathbb{R}^{n_y \times N}$ contains the open-loop output estimation given by the model dynamics, where $\hat{x}$ are the model states and u are the inputs that drive the SAV dynamics.

As seen in Section 2.2, according to Fig. 2.1 the equations that describe the motion of the SAV car are given by Eq. (2.1), with Eq. (2.1) representing the non linear model whose parameters we are interested to identify in order to describe accurately the SAV dynamics.

With regards the model inputs according to Eq. (2.1) and the tire forces Eq. (2.2) and Eq. (2.5), not all physical variables are available on the SAV platform. The rear wheel angular velocities ω_l and ω_r, which drive the longitudinal forces, are available thanks to the dedicated hall-effect encoders on the wheel BLDC motors. However, the actual steering angle δ of the front wheels is not measured. For this reason, the nonlinear model of the SAV dynamics for identification is augmented with the following second order model representing the steering servomotor actuator.

$$\begin{cases} \begin{bmatrix} \dot{\delta} \\ \ddot{\delta} \end{bmatrix} = \begin{bmatrix} 0 & 1 \\ -\omega_n^2 & -2\zeta\omega_n \end{bmatrix} \begin{bmatrix} \delta \\ \dot{\delta} \end{bmatrix} + \begin{bmatrix} 0 \\ \omega_n^2 \end{bmatrix} \delta^*(t - \tau) \\ \delta = \begin{bmatrix} 1 & 0 \end{bmatrix} \begin{bmatrix} \delta \\ \dot{\delta} \end{bmatrix} \end{cases} \tag{2.16}$$

which is a SS representation of the following second order transfer function with pure time delay, presented in Eq. (2.16) as an input delay.

$$S(s) = \frac{\delta(s)}{\delta^*(s)} = \frac{\omega_n^2}{s^2 + 2\zeta\omega_n s + \omega_n^2} e^{-\tau s} \tag{2.17}$$

The choice of steering actuator model have been influenced by the one used in [Kap+22]. Note that according with Eq. (2.16), the servo motor input is the steering angle command δ^* $[rad]$ that is sent from the Remote ROS PC to the servomotor on the SAV car, the servomotor model output δ is the actual front wheels angle, which will be feed into the model in Eq. (2.1). In addition, notice that the defining second order transfer function parameters ω_n, ζ and τ are also parameters to be found during the identification process. Now, using the nonlinear model Eq. (2.1) and the servomotor transfer function Eq. (2.16) the inputs of the extended dynamics are

$$u = \begin{bmatrix} \delta^* & \omega_l & \omega_n \end{bmatrix}^T \tag{2.18}$$

and the states of the extended model are

$$\hat{x} = \begin{bmatrix} \hat{v}_x & \hat{v}_y & \hat{\dot{\psi}} & \hat{\delta} & \hat{\dot{\delta}} \end{bmatrix}^T \tag{2.19}$$

where $\hat{\delta}$ and $\hat{\dot{\delta}}$ are the states of the servomotor model according to Eq. (2.16).

The tire forces have been modeled here considering some modifications of the previous models seen in Eq. (2.2) and Eq. (2.5). For the longitudinal forces we used the following representation:

$$\begin{aligned} F_{xl} &= C_\sigma(v_x)\sigma_l \\ F_{xr} &= C_\sigma(v_x)\sigma_r \end{aligned} \tag{2.20}$$

Meanwhile, the following model for the lateral wheel forces has been considered

$$\begin{aligned} F_{yf} &= C_{\alpha f}(v_x)\alpha_f \\ F_{yr} &= C_{\alpha r}(v_x)\alpha_r \end{aligned} \tag{2.21}$$

Remark 2.2

The differences in Eq. (2.20) *and Eq.* (2.21) *with respect Eq.* (2.2) *and Eq.* (2.5) *consists in the fact that the tire stiffness coefficients have been here modified to depend on the vehicle longitudinal speed* v_x. *For this dependency the following quadratic polynomials on* v_x *for each of the tire stiffness coefficients are considered.*

$$C_\sigma(v_x) = C_{\sigma 2}v_x^2 + C_{\sigma 1}v_x + C_{\sigma 0} \tag{2.22}$$

$$C_{\alpha f}(v_x) = C_{\alpha f2}v_x^2 + C_{\alpha f1}v_x + C_{\alpha f0} \tag{2.23}$$

$$C_{\alpha r}(v_x) = C_{\alpha r2}v_x^2 + C_{\alpha r1}v_x + C_{\alpha r0} \tag{2.24}$$

Given the dynamics model Eq. (2.1) extended with the servomotor model according to Eq. (2.16), tire forces according to Eq. (2.20) and Eq. (2.21), a set of parameters Ω, a series of length N of model inputs u and some initial conditions for $\hat{x}$; one could then compute the open-loop model output $\hat{y}(\hat{x}, u)$. Moreover, iterating over different values on the parameter set Ω and with a given series of measurements y one could try to solve the optimization problem given in Eq. (2.14). In practice, this was done using the FMINCON solver with values for the weight $Q = [1, 10, 1]$. See that according to the measured variables y as in Eq. (2.15), the weight $Q_i = 10$ is used to weight more the rms of $v_y - \hat{v}_y$ for the estimation error of the lateral velocity. Table 2.2 presents the values for each of the identified parameters of the model as well as the minimum and maximum values used as constraints for each parameter in the optimization. Meanwhile, in Table 2.3 the SAV car parameters that can be measured are collected.

From the identified values seen in Table 2.2, it is important to highlight the estimated value for the pure input delay present in the servomotor of 0.1761 seconds. Recall that according to

Table 2.2: SAV Identified Model Parameters

Parameter	Value	min	max
$C_{\sigma 2}$	3.2119	-50	50
$C_{\sigma 1}$	-2.3465	-50	50
$C_{\sigma 0}$	2.6469	-50	50
$C_{\alpha f2}$	0.4967	-50	50
$C_{\alpha f1}$	4.3104	-50	50
$C_{\alpha f0}$	-1.0640	-50	50
$C_{\alpha r2}$	5.9987	-50	50
$C_{\alpha r1}$	2.5630	-50	50
$C_{\alpha r0}$	-0.0770	-50	50
ζ	1.4513	0.3	10
ω_n	38.5022	1	50
τ	0.1761	0	1
I_z	0.0059	1×10^{-4}	0.5
r	0.0322	0.03	0.0325
μ_0	4.8314×10^{-4}	0	1
μ_1	0.0022	0	1

Table 2.3: SAV Measured Model Parameters

Parameter	Value
l_f	0.0691
l_r	0.1049
t_r	0.0435
m	1.1937

the SAV platform architecture in Fig. 2.4, the steering command is processed on the Remote ROS PC, then it is sent via WiFi to the SAV car where it is received by the onboard Arduino microcontroller and finally it is transmitted to the steering servomotor, which has its own internal electronics and internal servo positioning closed-loop system. As such, a large time delay on the SAV platform is not surprising and indeed can be felt when driving the car manually with a joystick. It is expected that the SAV control system design will need to deal with this delay in some way.

Another interesting point about the identified values of the SAV car model parameters are the optimal found values for the tire stiffness coefficients. For the simplicity of the analysis Fig. 2.5 shows the plot of the stiffness coefficients polynomial functions. Only the longitudinal stiffness coefficient C_σ present a quadratic form, while both cornering coefficients $C_{\alpha l}$ and $C_{\alpha r}$ present a linear relation on v_x. In all cases, it is interesting to see that the optimal values for the stiffness coefficients present an increase in value with v_x.

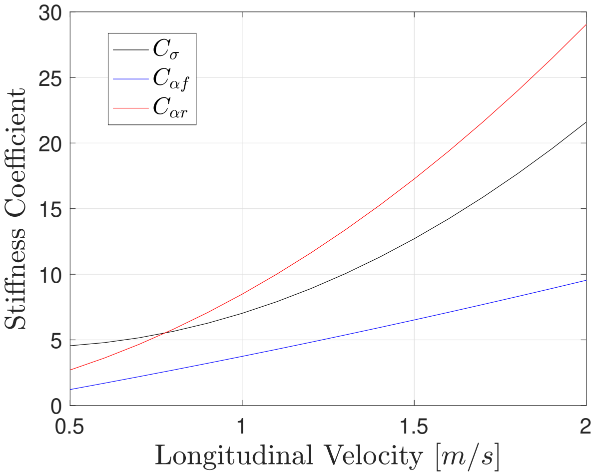

Figure 2.5: Scaled Automated Vehicle force diagram at local coordinate frame.

Finally, in order to visualize the accuracy of the identified model, Fig. (2.6) shows the measured data y and the identified model output $\hat{y}(\hat{x}, u)$. Note that this data-set of measured outputs y and inputs u is the one used for the optimization problem in Eq. (2.14) to obtain an estimation of model parameters Ω. It can be clearly seen that for all model outputs $\hat{y}(\hat{x}, u)$ it is closely matched the real state measurements y.

Fig. (2.7) and Fig. (2.8) show ground truth measured outputs y and simulated model outputs $\hat{y}(\hat{x}, u)$ with two data-sets the model was not trained with. The model simulated output $\hat{y}(\hat{x}, u)$ shows an almost perfect match with the real measurements in both cases, thus showing that indeed the identified model can generalize the behaviour of the SAV dynamics. Concerning all data-sets, Table 2.4 collects the RMS error of each three measured outputs. As it was seen from the previous mentioned figures, the estimation error is very small for the identification data and still remains quite small for the validation data-sets.

Table 2.4: Identified SAV Model Estimation Error rms

Data-set	rms$(v_x - \hat{v}_x)$	rms$(v_y - \hat{v}_y)$	rms$(\dot{\psi} - \hat{\dot{\psi}})$
Identification Data Fig. 2.6	0.0022	0.0562	0.0144
Validation Data 1 Fig. 2.7	0.0690	0.0175	0.3371
Validation Data 2 Fig. 2.8	0.1681	0.0183	0.2600

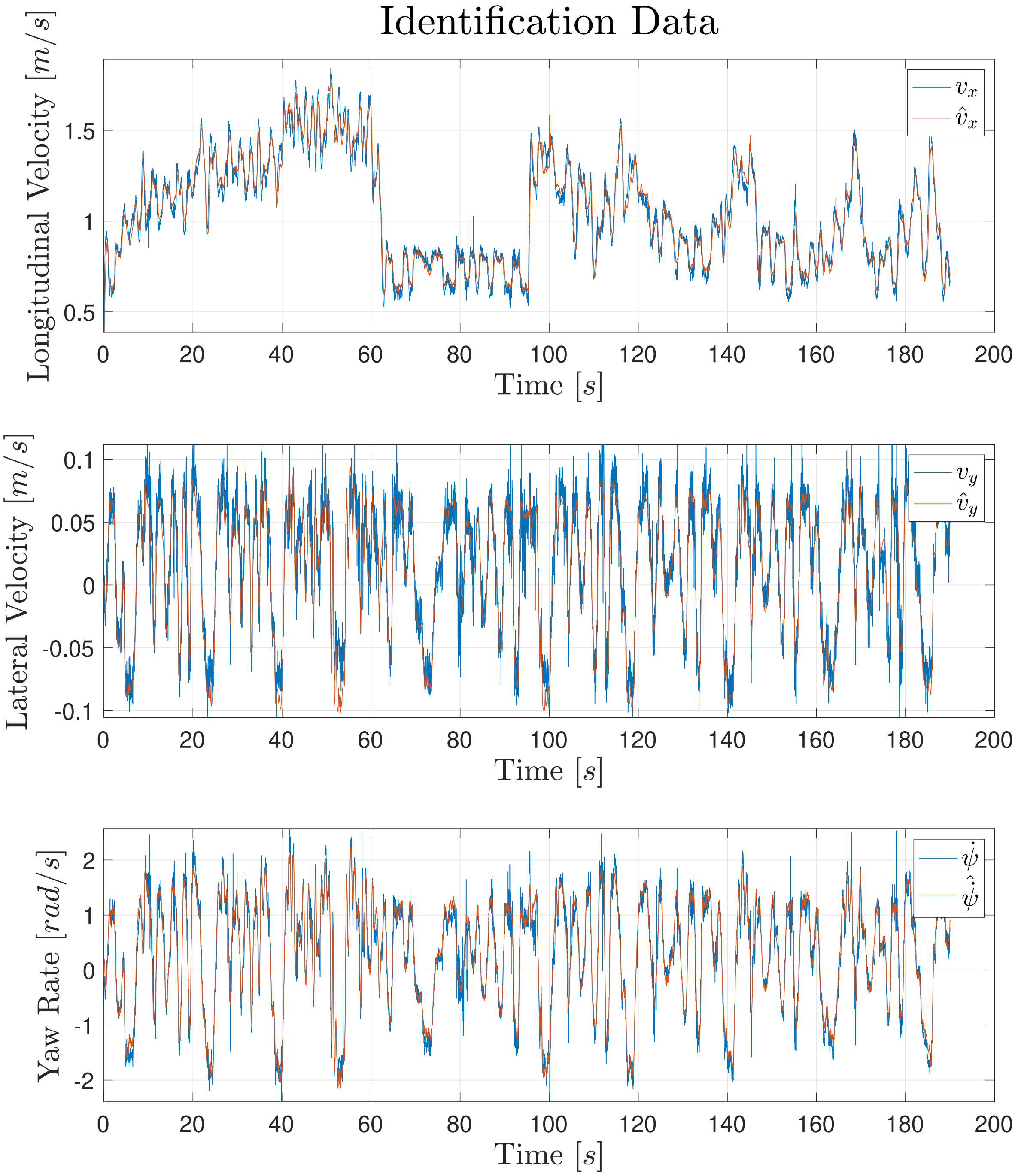

Figure 2.6: Identified model output VS identification data.

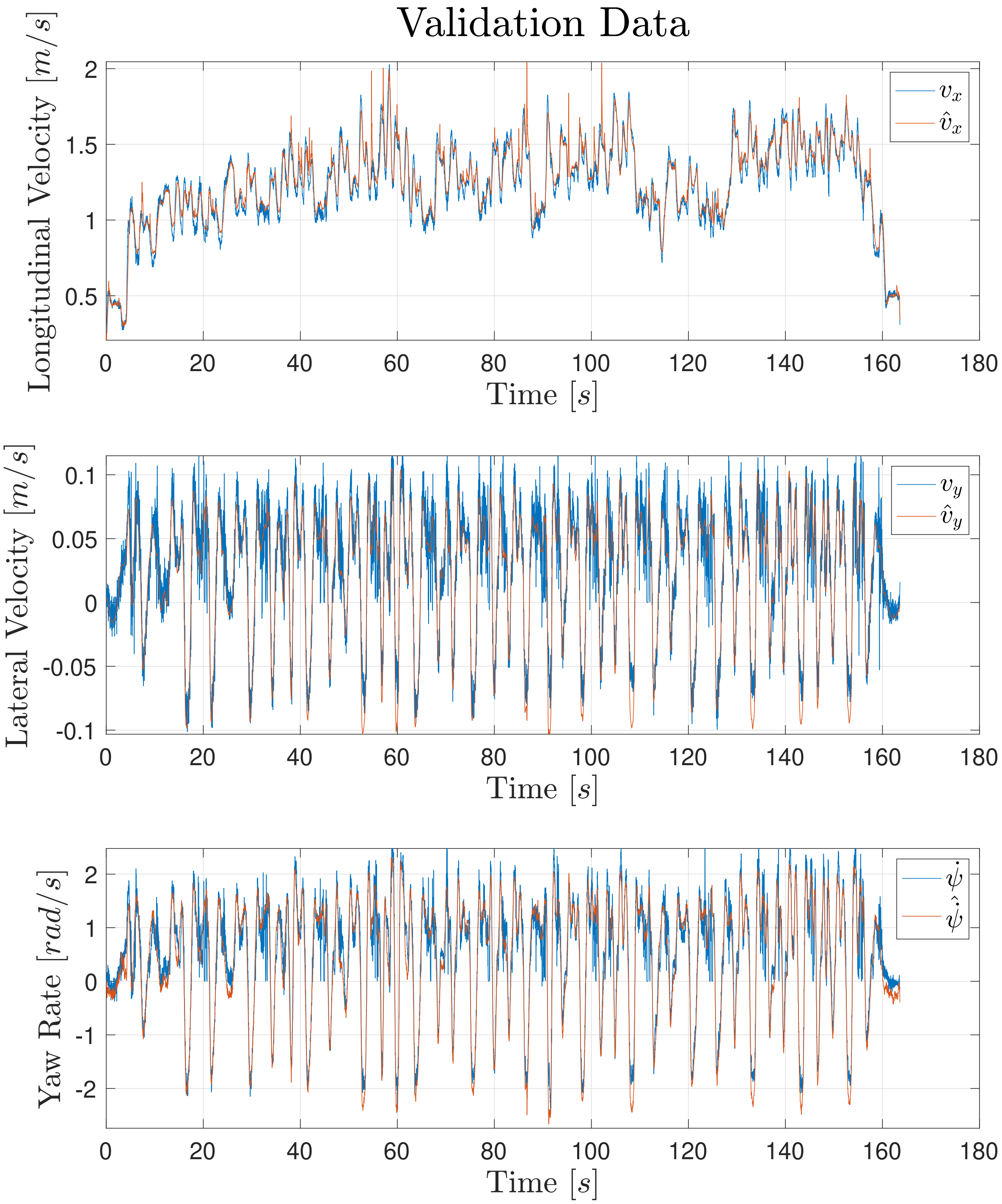

Figure 2.7: Identified model output VS the first validation data.

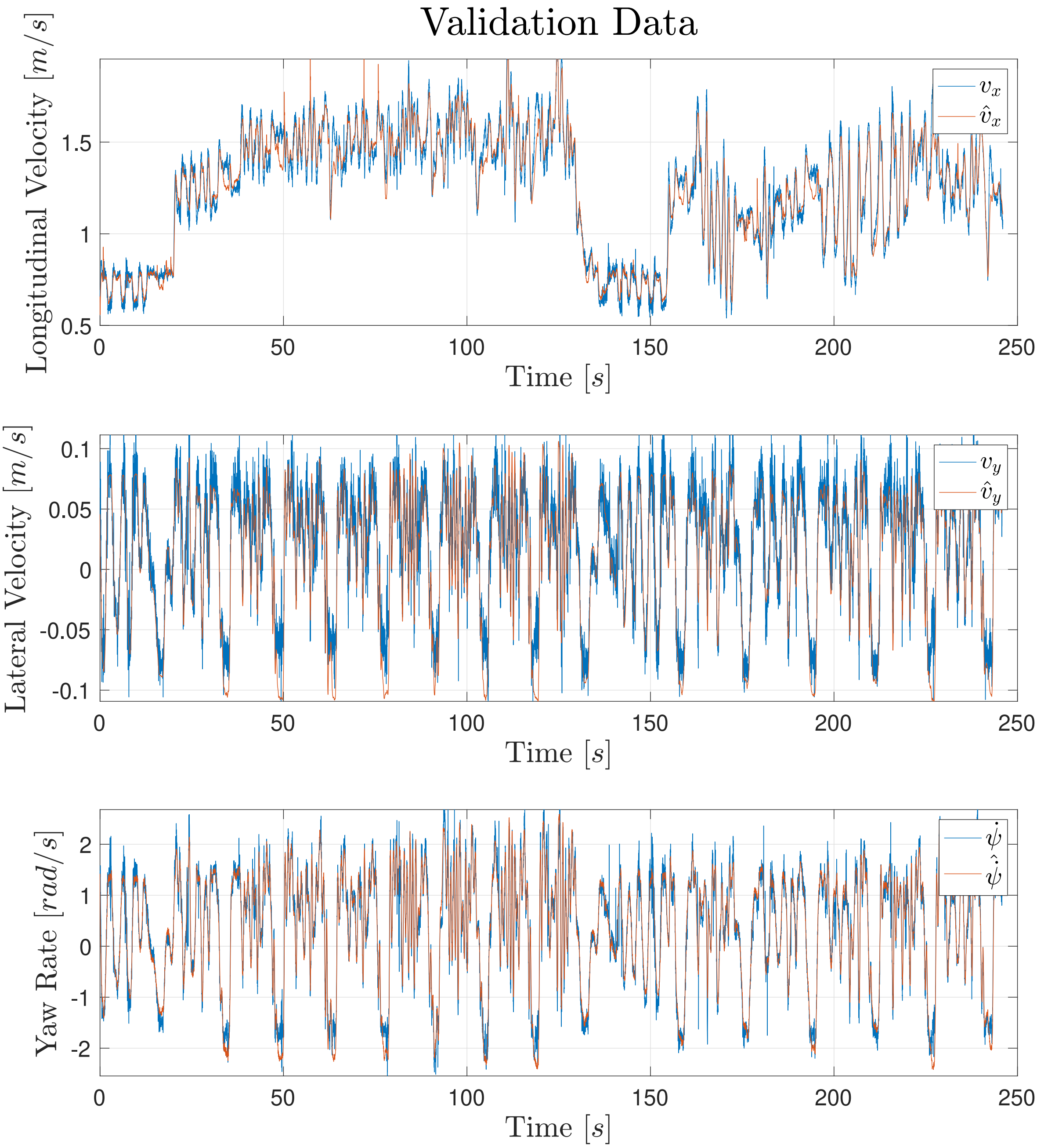

Figure 2.8: Identified model output VS the second validation data.

2.4.3 Standard Bicycle Model

From the model given in Eq. (2.1) and with Assumption 2.1, Assumption 2.2 and Assumption 2.3 one could derive the following control-oriented model for the lateral SAV control design.

Definition 2.3 (SAV Bicycle Model)

The lateral dynamics of the SAV is given by the following state-space model

$$\begin{bmatrix} \dot{v}_y \\ \ddot{\psi} \end{bmatrix} = \begin{bmatrix} -\frac{C_{\alpha f}(v_x)+C_{\alpha r}(v_x)}{m v_x} & -v_x - \frac{C_{\alpha f}(v_x)l_f - C_{\alpha r}(v_x)l_r}{m v_x} \\ -\frac{C_{\alpha f}(v_x)l_f - C_{\alpha r}(v_x)l_r}{I_z v_x} & -\frac{C_{\alpha f}(v_x)l_f^2 + C_{\alpha r}(v_x)l_r^2}{I_z v_x} \end{bmatrix} \begin{bmatrix} v_y \\ \dot{\psi} \end{bmatrix} + \begin{bmatrix} \frac{C_{\alpha f}(v_x)}{m} \\ \frac{C_{\alpha f}(v_x)l_f}{I_z} \end{bmatrix} \delta \tag{2.25}$$

with parameters given in Table 2.2 and Table 2.3 and where the tire cornering stiffness coefficients are given by the following polynomials

$$C_{\alpha f}(v_x) = C_{\alpha f2} v_x^2 + C_{\alpha f1} v_x + C_{\alpha f0} \tag{2.26}$$

$$C_{\alpha r}(v_x) = C_{\alpha r2} v_x^2 + C_{\alpha r1} v_x + C_{\alpha r0} \tag{2.27}$$

Note that although the SAV Bicycle Model still remains a pure LPV model, the dependency on the longitudinal speed v_x of the SAV model is more complex with respect the control-oriented from Definition 2.1. This is due to the polynomial relation of the tire cornering stiffness coefficients with respect to v_x. This increased model complexity allows to obtain a more accurate control-oriented model of the actual vehicle dynamics.

2.4.4 Augmented Bicycle Model with Steering Actuator

Given the large input delay estimated in the servomotor model, as seen from the estimated time delay τ in Table 2.2, it is interesting to consider a control-oriented model which takes into account the slow dynamics of the steering actuator on the SAV. The following control-oriented model can be derived from Eq. (2.1) and the servomotor model in Eq. (2.16).

Definition 2.4 (Augmented SAV Bicycle Model)
The augmented lateral dynamics of the SAV are given by the following state-space model

$$\begin{bmatrix} \dot{v}_y \\ \ddot{\psi} \\ \dot{\delta} \\ \ddot{\delta} \end{bmatrix} = \begin{bmatrix} -\frac{C_{\alpha f}(v_x)+C_{\alpha r}(v_x)}{m v_x} & -v_x - \frac{C_{\alpha f}(v_x)l_f - C_{\alpha r}(v_x)l_r}{m v_x} & \frac{C_{\alpha f}(v_x)}{m} & 0 \\ -\frac{C_{\alpha f}(v_x)l_f - C_{\alpha r}(v_x)l_r}{I_z v_x} & -\frac{C_{\alpha f}(v_x)l_f^2 + C_{\alpha r}(v_x)l_r^2}{I_z v_x} & \frac{C_{\alpha f}(v_x)l_f}{I_z} & 0 \\ 0 & 0 & 0 & 1 \\ 0 & 0 & -\omega_n^2 & -2\zeta\omega_n \end{bmatrix} \begin{bmatrix} v_y \\ \dot{\psi} \\ \delta \\ \dot{\delta} \end{bmatrix} + \begin{bmatrix} 0 \\ 0 \\ 0 \\ \omega_n^2 \end{bmatrix} \delta^*(t-\tau) \tag{2.28}$$

with parameters given in Table 2.2 and Table 2.3 and where the tire cornering stiffness coefficients are given by the following polynomials

$$C_{\alpha f}(v_x) = C_{\alpha f2} v_x^2 + C_{\alpha f1} v_x + C_{\alpha f0} \tag{2.29}$$

$$C_{\alpha r}(v_x) = C_{\alpha r2} v_x^2 + C_{\alpha r1} v_x + C_{\alpha r0} \tag{2.30}$$

2.5 Conclusions

In this chapter it was explored the development of vehicle longitudinal and lateral dynamics models from first principles under the assumptions of moderate accelerations. This assumption is important since it allows to consider decoupled dynamics and linear tire forces. Allowing to develop pure LPV control-oriented models.

From an existing model of a Renault Megane car it was given two variations of control-oriented Bicycle Models that can be used for the lateral control design of this vehicle. For the recently developed SAV platform it was explored the platform architecture and the identification process of the SAV dynamics. The identification process can be considered as successful, given how well the model outputs matched the ground truth measurements acquired on platform tests, which was true for both the data used in the identification phase as well as data used purely for model validation. This estimation performance by the identified model can be attributed to the identification process, based on a nonlinear optimization using a Prediction-Error Identification approach. This method has proved to be very flexible, as it could deal with model nonlinearities but also with the estimation of internal delays, all while producing estimated parameter values that are in line with what could be expected from physics.

The control-oriented models presented for both the Renault Megane and the SAV, will be used in following chapters for the development of control laws for the the vehicles lateral dynamics.

Chapter 3

Steering Driver Models

Contents

3.1 Introduction

In order to design model based control systems, it is important to have a good understanding of the dynamics of the system to be controlled. This is specially important for control systems that need to interact directly with the actions of a human. The design of Advanced Driver Assistance Systems (ADAS) being one of the most popular cases nowadays for such systems and offered in most modern road cars. For such systems, including some understanding of the human behaviour in the control design can help to achieve trade-offs between reduced interference and driver assistance aid.

One of the main focuses of this thesis is the vehicle lateral control task in view of incorporating driver assistance steering. To this aim, it is of importance to have some model for the driving behaviour of the human. Although obtaining a model of the human behaviour may seem complex, it has in fact been studied since back in 1960 and multiple models have been validated in recent years achieving great accuracy in capturing the steering behaviour of humans. The objectives in this thesis, in regards to modeling the driver steering, is to employ models that capture the human behaviour accurately while being simple enough to be used for control design.

3.1.1 Chapter Structure

The organization of the chapter is as follows. In Sec. 3.2 we cover different approaches present in the literature that have been proposed for the task of modeling the drivers steering behaviour. Then, in Sec. 3.3 two driver models which have been adapted from existing literature results are presented and in Sec. 3.4 for each these models it is given an identification based validation in which the parameters of the respective model are modified to try to capture real human steering behaviour.

3.2 Literature Background on Steering Driver Models

In order to model the driver behaviour, a first approach considered in the literature was to assume the driver acting as a compensator that minimizes some error signal. These signals are usually considered to be the lateral position deviation or the heading error of the vehicle with respect the desired trajectory, always computed at some look-ahead point on the forward direction of the car. One the simplest representation to appear of the driver as a compensator is the so-called Systems Technology Inc. (STI) pursuit model. According to [Rei83], a review on driver models published in 1983, this STI pursuit model was first introduced in 1967 by Systems Technology Inc. It considers the human driver acts as a lead term with time-delay

$$H(s) = (T_L s + 1)e^{-\tau s} , \tag{3.1}$$

where T_L is the lead time constant and τ incorporates the lag time due to the human reaction time and the neuromuscular activity. In Fig. 3.1 it can be seen an example of an application of such a model, extracted from [McR+77]. Note than in this model it is combined both the lateral error y_e and heading error ψ_e as the driver model inputs, but also the road curvature.

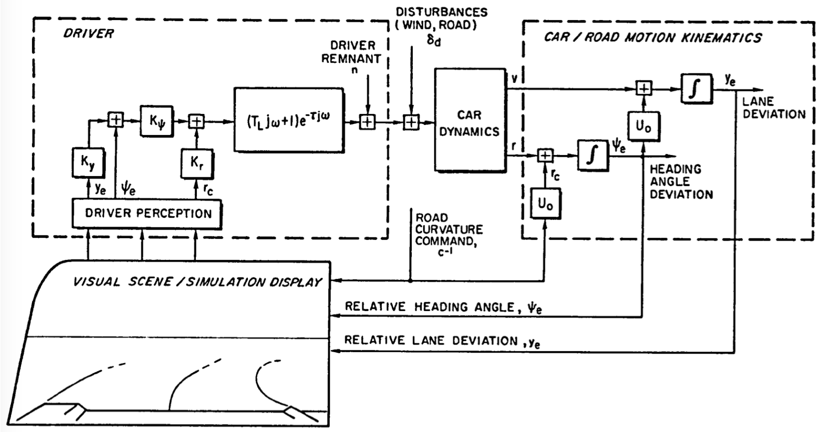

Figure 3.1: Driver/Vehicle model with STI pursuit model. [McR+77]

According to the previous mentioned review [Rei83], the STI pursuit model can model accurately the driving characteristics during lane tracking and disturbance rejection tasks, such as wind disturbances. However, for lane changes or more aggressive maneuvers more complex models are required.

Building from the STI pursuit model, a more comprehensive model is the so-called precision model. A detailed description of this model can be found in [MK74], which writes

$$H(s) = K_P \frac{T_L s + 1}{T_I s + 1} \frac{1}{(T_N s + 1)((\frac{s}{\omega_N})^2 + \frac{2\zeta_N}{\omega_N} s + 1)} e^{-\tau s} \tag{3.2}$$

where K_P is the model gain, τ is the human reaction time delay, T_L and T_I are the lag-lead time constant of the lag-lead compensator and T_N, ω_N and ζ_N are parameters of the driver neuromuscular system. This model can be simplified as

$$H(s) = K_P \frac{T_L s + 1}{T_I s + 1} \frac{1}{T_N s + 1} e^{-\tau s} \tag{3.3}$$

or even as

$$H(s) = K_P \frac{T_L s + 1}{T_N s + 1} e^{-\tau s} \tag{3.4}$$

The main hypothesis behind the precision model is the assumption that the driver-vehicle system behaves like a servo system [WM70] such that

- The driver-vehicle system can be stabilized.
- Given a transfer function $H_c(s)$ that describes the vehicle dynamics, then $|H(j\omega)H_c(j\omega)|$ has a slope of -20dB/decade around the crossover frequency.
- $|H(j\omega)H_c(j\omega)| >> 1$ at low frequencies.

This is equivalent to say that the driver-vehicle system behaves according to the cross-over model

$$H_L(s) = \frac{\omega_c}{s} e^{-\tau s} \tag{3.5}$$

where ω_c is the crossover frequency and the delay time τ is the inherited delay from the driver. Thus, according to [WM70] the values for the lag-lead compensator in the precision model Eq. (3.2) are chosen such that the previous points hold true.

As mentioned in the review work [PE07], this model has been very influential in the driver modeling literature and forms a key element for many other models that have been proposed afterwards, specially in the simplified manner seen in Eq. (3.4). Despite its simplicity, in an aerospace sector case study [JHB15], it was proven that the precision model description is able to fit accurately data from real human behaviour. Moreover, that study has shown that with different parameters fitted for each model, the behaviors of the complete precision model in Eq. (3.2) and of the simplified representation in Eq. (3.4) are similar.

These early type of models, as the STI pursuit model in Fig. 3.1 from [McR+77] or the simplified precision model used in [RSB81] to model the obstacle avoidance behaviour, only assume drivers as pure feedback element actors correcting its instantaneous lateral position and/or orientation. However, in [McR+77] it is acknowledged the existence of a feed-forward behaviour in drivers associated with the guidance task in addition to the pure stabilization control one. Specially it is mentioned that very experienced drivers rely mostly in this type of visual information. A major contribution in the idea of independent tasks behaviour modeling was introduced in [Don78] where a two level driver model is introduced. Interestingly, the feedback compensatory model employed in [Don78] is a discretization of the simplified precision model Eq. (3.4).

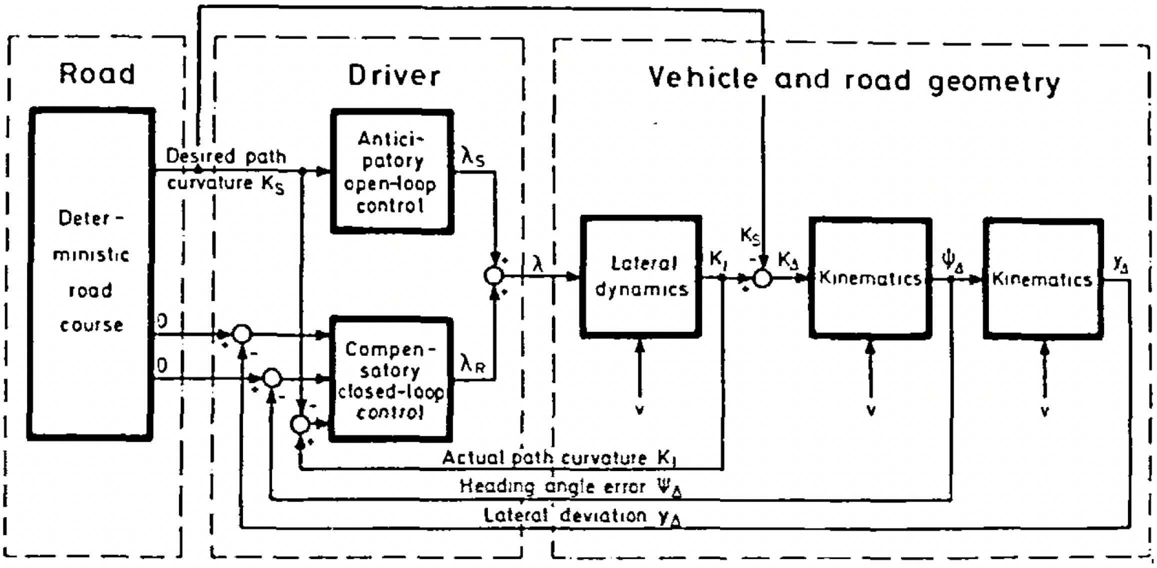

Figure 3.2: Two-level driver model with anticipatory and compensatory behaviours. [Don78]

As can be seen in Fig. 3.2, the two level models present a feedback path and in addition a pure feed-forward component based on the incoming road curvature. The feedback path models the neuromuscular human system and explains the physical actions carried by the driver in order to reduce the small errors between the vehicle's Center of Mass and the road center-line. The feed-forward steering represents the driver's visual system anticipatory action to the incoming road path curvature. The rationale behind this idea is that humans do not act purely as a correcting mechanism, instead as has been proved in the recent work [MC11], the human driving action is mostly based on this visual anticipatory behaviour.

Many driver models presented in recent works present a structure similar to the two-level structure introduced in [Don78] or a variant of this model known as the two-point model [SG04]. The two-point model also assumes an anticipatory behaviour from the human, but instead of acting as a feed-forward action, it is expressed as a feedback action with respect the road heading error. However, this heading error is computed at a far away look-ahead point different from the point where the feedback errors related to the neuromuscular reaction would be computed.

A popular version of the two-point model is the cybernetic driver model introduced in

[Sen+09] and which can be seen in Fig. 3.3. In contrast with the two-level model from [Don78] and [SG04], the cybernetic driver model does not model the steering angle as its output, instead, the model output is the steering torque applied on the steering column by the driver. The objective of this model was to study the relation of the human with haptic feedback and shared control strategies in ADAS functionalities. As so, the effect of the steering column torque is given as a feedback signal into the model. In connection with previous explored models, when analyzing the transfer function of the cybernetic driver model from the compensatory error signal to the driver torque, θ_{near} and T_d respectively in Fig. 3.3, the obtained transfer function coincides with the Precision Model simplified as in Eq. (3.3).

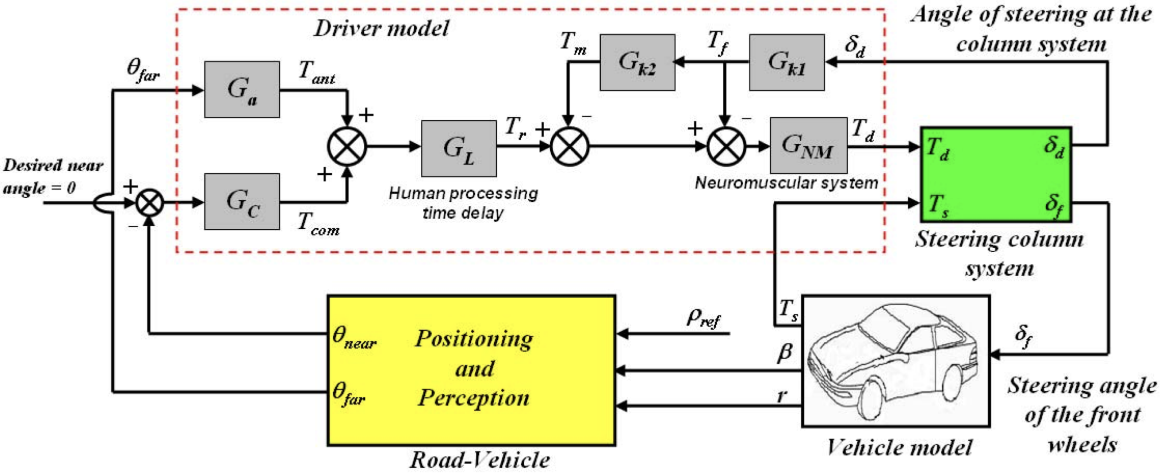

Figure 3.3: Cybernetic Driver Model. [Sen+09]

A forward evolution in the explored driver model literature consists in integrating into the driver model the path planning stage [MC11]; [Sch+16]. This is required as according to [Sch+16], given the same road it can be seen that drivers follow different trajectories based on their preferences. These extended models, as the driver model in Fig. 3.4 from [Sch+16], couple the path generation stage with a two level driver model similar to those mentioned before, allowing to generate simulated driver behaviour which matches closely the human response. Moreover, as the path planing stage parameters are unique to each driver, these models can capture the subtle differences between styles and skill levels between drivers.

In fact, an important contribution from the model introduced in [MC11] is to add a direct and simple way in which the driver skill can be incorporated into the driver model by simply weighting the levels of feedback compensatory steering δ_{FB} and feedforward anticipatory steering δ_{FF} as:

$$\delta = K_{FF}\delta_{FF} + K_{FB}\delta_{FB} \tag{3.6}$$

with

$$K_{FF} + K_{FB} = 1 \tag{3.7}$$

This is very interesting as even though it was known that skill plays an important factor in determining the steering behaviour, previous models failed to model it [Mac01]. Although the weighting strategy in Eq. (3.6) may seem over simplistic, it is indeed quite logical. In first place, as it has been said before, humans rely mostly in their visual anticipatory system for driving, and in second place as proven in [MC11], expert drivers rely more on the visual anticipatory system than novice ones. Both facts can be tuned with the correct choice of the K_{FF} weight. According to [MC11] a typical value for K_{FF} for an expert driver can be 0.85 while for a novice driver is around 0.75.

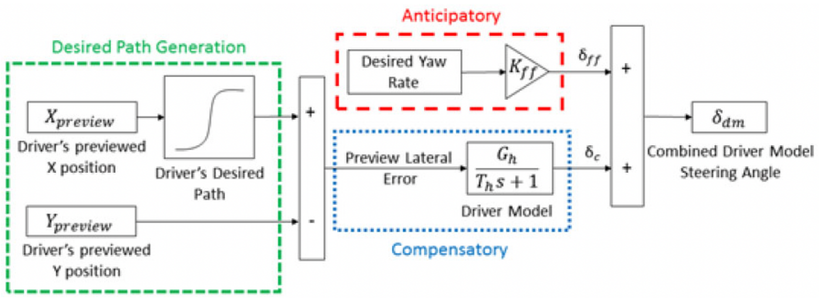

Figure 3.4: Two-level driver model with personalized path planner. [Sch+16]

As it can be seen from the different examples of models for the lateral driving behaviour explored so far, the literature in the field is quite extensive and works spans many decades. The presented studies are mainly based on the idea of modeling the behaviour of the human driver from its interaction with the road and its visual and neuromuscular systems. However, there are other approaches. The extensive review work on driver models [PE07] compile many different modeling perspectives and is recommended for the interested reader on the topic. Examples of works that model the driver from other perspectives could be the following. In [Lef+15] it is introduced a learning based approach to model the driver steering behaviour using Hidden Markov Models. In [HM90] it is developed a driver model based on control theory concepts and which need only the crossover frequency as a tuning parameter, with the lateral error acting as the model input. Another approach from the control theory community is introduced in [Jia+11], in which the driver behaviour is modeled as an optimal controller. In fact, the driver model in [MC11] includes a PID controller to model part of the compensatory decision making. The work [OT16] uses a hybrid approach of the cybernetic driver model [Sen+09] by incorporating Model Predictive Control based anticipatory actions to predict the amount of feedforward action required from the human, which changes according to the road situations, but other models fail to capture this phenomena.

3.3 Driver Models Used for ADAS Functions

In this section it is given an overview on the driver models which will be employed in later chapters of this thesis for the development of ADAS functions, such as driver fault detection and assisted lateral control. Both models are very similar in structure, the main differences being the input signals used to model the feedback compensatory behaviour. The following subsection detail each of the models characteristics.

3.3.1 Lateral Error Driver Model

The Lateral Error Driver Model (LEDM), seen in Fig. 3.5, borrows different characteristics from driver models seen in the literature as explored in Sect. 3.2. Like the model in [Don78], this model presents a two-level architecture. The feedback compensatory path uses the lateral error y_e with respect a reference trajectory as feedback signal used to model the driver corrective actions. On this feedback path of the driver model, the neuromuscular reaction of the driver is modeled using the simplified precision model [MK74] from Eq. (3.4).

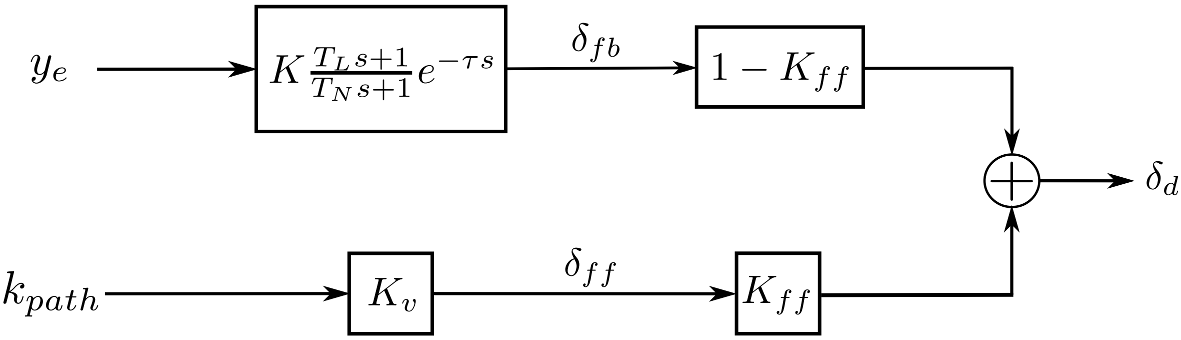

Figure 3.5: Driver Model Based on Lateral Error.

The anticipatory driver action, as in the case in [Don78], is modeled by using the incoming road curvature k_{path} as feedforward signal. The feedforward steering is modeled with a simple constant gain K_v, and as mentioned in [All+02]; [MC11] this anticipatory action is computed according to the feedforward Ackerman steering expression:

$$\delta_{ff} = k_{path} \cdot K_v = k_{path} \cdot K_f(a+b) \tag{3.8}$$

where K_f is an adjustable constant gain and $(a+b)$ is the vehicle wheel base. Finally, the resulting steering according to the driver model is a weighted combination as given in Eq. (3.6), taken from [MC11], which allows to model drivers with different skill levels.

It should be noted that the objective is here to obtain a simplistic control-oriented driver model, since the LEDM has only one state. This simple model can then be incorporated efficiently in the synthesis of ADAS functions, as the case of lateral ADAS controllers but also in algorithms for the detection of driver errors and driver performance. However, despite its simplicity the LEDM can capture many of the phenomena observed in real drivers. Importantly, the driver model given in Fig. 3.5 can capture the following driver characteristics:

- Driver physical condition thanks to appropriate choice of T_N and τ, which define the driver reaction time.
- Amount of driver reliance on anticipatory behaviour thanks to to appropriate choice of K_f from the feedforwad gain definition Eq. (3.8).
- Skill level by appropriately selecting the feedforward weight K_{ff}.

3.3.2 Heading Error Driver Model

The Heading Error Driver Model (HEDM), seen in Fig. 3.6, shares the same structure and parameters as the LEDM from Fig. 3.5. Given these similarities it will not be repeated here the description of the different elements that form the HEDM structure. However, it is interesting to point out that the structure of the feedback compensatory path, with simplified precision driver model as in Eq. (3.4) but with heading error ψ_e as its input, is identical to the obstacle avoidance driver model introduced in [RSB81].

The only difference of the driver model in Fig. 3.6 with respect the previously seen LEDM in Fig. 3.11 is that the input signal for the feedback path consists on the heading error ψ_e. Notice in Fig. 3.6 that this error signal is computed as the integral of the yaw rate error $\dot{\psi}_e$ with

$$\dot{\psi}_e = \dot{\psi}_{ref} - \dot{\psi} \tag{3.9}$$

where $\dot{\psi}_{ref}$ is the required yaw rate in order to follow a desired trajectory and $\dot{\psi}$ the actual yaw rate of the vehicle.

The objective of this model is mainly to be used for ADAS control design, and not for the estimation of driver performance. As such, describing the heading error ψ_e as the relation of yaw rate reference $\dot{\psi}_{ref}$ and vehicle yaw rate $\dot{\psi}$ is advantageous in order to connect the heading error driver model with the synthesis of controllers for the vehicle lateral dynamics. This is coherent as it will be seen in future chapters, the yaw rate error $\dot{\psi}_e$ is the signal that will be minimized in the controller design along this thesis to achieve tracking performances. Moreover, the introduction of an integrator in the driver model increases the low frequency gain of the driver vehicle system. As it was seen in Sect. 3.2, this is one of the good qualities a driver model needs to achieve according to the crossover driver vehicle model [WM70] assumptions.

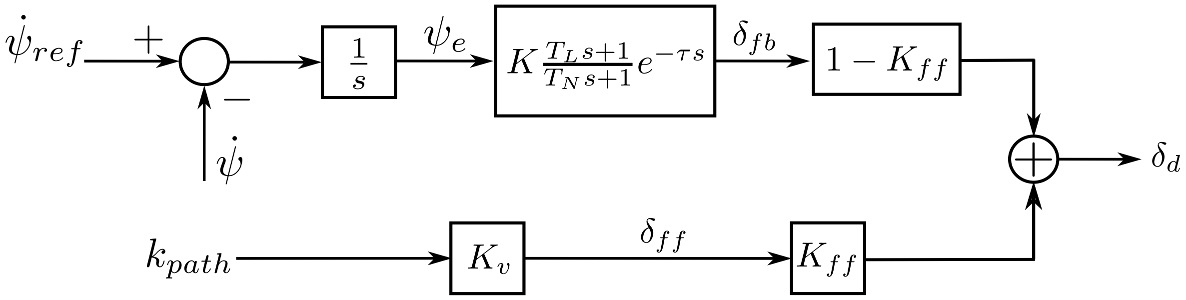

Figure 3.6: Driver Model Based on Heading Error.

Remark 3.1
With regard the connection of the driver models in Fig. 3.5 and Fig. 3.6 with the controller synthesis task. The incoming road curvature k_{path} *can be substituted by the following relation [Raj11]:*

$$k_{path} = \frac{\dot{\psi}_{ref}}{v_x} \tag{3.10}$$

This change of variable is advantageous for control synthesis purposes as it transforms one of the driver model inputs into a signal that is directly used to set control objectives.

3.4 Driver Model Validation

As it was pointed out, the driver models represented in Fig. 3.5 and Fig. 3.6 share many features from existing driver models in the literature, however, as they are adaptations of existing results, the validity of these driver models needs to be proved. For this reason, in this section it is validated both driver models introduced in Sect. 3.3 by means of parameter identification of a real driver from existing manual driving data on the SAV platform. The objective is to confirm whether the proposed driver models can explain the driving characteristics of a real human. The procedure to carry out the identification of the driver models is the following.

```
procedure DRIVER MODEL PARAMETER IDENTIFICATION
    Drive the SAV car around a specified track, see Sec. 3.4.1.
    Capture driver input data, vehicle state variables and error signals, see Sec. 3.4.1.
    Use the recorded data to identify the DM parameters, see Sec. 3.4.2.
    Validate the DM identification results, see Sec. 3.4.3.
end procedure
```

3.4.1 Data Acquisition for Identification

In order to carry out the DM validation, the joystick seen in Fig. 3.7 was incorporated on the SAV platform architecture given in Fig. 2.4 from Chapter 2 as input for the Remote ROS PC. The Remote ROS PC can read the value of the joystick sticks. This value then can be processed and transformed into a suitable steering angle, which is sent and applied on the SAV car steering servomotor.

Figure 3.7: Joystick used for driving the SAV manually.

However, there exists important limitations with this SAV setup for manual driving. First of all, driving the car with a joystick rather than with a steering wheel limits the level of precision that the driver has. More importantly, the fact that the SAV is driven remotely, means that there exists no direct feedback with the vehicle. Moreover, it is driven from a third person perspective, which is unnatural. Evidently, these limitations on the existing hardware setup hinder the effectiveness of the validation carried here. For this reason, the objective here is not to judge the identification performance on its accuracy but on its capacity to describe the underlying dynamics of the driver behaviour.

Using this SAV+Joystick setup, a driver is given the objective of driving on the following trajectory. During this manual driving exercise it is captured the state variables $(v_x, v_y, \dot{\psi})$ of the SAV car as well as lateral error y_e and heading error ψ_e.

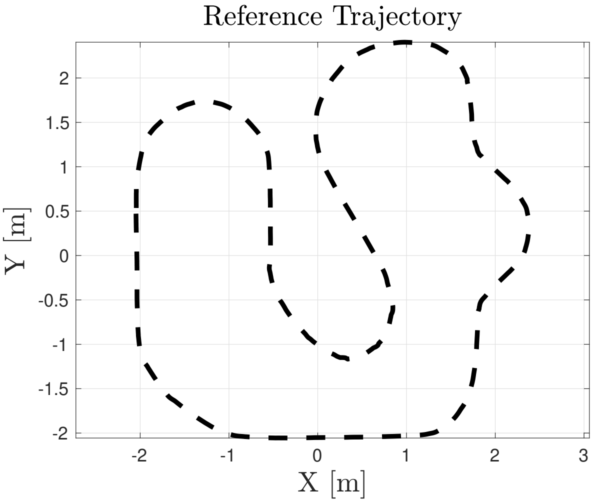

Figure 3.8: Followed Trajectory.

As it was mentioned in Sect. 2.4.1, from the motion capture cameras it can be measured in real time the SAV position and orientation. Deriving these then it is obtained the car states $(v_x, v_y, \dot{\psi})$. Moreover, from the position and orientation information in relation with the desired trajectory, it is possible to compute both the lateral deviation y_e and the heading error ψ_e with respect the circuit path. Note that in the SAV platform the computation of these error signals is done according with Sect. 2.2.3. Recall that the vehicle-road relation information is measured at a look-ahead distance L according to

$$L = t_p v_x \tag{3.11}$$

where t_p is in this case the driver preview time, assumed to be constant at $t_p = 1s$. Notice that this is an intrinsic limitation of the identification of driver models in general, as it is very difficult to accurately known what is the preview distance that the real driver is taking into consideration, which for sure it is not constant in reality.

In addition, from the information about the SAV position it is possible to obtain the road curvature k_{path} at the look-ahead point on the reference trajectory. As can be seen, the SAV platform allows to measure all the inputs and outputs that appear on the LEDM in Fig. 3.11 and HEDM in Fig. 3.12.

3.4.2 Identification Method

The identification method is a Prediction Error one, similar to the identification method for the parameters of the SAV model seen in Sect. 2.4.2. The parameter identification for both driver models is done using a shared data set, which was obtained by driving manually the SAV car as according to Sec. 3.4.1.

The set of parameters to identify from the LEDM in Fig. 3.5 and the HEDM in Fig. 3.6 are the following

$$\Omega = \{K, T_L, T_N, \tau, K_f, K_{ff}\} \in \mathbb{R}^6 \tag{3.12}$$

Remember that according to Eq. (3.8), $K_v = K_f(a+b)$, and $(a+b)$ is the wheelbase of the vehicle (see Table 2.3). The nonlinear optimization problem solved to identify these parameter is

$$\min_{\Omega} \left[Q_1 \cdot \mathrm{RMS}(\delta^* - \hat{\delta}^*) + Q_2 \cdot \mathrm{RMS}(\dot{\psi} - \hat{\dot{\psi}}) \right] \tag{3.13}$$

where δ^* and $\dot{\psi}$ are respectively the real steering command and vehicle yaw rate captured from the real driving test. $\hat{\delta}^*$ is the output of the correspondent driver model to be identified. In addition, $\hat{\dot{\psi}}$ is the simulated output of the SAV dynamics given $\hat{\delta}^*$ as steering input.

A possible approach to solve the identification problem would be to focus on the driver models from an input-output perspective, according to Fig. 3.5 and Fig. 3.6 respectively. This is possible as all inputs and outputs signals of both driver models are available. However, due to the hardware setup limitation, it was found out that best results can be achieved by carrying the identification using a holistic approach.

In this holistic approach, for simulating the driver command δ^*, the driver model is coupled with the nonlinear SAV model. This closed-loop driver-vehicle model can be generalized for both driver models according to Fig. 3.9.

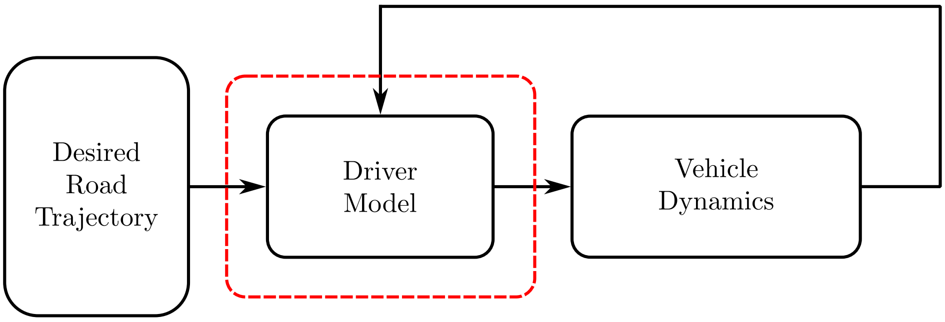

Figure 3.9: Data Scheme for the Identification Method.

The vehicle dynamics used in the identification process is the nonlinear model of the SAV dynamics seen in Sect. 2.4.2, including the equations of motions but also the servomotor dynamics with time delay. Note that as seen in the nonlinear optimization problem definition in Eq. (3.13), the SAV parameters are not optimization variables in this case. The SAV model is just used to provide a simulation of the vehicle yaw rate response $\hat{\dot{\psi}}$ given the simulated driver model command $\hat{\delta}^*$. Then, as seen in Eq. (3.13), minimization of the estimation error $\dot{\psi} - \hat{\dot{\psi}}$ RMS is another objective on the cost function. The objective of including this term on the objective function is to steer the optimization towards a set Ω of driver model parameters that explains well the driver model steering but also takes into account the observed vehicle response.

Finally, the nonlinear optimization problem in Eq. (3.13), with scalar weights $Q_1 = 100$ and $Q_2 = 1$, is solved using the FMINCON solver in Matlab. This is done using the road information data with respect the circuit k_{path}, y_e and ψ_e, data from the real steering commands δ^* executed by a human driver and simulated driver steering commands $\hat{\delta}^*$ generated by either of the correspondent driver model in Fig. 3.5 or Fig. 3.6 and simulated vehicle response from the identified SAV dynamics in Sect. 2.4.2.

3.4.3 Validation results

For each of the two driver models, their identified parameters as well as the considered minimum and maximum boundaries are given in Table 3.1. The identified values between both driver models are consistent with each other. They are consistent in the sense that the identified parameters in both cases characterize a driver with high preference in its anticipatory behaviour. Note that for both driver models, the values for the skill weight K_{ff} and specially the gain K_f of the Ackerman feedforward steering present high values, close to the consider upper bounds. This is indeed a coherent result given the poor steering characteristics of the SAV [AM97]. As seen in Sect. 2.4.2, the steering servomotor presents slow dynamics and a large delay time, which hinders the driving experience. This makes the SAV behave like a poor performing vehicle when driving it manually. As a result, the driver needs to take an active role and focus more on preview feed-forward information and behaviours to follow successfully the desired trajectory.

Table 3.1: Driver Models Identified Parameters

Parameter	Driver Model Fig. 3.5	Driver Model Fig. 3.6	Value min	Value max
T_L	0.7124	0.3413	0.2	3
T_N	0.5504	0.3648	0.15	1
τ	0.2112	0.2336	0.15	0.3
K	0.9013	0.2616	0.1	50
K_f	6.1786	8.9023	1	10
K_{ff}	0.8034	0.8498	0.75	0.85

Table 3.2 presents the RMS estimation errors for the two signals considered in the objective function of the nonlinear optimization problem Eq. (3.13) for the Prediction Error identification approach. It can be seen that the performance of the two identified driver model is almost identical. This can be confirmed when comparing Fig. 3.11 and Fig. 3.12.

Table 3.2: Identified Driver Models Estimation Error RMS

Model	RMS($\delta^* - \hat{\delta}^*$)	RMS($\dot{\psi} - \hat{\dot{\psi}}$)
LEDM Fig. 3.5	0.2389	0.4924
HEDM Fig. 3.6	0.2396	0.4817

Fig. 3.11 and Fig. 3.12 presents the ground truth data for the real human steering command and the simulated steering according to the driver models output on top; on the bottom it is given the measured vehicle yaw rate and the simulated yaw rate of the SAV model as consequence of the driver model input. As previously mentioned, note that the ground truth data set is the same for the identification effort of the two driver models. Additionally, Fig. 3.10 presents the range of speeds at which the driver data acquisition experiment was carried out.

From Fig. 3.11 and Fig. 3.12, and as it was seen in Table 3.2, the steering behaviour according to both driver models is similar. From the ground truth steering angle commands it can be clearly seen the mentioned limitations due to using a joystick as input device. The joystick sticks have a short travel distance and dead-zone behaviour around the neutral position. This produces an steering signal which is hard to control with precision for the driver. As a result the driver commands on the SAV+Joystick setup present a very digital (almost Boolean) behaviour. Despite this unnatural steering, both driver models capture the overall behaviour that can be seen from the human steering. On the other hand, when focusing on the vehicle behaviour, it can be seen that simulated steering from the driver model causes a simulated yaw rate on the vehicle model that closely matches the general yaw rate dynamics observed on the actual SAV car.

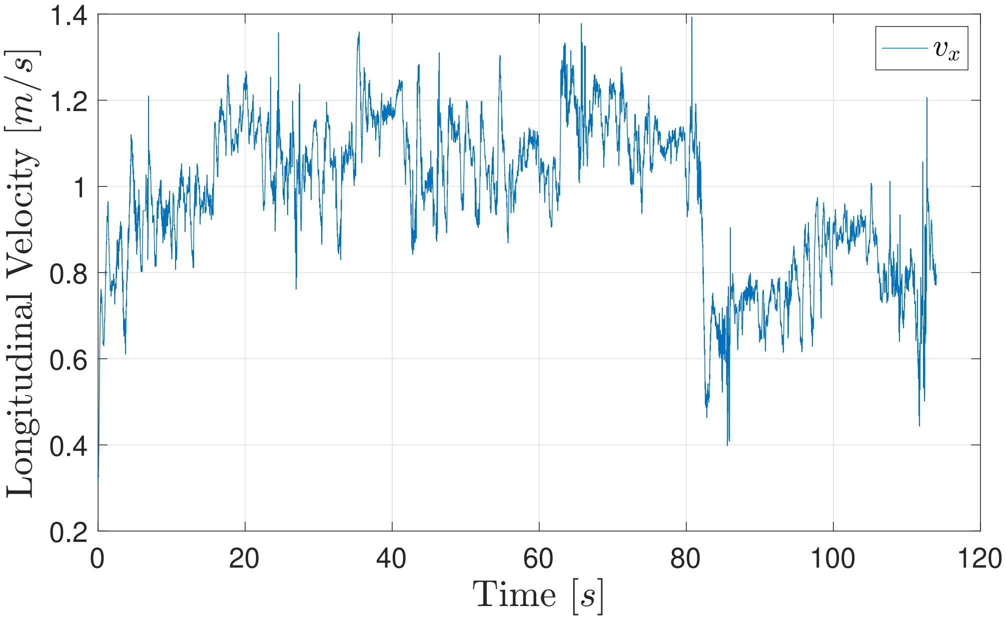

Figure 3.10: Two-level driver model with personalized path planner. [Sch+16]

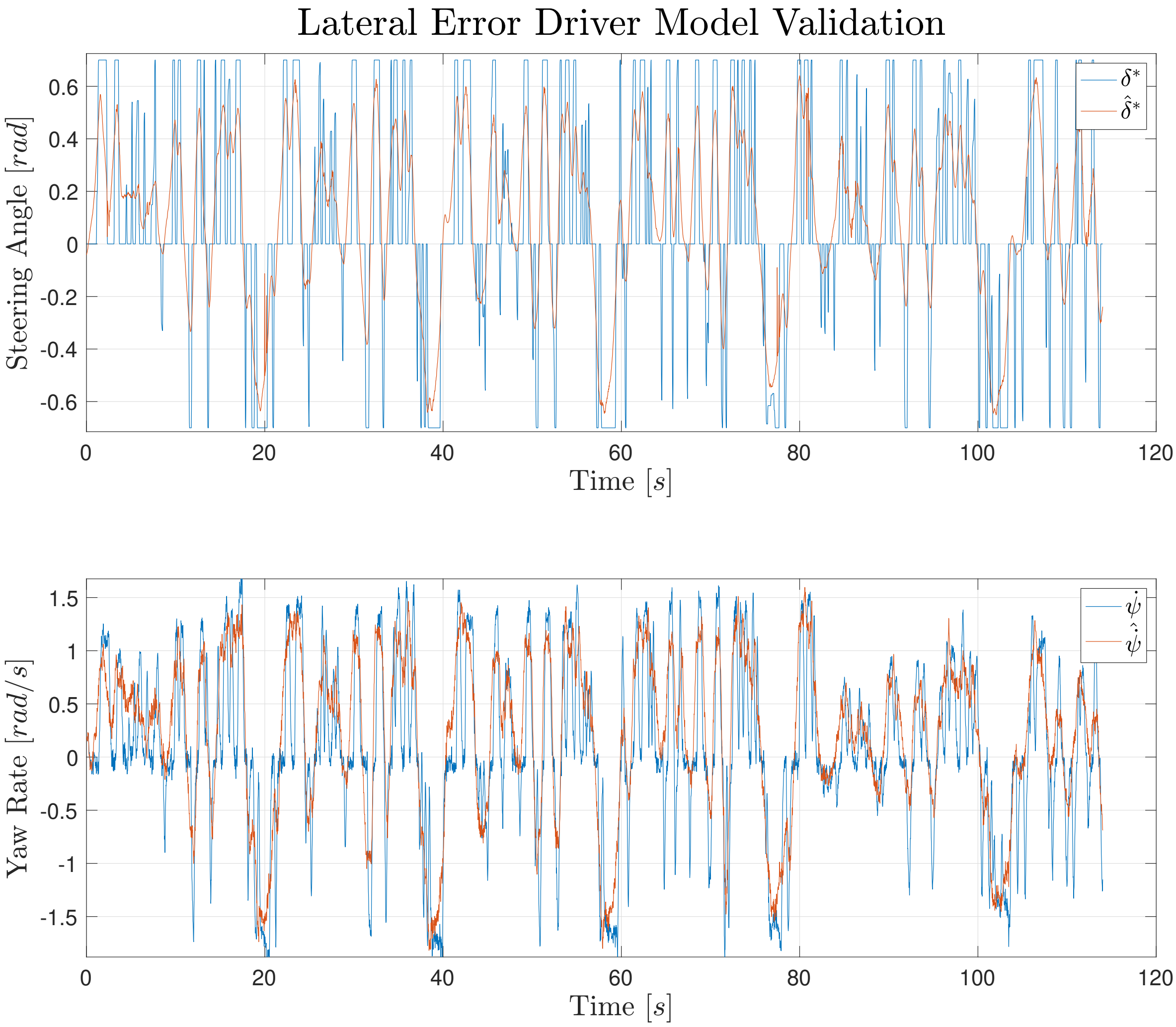

Figure 3.11: Estimated Lateral Error DM steering and model vehicle responses vs ground truth data.

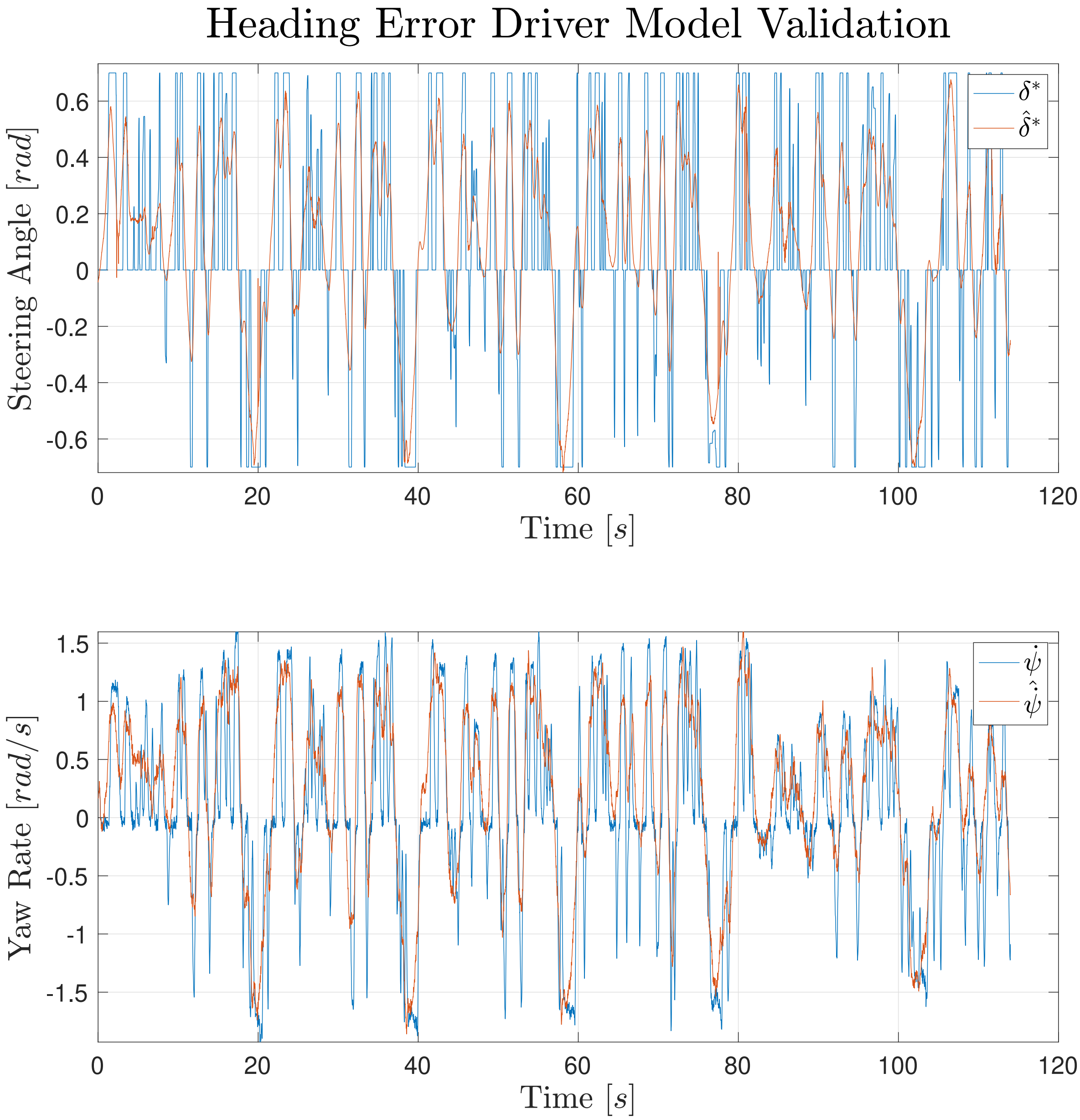

Figure 3.12: Heading Error DM steering and model vehicle responses vs ground truth data.

3.5 Conclusions

In this chapter it has been explored some of the works available in the literature concerning driver models. Special attention has been put on works which model the behaviour of the human driver from its interaction with the road and its visual and neuromuscular systems. These works have been the basis for the development of the the driver models selected in order to develop ADAS functions in this thesis.

Borrowing from different works, two driver models have been presented. Both use a similar two-level structure with feedforward anticipatory and feedback compensatory actions to model the driver behaviour. The first model uses the lateral error for feedback, while the second model here presented uses the heading error instead. The chosen structure for both models can capture a high amount of driver characteristics, as physical condition but also level of skill. This is achieved while maintaining a simple structure and low number of states as a key objective in order to obtain simple models, which can then be used efficiently for control synthesis problems.

Finally, the driver models have been validated by means of parameter identification to test whether the models are able to capture real human driving behaviours. Due to limitations on the hardware setup this validation cannot be judged with a high level of confidence when compared to a real vehicle driving experience scenario. Despite the hardware constraints, the identified models showed coherent results and their simulated driver steering resembled overall the real steering executed by a human driver.

Part II

Lateral LPV Control for Autonomous Vehicles

Part II: Introduction

Part II is focused on the development of steering control for autonomous vehicles using LPV approaches. The LPV approach used for most of this Thesis is based in a novel framework for Discrete-Time (DT) Grid-Based LPV control which is presented in Chapter 4, referred to as grid and local variation bound. This framework allows to propose finite LMI optimization problems based on the LMI conditions presented in Chapter 1. The novelty of the frameworks lies on the fact that it allows to make use of Parameter-Dependent Lyapunov Matrices in the synthesis conditions for Grid-Based DT-LPV systems, which has not been presented previously in the literature.

Within this framework, Chapter 4 introduces the Parameter-Dependent State-Feedback (PDSF) control approach. The PDSF controller is synthesized in a two-step LMI, its key feature is that the synthesized controller has a designer chosen parameter-dependent structure independent of the number of grid-points considered on the LPV design. The PDSF approach is then used and experimentally validated for the design of an autonomous steering controller for the Scaled Automated Vehicle (SAV). The LPV design for the lateral SAV control considered 151 grid-points, despite that, the synthesized PDSF controller has only four constant gain matrices.

Chapter 5 uses the grid and local variation bound framework to introduce Gain-Scheduled Grid-Based SF DT-LPV control synthesis LMI conditions. This approach is then used to extend the autonomous steering design from Chapter 4 by adding a design-related varying parameter on the LPV design. The objective of this parameter is to provide a mean to modulate the maximum allowable magnitude of the steering controller output. A scheduling function will then be proposed to utilize this parameter in order to emulate an Anti-Windup mechanism. Experimental tests are then carried to validate the approach.

The following of this introduction to Part II is dedicated with providing literature background on lateral LPV vehicle control and in works which exploit the use of design-related varying parameter in the LPV framework, a concept that is key for the development of the results in Chapter 5.

Literature Background on Lateral LPV Vehicle Control

The lateral vehicle control is responsible of the control of the steering system of the vehicle in order to follow some desired trajectory. Some common applications of vehicle lateral control on modern cars could be the lane keeping [MSN11]; [Chu+18] or obstacle avoidance [Gao+10] systems.

The lateral dynamics of the vehicle can be modeled with the so called Bicycle Model, covered in Chapter 2. This model is a pure LPV system as the vehicle longitudinal velocity appears as a parameter in the model, which is obviously a time-varying parameter. The effect of the speed on the steering behaviour of cars is quite clear, at low speeds it is required large rotations of the steering wheels to turn the car while at highway speeds small corrections on the steering wheel result in large rotations. Thus, exploiting the knowledge about vehicle dynamics dependency on speed is key for autonomous steering to achieve acceptable performances. For this reason the LPV method has gain the interest of researchers working on vehicle lateral control applications.

In [Ato+22b] the authors compare for a real autonomous Renault ZOE electric vehicle the Polytopic, Grid Based and Linear Fractional Transformation (LFT) LPV control approaches applied to the autonomous steering problem. The findings of the authors point to the Grid Based and LFT approaches to provide good performances for this application. Meanwhile, their experimental results suggest that the Polytopic approach does not perform well at the whole range of speeds, resulting in noisy control signal deemed unsafe at higher speeds. Note that according to the Bicycle Model, see Definition 2.1, the longitudinal speed appears in the model as v_x and $\frac{1}{v_x}$, as the Polytopic approach requires the LPV model to be convex on its scheduling parameters [AGB95], the scheduling parameter vector is then $[\rho_1, \rho_2]$ with $\rho_1 = v_x$ and $\rho_2 = \frac{1}{v_x}$. Obviously a convex polytope of the parameters ρ_1 and ρ_2 have vertexes which are not feasible in reality.

To solve this issue, [Kap+22] proposed a Polytopic approach based on polytope vertex reduction algorithm in order to reduce the number of vertices of the initial over-bounded polytope. This strategy was implemented on the same autonomous Renault ZOE platform, leading now to good tracking results and good controller behaviour in terms of low noise on the control signal. However, it should be mentioned that the real-time implementation of the proposed vertex reduction algorithm requires solving in real-time a quadratic optimization problem to find the correct controller scheduling.

In addition to schedule the LPV controller based only on vehicle speed, some authors have proposed LPV approaches to account for other effects that affect the vehicle behaviour. In [Cor+21] it is proposed an LPV control strategy that accounts for non linearities on the car steering column. This was achieved by adding an additional varying parameter used to modify the online tuning of the controller. The objective being to adapt the controller frequency behaviour based on the curvature, such that when in a straight line driving situation with low accuracy requirements the controller provides soft control signals to improve passenger comfort, but can be more aggressive when turning to maintain good tracking performance. Meanwhile, in [FNG22] it is proposed an LPV approach that can cope with changes in the road condition. Employing machine learning algorithms it is proposed an approach to estimate the friction coefficient, then, by incorporating this coefficient into the vehicle model as an additional varying parameter, the LPV controller can adapt to different road conditions as wet and icy roads.

Another interest of using LPV approaches for lateral control in autonomous vehicle is the coordination of multiple control inputs. In [Dou+13] it is considered the development of an integrated control strategy involving front steering command and Direct Yaw Control using differential rear braking. Using LPV/$\mathcal{H}_\infty$ approaches the controller manages the level of yaw braking control in addition to the steering control. A similar approach is evaluated in [Cao+23] in a Hardware-In-the-Loop platform, proving improved vehicle performances when in critical conditions. In both of these works the steering control is used as the main actuator of the MIMO controller, meanwhile some car stability performance is computed in real-time to activate the level of Direct Yaw Control thanks to LPV scheduling.

In [GCS21] a similar problem is evaluated, this time considering the control possibilities that new all electric vehicle drive-train enables. Employing a multi-layer scheme, a first torque vectoring controller layer is designed exploiting the four wheels drive (4WD) electric architecture. Then, a second layer, which incorporates the knowledge of the torque vectoring controller model, is designed to control the steering of the vehicle. Additionally, in this work the authors consider tires non-linearites embedded on the LPV model of the vehicle dynamics. As a result, the synthesized steering controller can adapt in real-time to the wheels side-slip angles, thus, to the available lateral grip.

A popular control approach for autonomous vehicle control is the Model Predictive Control (MPC) technique [Bor+05]; [Zan+14]; [Liu+17]; [NCA19]. Some recent works are extending the use of LPV models into the MPC framework [MNRS20], the objective being to solve nonlinear MPC problems making use of the LPV formulation using Quadratic Programming (QP) solvers. This then enables faster performance in real-time implementation, without loss of model accuracy with respect a nonlinear MPC approach thanks to the use of LPV models. The LPV MPC technique was employed in [Alc+20] considering coupled longitudinal and lateral dynamics in order to increase the autonomous vehicle performance for racing. As a result, the MPC does not only compute the steering control signal but also the required acceleration command for speed control. In [APQ20], the same authors extended the approach to additionally consider the planning task within the LPV MPC formulation considering obstacle avoidance. They show that the computational time for solving this planning/controller MPC problem using nonlinear MPC techniques is not efficient for real-time implementation. However, the LPV MPC solution allows to solve the MPC at each iteration in less than 0.06 seconds in average.

As can be seen, the LPV approach has been widely employed in the literature to deal with the lateral control of autonomous vehicles. It does not only provide a natural methodology to provide adaptation of the lateral control system to changes in velocity, but as it has been seen, smart use of LPV models and LPV scheduling allow to provide robustness mechanism to a number of important vehicle control issues, as loss of stability, actuator nonlinearities and changes in road condition. Moreover, exploiting the LPV formulation it is possible to use MPC methods in a way that results in quick computational times.

About Design-Related Varying Parameters

The use of design-related varying parameters in LPV designs have been pioneered by the control schools of Grenoble and Budapest [GSB05]; [Zin+08]; [PV08]; [SGB13]; [Fer14]; [Gás+16]. The design-related varying parameters are parameters artificially added to the LPV model by the control designer to achieve some specific objectives. These parameters are included in the augmented plant or weighting functions used on the LMI optimization that characterizes the control problem. They allow for changes in the behavior of the control system, such as tuning controller bandwidth or limiting the maximum control signal output.

Unlike standard physics-related varying parameters, design-related parameters are not defined by physics or directly estimated from system behavior. Instead, their values are determined by mathematical functions chosen by the control designer to adapt the control system to various situations. This flexibility provide LPV designs with the capability to achieve higher levels goals, beyond stability and tracking performances.

There are three key aspects when considering design-related varying parameters in the control design.

- Satisfactory incorporation of the design-related varying parameter in the control design. This is accomplished when scheduling of the design-related varying parameter allows to achieve the desired adaptation goal, without sacrificing the control design performance.
- Defining an appropriate mathematical expression or functions that will describe the parameter evolution during real-time implementation.
- Tuning the hyperparameters of the scheduling function to achieve the the desired behavior of the design-related varying parameter.

Remark
When incorporating design-related varying parameter in the LPV design, the control synthesis is carried offline independently of how the design varying parameter scheduling function is defined. For control design and synthesis, only fixed points of the parameter are used. Once the controller has been synthesized, then, the definition and tuning of the mathematical expression for scheduling become important issues for the online implementation of the LPV controller with design-related varying parameters.

In the just presented Literature Background on Lateral LPV Vehicle Control it was already explored examples of works which propose LPV control systems that exploit design varying parameters. In [Cor+21] a design-related varying parameter is added in one of the weighting transfer function of the augmented plant for $\mathcal{H}_\infty$/LPV design. The objective is to adapt the controller frequency behaviour based on the curvature, such that when in a straight line situation with low accuracy requirement, the controller provides soft control signals to improve passenger comfort, but can be more aggressive when turning to maintain good tracking performance. In [Dou+13] it is used a design-related varying parameter to modulate the amount of differential braking used in order to enforce vehicle stability. In this work an stability index is used to determine when the lateral dynamics of the vehicle are within the stable region. Then, a linear interpolation rule is used to set the varying parameter value, the scheduling objective being to use only steering action and disable the differential braking in stable conditions. On the other side, when vehicle stability degrades, differential braking is enabled in addition to the steering action. This shows how design varying parameters allows the use LPV scheduling as a simple mechanism to handle the interaction between multiple actuators of the control system.

The work [WGP00] provides a methodology that exploits the LPV design technique to achieve integrated controller and Anti-Windup design. This is done by incorporating new design-related varying parameters in the LPV plant model such that the parameters provide an evaluation of the degree of saturation for each individual actuator. Importantly, this work shows that for these kind of designs, it is required the design weighting functions to be parameter dependent in order to achieve a successful control design.

A similar problem have been studied in [PV+08]. In this work it is studied the control of a vehicle suspension system with semi-active dampers. These actuators can only dissipate energy, which means that the region of forces in which they can act is restricted. For this reason classical designs for these systems suffer saturation problems as they may produce force requirements outside the allowable force regions. The addition of a design varying parameter acting as the control performance weight is then considered to penalize the control action any time it is outside the allowable force regions of the semi-active damper. An advantage pointed out in this work with regards the use of design strategies based on design-related varying parameter, is that as the design-related varying parameter are an abstraction to achieve some goal, they are simple to transfer to other systems.

In [Oud+22] an LPV design is proposed to mitigate conflicts between the driver and a Lane Keeping System for lateral ADAS applications. To achieve this it is proposed an LPV design in which the control problem is posed with the aid of a parameter dependent cost function in an LMI optimization. A varying parameter, considered in the range [0, 1] and which represents the level of shared control between driver and ADAS System, multiplies one of the cost function terms. This has the effect of either giving full authority to the ADAS system or disabling it. Then, once the controller has been synthesized, a fuzzy logic approach is proposed to determine the level of assistance based on driver activity and a cooperation index. This application shows how smart use of design varying parameters can be used to accomplish complex design requirements, while keeping the LMI optimization problem straightforward to solve.

The work [Ato+22a] proposes an interesting alternative to those existing so far in the literature for the selection of scheduling functions. Instead of manually selecting and tuning the structure and values of a mathematical expression for scheduling design-related varying parameters, it is proposed Deep Reinforcement Learning (DRL) methods to achieve this. In this work a scheduling variable in a multi-LPV controller based on Youla–Kucera parameterization [Ato+21] acts as the design varying parameter. Two LPV controllers with different performance objectives are designed, one tuned for smooth driving and a second for fast lateral transitions. The design scheduling variable then interpolates between both controller based on the driving situation. The interest of using DRL techniques to select the value for the scheduling variable, and thus control the amount of interpolation, lies in the flexibility that this technique offers to capture multiple objectives within the DRL reward function. Thus obtaining an optimal scheduling function with respect the problem requirements, something that with manual tuning is hard to accomplish, specially when there are multiple objectives involved.

In conclusion, the incorporation of design varying parameters in LPV control designs has been demonstrated to enhance the capabilities of the LPV approach. The LPV techniques enable the development of robust and adaptable control strategies that can handle varying operating conditions. By introducing design varying parameters, it becomes possible to adapt the control system in real-time to address several situations or requirements that cannot be represented in a dynamical model or resolved through other means. The incorporation of design varying parameters in LPV control designs provides an innovative and promising direction for the development of next-generation control systems capable of handling the challenges of modern-day control applications.

Chapter 4

Lateral LPV Control of Autonomous Vehicles Using a Fixed-Structure Parameter-Dependent State-Feedback Controller

---

Contents

4.1 Introduction

In this chapter the autonomous lateral control of the SAV car is tackled with a newly developed approach, here called Parameter-Dependent State-Feedback control. The computation of this type of state-feedback controller makes use of Linear Parameter Varying (LPV) approaches. The novelty lies on the fact that the controller has a fixed structure with constants matrix gains. However, the controller gains are affine with respect to a parameter dependent basis function, which provides a self-scheduled controller according to real-time changes of the varying parameters. The implementation of this Parameter-Dependent State-Feedback (PDSF) controller does not require any online interpolation or matrix inverse operations, independently of the number of varying parameters. The synthesis approach as well as the performance of the PDSF for the lateral control task on the SAV car applied to a Path Tracking application will be demonstrated in this chapter.

In the following subsections a general overview of LPV approaches applied to lateral vehicle control will be presented, as well as the motivations for the development and the definition of the PDSF.

The contents of this chapters are based on the following publications:

- Ariel M. Borrell, Olivier Sename, Vicenç Puig. "State-Feedback and Static-Output-Feedback Parametric Controllers Based on a Discrete-Time LPV Grid Based Approach". In: *IFAC-PapersOnLine*, Volume 55, Issue 35, 2022, Pages 109-114, ISSN 2405-8963, https://doi.org/10.1016/j.ifacol.2022.11.298.
- Ariel M. Borrell, Olivier Sename, Vicenç Puig. "Fixed-Structure Parameter-Dependent State Feedback Controller: an Scaled Autonomous Vehicle Path-Tracking Application". In: *Control Engineering Practice* [*Under Review, 2023*]

4.1.1 About Fixed-Structure Parameter-Dependent State Feedback Controllers

4.1.1.1 Motivation

Although successfully validated, and clearly better than pure robust LTI approaches [KAG99], the LPV approaches can suffer from practical difficulties during implementation, specially as the complexity of the controlled system increases. The Polytopic method requires 2^n controllers to be computed and implemented, n being the number of vertices for the convex polytope. Similarly, in the Grid-Based approach the number of point-wise controllers increases exponentially with the number of frozen values of the varying parameters (remember that it is recommended a quite dense grid in order to obtain robustness guarantees). It can be easily seen how for the Polytopic and Grid based approaches the amount of point-wise controllers to be implemented and stored in memory quickly increases in number as the complexity of the system increases.

For these reasons, the main motivation behind the Fixed-Structure Parameter-Dependent State-Feedback Controllers is to propose a new LPV approach that can be easily implementable. The control problem formulation for this new type of controllers is given in the following subsection.

4.1.1.2 Control Problem Definition

The control problem introduced in this chapter is to find a Parameter-Dependent State-Feedback (PDSF) controller with a fixed structure, which is defined as follows:

Definition 4.1 (Parameter-Dependent State-Feedback Controller)
Considering an affine dependency on some scheduling basis function $\theta(\rho) = (1, \theta_1(\rho), \dots, \theta_N(\rho))$, *with* $\theta_n \in \mathbb{R}$, $n = 1, \dots, N$ *and* $\rho \in \mathbb{R}^m$ *the vector of varying parameters, the structure of the PDSF Controller is of the following form*

$$K(\rho) = K_0 + \sum_{n=1}^{N} \theta_n(\rho) K_n \ , \tag{4.1}$$

where the controller gains $K_0, \dots, K_N$ *are constant matrices.*

The PDSF control problem is defined in the LPV/$\mathcal{H}_\infty$ framework such that the PDSF synthesis objective is posed as the minimization of the induced L_2-norm of a closed-loop LPV system. Such control problem is given in the following definition.

Definition 4.2 (PDSF Induced L_2-norm Control Problem)
Given an LPV system $\Xi(\rho)$ *and considering an State-Feedback control law* $u = K(\rho)x$, *the resulting LPV closed-loop system is:*

$$\Xi_{CL}(\rho) := \begin{cases} x^+ = (A(\rho) + B_u(\rho)K(\rho))x + B_w(\rho)w \\ z = (C_z(\rho) + D_u(\rho)K(\rho))x + D_w(\rho)w \end{cases} \tag{4.2}$$

Considering the induced L_2*-norm of a system, given in Definition 1.5, the control problem is then to find a PDSF controller* $K(\rho)$ *according to Definition 4.1 that renders the LPV closed-loop system* Ξ_{CL} *robustly stable and minimizes its* L_2*-norm as:*

$$\min_{\mathbf{K}(\rho), \gamma_\infty} \gamma_\infty \ s.t. \ \frac{\|z\|_2}{\|w\|_2} \leq \gamma_\infty \tag{4.3}$$

4.1.2 Chapter Structure

The structure of the rest of the paper is the following. In Sec. 4.2 some preliminaries on the analysis of DT-LPV systems through LMI is given. In Sec. 4.3 it is introduced a new LMI conditions that are used to prove the existence of the controller for a given system and numerical proposition for the computation of the PDSF controller gains. In Sec. 4.4 and section Sec. 4.5 it is explained the synthesis approach for the path tracking application on the SAV and it is given experimental results respectively. Finally, in Sec. 4.6 some conclusions are given.

4.2 Reduction of Grid Based DT-LPV Systems Analysis to Finite LMI Problems

In Chapter 1 it was introduced LMI techniques for the analysis of DT-LPV systems using Parameter Dependent Lyapunov Matrices (PDLM). However, the given conditions cannot be numerically solved. In this section it is given an approach in which such conditions can be recasted into LMI problems which can be solved efficiently with standard SDP solver, this will be done using the referred to as grid and local variation bound framework.

For illustration purposes let us consider a DT-LPV system constrained to its autonomous dynamics, as in Sect. 1.3.2, given by

$$x^{+} = A(\rho)x, \tag{4.4}$$

The stability of the system given in Eq. (4.4) can be tested making use of Theorem 1.1. From a numerical point of view there exist however two important issues with the LMI condition given in Theorem 1.1. Firstly, it is an infinitely constrained LMI due to the infinite possible values ρ can take within its bounds. Moreover, it involves both $\rho(k)$ and $\rho(k+1)$ and only $\rho(k)$ is known, while $\rho(k+1)$ generally unknown.

A common solution to the first issue is to consider a dense grid $\mathcal{G} \in \Omega$ at fixed ρ values within the varying parameter known bounds according to Assumption 1.1 and evaluate the stability condition at each grid-point $g_p \in \mathcal{G}$ [Wu+96]. Despite considering a frozen grid of values for the varying parameter vector ρ, it still remains an issue the fact that ρ^{+} appearing within the stability condition in Eq. (1.17) is unknown.

However, with known information on the bounded variation rates ν_i according to Assumption 1.2, it is possible to build a polytope $\mathcal{V}_i \in \Omega$ that bounds ρ_i^{+} for each element ρ_i of the varying parameter vector ρ. The extremes of the polytope $\mathcal{V}_i$ bounding each individual parameter future value ρ_i^{+} are given by the following relation:

$$\rho_i^{+} \in [\rho_i - \underline{\nu}_i,\, \rho_i + \overline{\nu}_i] \tag{4.5}$$

Thus, for each varying parameter ρ_i the min/max values $\mathcal{V}_{p,i}$ that define the polytope $\mathcal{V}_p$ at each grid point $g_p \in \mathcal{G}$ are given by:

$$\mathcal{V}_{p,i} := \left[g_{p,i} - \underline{\nu}_i,\, g_{p,i} + \overline{\nu}_i\right], \forall i = 1, \dots, m. \tag{4.6}$$

All the 2^m min/max combinations of $\mathcal{V}_{p,i}$, $\forall i = 1, \dots, m$, form then the vertices of the bounding polytope $\mathcal{V}_p \in \Omega$, each vertex defined as $g_p^v \in \mathcal{V}_p$, with $v = 1, \dots, 2^m$.

To better visualize this approach Fig. 4.1 is introduced. In this figure it is represented a gridded varying parameter space $\mathcal{G} \in \mathbb{R}^2$. For simplicity we focus on a single grid point $g_p \in \mathcal{G}$. Knowing the parameter variation limits on ρ, $\underline{\nu}$ and $\overline{\nu}$ respectively, then it is possible to build a local bounding polytope $\mathcal{V}_p$ such that $g_p^{+} \in \mathcal{V}_p$. Notice that the order of the vertices g_p^v, $v = 1, \dots, 4$, of $\mathcal{V}_p$ is not representative of any strict ordering requirement.

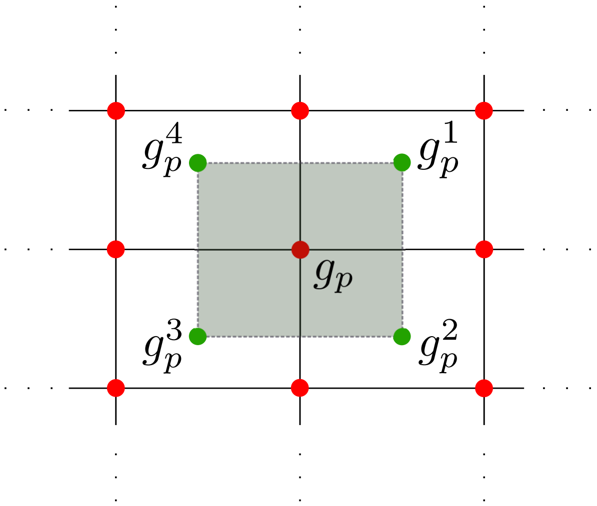

Figure 4.1: Vertices of the polytope $\mathcal{V}_p$ bounding g_p^+.

Applying this parameter grid and local variation bounds framework, one would first grid the parameter space with a grid $\mathcal{G} \in \Omega$ and at each grid point g_p compute a polytope $\mathcal{V}_p$ that bounds g_p^+, e.g. $\rho(k+1)$ when $\rho(k) = g_p$. Then for all combinations of grid point g_p and polytope vertex g_p^v one can define the condition in Eq. (1.17) from Theorem 1.1. The following proposition exemplifies this approach, using this proposition one can test the stability of the autonomous DT-LPV in Eq. (4.4).

Proposition 4.1

Consider an autonomous DT-LPV system Eq. (4.4), *with parameter space* $\Omega \in \mathbb{R}^m$ *gridded by a grid space* $\mathcal{G} \in \Omega$ *and assuming bounded parameter rate of variation* $\nu \in \mathbb{R}^m$ *such that for all* $g_p \in \mathcal{G}$ *there exists a bounding polytope* $\mathcal{V}_p$ *for* g_p^+ *with* 2^m *vertices* $g_p^v \in \mathcal{V}_p$. *If there exist constant matrices* $\mathbf{X_0}, \dots, \mathbf{X_N} \in \mathbb{R}^{n_x \times n_x}$, *which form a symmetric positive-definite PDLM* $X(\rho)$ *with basis function* $\theta(\rho) = (1, \theta_1, \dots, \theta_N)$, *with* $\theta_n \in \mathbb{R}$, $n = 1, \dots, N$, *and a set of matrices* $\mathbf{G_p} \in \mathbb{R}^{n_x \times n_x}$ *such that for all* (g_p, g_p^v) *pairs the following condition holds*

$$\begin{bmatrix} \mathbf{G_p}^T + \mathbf{G_p} - X(\theta_p^v) & \mathbf{G_p}^T A(\theta_p) \\ \star & X(\theta_p) \end{bmatrix} > 0 \ , \tag{4.7}$$

with

$$X(\theta_p) = \mathbf{X_0} + \sum_{n=1}^{N} \theta_{n,p} \mathbf{X_n}, \tag{4.8}$$

$$X(\theta_p^v) = \mathbf{X_0} + \sum_{n=1}^{N} \theta_{n,p}^v \mathbf{X_n}, \tag{4.9}$$

then, the autonomous DT-LPV system Eq. (4.4) *is robustly stable.*

Remark 4.1

As $X(\rho^+)$ *enters linearly on LMI* (1.17), *there is only need to check* $X(\rho^+)$ *on the vertices of* $\mathcal{V}_p \in \Omega$ *to bound it around a fixed grid point* g_p *[AA98]. Thus, it suffice to replace* $X(\rho^+)$ *by* X_p^v *for all* $(g_p,\, g_p^v)$ *pairs as done in Eq.* (4.7) .

Notice that in Proposition 4.1 it is replaced $A(\rho)$ from Eq. (4.4) by $A(\theta_p)$. This is done to emphasize that according to Definition 1.4 the parameter dependency on ρ is assumed affine on a basis function $\theta(\rho)$. Moreover, $A(\theta_p)$ is the frozen matrix value of evaluating $A(\theta(\rho))$ at a fixed grid point g_p. Additionally, note that the structure of the PDLM $X(\rho)$ copies the affine dependency on the basis function $\theta(\rho)$ as the system matrices according to Definition 1.3. Although this is not strictly required, this simple strategy has been proved effective [Wu+96]; [AA98].

4.3 Synthesis Conditions for Parameter-Dependent State-Feedback Controllers with Fixed Structure

In this section the steps and conditions for the synthesis of PDSF controllers are given. In order to achieve the synthesis for this type of controllers, it is required a two-steps sequential LMI optimization problem procedure. The inspiration for this approach comes from the work [AG95], in which a similar two-steps process was proposed for the computation of LFT LPV $\mathcal{H}_\infty$ controllers.

In a first step, we make use of the Projection Lemma over the Extended DT Bounded Real Lemma (BRL), see Theorem 1.4 in Chapter 1, in order to obtain an LMI independent of the controller $K(\rho)$. At this first step, a feasible PDLM $X(\rho)$ and slack variable $G(\rho)$ are found as the decision variables on the LMI optimization Problem. In Sect. 4.3.1 and Sect. 4.3.2 general conditions and numerical propositions are given respectively to solve this first step LMI problem.

Using the numerical values for the PDLM $X(\rho)$ and $G(\rho)$, then the Extended DT BRL gives an LMI optimization problem where the only decision variable are the constant gains of the PDSF controller $K(\rho)$, which has a fixed parameter dependent structure. In Sect. 4.3.3 we give numerical conditions to solve this problem and compute the gains for $K(\rho)$.

4.3.1 $\mathcal{H}_\infty$ State-Feedback Controller Existence Conditions for DT-LPV Systems

Let us consider a DT-LPV system of the form:

$$\Xi(\rho) := \begin{cases} x^+ = A(\rho)x + B_u(\rho)u + B_w(\rho)w \\ z = C_z(\rho)x + D_u(\rho)u + D_w(\rho)w \end{cases} \tag{4.10}$$

where $x \in \mathbb{R}^{n_x}$ is the state vector, $u \in \mathbb{R}^{n_u}$ are the control inputs, $w \in \mathbb{R}^{n_w}$ are the exogenous inputs with bounded energy such that $w \in L_2$ and $z \in \mathbb{R}^{n_z}$ are the exogenous outputs. The varying parameter vector $\rho \in \mathbb{R}^m$ is constrained according to Assumption 1.1 and Assumption 1.2 and the system matrices have affine dependency on a basis function $\theta(\rho)$ according to Definition 1.4.

The existence of a PDSF controller according to Definition 4.1 for the control of the LPV system $\Xi(\rho)$ according to the control problem in Definition 4.2 can be proved if the following theorem holds true.

Theorem 4.1
Consider a DT-LPV system $\Xi(\rho)$ and scalar $\gamma_\infty > 0$. If there exist constant matrices $\mathbf{X_0}, \dots, \mathbf{X_N}$, which form a symmetric positive-definite PDLM $X(\rho) \in \mathbb{R}^{n_x \times n_x}$ with basis function $\theta(\rho) = (1, \theta_1, \dots, \theta_N)$, with $\theta_n \in \mathbb{R}$, $n = 1, \dots, N$, and a slack matrix $\mathbf{G}(\rho) \in \mathbb{R}^{n_x \times n_x}$ such that the following condition holds:

$$\mathcal{N}_M^T(\rho) \begin{bmatrix} \mathbf{G}^T(\rho) + \mathbf{G}(\rho) - X(\rho^+) & \star & \star & \star \\ A(\rho)\mathbf{G}(\rho) & X(\rho) & \star & \star \\ C_z(\rho)\mathbf{G}(\rho) & 0 & \gamma_\infty I & \star \\ 0 & B_w^T(\rho) & D_w^T(\rho) & \gamma_\infty I \end{bmatrix} \mathcal{N}_M(\rho) > 0 \tag{4.11}$$

with

$$X(\rho) = \mathbf{X_0} + \sum_{n=1}^{N} \theta_n(\rho)\mathbf{X_n}, \tag{4.12}$$

$$X(\rho^+) = \mathbf{X_0} + \sum_{n=1}^{N} \theta_n(\rho^+)\mathbf{X_n}, \tag{4.13}$$

$$\mathcal{N}_M(\rho) = \mathit{ker}(\begin{bmatrix} 0 & B_u^T(\rho) & D_u^T(\rho) & 0 \end{bmatrix}), \tag{4.14}$$

then, there exists a SF control gain $K(\rho)$ such that the closed-loop form of $\Xi(\rho)$ is robustly stable and γ_∞ is an upper bound on its induced L_2-norm, with control law given by $u = K(\rho)x$.

Proof. Considering a SF control law $u = K(\rho)x$, the closed-loop dynamics of $\Xi(\rho)$ are as follows:

$$\begin{aligned} \Xi_{CL}(\rho) \quad &= \begin{cases} x^+ = (A(\rho) + B_u(\rho)K(\rho))x + B_w(\rho)w \\ z = (C_z(\rho) + D_u(\rho)K(\rho))x + D_w(\rho)w \end{cases} \\ &= \begin{cases} x^+ = \mathcal{A}(\rho)x + \mathcal{B}(\rho)w \\ z = \mathcal{C}(\rho)x + \mathcal{D}(\rho)w \end{cases} \end{aligned} \tag{4.15}$$

Substituting Eq. (4.15) into the sufficient condition in Eq. (1.30) for the L_2-norm computation of LPV systems in Theorem 1.4 from Chapter 1, we obtain the following LMI condition

$$\Psi(\rho, \rho^+) + \mathrm{He}\left(\begin{bmatrix} 0 \\ B_u(\rho) \\ D_u(\rho) \\ 0 \end{bmatrix} K(\rho) \begin{bmatrix} G(\rho) & 0 & 0 & 0 \end{bmatrix} \right) > 0 \tag{4.16}$$

where

$$\Psi(\rho, \rho^+) = \begin{bmatrix} G^T(\rho) + G(\rho) - X(\rho^+) & \star & \star & \star \\ A(\rho)G(\rho) & X(\rho) & \star & \star \\ C_z(\rho)G(\rho) & 0 & \gamma_\infty I & \star \\ 0 & B_w^T(\rho) & D_w^T(\rho) & \gamma_\infty I \end{bmatrix} \tag{4.17}$$

Applying the Projection Lemma over condition (4.16) to eliminate the matrix block $K(\rho)$, then Eq. (4.11) is recovered as an equivalent condition to Eq. (4.16). As such, Eq. (4.11) is a sufficient condition to demonstrate the existence of a State-Feedback control gain $K(\rho)$ such that $\Xi_{CL}(\rho)$ is robustly stable with induced L_2-norm less than γ_∞. □

Notice that when applying the projection lemma on (4.16), it imposes condition (4.11) and additionally

$$\mathcal{N}_N^T(\rho)\Psi(\rho)\mathcal{N}_N(\rho) > 0, \tag{4.18}$$

with

$$\mathcal{N}_N(\rho) = \ker(\begin{bmatrix} G(\rho) & 0 & 0 & 0 \end{bmatrix}). \tag{4.19}$$

Now equation (4.19) can be rewritten as [GA94]

$$\begin{aligned} \mathcal{N}_N(\rho) &= \begin{bmatrix} G(\rho)^{-1} & \star & \star & \star \\ 0 & I & \star & \star \\ 0 & 0 & I & \star \\ 0 & 0 & 0 & I \end{bmatrix} \ker(\begin{bmatrix} I & 0 & 0 & 0 \end{bmatrix}) \\ &:= \hat{G}(\rho)^{-1}\hat{\mathcal{N}}_N(\rho) \end{aligned} \tag{4.20}$$

Replacing (4.20) in condition (4.18) leads to:

$$\hat{\mathcal{N}}_N^T(\rho)\left\{\begin{bmatrix} G(\rho)^{-T} & \star & \star & \star \\ 0 & I & \star & \star \\ 0 & 0 & I & \star \\ 0 & 0 & 0 & I \end{bmatrix} \Psi(\rho) \begin{bmatrix} G(\rho)^{-1} & \star & \star & \star \\ 0 & I & \star & \star \\ 0 & 0 & I & \star \\ 0 & 0 & 0 & I \end{bmatrix}\right\}\hat{\mathcal{N}}_N(\rho) > 0 \tag{4.21}$$

Using Eq. (4.17), this condition leads to the already known constraint $X(\rho) > 0$. As a result, condition (4.18) can then be discarded to prove the equivalency between conditions in Eq. (4.11) and Eq. (4.16) due to the Projection Lemma, for the case of the SF control problem. This fact is similar to the one seen in *Corollary 1* of [LW04], when applying the Projection Lemma over the BRL for the SF case, only the condition involving the null space of $[B_u^T, D_u^T]$ is considered.

4.3.2 Reduction of Theorem 4.1 to a Finite-Dimensional LMI Problem

Theorem 4.1 provides general conditions to prove the existence of some controller $K(\rho)$ for the control of the DT LPV system $\Xi(\rho)$. However, it is numerically very hard to implement, since it is infinitely constrained as it must hold true $\forall\rho \in \Omega$. Moreover, Eq. (4.11) requires the knowledge of ρ^+, which again, can take on infinite possible values and imposes an infinite number of constraints. Nonetheless, Theorem 4.1 can be recasted into a finite number of LMIs using the parameter grid and local variation bounds approach presented in Sect. 4.2. The following proposition gives a numerically tractable implementation of Theorem 4.1 that can be efficiently solved with available SDP solvers.

Proposition 4.2
Consider a DT-LPV system $\Xi(\rho)$, with parameter space $\Omega \in \mathbb{R}^m$ gridded by a grid space $\mathcal{G} \in \Omega$ and assuming bounded parameter rate of variation $\nu \in \mathbb{R}^m$ such that $\forall g_p \in \mathcal{G}$ there exists a bounding polytope $\mathcal{V}_p$ for g_p^+ with 2^m vertices $g_p^v \in \mathcal{V}_p$, and scalar $\gamma_\infty > 0$. If there exist constant matrices $\mathbf{X_0}, \ldots, \mathbf{X_N} \in \mathbb{R}^{n_x \times n_x}$, which form a symmetric positive-definite PDLM $X(\rho)$ with basis function $\theta(\rho) = (1, \theta_1, \ldots, \theta_N)$, with $\theta_n \in \mathbb{R}$, $n = 1, \ldots, N$, and a set of matrices $\mathbf{G_p} \in \mathbb{R}^{n_x \times n_x}$ such that for all (g_p, g_p^v) pairs the following condition holds

$$\mathcal{N}_M^T(\theta_p) \begin{bmatrix} \mathbf{G_p}^T + \mathbf{G_p} - X(\theta_p^v) & \star & \star & \star \\ A(\theta_p)\mathbf{G_p} & X(\theta_p) & \star & \star \\ C_z(\theta_p)\mathbf{G_p} & 0 & \gamma_\infty I & \star \\ 0 & B_w^T(\theta_p) & D_w^T(\theta_p) & \gamma_\infty I \end{bmatrix} \mathcal{N}_M(\theta_p) > 0 \tag{4.22}$$

with

$$X(\theta_p) = \mathbf{X_0} + \sum_{n=1}^{N} \theta_{n,p} \mathbf{X_n}, \tag{4.23}$$

$$X(\theta_p^v) = \mathbf{X_0} + \sum_{n=1}^{N} \theta_{n,p}^v \mathbf{X_n}, \tag{4.24}$$

$$\mathcal{N}_M(\theta_p) = ker(\begin{bmatrix} 0 & B_u^T(\theta_p) & D_u^T(\theta_p) & 0 \end{bmatrix}), \tag{4.25}$$

then, there exists a SF control gain $K(\rho)$ such that the closed-loop form of $\Xi(\rho)$ is robustly stable and where γ_∞ is an upper bound on its induced L_2-norm.

Proof. Proposition 4.2 is a direct application of Theorem 4.1 using the parameter grid and local variation bounds approach detailed in Sect. 4.2. The varying parameter vector ρ is gridded at fixed points g_p alongside the varying parameter space Ω. At each fix grid point g_p the LPV system $\Xi(\rho)$, with affine dependency on some scheduling signal $\theta(\rho)$, is then frozen as an LTI representation $\Xi(\theta_p)$. Meanwhile, using the maximum rates of parameter variation ν, ρ^+ is bounded at each fixed grid point g_p by a polytope $\mathcal{V}_p$, each vertex of this polytope around g_p defined as g_p^v. This concludes the proof. □

The following remarks give some hints on the implementation of Proposition 4.2.

Remark 4.2
According to Definition 4.2, the control problem objective is the minimization of the induced L_2-norm upper bound γ_∞ of the closed-loop form of $\Xi(\rho)$. However, Theorem 4.1 and Proposition 4.2 are given with an arbitrary upper bound γ_∞ for the purpose of generalization. Nonetheless, once Proposition 4.2 has been implemented, the LMI optimization problem can be solved as the minimization of the induced L_2-norm upper bound γ_∞^* as follows:

$$\gamma_\infty^* = \min_{\mathbf{X_0}, \ldots, \mathbf{X_N}, \mathbf{G_p}, \gamma_\infty} \gamma_\infty \quad s.t. \;\; (4.22) \; \forall (g_p, g_p^v) \tag{4.26}$$

Due to numerical issues, once an optimal upper bound γ_∞^* is found according to Eq. (4.26), it is convenient to recompute the values of $X_0, \ldots, X_N, G_p$ employing Proposition 4.2 with fixed $\gamma_\infty = \gamma_\infty^*(1 + h)$, where h is a percentage [PV08].

Remark 4.3
It is hard to determine exactly how dense needs to be the grid space $\mathcal{G} \in \Omega$. An ad-hoc solution is to solve the design LMI problem from Proposition 4.2, then check if stability and performances holds in a much denser grid [Bec96].

Remark 4.4
Note that in Theorem 4.1 the slack matrix $G(\rho)$ is assumed to be parameter dependent but its structure is not given. One option is to assume an affine dependency on the scheduling function

$$G(\rho) = G_0 + \sum_{n=1}^{N} \theta_n(\rho) G_n, \tag{4.27}$$

However, given that $G(\rho)$ does not play an important role on the proof of system stability as $X(\rho)$ does, forcing an affine parametric dependency could lead to a conservative solution. To avoid this conservatism, the slack matrix $G(\rho)$ in Proposition 4.2 is expressed as a set of matrices. This solution assumes a parameter dependency such that

$$G(\rho) = \sum_{p=1}^{P} \zeta_p(\rho) G_p \tag{4.28}$$

with

$$\zeta_p(\rho) = \begin{cases} 1, & \text{if } \rho = g_p \\ 0, & \text{otherwise} \end{cases} \tag{4.29}$$

where P is the total number of grid-points in $\mathcal{G}$. This parameter dependency means that for each grid point g_p there exists a unique constant slack matrix G_p.

4.3.3 Computation of the PDSF Controller $K(\rho)$

If a valid solution to the LMI problem from Proposition 4.2 exists, then we obtain numerical candidate values for the PDLM $X(\rho)$ and the slack variable $G(\rho)$. Note that with an existing candidate solution for $X(\rho)$ and $G(\rho)$, applying the Extended DT BRL from Theorem 1.4 in Chapter 1 over $\Xi_{CL}(\rho)$ in (4.15), the BRL now results in an LMI with $K(\rho)$ as the only decision variable.

Let us assume a PDSF controller $K(\rho)$, according to Definition 4.1, with affine dependency on the scheduling basis functions θ_n such that

$$K(\rho) = K_0 + \sum_{n=1}^{N} \theta_n(\rho) K_n \tag{4.30}$$

The following proposition provides an LMI optimization problem that allows to compute the constant gains $K_0, \ldots, K_N$ for the PDSF controller $K(\rho)$.

Proposition 4.3

Consider a DT-LPV system $\Xi(\rho)$, with parameter space $\Omega \in \mathbb{R}^m$ gridded by a grid space $\mathcal{G} \in \Omega$ and assuming bounded parameter rate of variation $\nu \in \mathbb{R}^m$ such that $\forall g_p \in \mathcal{G}$ there exists a bounding polytope $\mathcal{V}_p$ for g_p^+ with 2^m vertices $g_p^v \in \mathcal{V}_p$, and scalar γ_∞. Moreover, consider a given symmetric positive-definite PDLM $X(\rho) \in \mathbb{R}^{n_x \times n_x}$ and a set of matrices $G_p \in \mathbb{R}^{n_x \times n_x}$, both computed as the solutions to Proposition 4.2. If there exist constant matrices $\mathbf{K_0}, \ldots, \mathbf{K_N}$, which form a PDSF controller $K(\rho) \in \mathbb{R}^{n_u \times n_x}$ with basis function $\theta(\rho) = (1, \theta_1, \ldots, \theta_N)$, with $\theta_n \in \mathbb{R}$, $n = 1, \ldots, N$, such that for all (g_p, g_p^v) pairs the following condition holds

$$\Psi(\theta_p, \theta_p^v) + \mathrm{He}\left(\begin{bmatrix} 0 \\ B_u(\theta_p) \\ D_u(\theta_p) \\ 0 \end{bmatrix} K(\theta_p) \begin{bmatrix} G_p & 0 & 0 & 0 \end{bmatrix} \right) > 0 \tag{4.31}$$

where

$$K(\theta_p) = \mathbf{K_0} + \sum_{n=1}^{N} \theta_{n,p} \mathbf{K_n}, \tag{4.32}$$

$$\Psi(\theta_p, \theta_p^v) = \begin{bmatrix} G_p^T + G_p - X(\theta_p^v) & \star & \star & \star \\ A(\theta_p) G_p & X(\theta_p) & \star & \star \\ C_z(\theta_p) G_p & 0 & \gamma_\infty I & \star \\ 0 & B_w^T(\theta_p) & D_w^T(\theta_p) & \gamma_\infty I \end{bmatrix} \tag{4.33}$$

then the closed-loop form of $\Xi(\rho)$ is exponentially stable and γ_∞ is an upper bound on its induced L_2-norm, with control law given by $u = K(\rho)x$.

Proof. Proposition 4.3 is a direct application of Theorem 1.4, with gridding relaxations as seen in Sect. 4.2 and with the SF control gains of $K(\rho)$ as the only unknown variables on the LMI problem.

Consider the closed-loop dynamics $\Xi_{CL}(\rho)$ as in (4.15). Applying the Extended DT BRL over $\Xi_{CL}(\rho)$ condition (4.16) is recovered. With a given symmetric positive-definite matrix $X(\rho)$ and given slack variable $G(\rho)$, assume that there exists a SF control gain $K(\rho)$ such that (4.16) holds true according to Theorem 1.4. Applying the parameter grid and local variation bounds approach for relaxations on ρ and ρ^+ in (4.16), results for all (g_p, g_p^v) pairs in condition (4.31). This concludes the proof. □

Remark 4.5

It should be noted that there is no strict requirement for $X(\rho)$ and $K(\rho)$ to share the same parameter dependent structure, although this represents the most straightforward solution. One possible structure for the SF controller could simply be $K = K_0$. This represents computing a constant robust SF controller gain K_0 for the whole parameter space Ω which is obviously very conservative. Nonetheless, this highlights that the PDSF controller (4.30) *is in fact a parameter dependent robust controller as the controller gains $K_0, \ldots, K_N$ are fixed $\forall \rho \in \Omega$. For this reason the choice of the parametric dependent basis function $\theta(\rho)$ in Eq.* (4.30) *is a very important degree of freedom in the synthesis process to achieve non conservatives solutions.*

4.4 Lateral Control of the Scaled Automated Vehicle (SAV) Using a PDSF Controller

So far the previous sections of this chapter have focused on LMI conditions for the general synthesis problem of PDSF controllers. In what follows it is explained the control problem in the context of the lateral control of the SAV platform for autonomous steering in Path Tracking applications.

4.4.1 Reference Generation for Path Tracking

The objective of the control task is to achieve robust path tracking of a given trajectory. The trajectory that has been considered for this task is the circuit shown in Fig. 4.2. The X and Y coordinates that make the circuit have been sampled at $0.01m$ intervals and all the coordinates data points stored as vectors on the Remote PC of the SAV Platform, see Chapter 2.

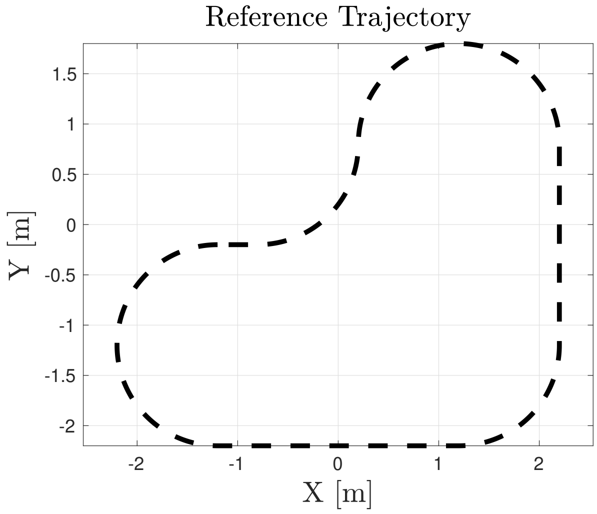

Figure 4.2: Reference Trajectory.

In order to generate the yaw rate reference signal $\dot{\psi}_{ref}$ that will drive the low-level PDSF controller to track the given trajectory, the Pure Pursuit Algorithm is used. This reference generation algorithm has been selected for its simplicity of implementation, good performance and simple tuning with only one parameter to modify [Cou92]; [Pad+16]. A brief description of the algorithm is given in the following.

Consider a given configuration $(x, y, \psi)^T$ of the vehicle, where x and y are the coordinates of the vehicle on the track and ψ is the heading angle in the inertial frame. Note that all of these variables are available on the SAV platform provided by the Vicon Tracker system, see Chapter 2.

Given a look-ahead distance

$$L = t_p v_x, \tag{4.34}$$

where t_p is the look-ahead time and v_x the vehicle longitudinal velocity, find a point (x_{ref}, y_{ref}) on the reference trajectory such that $\|(x_{ref}, y_{ref}) - (x, y)\| = L$. Compute the angle α according to

$$\alpha = \arctan\left(\frac{y_{ref} - y}{x_{ref} - x}\right) - \psi \tag{4.35}$$

Then the reference yaw rate signal to achieve path tracking is given by

$$\dot{\psi}_{ref} = \frac{2v_x \sin\alpha}{L} \tag{4.36}$$

Note that the only tuning parameter on the algorithm is the look-ahead time t_p as seen in (4.34). For this work it has been considered a look-ahead time value of $t_p = 1s$.

4.4.2 PDSF Control Problem Formulation for Path Tracking on the SAV

In the PDSF controller design process the first step is to grid the varying parameter space, in this case for the longitudinal velocity v_x. For control design purpose it is assumed the following bounds $v_x \in [0.5,\ 2] m/s$ for the parameter range and $|\nu| \leq 0.02 = a_{max}T_s$ for the maximum rate of parameter variation between consecutive sampling instances, where $a_{max} = 1m/s^2$ is the assumed maximum vehicle acceleration and $T_s = 0.02s$ is the sampling time at which the controller will be implemented. For the gridding space $\mathcal{G}$, the varying parameter v_x has been uniformly gridded at a constant interval of $0.01m/s$, this represents 151 grid-points on the parameter range from $0.5m/s$ to $2m/s$.

From the chosen grid space $\mathcal{G}$, at each frozen speed gridpoint $v_{x,p}$ we define the reference tracking control problem on the $\mathcal{H}_\infty$ framework by building a generalized plant $P(v_{x,p})$ that includes the weighted performances for tracking and actuator behaviour [ZD98]. The chosen scheme for the generalized plant at each grid-point $v_{x,p}$ is given in Fig. 4.3.

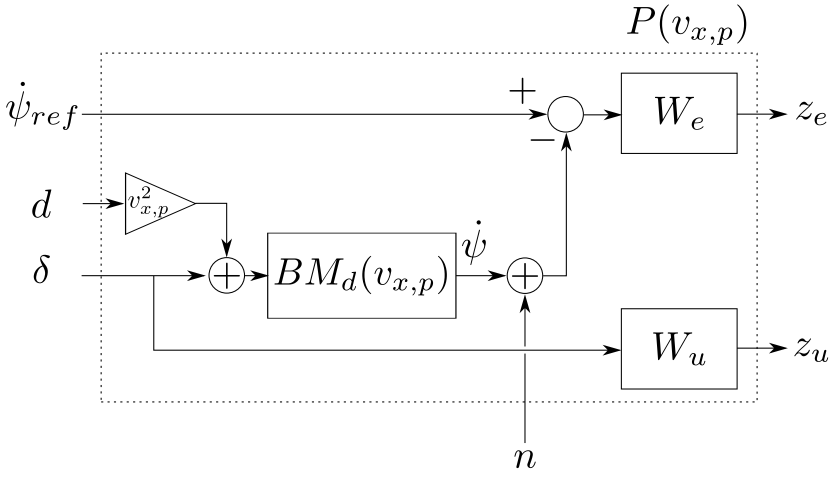

Figure 4.3: Generalized Plant Scheme at grid-point $v_{x,p}$.

The exogenous inputs of the generalized plant $P(v_x)$ are $w = (\dot{\psi}_{ref}, d, n)^T$. $\dot{\psi}_{ref}$ is the yaw rate reference signal to be followed, d represents an input disturbance and n represents sensor noises in the measurements from the signal $\dot{\psi}$. Note that the input disturbance d at each grid-point is multiplied by the squared value of v_x, e.g. $v_{x,p}^2$. This term is introduced to account for observed disturbance effects on the SAV due to interactions between the lateral dynamics with the longitudinal behaviour, to which the vehicle is more sensitive at higher speeds.

The vector of control performances is $z = (z_e, z_u)^T$, with z_e being the tracking error performance and z_u the actuator performance signal respectively. The used weight W_e to set the tracking specification is the following:

$$W_e = \mathcal{Z}_T \left(\frac{s/M_s + f_b}{s + f_b \epsilon} \right) \tag{4.37}$$

Considering $M_s = 2$, $f_b = 2\pi 0.3\ rad/s$ and $\epsilon = 0.01$. Meanwhile, the weight W_u used to specify the constraints on the control signal δ is:

$$W_u = \mathcal{Z}_T \left(\frac{s + f_{bc}/M_u}{\epsilon_u s + f_{bc}} \right) \tag{4.38}$$

Considering $M_u = 0.4$, $f_{bc} = 2\pi 10\ rad/s$ and $\epsilon_u = 0.001$. For both weights W_e (4.37) and W_u (4.38) the discretization operator $\mathcal{Z}$ has been executed using the Tustin transform.

The expression $BM(v_{x,p})$ defines the SAV bicycle model at a frozen grid point $v_{x,p}$, taking in this chapter the bicycle model from Definition 2.3. Then $BM_d(v_{x,p})$, as seen in Fig. 4.3, is computed at each of the grid-point $v_{x,p}$ as $BM_d(v_{x,p}) = \mathcal{Z}_{ZOH}(BM(v_{x,p}))$, where in this case the $\mathcal{Z}$ operator is executed using a zero-order hold discretization.

Putting all these elements together the generalized plant can be computed for a for a fixed speed grid point $v_{x,p}$ according to the scheme in Fig. 4.3 with the frozen LTI representation of $P(v_{x,p})$ given by

$$P(v_{x,p}) := \begin{cases} x^+ = A(v_{x,p})x + B_u(v_{x,p})u + B_w(v_{x,p})w \\ z = C_z(v_{x,p})x + D_u(v_{x,p})u + D_w(v_{x,p})w \end{cases} \tag{4.39}$$

4.4.3 PDSF Controller Synthesis

Having the generalized plant defined at each the grid-point $v_{x,p}$ by Eq. (4.39), then, the control problem is to find a PDSF controller $K(v_x)$ such that the control law $\delta = K(v_x)x$ minimizes the induced L_2-norm γ_∞ over the generalized plant $P(v_x)$ and controller $K(v_x)$ interconnection, as shown in Fig. 4.4, according to Definition 4.2. Notice that in Fig. 4.4 $x = (v_y, \dot{\psi}, x_e, x_u)^T$ are the states of the generalized plant $P(v_x)$, with v_y and $\dot{\psi}$ the states of the Bicycle Model according to Definition 2.3 and x_e and x_u are the states of the weights W_e and W_u respectively.

The existence of such a PDSF controller $K(v_x)$ can then be tested by solving the LMI problem presented in Proposition 4.2 as a minimization over the scalar γ_∞, according to

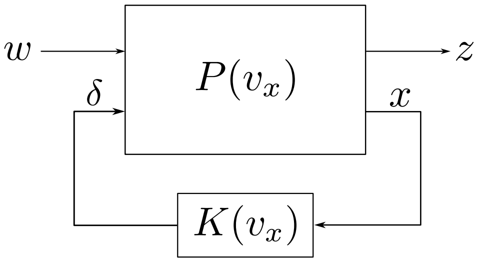

Figure 4.4: Generalized Plant and controller interconnection.

Remark 4.2. The parameter dependent structure that has been assigned for the PDLM $X(\rho)$ for this LMI problem is as follows:

$$X(v_x) = X_0 + \frac{1}{v_x}X_1 + v_xX_2 + v_x^2X_3 \tag{4.40}$$

This structure is chosen as it mimics all the ways in which the varying parameter v_x appear in both the generalized plant $P(v_x)$ and correspondingly the Bicycle Model $BM(v_x)$. On the other hand, the parameter dependent slack variable $G(v_x)$ has been chosen such that for each grid-point $v_{x,p}$ there exists a unique slack variable G_p value, as explained in Remark 4.4.

Using the parser Yalmip [Löf04] and the SDPT3 solver [TTT04], Proposition 4.2 can be efficiently solved. It is proved to be feasible with an optimal induced L_2-norm found to be $\gamma_\infty = 10.0184$.

From the solution to Proposition 4.2 we now have numerical values for the PDLM $X(v_x)$ and the slack matrix $G(v_x)$. Using these values, we can solve Proposition 4.3 in order to compute the gains of a PDSF controller as seen in Definition 4.1. For this, we select a PDSF controller with the following fixed structure

$$K(v_x) = K_0 + \frac{1}{v_x}K_1 + v_xK_2 + v_x^2K_3. \tag{4.41}$$

Employing this choice of structure for the PDSF controller $K(v_x)$, Proposition 4.3 can be solved with $K_0, \dots, K_3$ as the only decision variables to be found.

Note that despite having a grid space $\mathcal{G}$ consisting of 151 grid-points, the controller gains in Eq. (4.41) reduces to the four vectors $K_0, \dots, K_3$, with each $K_n \in \mathbb{R}^4$. In comparison, the usual grid-based LPV approach would require an individual controller gain for each grid-point. Thus the PDSF controller solution allows to greatly save the memory space that will be required for real-time controller implementation. Moreover, the fact that the number of controller gains is chosen by the control designer through the basis function that forms $K(\rho)$ and not by the number of grid-points, allows one to grid the varying parameter space with a density that simply would not be feasible otherwise for controller synthesis. At the same time, the real-time implementation of the controller $K(v_x)$ is performed by directly implementing Eq. 4.41 in the software, without requiring any interpolation of point-wise controllers.

4.4.4 Frequency Analysis of the PDSF Control Design

A first validation of the controller design is carried out on the frequency domain. We consider the closed-loop interconnection between the generalized plant $P(v_x)$ and the PDSF controller $K(v_x)$, as illustrated in Fig. 4.4, evaluated at some frozen values of the varying parameter $v_{x,p} = (0.5, 0.75, 1, 1.25, 1.5, 1.75, 2)m/s$. Note that this is just small sample of the 151 grid-points used for the synthesis of the PDSF controller, however it is enough to illustrate the frequency domain response of the closed-loop alongside the whole range of the varying parameter.

In order to validate the yaw rate tracking error $\dot{\psi}_e = \dot{\psi}_{ref} - \dot{\psi}$ response to changes in the yaw rate reference $\dot{\psi}_{ref}$, we compare the sensitivity transfer function $S = \frac{\dot{\psi}_e}{\dot{\psi}_{ref}}$ with respect the employed tracking error template $1/W_e$, with weight W_e given in Eq. (4.37). Meanwhile, the validation of the constrains of control signal δ response to changes in the yaw rate reference signal $\dot{\psi}_{ref}$ is done by comparing the controller sensitivity transfer function $KS = \frac{\delta}{\dot{\psi}_{ref}}$ with respect the control action template $1/W_u$, with weight W_u given by Eq. (4.38). From the frequency response results shown in Fig. 4.5 it can be seen that both design requirements for the controller $K(v_x)$ are satisfactorily fulfilled for the whole range of values that was consider of the varying parameter v_x in the PDSF design.

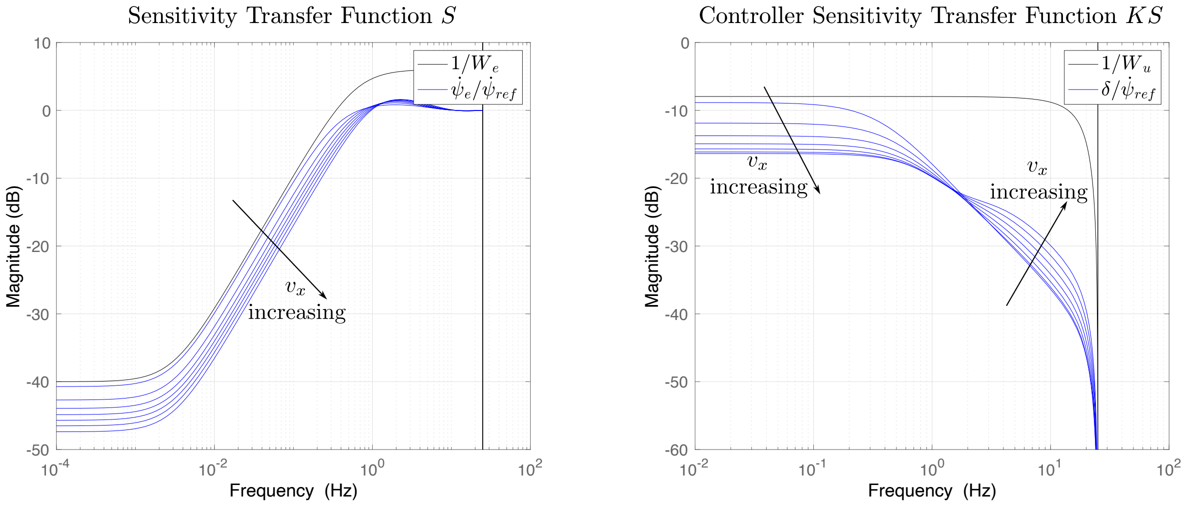

Figure 4.5: Sensitivity Transfer Function $S = \frac{\dot{\psi}_e}{\dot{\psi}_{ref}}$ versus tracking performance template W_e^{-1} (left) and Controller Sensitivity Transfer Function $KS = \frac{\delta}{\dot{\psi}_{ref}}$ versus actuator performance template W_u^{-1} (right) at frozen values of the varying parameter v_x.

4.5 Experimental Results

The real-time implementation of the PDSF controller is realized in the remote ROS PC from the SAV test platform. As seen in Chapter 2, the system states, e.g. v_y and $\dot{\psi}$, as well as the value of the varying parameter v_x are available online from the data measured by the Vicon Tracker. Then, with the gains of the PDSF controller $K(v_x)$ designed and computed as described in Sect. 4.4.2 and in Sect. 4.4.3, the control law $\delta = K(v_x)x$ for the SAV steering can be easily implemented on the ROS2 environment of the SAV platform, with $K(v_x)$ given by (4.41).

The test scenario to demonstrate the path tracking performance of the SAV with PDSF steering controller consists in driving the SAV autonomously on the circuit from Fig. 4.2 at varying speeds. The speed profile used during the test can be seen in Fig. 4.6. Recall that the v_x speed profile, shown in Fig. 4.6, also acts as the varying parameter for the controller $K(v_x)$. Figure 4.7 and Fig. 4.8 present the tracking performance for the reference yaw rate and the control signal respectively.

Figure 4.7 shows in black the yaw rate reference $\dot{\psi}_{ref}$ generated by the Pure Pursuit algorithm, see Sect. 4.4.1, as the SAV moves through the track, in blue it is given the measured yaw rate by the Vicon Tracker system for the SAV during the test. In Fig. 4.8 the commanded steering angle δ computed by the PDSF controller $K(v_x)$ is presented.

In order to better visualize the path tracking performance of SAV when using the PDSF controller, Fig. 4.9 presents information regarding the followed trajectory by the SAV during the test on the X and Y coordinates of the track. On the left of the figure it is represented the reference circuit in black and the trajectory followed by the SAV during the complete test. Note that in order to better identify the multiple laps the SAV has done around the circuit, the followed trajectory is color mapped with the instantaneous longitudinal velocity, corresponding with the information given in Fig. 4.6. On the right side of the figure it is given in black the reference trajectory and with blue triangles the orientation and position of the SAV, with the orientation and position taken from a time window of the test from $t \in [40,\, 50] sec$. Note from Fig. 4.6 that this time window coincides with a lap made by the SAV at high speeds.

From the results of the test we can conclude that with the PDSF controller $K(v_x)$ (4.41) the SAV manages to achieve very satisfactory path tracking performances. From Fig. 4.7 it can be seen that the controller manages to track the given reference signal while providing a control signal that is smooth for all the range of speeds seen during the test, as demonstrated by the steering command in Fig. 4.8. In can be noticed in Fig. 4.7 the effect of the pure input delay that was ignored during synthesis of the controller. It is well known that unaccounted system delays may lead the closed-loop to produce unstable behaviours, despite that, the PDSF controller $K(v_x)$ is able to maintain the vehicle stable and with acceptable reference tracking performance, proving the controller stability in face of critical unmodeled dynamics.

It should be noted however that at higher speeds, for $t \in [40,\, 55] sec$, it can be seen in

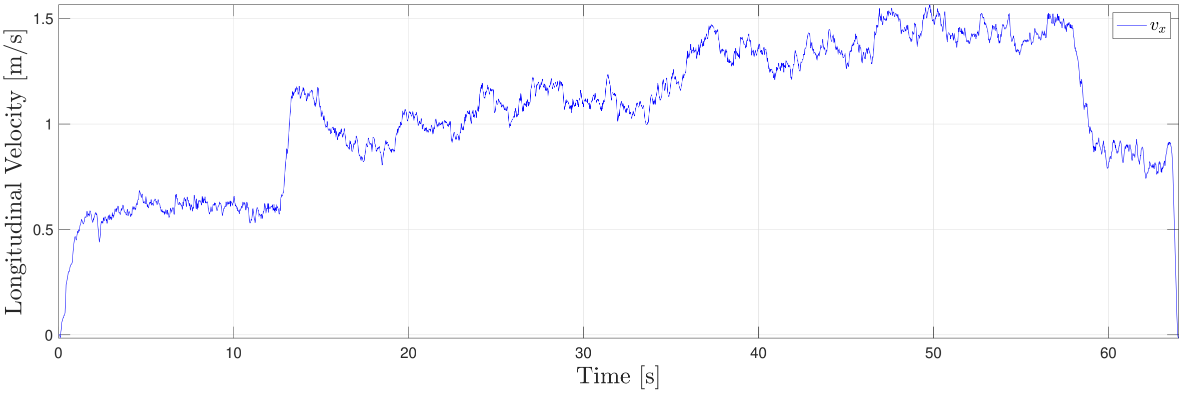

Figure 4.6: Longitudinal Velocity of the SAV during the test.

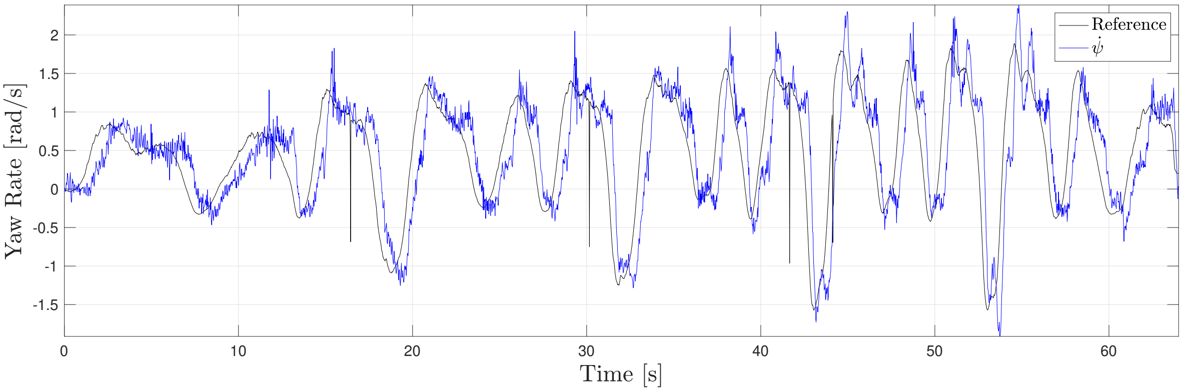

Figure 4.7: Yaw rate reference (black) and SAV yaw rate (blue) during the test.

Fig. 4.7 that some oscillations appear in the yaw rate signal $\dot{\psi}$ after fast changes on the reference. This is a known issue on the platform, caused by the interaction with the longitudinal dynamics of the vehicle due to the behaviour of the dual BLDC motors, which can cause a disturbance torque on the lateral dynamics if their speeds diverge from each other. To attenuate this disturbance effect, higher at larger speeds, it was introduced during the controller design the term $v_{x,p}^2$ on the input disturbance, see Fig. 4.3.

The tracking performance can specially be verified in Fig. 4.9 (left). It can be seen how the trajectory of the SAV during multiple laps overlap with each other almost perfectly, even though there exist an important variation in speed during the complete test. This demonstrates that while being very simple to implement, the PDSF controller allows for a consistent performance throughout the considered parameter space for v_x. Moreover on Fig. 4.9 (right), during the evolution of the SAV position and orientation there is no noticeable evidence of sliding during trajectory even at high speed, meaning that the PDSF controller can cope with demanding situations while keeping the stability of the system.

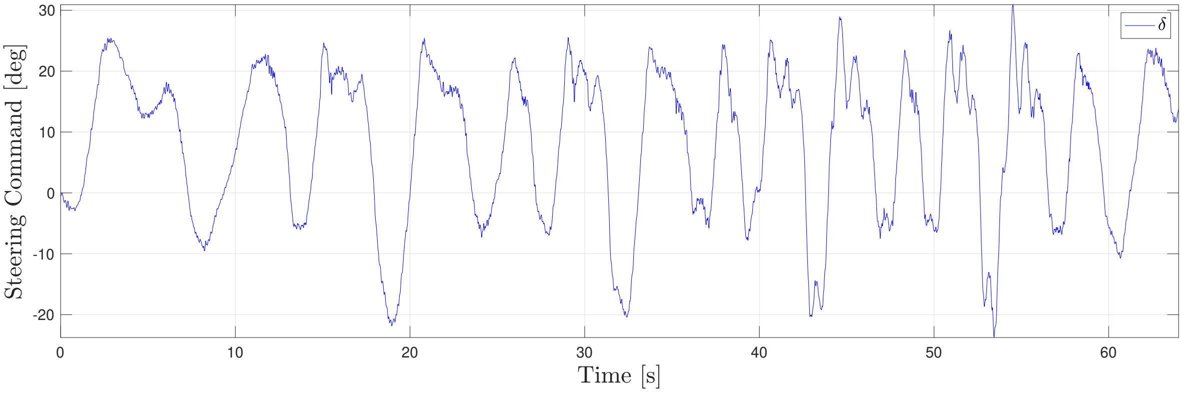

Figure 4.8: Steering command computed by the PDSF controller.

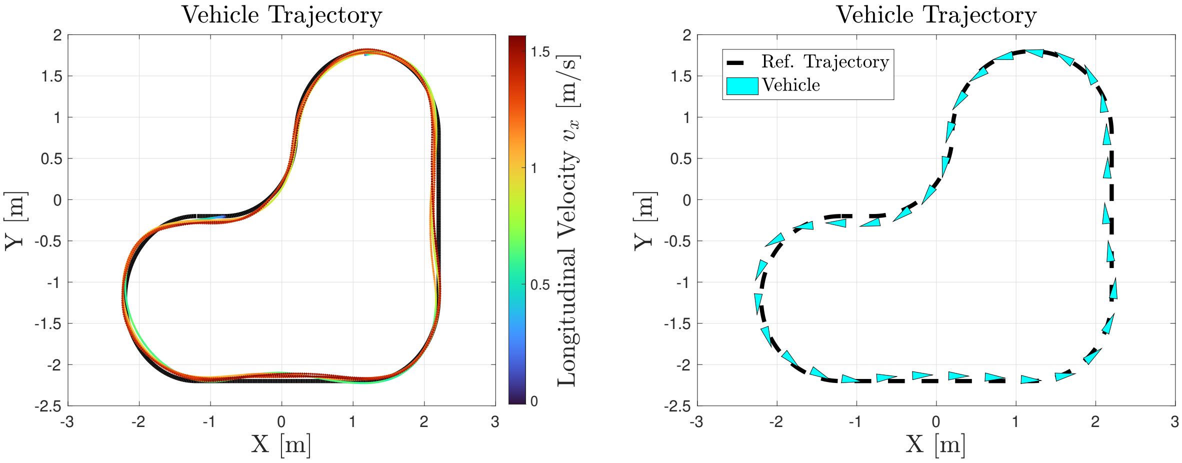

Figure 4.9: Reference trajectory and actual vehicle trajectory color coded with the instantaneous longitudinal velocity (left). Reference Trajectory and position and orientation of the SAV during a lap done at high speed at $t \in [40,\, 50] sec$(right).

4.6 Conclusions

In this chapter it has been introduced an approach to reduce the infinitely constrained LMI conditions from Chapter 1 into finite LMI problems using a Grid Based DT-LPV approach. In particular it was proposed conditions for the computation of PDSF controllers. The advantages of the PDSF control approach are the following. First of all, the resulting controller is straightforward to implement as it is self-scheduled based on the imposed parametric basis function (no online interpolation is required) and lightweight on the required memory space. On the other hand, the Parametric LPV synthesis approach allows to use very dense grids on the parameter space without increasing the number of controller gains to be implemented, something which is desirable when using grid-based LPV approaches in order to obtain better stability and performances guarantees.

The performance of this control strategy has been tested on the SAV platform for the task of trajectory tracking proving good path following performances. This has been achieved with a PDSF controller that only required four controller gains to be implemented, despite using 151 grid points for the synthesis step. The found controller provided a satisfactory tracking of the desired reference signal for the whole range of the parameter space of varying parameter, this was achieved in spite of unaccounted model uncertainties as the presence of actuator input delays, thus proving the robustness of the proposed approach.

Chapter 5

Lateral Control of Autonomous Vehicles Using Anti-Windup Effects by Means of LPV Scheduling

Contents

5.1 Introduction

In the previous chapter it was seen the design of a PDSF controller to achieve autonomous steering of the SAV car for Path Tracking applications. Although its performance was found to be satisfactory in experimentally validation, the experiment was performed in nominal conditions and in a trajectory with gentle curvature. In this chapter we are interested in studying the control system performance deterioration when driving autonomous vehicles at the limits of its capabilities. In particular, we are interested in tackling the saturation nonlinearity issues that occurs when the controller demands cannot be met by the real actuator. This leads to the well known problem in control of controller Windup.

The objective of this chapter is to enhance the existing lateral control system introduced in Chapter 4 by incorporating a design-related varying parameter. This modification aims to address the issue of controller windup that can occur in the presence of actuator saturation. The goal is to introduce a means of adjusting the controller gain in the LPV/$\mathcal{H}_\infty$ design by utilizing this varying parameter. In real-time, this parameter can be dynamically adjusted through LPV scheduling to emulate the effect of an Anti-Windup mechanism, mitigating the impact of actuator saturation on the controller performance.

The contents of this chapter have been recently developed and have not yet been published at the time of writing this thesis manuscript.

5.1.1 Anti-Windup Strategy with LPV Methods

Here it is given a quick overview of how design-related varying parameters are used in this chapter to achieve a LPV controller design with Anti-Windup behaviour in the presence of actuator saturation. The strategy here presented is inspired by those in [WGP00] and [PV+08]. As can be seen in the scheme in Fig. 5.1, design-related varying parameters are incorporated into the performance weights of the $\mathcal{H}_\infty$ Generalized Plant problem. Consequently, changes in these parameter dependent weighting functions may lead to drastic changes in the resulting $\mathcal{H}_\infty$ controller.

Considering the problem of emulating an Anti-Windup mechanism, as in [PV+08], the parameter dependency will be used to penalize the control performance weight $W_u(\rho)$ whenever the control action is outside of its allowable range. However, as indicated in [WGP00], this requires to use a parameter dependent tracking performance weight $W_e(\rho)$ to relax the tracking criterion when the control action is being penalized.

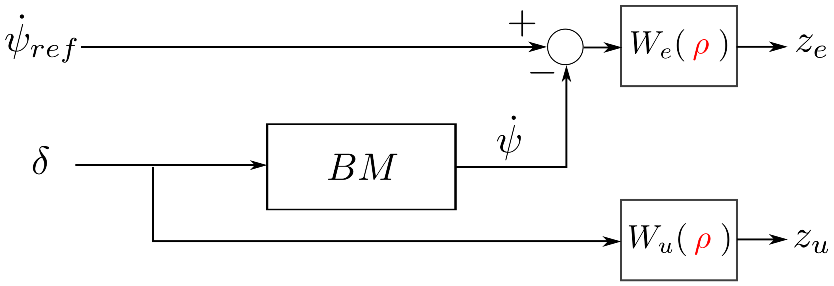

Figure 5.1: Design-Related Varying Parameter ρ added in the Generalized Plant.

Once the LPV controller has been synthesized offline, considering frozen values of the design-related varying parameter ρ, then, a scheduling function is implemented for real-time operation. This function is responsible for dynamically adjusting the design-related parameter to limit the maximum controller output when actuator saturation is present. Thus preventing the build up of controller Windup. The key concept here is that the controller output limitation is straightforwardly accomplished through the dynamic scheduling of the LPV controller using the design-related varying parameter ρ.

5.1.2 Chapter Structure

The structure of the rest of the chapter is the following. In Sec. 5.2 it is introduced new LMI conditions for the computation of Grid-Based DT-LPV controllers. Using this new condition, Sec. 5.3 describes the LPV/$\mathcal{H}_\infty$ synthesis design for an autonomous path tracking controller with Anti-Windup effects applied to the SAV platform. Then, in Sec. 5.4 it is compared the path tracking performance of the LPV controller with Anti-Windup effects with a similarly designed controller without Anti-Windup correction.

5.2 Synthesis Conditions for Grid Based DT-LPV SF Controllers

This section is dedicated to propose a gain-scheduled LPV controller synthesis for Grid Based DT-LPV systems. In contrast with the Parameter Dependent State-Feedback (PDSF) controller approach introduced in Chapter 4, the grid-based gain-scheduled LPV approach results in dedicated point-wise controllers at each grid-point. To the best of the author knowledge, Grid Based DT-LPV synthesis has not been explored in the literature, most works dealing with DT-LPV systems focus on Polytopic approaches [DC+10] and some in LFT LPV methods [Chr+07].

The following subsections provide general conditions for synthesis of gain-scheduled Grid Based DT-LPV SF controllers as well as a proposition for the practical implementation of the LMI optimization problem.

5.2.1 Control Problem Definition

Let us consider a DT-LPV system of the form:

$$\Xi(\rho) := \begin{cases} x^+ = A(\rho)x + B_u(\rho)u + B_w(\rho)w \\ z = C_z(\rho)x + D_u(\rho)u + D_w(\rho)w \end{cases} \tag{5.1}$$

where $x \in \mathbb{R}^{n_x}$ is the state vector, $u \in \mathbb{R}^{n_u}$ are the control inputs, $w \in \mathbb{R}^{n_w}$ are the exogenous inputs with bounded energy such that $w \in L_2$ and $z \in \mathbb{R}^{n_z}$ are the exogenous outputs. The varying parameter vector $\rho \in \mathbb{R}^m$ is constrained according to Assumption 1.1 and Assumption 1.2 and the system matrices have affine dependency on a basis function $\theta(\rho)$ according to Definition 1.4.

Considering such systems, the control problem introduced in this chapter is to find a Gain-Scheduled SF Grid-Based DT-LPV controller, which is defined as follows:

Definition 5.1 (Gain-Scheduled State-Feedback Grid-Based DT-LPV Controller)
Consider a DT-LPV system $\Xi(\rho)$ with parameter space $\Omega \in \mathbb{R}^m$ gridded by a grid space $\mathcal{G} \in \Omega$. A Grid-Based DT-LPV SF controller for the gridded DT-LPV system $\Xi(\rho)$ is of the following form:

$$K(\rho) = \sum_{p=1}^{P} \zeta_p(\rho) K_p \tag{5.2}$$

with

$$\sum_{p=1}^{P} \zeta_p(\rho) = 1 \tag{5.3}$$

where K_p is a constant matrix, P is the total number of grid-points considered in the grid space $\mathcal{G}$, $\zeta(\rho)$ can be any interpolation rule over $\mathcal{G}$ and $\zeta_p(\rho)$ gives a magnitude of the distance between $\rho(k) \in \Omega$ and the grid-point $g_p \in \mathcal{G}$ according to the interpolation rule $\zeta(\rho)$.

Considering such a controller, the control problem is then defined in the LPV/$\mathcal{H}_\infty$ framework such that the synthesis objective is posed as the minimization of the induced L_2-norm of a closed-loop LPV system. Such control problem is given in the following definition.

Definition 5.2 (Grid-Based DT-LPV SF Induced L_2-norm Control Problem)
Given an LPV system $\Xi(\rho)$ and considering an State-Feedback control law $u = K(\rho)x$, the resulting LPV closed-loop system is:

$$\Xi_{CL}(\rho) := \begin{cases} x^+ = (A(\rho) + B_u(\rho)K(\rho))x + B_w(\rho)w \\ z = (C_z(\rho) + D_u(\rho)K(\rho))x + D_w(\rho)w \end{cases} \tag{5.4}$$

Considering the induced L_2-norm of a system, given in Definition 1.5, the control problem is then to find a Grid-Based DT-LPV SF controller $K(\rho)$ according to Definition 5.1 that renders the LPV closed-loop system Ξ_{CL} robustly stable and minimizes its L_2-norm as:

$$\min_{\mathbf{K}(\rho),\gamma_\infty} \gamma_\infty \ s.t. \ \frac{\|z\|_2}{\|w\|_2} \leq \gamma_\infty \tag{5.5}$$

5.2.2 LPV/$\mathcal{H}_\infty$ State-Feedback Controller Conditions for DT-LPV Systems

The following theorem provides a general condition to solve the Grid-Based SF control problem given in Definition 5.2 for DT-LPV systems.

Theorem 5.1
Consider a DT-LPV system $\Xi(\rho)$ and scalar $\gamma_\infty > 0$. If there exist constant matrices $\mathbf{X_0}, \ldots, \mathbf{X_N}$, which form a symmetric positive-definite PDLM $X(\rho) \in \mathbb{R}^{n_x \times n_x}$ with basis function $\theta(\rho) = (1, \theta_1, \ldots, \theta_N)$, with $\theta_n \in \mathbb{R}$, $n = 1, \ldots, N$, and slack matrices $\mathbf{G}(\rho) \in \mathbb{R}^{n_x \times n_x}$ and $\mathbf{Y}(\rho) \in$

$\mathbb{R}^{n_u \times n_x}$ *such that the following condition holds:*

$$\begin{bmatrix} \mathbf{G}^T(\rho) + \mathbf{G}(\rho) - X(\rho^+) & \star & \star & \star \\ A(\rho)\mathbf{G}(\rho) + B_u(\rho)\mathbf{Y}(\rho) & X(\rho) & \star & \star \\ C_z(\rho)\mathbf{G}(\rho) + D_u(\rho)\mathbf{Y}(\rho) & 0 & \gamma_\infty I & \star \\ 0 & B_w^T(\rho) & D_w^T(\rho) & \gamma_\infty I \end{bmatrix} > 0 \tag{5.6}$$

with

$$X(\rho) = \mathbf{X_0} + \sum_{n=1}^{N} \theta_n(\rho)\mathbf{X_n}, \tag{5.7}$$

$$X(\rho^+) = \mathbf{X_0} + \sum_{n=1}^{N} \theta_n(\rho^+)\mathbf{X_n}, \tag{5.8}$$

then, the control law $u = K(\rho)x$ *makes the closed-loop form of* $\Xi(\rho)$ *robustly stable with* γ_∞ *an upper bound on its induced* L_2*-norm. The controller gain computed as* $K(\rho) = Y(\rho)G^{-1}(\rho)$.

Proof. Consider a given positive scalar γ_∞ and given SF control law $u = K(\rho)x$, the closed-loop dynamics of $\Xi(\rho)$ are as follows:

$$\begin{aligned} \Xi_{CL}(\rho) &= \begin{cases} x^+ = (A(\rho) + B_u(\rho)K(\rho))x + B_w(\rho)w \\ z = (C_z(\rho) + D_u(\rho)K(\rho))x + D_w(\rho)w \end{cases} \\ &= \begin{cases} x^+ = \mathcal{A}(\rho)x + \mathcal{B}(\rho)w \\ z = \mathcal{C}(\rho)x + \mathcal{D}(\rho)w \end{cases} \end{aligned} \tag{5.9}$$

$\Xi_{CL}(\rho)$ is exponentially stable with induced L_2-norm less than γ_∞, if, according to Theorem 1.4 in Chapter 1 the following sufficient condition is true:

$$\begin{bmatrix} G^T(\rho) + G(\rho) - X(\rho^+) & \star & \star & \star \\ A(\rho)G(\rho) + B_u(\rho)K(\rho)G(\rho) & X(\rho) & \star & \star \\ C_z(\rho)G(\rho) + D_u(\rho)K(\rho)G(\rho) & 0 & \gamma_\infty I & \star \\ 0 & B_w^T(\rho) & D_w^T(\rho) & \gamma_\infty I \end{bmatrix} > 0 \tag{5.10}$$

Note that this condition is the same condition as Eq. (1.30), from Theorem 1.4, when $\mathcal{A}$, $\mathcal{B}$, $\mathcal{C}$ and $\mathcal{D}$ are given as in Eq. (5.9). Applying the change of variable $Y(\rho) = K(\rho)G(\rho)$ in Eq. (5.10) recovers the LMI condition in Eq. (5.6). This proves that Eq. (5.6) is a sufficient condition for the computation of SF control gain $K(\rho)$ such that $\Xi_{CL}(\rho)$ is robustly stable with induced L_2-norm less than γ_∞. □

5.2.3 Reduction of Theorem 5.1 to a Finite-Dimensional LMI Problem

Theorem 5.1 provides general conditions to compute an LPV SF controller for the DT-LPV system $\Xi(\rho)$ (5.1). However, it is numerically very hard to implement, since it is infinitely constrained as it must hold true $\forall \rho \in \Omega$. Moreover, Eq. (5.6) requires the knowledge of ρ^+, which again, can take on infinite possible values and imposes an infinite number of constraints. Nonetheless, Theorem 5.1 can be recasted to a finite number of LMI using the parameter grid and local variation bounds approach explored in Sect. 4.2 of Chapter 4. The following proposition gives a numerically tractable implementation of Theorem 5.1 to compute the controller gains of a Grid Based DT-LPV SF controller.

Proposition 5.1
Consider a DT-LPV system $\Xi(\rho)$, with parameter space $\Omega \in \mathbb{R}^m$ gridded by a grid space $\mathcal{G} \in \Omega$ and assuming bounded parameter rate of variation $\nu \in \mathbb{R}^m$ such that $\forall g_p \in \mathcal{G}$ there exists a bounding polytope $\mathcal{V}_p$ for g_p^+ with 2^m vertices $g_p^v \in \mathcal{V}_p$, and scalar $\gamma_\infty > 0$. If there exist constant matrices $\mathbf{X_0}, \dots, \mathbf{X_N}$, which form a symmetric positive-definite PDLM $X(\rho) \in \mathbb{R}^{n_x \times n_x}$ with basis function $\theta(\rho) = (1, \theta_1, \dots, \theta_N)$, with $\theta_n \in \mathbb{R}$, $n = 1, \dots, N$, and a set of matrices $\mathbf{G_p} \in \mathbb{R}^{n_x \times n_x}$ and $\mathbf{Y_p} \in \mathbb{R}^{n_u \times n_x}$ such that for all (g_p, g_p^v) pairs the following condition holds

$$\begin{bmatrix} \mathbf{G_p}^T + \mathbf{G_p} - X(\theta_p^v) & \star & \star & \star \\ A(\theta_p)\mathbf{G_p} + B_u(\theta_p)\mathbf{Y_p} & X(\theta_p) & \star & \star \\ C_z(\theta_p)\mathbf{G_p} + D_u(\theta_p)\mathbf{Y_p} & 0 & \gamma_\infty I & \star \\ 0 & B_w^T(\theta_p) & D_w^T(\theta_p) & \gamma_\infty I \end{bmatrix} > 0 \tag{5.11}$$

with

$$X(\theta_p) = \mathbf{X_0} + \sum_{n=1}^{N} \theta_{n,p} \mathbf{X_n}, \tag{5.12}$$

$$X(\theta_p^v) = \mathbf{X_0} + \sum_{n=1}^{N} \theta_{n,p}^v \mathbf{X_n}, \tag{5.13}$$

then, the control law $u = K(\rho)x$ makes the closed-loop form of $\Xi(\rho)$ robustly stable with γ_∞ an upper bound on its induced L_2-norm. The controller gain at each grid-point computed as $K_p = Y_p G_p^{-1}$.

Proof. Proposition 5.1 is a direct application of Theorem 5.1 using the parameter grid and local variation bounds approach detailed in Sect. 4.2 from Chapter 4. The varying parameter vector ρ is gridded at fixed points g_p alongside the varying parameter space Ω. At each fix grid point g_p the LPV system $\Xi(\rho)$, with affine dependency on some scheduling signal $\theta(\rho)$, is then frozen as an LTI representation $\Xi(\theta_p)$. Meanwhile, using the maximum rates of parameter variation ν, ρ^+ is bounded at each fixed grid point g_p by a polytope $\mathcal{V}_p$, each vertex of this polytope around g_p defined as g_p^v. This concludes the proof. □

Note that Remark 4.2, made in Chapter 4, with respect to the minimization of the upper bound γ_∞ on the induced L_2 norm of the closed-loop form of $\Xi(\rho)$ also applies for Proposition 5.1. Equally, Remark 4.4 made with respect to the slack variable $G(\rho)$ also applies to the slack variable $Y(\rho)$ in Proposition 5.1. As done for $G(\rho)$, at each grid-point g_p it is proposed to consider a unique matrix Y_p. With this, the individual gain K_p of the LPV SF controller $K(\rho)$ is computed with the least amount of conservatism.

5.3 LPV/$\mathcal{H}_\infty$ Lateral Control for the SAV with Anti Windup Effects

In this section, the design of the Grid Based DT-LPV controller with Anti-Windup scheduling for the autonomous path tracking control of the SAV platform is presented. The design is defined within the LPV/$\mathcal{H}_\infty$ design framework, with the longitudinal speed v_x and an Anti-Windup activation variable ρ used as varying parameters to schedule the controller gains. The controller gains are computed offline employing Proposition 5.1 from Sec. 5.2.

5.3.1 Control Problem Formulation

The control problem formulation consists in a yaw rate tracking problem for the LPV lateral dynamics of the SAV for a range of longitudinal speeds v_x. This is similar as in Chapter 4. The novelty in this chapter consists in adding a new varying parameter ρ. The scheduling of this design-related parameter is not defined in any way by the dynamics of the system. Instead, its online value is a free decision of the control designer. See Sec. II for an overview of works that propose a similar approach.

With this new varying parameter, the LPV control design for lateral control with Anti Windup effects have two varying parameters: the longitudinal effect v_x and the Anti-Windup activation parameter ρ. The longitudinal speed v_x is assumed bounded by $v_x \in [0.5,\, 2] m/s$ for the parameter range and $|\nu_{v_x}| \leq 0.02 = a_{max} T_s$ for the maximum rate of parameter variation between consecutive sampling instances, where $a_{max} = 1 m/s^2$ is the assumed maximum vehicle acceleration and $T_s = 0.02 s$ is the sampling time at which the controller will be implemented.

Meanwhile, the Anti-Windup activation parameter ρ is assumed bounded by $\rho \in [1,\, 100]$ for the parameter range and $|\nu_\rho| \leq 2 = \dot{\rho}_{max} T_s$ for the maximum rate of parameter variation between consecutive sampling instances, where $\dot{\rho}_{max} = 100\ 1/s$ is the assumed maximum parameter rate of change.

Concerning the gridding space $\mathcal{G}$, the varying parameter v_x has been uniformly gridded at a constant interval of $0.5 m/s$ such that $v_{x,p} = [0.5,\, 1,\, 1.5,\, 2] m/s$ and for the Anti-Windup activation parameter ρ it is only considered the extremes values such that $\rho_p = [1,\, 100]$. This represents 2D grid space $\mathcal{G}$ with 8 grid-points.

From the chosen grid space $\mathcal{G}$, at each frozen speed grid-point we define the reference tracking control problem on the $\mathcal{H}_\infty$ framework by building a generalized plant $P(v_{x,p}, \rho_p)$ that includes the weighted performances for tracking and actuator behaviour [ZD98]. The chosen scheme for the generalized plant at each grid-point is given in Fig. 5.2.

The exogenous inputs of the generalized plant $P(v_{x,p}, \rho_p)$ are $w = (\dot{\psi}_{ref}, d, n)^T$. $\dot{\psi}_{ref}$ is the yaw rate reference signal to be followed, d represents an input disturbance and n represents sensor noises in the measurements from the signal $\dot{\psi}$. Note that the input disturbance d at

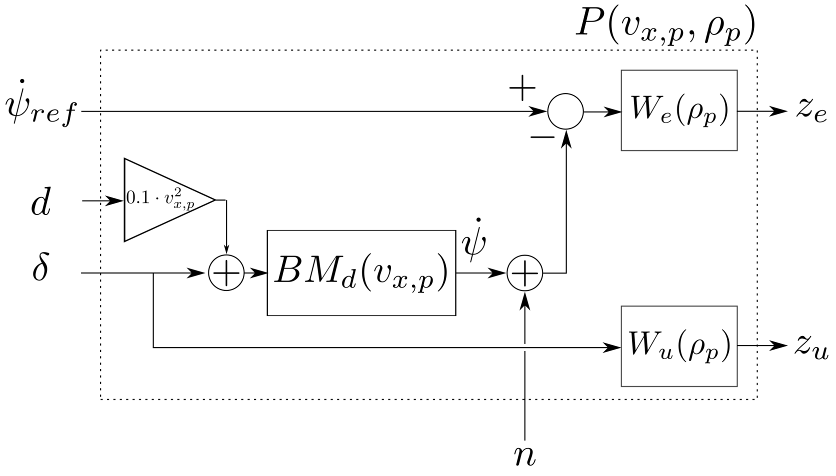

Figure 5.2: Generalized Plant Scheme at grid-point $(v_{x,p}, \rho_p)$.

each grid-point is multiplied by the squared value of v_x, e.g. $v_{x,p}^2$. This term is introduced to account for observed disturbance effects on the SAV due to interactions between the lateral dynamics with the longitudinal behaviour, to which the vehicle is more sensitive at higher speeds. The vector of control performances is $z = (z_e, z_u)^T$, with z_e being the tracking error performance and z_u the actuator performance signal, respectively.

The expression $BM(v_{x,p})$ defines the SAV bicycle model at a frozen grid point $v_{x,p}$, taking in this chapter the bicycle model from Definition 2.3. Note that within the design it is not taking into account the presence of actuator delay in the steering servo-motor, see Chapter 2. Then, $BM_d(v_{x,p})$, is computed at each of the grid-point $v_{x,p}$ as $BM_d(v_{x,p}) = \mathcal{Z}_{ZOH}(BM(v_{x,p}))$, where the $\mathcal{Z}$ operator is executed using a zero-order hold discretization.

Note from Fig. 5.2 that the control performance weights depend on the Anti Windup activation parameter ρ. The weight $W_u(\rho)$ used to specify the constraints on the control signal δ is:

$$W_u(\rho) = \mathcal{Z}_T \left(\rho \cdot \frac{s + f_{bc}/M_u}{\epsilon_u s + f_{bc}} \right) \tag{5.14}$$

Considering $M_u = 0.4$, $f_{bc} = 2\pi 10 \ rad/s$ and $\epsilon_u = 0.001$. The Anti-Windup activation parameter ρ modifies the gain of the control weight. The grid-points $g_p = (v_{x,p}, \rho_p)$ were $\rho_p = 1$, correspond with the nominal design with the control performance weight unaffected. However, when at grid-points such that $\rho_p = 100$, then, the $\mathcal{H}_\infty$ design heavily penalizes the actuator performance objective z_u and as a result it is greatly reduced the allowable gain for the control signal.

Following the guidelines in [WGP00], to maximize the performance of the LPV control design, scheduling the control performance weight $W_u(\rho)$ requires scheduling the tracking performance weight $W_e(\rho)$ as well. For the case of the LPV scheduling Anti-Windup design this requirement is logical. A control design having constant tracking performance requirement independent of the control actuator allowed magnitude gain is inconsistent. One can imagine that requiring a tight tracking error when the control action is being heavily penalized, e.g.

as in the case $W_u(\rho_p = 100)$, would lead to a bad synthesis solution. As a result, the tracking error weight is adapted based on the Anti-Windup activation parameter according to the following expression

$$W_e(\rho) = \begin{cases} = \mathcal{Z}_T\left(\frac{s/M_s + f_b}{s + f_b\underline{\epsilon}}\right), & \text{if } \rho = 1 \\ = \mathcal{Z}_T\left(\frac{s/M_s + f_b}{s + f_b\overline{\epsilon}}\right), & \text{if } \rho = 100 \end{cases} \tag{5.15}$$

Considering $M_s = 2$, $f_b = 2\pi 0.3\ rad/s$, $\underline{\epsilon} = 0.01$ and $\overline{\epsilon} = 2$. Note that in the nominal design point, e.g. $\rho = 1$, demanding $\underline{\epsilon} = 0.01$ is equivalent to demanding less than 1% of tracking error at low frequencies. However, when in the design point with heavily penalized actuator gain, e.g. $\rho = 100$, $\overline{\epsilon} = 2$ is used to relax the tracking specification by that of stability. In fact, as the SAV Bicycle Model is stable at all frozen grid-points for v_x, the stability condition is an undemanding condition, which simplifies the effort of finding a controller solution for the LPV design.

Concerning both weights $W_e(\rho_p)$ (5.15) and $W_u(\rho_p)$ (5.14), frozen at some grid-point for ρ, the discretization operator $\mathcal{Z}$ has been executed using the Tustin transform. Putting all these elements together, the generalized plant can be computed for a for a fixed grid-point according to the scheme in Fig. 5.2 with the frozen LTI representation of $P(v_{x,p}, \rho_p)$ given by

$$P(v_{x,p}, \rho_p) := \begin{cases} x^+ = A(v_{x,p}, \rho_p)x + B_u(v_{x,p}, \rho_p)u + B_w(v_{x,p}, \rho_p)w \\ z = C_z(v_{x,p}, \rho_p)x + D_u(v_{x,p}, \rho_p)u + D_w(v_{x,p}, \rho_p)w \end{cases} \tag{5.16}$$

5.3.2 DT-LPV Grid Based Controller Synthesis

Having the generalized plant defined at each grid-point $g_p = (v_{x,p}, \rho_p)$ by Eq. (5.16), then, the control problem is to find a Grid-Based DT-LPV controller $K(v_x, \rho)$ such that the control law $\delta = K(v_x, \rho)x$ minimizes the induced L_2-norm γ_∞ over the generalized plant $P(v_x, \rho)$ and controller $K(v_x, \rho)$ interconnection, as shown in Fig. 5.3, according to Definition 5.2. Notice that in Fig. 5.3, $x = (v_y, \dot{\psi}, x_e, x_u)^T$ are the states of the generalized plant $P(v_x, \rho)$, with v_y and $\dot{\psi}$ the states of the Bicycle Model according to Definition 2.3 and x_e and x_u are the states of the weights $W_e(\rho)$ and $W_u(\rho)$, respectively.

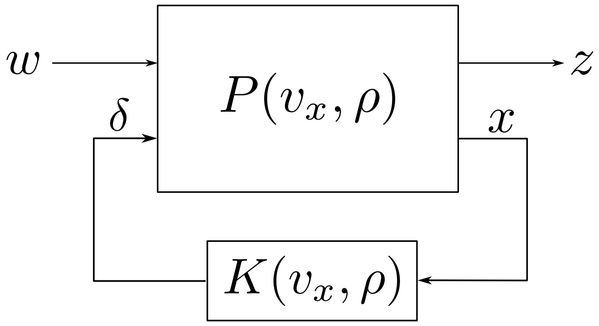

Figure 5.3: Generalized Plant and controller interconnection.

The synthesis of such the LPV controller $K(v_x, \rho)$ can then be done by solving the LMI problem presented in Proposition 5.1 as a minimization over the scalar γ_∞. The parameter dependent structure that has been assigned for the PDLM $X(v_x, \rho)$ for this LMI problem is as follows:

$$X(v_x, \rho) = X_0 + \rho X_1 + \frac{1}{v_x} X_2 + v_x X_3 + v_x^2 X_4 \tag{5.17}$$

This structure is chosen as it mimics all the ways in which the varying parameter v_x appear in the Bicycle Model $BM(v_x)$ and generalized plant $P(v_x, \rho)$ and it mimics the way the Anti-Windup activation parameter ρ is applied in the control performance weight $W_u(\rho)$ (5.15).

Using the parser Yalmip [Löf04] and the SDPT3 solver [TTT04], Proposition 5.1 can be efficiently solved. It is proved to be feasible with an optimal induced L_2-norm upper bound found to be $\gamma_\infty = 1.5589$.

Note in the generalized plant $P(v_x, \rho)$ in Fig. 5.2 that the disturbance term is multiplied by a factor of 0.1. As the parameter ρ already provides by design an active way to reduce the amount of steering in the presence of uncertainties, it was consider in the design to diminish the effect of the input disturbance. This reduces the conservatism of the design and explains why the bound on γ_∞ has a reduction of an order of magnitude with respect the design carried in Chapter 4.

5.3.3 Frequency Analysis of the PDSF Control Design

A first validation of the controller design is carried out on the frequency domain. For this, we consider the closed-loop interconnection between the generalized plant $P(v_x, \rho)$ and the Grid-Based DT-LPV controller $K(v_x, \rho)$, as illustrated in Fig. 5.3, evaluated at all eight frozen grid-points.

In order to validate the yaw rate tracking error $\dot{\psi}_e = \dot{\psi}_{ref} - \dot{\psi}$ response to changes in the yaw rate reference $\dot{\psi}_{ref}$, we compare the sensitivity transfer function $S = \frac{\dot{\psi}_e}{\dot{\psi}_{ref}}$ with respect to the tracking error template $1/W_e$, with the weight $W_e(\rho)$ given in Eq. (5.15). Meanwhile, the validation of the constraints on the control signal δ response to changes in the yaw rate reference signal $\dot{\psi}_{ref}$ is done by comparing the controller sensitivity transfer function $KS = \frac{\delta}{\dot{\psi}_{ref}}$ with respect to the control performance template $1/W_u$, with the weight $W_u(\rho)$ given by Eq. (5.14).

From the frequency response results shown in Fig. 5.4 and Fig. 5.5 it can be seen that both design requirements for the controller $K(v_x)$ are satisfactorily fulfilled for most of the frozen grid-point values. Fig. 5.4 shows that when the controller is given full control authority, e.g. $\rho = 1$, the tracking performance is in accordance to the nominal design requirement according to the chosen template $W_e^{-1}(\rho_p = 1)$.

Figure 5.5 presents in a clear way the effect of the design varying paramter ρ on the control performance weight $W_u(\rho)$. When there is no penalization in the control magnitude, e.g. $\rho = 1$, the controller constraints are fulfilled for most grid-points. The grid-point response above the template $W_u^{-1}(\rho_p = 1)$ is for the grid-point $g_p = (v_{x,p} = 0.5, \, \rho_p = 1)$, at this speed it is to be expected that the control magnitude required to achieve the same tracking performance needs to be larger. On the other hand, when the control action is penalized, e.g. $\rho = 100$, the magnitude response of the control action is decreased by many orders of magnitudes, basically deactivating the controller output.

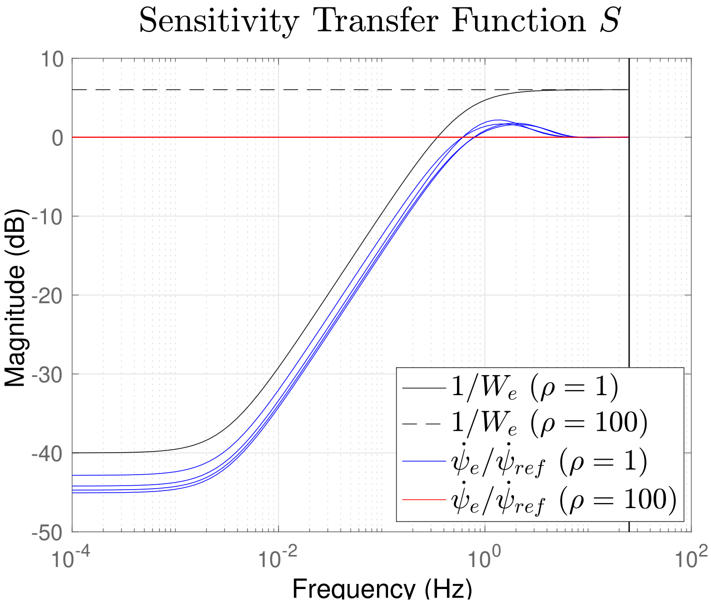

Figure 5.4: Sensitivity Transfer Function $S = \frac{\dot\psi_e}{\dot\psi_{ref}}$ versus tracking performance template W_e^{-1} at frozen grid points.

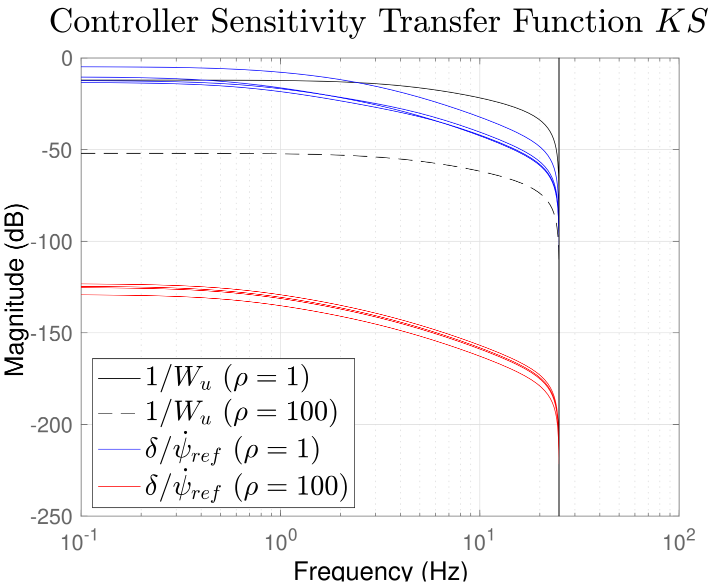

Figure 5.5: Controller Sensitivity Transfer Function $KS = \frac{\delta}{\dot\psi_{ref}}$ versus actuator performance template W_u^{-1} at frozen grid points.

This flexibility in the LPV design is facilitated by the fact that at the grid-points with

$\rho = 100$ only stability is demanded, according to the template $W_e^{-1}(\rho_p = 100)$ in Fig. 5.4. Another key to obtain a flexible solution for the LPV scheduling Anti-Windup design, is the use of Proposition 5.1, which uses dedicated slack variables Y_p and G_p to compute the controller gains for each grid-point, independently of the PDLM $X(v_x, \rho)$.

5.3.4 Real-Time Implementation of the Anti-Windup Grid-Based DT-LPV SF Controller

The control law $u = K(v_x, \rho)x$ requires feedback of the full state vector $x = (v_y, \dot{\psi}, x_e, x_u)^T$. Whereas v_y and $\dot{\psi}$ are directly measured on the SAV platform, the computation of states x_e and x_u from $W_e(\rho)$ and $W_u(\rho)$ deserve some attention due to their dependency on the varying parameter ρ.

Concerning the computation of the state x_u, from the control action performance weight $W_u(\rho)$, the parameter dependency on ρ, according to Eq. (5.14) does not affect the system matrices A_u and B_u from $W_u(\rho)$. So the online computation of x_u remains easy:

$$x_u^+ = A_u x_u + B_u \delta \tag{5.18}$$

On the other hand, for the state x_e from the tracking performance weight $W_e(\rho)$, the system matrices A_e and B_e from $W_e(\rho)$ do change in value with the Anti-Windup activation parameter ρ. Notice in Eq. (5.15) that changes in ρ lead to changes in the poles of the performance weight transfer function. A practical solution to this issue is to compute offline the system matrices of $W_e(\rho)$ at the frozen values $W_e(\rho_p = 1)$ and $W_e(\rho_p = 100)$. Then, the online values for A_e and B_e are computed by interpolation based on the online value of $\rho(k)$:

$$x_e^+ = A_e(\rho) x_e + B_e(\rho)(\dot{\psi}_{ref} - \dot{\psi}) \tag{5.19}$$

where

$$A_e(\rho) = A_e(\rho_p = 1) \cdot \left(1 - \frac{\rho(k) - 1}{100 - 1}\right) + A_e(\rho_p = 100) \cdot \frac{\rho(k) - 1}{100 - 1} \tag{5.20}$$

$$B_e(\rho) = B_e(\rho_p = 1) \cdot \left(1 - \frac{\rho(k) - 1}{100 - 1}\right) + B_e(\rho_p = 100) \cdot \frac{\rho(k) - 1}{100 - 1} \tag{5.21}$$

The online value of the Gain-Scheduled SF controller $K(v_x, \rho)$ is computed by interpolating between the computed controller gains K_p at frozen grid-points. The interpolation, according to Definition 5.1, can be made according to any multivariable interpolation rule $\zeta(v_x, \rho)$.

Finally, as the Anti-Windup activation parameter ρ is not defined by the physics of the system, its scheduling rule is an open choice in the control design. To achieve the task of simulating an Anti-Windup effect, the following scheduling rule is chosen

$$\rho(k) = \underset{[1, 100]}{\mathrm{SAT}} \left(e^{\delta(k) - \bar{\delta}}\right) \tag{5.22}$$

with

$$\delta(k) = \text{MAX}\left(\delta^*(k),\, \bar{\delta}\right) \tag{5.23}$$

where δ^* is the steering angle computed from the LPV controller and $\bar{\delta} = 38°$ is the maximum desired steering angle. Note that the physical limit for steering angle in the SAV is at 40°, the choice of $\bar{\delta} = 38°$ is done to activate the Anti-Windup effect just before saturation can occur.

The designed response for the Anti-Windup scheduling rule is that when no saturation occurs, the mathematical expression in Eq. (5.22) computes to $\rho(k) = 1$. This corresponds to the control action given maximum authority according to the nominal design. On the other hand, when the controller output is greater than $\bar{\delta}$ then $\rho(k)$ will increase, leading to an scheduled LPV controller with penalized controller output. Thus preventing the build up of the Windup effect.

5.4 Experimental Results

This section presents experimental results obtained from the Grid-Based DT-LPV Controller with Anti-Windup effects applied on the SAV platform. The tests were carried out considering the Reference Trajectory given in Fig. 5.6. This trajectory was specifically designed to have more aggressive curvatures compared to the one used in the previous chapter, see Fig. 4.2, creating a challenging scenario for the controller, particularly at high speeds where actuator saturation is now more likely to occur.

In this challenging track, the objective is to drive autonomously the SAV car for two laps as fast as possible in two different scenarios.

1. Grid-Based DT-LPV controller used for autonomous steering, with the longitudinal speed v_x as the only scheduling parameter. No Anti-Windup mechanism is present.

2. Grid-Based DT-LPV controller used for autonomous steering according to Sec. 5.3, with scheduling based on longitudinal speed v_x plus Anti-Windup activation parameter ρ.

Note that the design of the controller for the first scenario is identical to that of Sect. 5.3, the difference being that the Anti-Windup activation parameter is not considered for synthesis. As a result, the synthesis for this Grid-Based DT-LPV controller considered only the grid-points $v_{x,p} = [0.5,\ 1,\ 1.5,\ 2] m/s$. For this simpler design, the performance weights W_e and W_u are considered at $\rho = 1$ in Eq. (5.15) and Eq. (5.14), respectively.

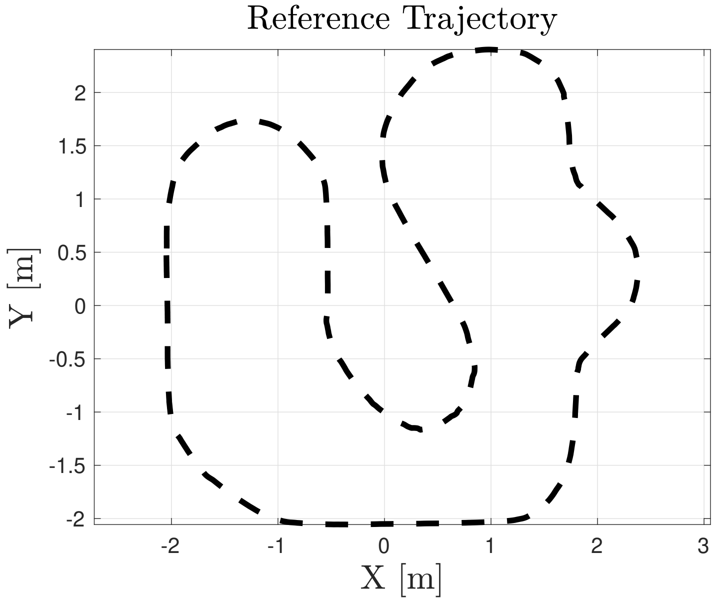

Figure 5.6: Reference Trajectory.

5.4.1 High-Speed Test Without LPV Scheduling Anti-Windup Mechanism

Considering the test when the LPV controller without Anti-Windup scheduling is employed, Fig. 5.7 shows the evolution of the SAV longitudinal speed v_x during the test. Figure 5.8 shows in black the yaw rate reference $\dot{\psi}_{ref}$ generated by the Pure Pursuit algorithm, see Sect. 4.4.1 from Chapter 4, in blue it is given the measured yaw rate by the Vicon Tracker system for the SAV during the test. In Fig. 5.9 is presented the commanded steering angle δ computed by the LPV controller in red while in blue it is presented the actual steering applied in the SAV, with saturation at 40°.

Figure 5.10 presents information regarding the followed trajectory by the SAV during the test on the X and Y coordinates of the track. On the left of the figure it is represented the reference circuit in black and the trajectory followed by the SAV during the complete test. Note that in order to better identify the multiple laps the SAV has done around the circuit, the followed trajectory is color mapped with the instantaneous longitudinal velocity, corresponding with the information given in Fig. 5.7. On the right side of the figure it is given in black the reference trajectory and with blue triangles the orientation and position of the SAV, with the orientation and position taken from a time window of the test from $t \in [17, 35]sec.$

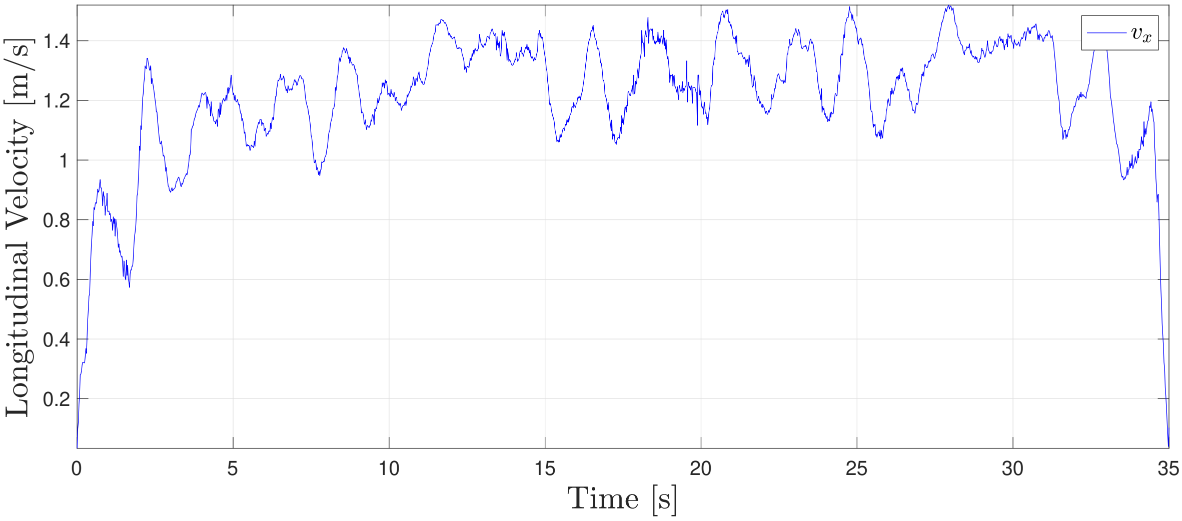

Figure 5.7: Longitudinal Velocity of the SAV during the test w/o Anti-Windup.

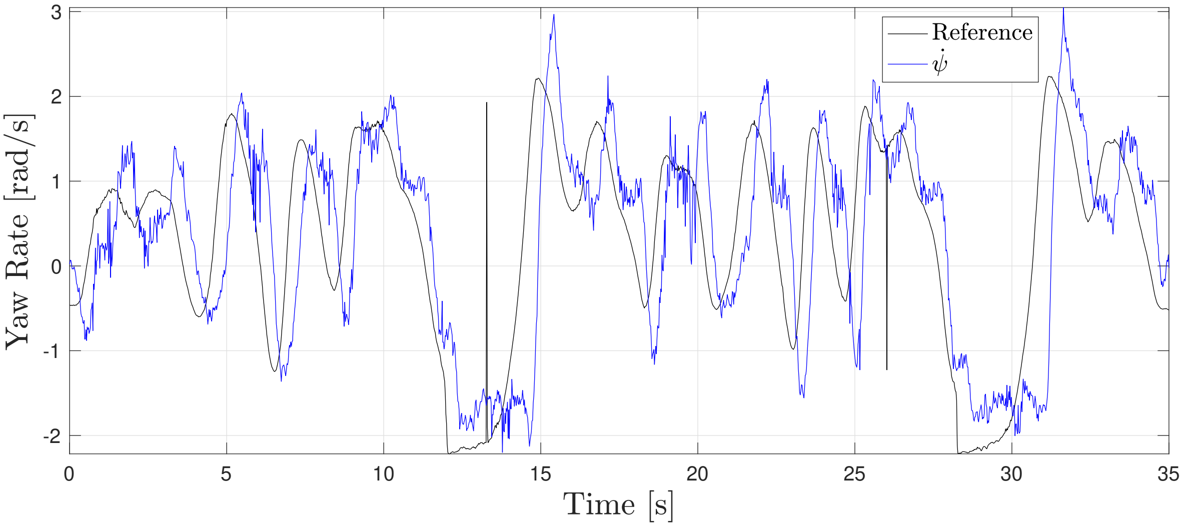

Figure 5.8: Yaw rate reference (black) and SAV yaw rate (blue) during the test w/o Anti-Windup.

From the velocity evolution in Fig. 5.7, it can be seen that the maximum speed the SAV can achieve in this test is slightly superior to $1.4 m/s$. According to the tracking error data given in Fig. 5.8, the tracking performance is good for most of the test, although the presence of the servo motor actuator delay is evident, see Chapter 2. However, it can be seen after the maneuvers at $t = 12sec$ and $t = 27sec$, with a high sustained level of yaw rate reference demand, that the required yaw rate reference can not be achieved and the maneuvers are followed by large overshoots in the next actions, at $t = 15sec$ and $t = 32sec$ respectively.

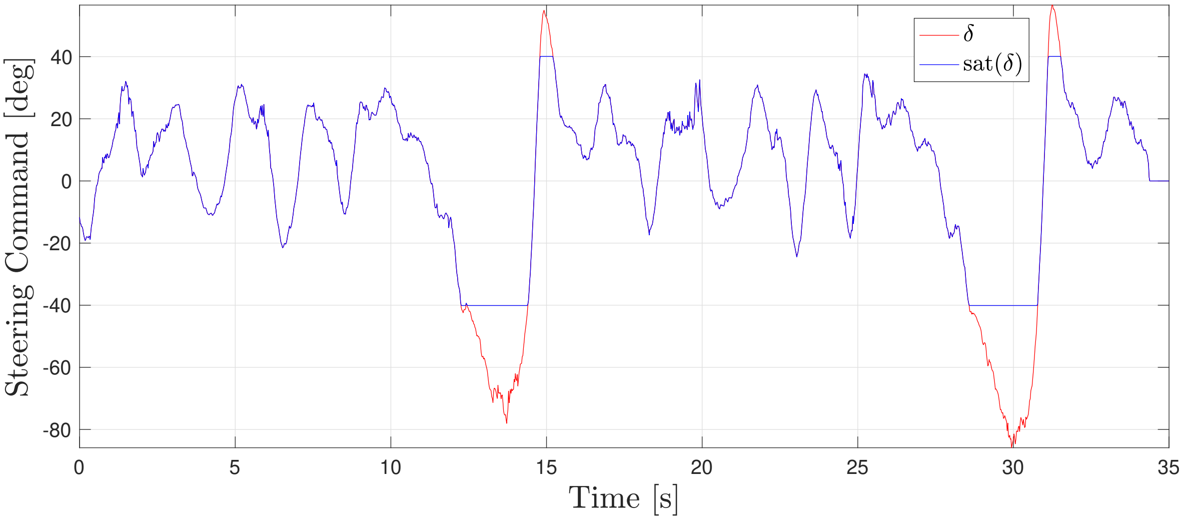

Figure 5.9: Steering command computed by the controller w/o Anti-Windup.

Figure 5.9 shows that the origin for these tracking errors is the presence of actuator saturation, which limits the yaw rate rotation speed the vehicle can achieve at a given speed. Importantly, this induces controller Windup, which slows the controller response after saturation occurs and generate oscillations that degrade the tracking performance.

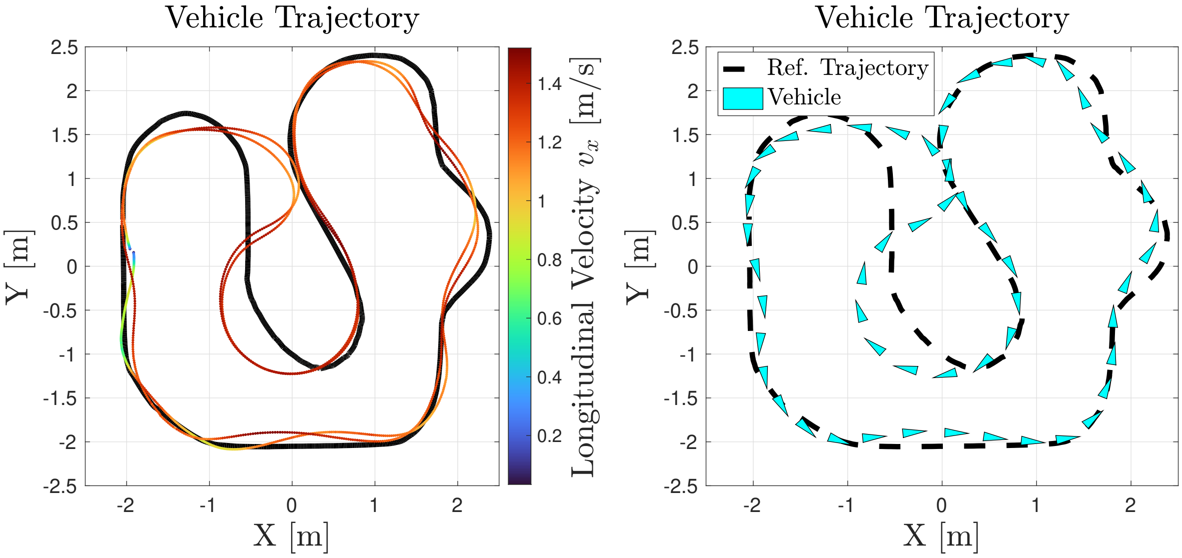

Figure 5.10: Reference trajectory and actual vehicle trajectory color coded with the instantaneous longitudinal velocity (left). Reference Trajectory and position and orientation of the SAV during the second lap at $t \in [17, 35] sec$(right). Data from the test without Anti-Windup.

The tracking errors induced by the actuator saturation and Windup effects can be seen in Fig. 5.10. After the circuit section with the highest curvature, it can be clearly observed that the trajectory tracking performance is degraded. From the color mapped plot, Fig. 5.10 (left), it is seen that the SAV car enters this high curvature section at high speeds, around $1.4m/s$. However, the degradation in tracking performance and the appearance of large oscillations in the SAV trajectory requires the car to slow down its speed significantly. Fig. 5.10 (left) shows how during the high curvature section, the velocity color mapped trajectory line goes from red to light orange. See also from Fig. 5.7 how, at $t = 15sec$ and $t = 32sec$ respectively, the longitudinal velocity is throttled down from $1.4m/s$ to $1.1m/s$. Only this reduction in speed is what allows the SAV to continue the test without lose of stability due to the Windup effect.

5.4.2 High-Speed Test With LPV Scheduling Anti-Windup Mechanism

For the second test, employing the LPV controller with Anti-Windup scheduling designed in Sect. 5.3, Fig. 5.11, Fig. 5.12, Fig. 5.13 and Fig. 5.15 present analogous information to the figures seen previously in Sect. 5.4.1. Additionally, it is given here Fig. 5.14 which presents information on the online value of the Anti-Windup activation parameter $\rho(k)$, computed according to Eq. (5.22).

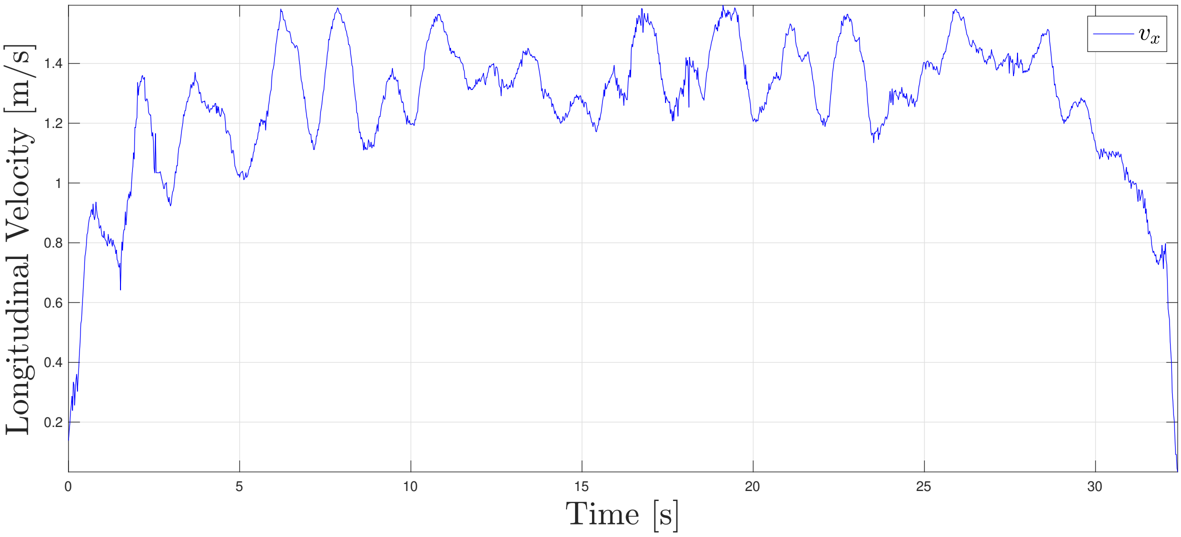

Figure 5.11: Longitudinal Velocity of the SAV during the test.

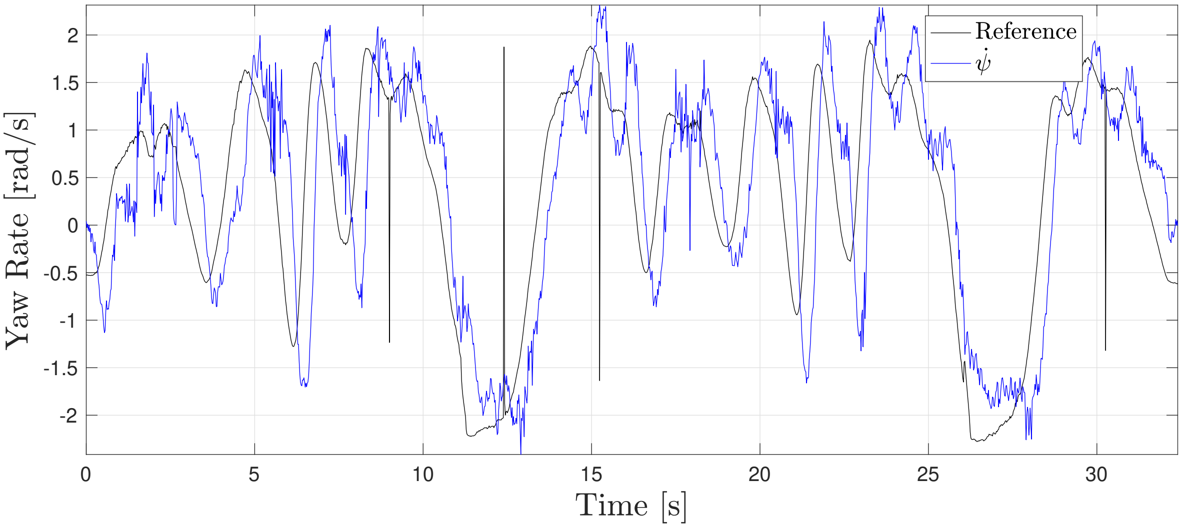

Figure 5.12: Yaw rate reference (black) and SAV yaw rate (blue) during the test.

In this second test, the maximum speed that the SAV vehicle can achieve reaches $1.6m/s$ as can be seen in Fig 5.11, which is 14.3% higher than was possible during the test without Anti-Windup LPV scheduling. Note also a reduction on the test time from $35sec$ to $32sec$ in this second test. Moreover, when comparing the tracking error performance, the LPV controller solution with Anti-Windup has improved tracking performance throughout all the test, as seen in Fig. 5.12 compared with the previous yaw rate tracking error results seen in Fig. 5.8. When computing the RMS error of the reference signal with the actual achieved yaw rate, e.g. RMS($\dot{\psi}_{ref} - \dot{\psi}$), the results show a clear improvement in tracking accuracy when utilizing the Anti-Windup emulation strategy:

	With Anti-Windup	NoAnti-Windup
RMS($\dot{\psi}_{ref} - \dot{\psi}$)	0.8438	0.9719

Still, the presence of the actuator delay is indeed noticeable in the yaw rate tracking response seen in Fig. 5.12. Additionally, during the maneuvers demanding sustained high yaw rate rotation speeds, starting at $t = 11sec$ and $t = 26sec$ respectively, the SAV car is still unable to reach the maximum yaw rate set by the Pure Pursuit planner.

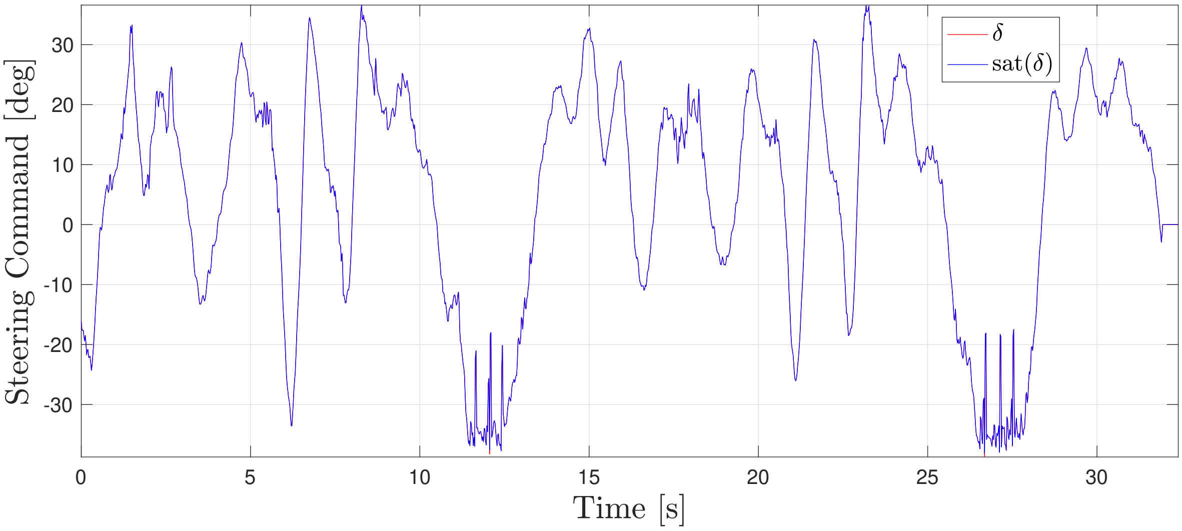

Figure 5.13: Steering command computed by the PDSF controller.

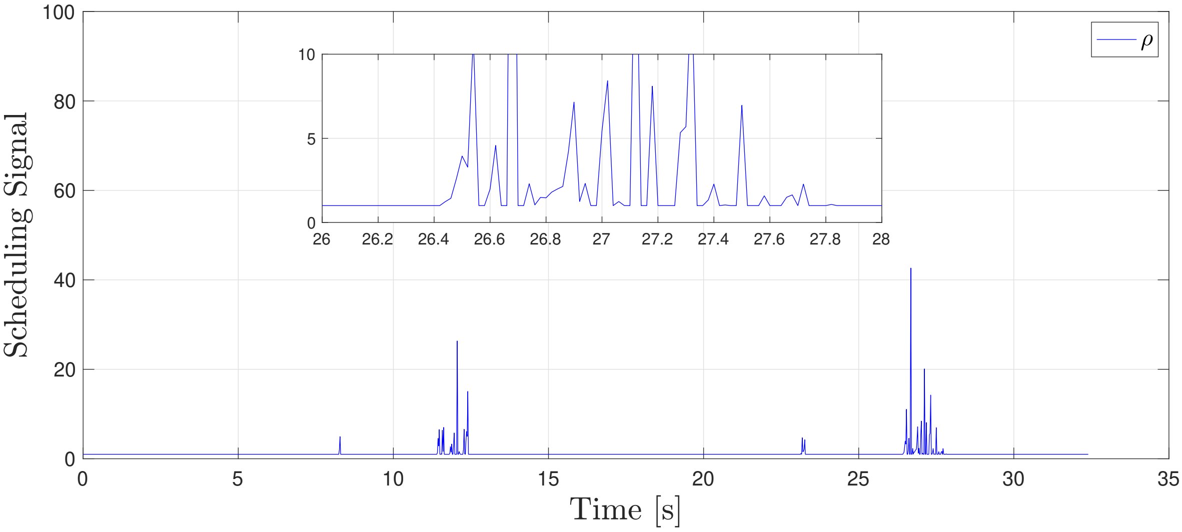

Figure 5.14: Steering command computed by the PDSF controller.

This is caused, as it can be seen in Fig. 5.13, due to these high yaw rate maneuvers leading to actuator saturation. However, this time it can be seen that despite observing a clear saturation effect, the controller Windup effect is avoided thanks to the LPV Anti-Windup scheduling design. As can be seen in Fig. 5.14, during those maneuvers the Anti-Windup activation parameter ρ is quickly scheduled in the presence of actuator saturation. In fact, the effect of scheduling the Anti-Windup activation parameter ρ is noticeable in Fig. 5.13 by the presence of control signal artifacts during the high demand maneuvers, when ρ is being activated to prevent controller Windup.

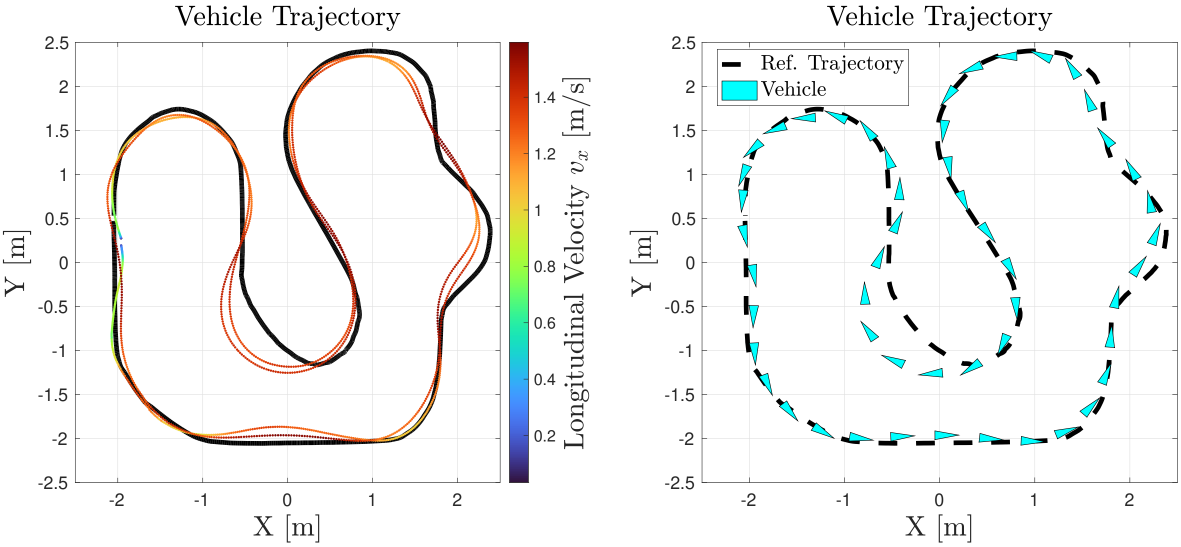

Figure 5.15: Reference trajectory and actual vehicle trajectory color coded with the instantaneous longitudinal velocity (left). Reference Trajectory and position and orientation of the SAV during a lap done at high speed at $t \in [16,\ 32] sec$(right).

Finally, the improvement generated by the use of the LPV scheduling Anti-Windup solution on the trajectory tracking problem can be seen in Fig. 5.15. Due to the presence of steering saturation there is still some noticeable loss of tracking performance in the zones of the track with higher curvature. However, the presence of dangerous trajectory oscillation are completely avoided this time, which allows to carry the test at higher speeds in a safe and stable manner.

5.5 Conclusions

In this chapter, conditions to compute Grid-Based DT-LPV controllers based on LMI conditions from Chapter 1 have been derived. The LMI synthesis conditions here introduced provide a low level of conservatism, which then allows to solve efficiently LMI problems for demanding LPV control designs where some the scheduling of some parameters cause important changes in the system behaviour. This has been demonstrated with the design of an LPV controller with a design-related varying parameter used to disable the controller output, the real-time scheduling of this parameter then enables the emulation of an Anti-Windup mechanism. This combination of Grid-Based DT-LPV synthesis conditions and use of design varying parameters will be heavily used in following chapters.

The effectiveness of the Grid-Based DT-LPV controller with Anti-Windup scheduling strategy was evaluated on the SAV platform for trajectory tracking in a demanding circuit. The Anti-Windup scheduling mechanism demonstrated efficacy in preventing controller Windup during saturation, thereby rendering the LPV Anti-Windup scheduling strategy dependable in enhancing system tracking performance and, more notably, system stability at high velocities.

Part III

Lateral LPV Control for Advance Driver Assistance Systems

Part III: Introduction

Part III presents the integrated ADAS strategy for vehicle lateral control proposed in this Thesis. This strategy follows a consistent philosophy throughout all chapters in Part III, namely:

- Estimation of driver performances based on fault detection techniques.
- Reconfigurable lateral ADAS controller using LPV/$\mathcal{H}_\infty$ approaches.
- ADAS LPV controller scheduling rule based on the online estimation of driver performances.

The estimation of driver performances is presented in Chapter 6 using Parity Space approaches an considering a nominal driver model as the baseline for driver steering behaviour. In later chapters, this tasks is made by employing an LPV PI observer, the objective with this approach is to add robustness with respect to measurement noises and to accommodate for LPV nominal driver models if available.

The design of the LPV/$\mathcal{H}_\infty$ ADAS lateral controller considers as the controlled plant the joint driver-vehicle system, for which the human steering behaviour is taken into account by utilizing driver models. In order to reduce the sensation of intrusiveness the driver can feel from the ADAS system, the proposed control strategy present two features. Firstly, on the $\mathcal{H}_\infty$ design it will be considered bandpass filters such that the control action is restricted in a frequency range transparent to the human. Secondly, the LPV design is made with the inclusion of design-related varying parameters that can modulate the allowable control output magnitude in an adaptive manner. Similar to the approach introduced in Chapter 5.

Finally, the scheduling strategy merges the driver performances estimation algorithm with the LPV/$\mathcal{H}_\infty$ ADAS lateral controller. This is accomplished by using the driver performance estimation as an indicator to schedule the design-related varying parameters from the LPV ADAS controller. In Chapter 6 and 8 this joint strategy is used to modulate the amount of required additive steering. On the other hand, in Chapter 7 it is shown how this strategy can be used to incorporate and mix multiple actuators on the control design by considering both additive steering and direct yaw moment control as control actions.

The following of this introduction to Part III is dedicated with providing literature background on lateral ADAS control approaches.

Literature Overview on Lateral ADAS Control

There have been many propositions in the field of Advanced Driver Assisted Systems (ADAS) to design automated systems with the objective of increasing vehicle's safety. In this literature background the focus is on works employing model based techniques and which take into account the driver in the loop for lateral vehicle control design. As such, this excludes ADAS systems that just provide warnings to the driver and studies which consider full automated driving. In fact, considering the driver in the loop results in a more intricate design than that of full autonomy from a control theory perspective. This is due to the satisfactory interaction between human and automation becoming a key objective, in addition to those of tracking performance and vehicle stability. The works explored in this literature overview are part of two trends observed in the lateral ADAS control literature. One is the LPV/$\mathcal{H}_\infty$ approach, focused in developing robust controllers that work side by side with the human driver. The second approach is the shared control proposition. Within this approach the human driver shares control of the vehicle with a full autonomous controller, however, the level of control is varying such that either the human or the automation can have full authority at given instances.

Previous thesis and publications developed at GIPSA-Lab in Grenoble have considered the LPV/$\mathcal{H}_\infty$ approach for ADAS control. In [Dou+13] it is developed a yaw rate stabilizing controller for the vehicle lateral dynamics employing steering actions and Direct Yaw Control (DYC) through differential rear braking. The steering action is considered the primary actuator, while the DYC action is activated only during critical situations, facilitated by design-related varying parameters. The desired yaw rate of the controller is based on the steering angle set by the human driver, and driver comfort is taken into account during the $\mathcal{H}_\infty$ control design. The design uses the bandpass filter from [GGK08] as a constraint on the steering action, which then allows to restrict the steering control output to a frequency range were the driver cannot act. In [PV+11] a similar approach is considered, although in this work the braking action is considered as the principal actuator. In this case a design-related parameter is used for the activation of the steering actuator if a critical situation is detected. Having a reduced effect on the steering wheel may make this design more transparent for human drivers. A second design-related parameter is also employed to distribute the braking action between the left and right rear wheels of the vehicles. This constitutes an innovative approach to incorporate DYC in vehicle control design. The work done in [Fer14] expands on [Dou+13] by simultaneously considering the suspension system in addition to steering and braking actions. Design-related varying parameters are used to coordinate the controllers of both systems, resulting in improved vehicle comfort and enhanced performance through more efficient load transfer distribution.

In [GNB12] the authors consider a lateral ADAS controller based on LPV/$\mathcal{H}_\infty$ control design techniques. The ADAS controller can provide both additive steering and direct torque control on the yaw vehicle axis by means of differential braking. The $\mathcal{H}_\infty$ approach is used to enforce design objectives as well as to account for multiple uncertainties and disturbances. The LPV approach then enables to adapt the controller to a wide range of vehicle velocities as well as handling the mix of steering and braking actuator use. This is done by incorporating a design-related parameter. The driver actions are directly considered in the design by incorporating the control theoretic driver model from [HM90]. The results from [GNB12] shows that LPV/$\mathcal{H}_\infty$ ADAS designs are robust to uncertainties while reducing the driver effort.

The work in [CZW19] also deals with lateral ADAS controller based on LPV/$\mathcal{H}_\infty$ techniques. The driver is considered in the loop by incorporating the driver model from [Sch+16] during the design. Interestingly, to cover a whole range of possible driver performances the authors include driver model uncertainties on the LPV/$\mathcal{H}_\infty$ design LMIs. This allows to prove in a driving simulator that the designed ADAS controller provides efficient aid and reduce driver load on multiple subjects with varied driving performances. However, a limiting factor in the works using LPV/$\mathcal{H}_\infty$ approaches is that the ADAS controller is always active. This is known to not be desirable to the driver unless there exists a dangerous situation [MDH14].

One prominent field in the vehicle lateral control problem with human drivers in the loop is the shared control proposition. The works [Sal+13]; [EFG15]; [Ji+18]; [Pan+20] employ optimal control theory as their main control approach in order to solve some Model Predictive Control or $LQ/\mathcal{H}_2$ problems. The objective of these works being to reduce conflicts between the driver and the lateral ADAS steering actions when merging two driving modes: fully manual and fully autonomous driving. In [Ino+16], the authors propose a shared control scheme that uses both steering actions and direct yaw torque control. By using direct yaw torque as a control input for the ADAS system it is shown that the ADAS steering actions is reduced and as a result steering conflicts are decreased.

In [Pan+20], the ADAS controller synthesis is proposed as the minimization of an $\mathcal{H}_2$ norm criterion that accounts for different levels of shared control. However, in the synthesis the level of shared control is fixed at a set value. Instead, the approaches proposed in [Sen+19]; [Oud+22] make use of the LPV techniques to account for time-varying levels of shared control. In these works the level of shared control is included on a cost function used to derive the LMI synthesis problem, for which the shared control amount acts then as design-related varying parameter. Moreover, the authors propose active driver monitoring techniques to select the appropriate level of shared control. As a result, the shared control amount is modified online based on driver awareness and risk of lane departure while minimizing some driver/ADAS conflict criterion. The advantage of this approach is that employing LPV techniques provides with stability guarantees for the transition period from manual to autonomous driving and vice-versa.

In conclusion, this literature review has examined various approaches to lateral ADAS control with the primary goal of enhancing vehicle safety. The involvement of the driver in the control loop for lateral vehicle control presents a more complex design challenge compared to fully autonomous systems. Nevertheless, the use of LPV/$\mathcal{H}_\infty$ control has demonstrated promising outcomes in achieving robustness against uncertainties while minimizing driver effort. The integration of driver models into the design process has facilitated efficient assistance and reduced driver workload across different driving abilities. The shared control approach has also shown potential in resolving conflicts between the driver and automated systems. However, this approach assumes that the automation mode can assume most of the control authority, which may feel intrusive to the driver and lead to disengagement of such systems. Nonetheless, recent studies exploring the application of LPV techniques to modulate the level of ADAS influence based on driver monitoring have displayed significant potential. This approach holds promise in addressing the concerns associated with driver acceptance and engagement by tailoring the ADAS system's behavior to the driver's needs and preferences.

Chapter 6

Reconfiguration of Lateral ADAS Steering Control in the Presence of Driver Errors Using Combined Parity Space / LPV Approaches

---

Contents

6.1 Introduction

This chapter serves as a preliminary study for the proposed integrated lateral ADAS strategy in this thesis. The strategy consists in using model based fault diagnosis techniques [Din08] to detect the presence of errors in the driver steering. This error estimation is then mapped to a design-related varying parameter which is used to activate the ADAS lateral control by means of LPV scheduling. The assumption is that large driver errors are either caused by or are the origin of a dangerous situation.

Here the detection of driver errors is proposed to be formulated as a Fault Detection problem using the Parity Space approach, and the computed residual signal then schedules the LPV/$\mathcal{H}_\infty$ controller. The overall goal is to compute an ADAS controller that helps in stabilizing the vehicle when driver errors are detected while otherwise minimizing the level of intrusiveness. With this goal in mind, the proposed method will be tested in simulation using a full dynamical model of a Renault Megane car, see Chapter 2, and driver models for simulation of the human steering action during a critical scenario, see Chapter 3.

Different from most of this thesis, the controller synthesis is performed here in Continuous-Time using the Grid-Based LPV toolbox LPVTools [HSP15]. The reason for this is that the results in this chapter predate the development of the Grid-Based DT-LPV framework used for the rest of the thesis.

The contents of this chapters are based on the following publication:

- Ariel M. Borrell, Olivier Sename and Vicenç Puig. "Control Reconfiguration of Lateral ADAS Steering Control in the Presence of Driver Errors Using Combined Parity Space / LPV Approaches". In: *2021 5th International Conference on Control and Fault-Tolerant Systems (SysTol)*, Saint-Raphael, France, 2021, pp. 7-12, doi: 10.1109/SysTol52990.2021.9595648.

6.1.1 ADAS Strategy based on Driver Errors Detection

The integrated ADAS lateral strategy is presented in Fig. 6.1. Higher levels of the ADAS system provide appropriate reference signals as well as information of the vehicle with respect the road, as the lateral error y_e seen in Sec. 2.2.3 from Chapter 2. Then, the driver steering behaviour is evaluated based on the road and environment information employing the Parity Space approach. The generated residual according to the detected driver errors is then used to provide an scheduling signal for the LPV/$\mathcal{H}_\infty$ ADAS lateral controller, which acts in parallel to driver.

By evaluating the driver's performance in real-time allows the ADAS system to act on the steering input only when needed. Moreover, using LPV/$\mathcal{H}_\infty$ controllers allows us to carry out offline the computation of the controller synthesis. The LPV controller then allows to react quickly to changes online, thanks to real-time LPV scheduling while maintaining a high degree of robustness thanks to a controller synthesis based on $\mathcal{H}_\infty$ methods. The objectives of the proposed integrated ADAS strategy can then be summarized as follow:

- Provide aid to the driver in the case when a dangerous situation is detected. Large estimated driver errors are here assumed as correlated with dangerous scenarios.

- Do not interfere on the driving experience if the driving scenario does not pose any danger of loss of vehicle stability.

Note that the localization and planning block in Fig. 6.1 is provided as reference but these algorithms are outside of the scope of this work.

Remark 6.1
In the proposed strategy, the steering applied to the vehicle is a direct combination of the driver's steering input and the ADAS controller's steering input. Unlike the shared control proposition, this strategy does not assume that the ADAS system can take complete control of the driving situation in an autonomous way. On the contrary, the intention here is to allow the driver to maintain full authority, with the ADAS control system providing only minor corrections as needed.

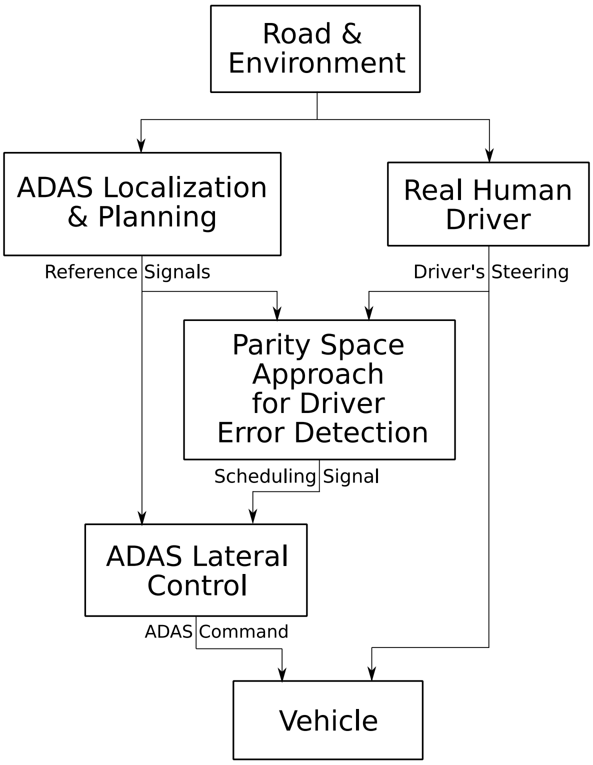

Figure 6.1: Proposed ADAS Structure for Lateral Steering Control with Controller Reconfiguration Based on Driver Error Detection.

6.1.2 Chapter Structure

The structure of the rest of the chapter is the following. Section 6.2 introduces the combined driver-vehicle model that will be used for ADAS controller design. In Sec. 6.3 it is introduced the fault detection approach for detecting driver errors based on the Parity Approach technique. Then Sec. 6.4 explains the design and synthesis of the lateral ADAS controller as well as the scheduling strategy used for the activation/deactivation of the LPV controller. Finally, Sec. 6.5 presents simulation results validating the proposed integrated ADAS design.

6.2 Integrated Driver-Vehicle System Modelling

Concerning the design of ADAS system, it is not enough to consider the vehicle as an independent entity, as the human interaction with the vehicle has an important impact in the overall system performance and stability. Therefore, the control-oriented model should be a combined Driver-Vehicle one. The Driver Model is included considering the Lateral Error Driver Model (LEDM) from Sect. 3.3.1 in Chapter 3. Recall that this model has $n_x = 1$ states, $n_u = 2$ inputs (vehicle lateral error y_e and incoming road curvature k_{path}) and $n_y = 1$ output corresponding with the driver steering applied on the vehicle. On the other hand, regarding the control-oriented vehicle model, in this chapter it is considered the Bicycle Mode from Definition 2.1 with the Renault Megane parameters presented in Table 2.1.

Let us consider a nominal DM with parameters $P_0 \in \mathbb{R}^6$ given in Table 6.2. The choice of nominal parameters P_0 is so that the DM in the open-loop nominal driver / Renault vehicle system is able to steer the vehicle in a way such that lateral accelerations and overshoots are minimized during obstacle avoidance maneuvers. Parameters P_0 chosen to perform best these critical maneuvers at a longitudinal speed of $v_x = 35m/s$.

Parameters	Nominal
K_0	1/20
T_{L0}	0.3
T_{N0}	0.1
τ_0	0.1
K_{v0}	1
K_{ff0}	0.85

On the other hand, to obtain a combined Driver-Vehicle model for control purposes two modifications are carried out in the DM from Sect. 3.3.1 in Chapter 3. Firstly, according to Remark 3.1 from Chapter 3, the road curvature k_{path} input should be expressed in terms of desired yaw rate reference $\dot{\psi}_{ref}$. So that the DM inputs can be easily related to vehicle dynamic variables that will be used for control design. Using the expression for $\dot{\psi}_{ref}$ in [Raj11], k_{path} is then substituted by:

$$k_{path} = \frac{\dot{\psi}_{ref}}{v_x} \tag{6.1}$$

where v_x represents the vehicle longitudinal velocity.

The second modification is to approximate the pure delay present in the LEDM by means of a Padé approximation, considered in this work as of order $n_{pade} = 4$. Then, the modified DM can be expressed in continuous-time state-space form as:

$$\begin{cases} \dot{x}_c = a_c \cdot x_c + [b_c \;\; 0] \cdot u_c \\ \delta_0 = (1 - K_{ff0})c_c \cdot x_c + [(1 - K_{ff0})c_c \;\; K_{ff0}K_{v0}/v_x] \cdot u_c \end{cases} \tag{6.2}$$

where $x_c \in \mathbb{R}^{n_x+n_{pade}}$ is the DM continuous-time state vector, $a_c \in \mathbb{R}^{n_x+n_{pade} \times n_x+n_{pade}}$, $b_c \in \mathbb{R}^{n_x+n_{pade}}$, $c_c \in \mathbb{R}^{n_y \times n_x+n_{pade}}$, $d_c \in \mathbb{R}^{n_u \times n_y}$ are the state-space matrices of the modified SDPM and their values depend on $[T_{L0}, T_{N0}, \tau_0, K_0] \in P_0$ as well as $[K_{ff0}, K_{v0}] \in P_0$ and the input vector $u_c(t) \in \mathbb{R}^{n_u}$ is

$$u_c(t) = \begin{bmatrix} y_e(t) \\ \dot{\psi}_{ref}(t) \end{bmatrix} \tag{6.3}$$

The combined Driver-Vehicle model for control purposes considered in this work, is then the series connection of the state-space representation for the nominal driver in Eq. (6.2) and Renault Megane Bicycle Mode. Note that both the nominal driver and the vehicle lateral dynamics models do depend on the longitudinal vehicle speed v_x, which for control design is assumed to be constant in this chapter. The extension to varying speed LPV models is a topic of future chapters.

6.3 Parity Space Approach for Driver Error Detection

In the previous section, the joint driver-vehicle control oriented model was obtained assuming a nominal driver model. However, it is to be expected that most of human drivers would perform differently than the nominal one. Specifically, it can be assumed that, in a critical driving situation, a human driver would perform worst than the nominal one (so making errors), since the parameters of the nominal driver model $P_0 \in \mathcal{P}$ are chosen to get an ideal performance. In order to detect driver errors, it is proposed to formulate a Fault Detection problem, for which the fault-free system is the nominal driver model, while the difference in steering between the real human driver δ_f and the nominal driver δ_0 will be considered as the fault signal.

$$\delta_f(k) = \delta_0(k) + f(k) \tag{6.4}$$

The chosen fault detection method on this chapter is the parity space approach, which requires a discrete state-space model of the nominal LEDM. Using a sampling period $T_s = 10ms$ and an exact Zero-Order Hold discretization method, assuming the pure time delay present in the LEDM as an input delay, then, the discrete-time state-space representation of the nominal DM is defined by the following system matrices:

$$\begin{aligned} A_0 &= a_0 \in \mathbb{R} && (6.5)\\ B_0 &= [b_0 \;\; 0] \in \mathbb{R}^{n_x \times n_u}, && (6.6)\\ C_0 &= (1 - K_{ff0})c_0 \in \mathbb{R}, && (6.7)\\ D_0 &= [(1 - K_{ff0})d_0 \;\; K_{ff0}K_{v0}] \in \mathbb{R}^{n_u \times n_y}, && (6.8) \end{aligned}$$

and can be expressed as:

$$\begin{cases} x_d(k+1) = A_0 \cdot x_d(k) + B_0 \cdot u_d(k) \\ \delta_0(k) = C_0 \cdot x_d(k) + D_0 \cdot u_d(k) \end{cases} \tag{6.9}$$

with $x_d(k) \in \mathbb{R}$ is the DM discrete-time state vector, a_0, b_0, c_0, $d_0 \in \mathbb{R}$ are the elements of the state-space representation for the discretized nominal simplified precision model used on the LEDM, whose values depend on the chosen sampling time T_s and the DM parameters $[K_0, T_{L0}, T_{N0}] \in P_0$ as well as $[K_{ff0}, K_{v0}] \in P_0$ and the input vector $u_d(k) \in \mathbb{R}^{n_u}$ is

$$u_d(k) = \begin{bmatrix} y_e(k - \tau_0/T_s) \\ k_{path}(k) \end{bmatrix} \tag{6.10}$$

with $\tau_0 \in P_0$.

Let us assume now that the real human driver is doing an erroneous action, considered as an additive fault $f(k)$ with respect the nominal driver as previously defined in Eq. (6.4). The faulty driver model is then given as:

$$\begin{cases} x_d(k+1) = A_0 x_d(k) + B_0 u_d(k) \\ \delta_f(k) = C_0 x_d(k) + D_0 u_d(k) + f(k) \end{cases} \tag{6.11}$$

Then, regarding the detection of the driver error $f(k)$, the Parity Space representation of the system is defined as:

$$Y(k) - HU(k) = Wx(k-L) + MF(k) \tag{6.12}$$

with $Y(k) \in \mathbb{R}^{n_y \cdot (L+1)}$ a buffer of $\delta_f(k)$ and $U(k) \in \mathbb{R}^{n_u \cdot (L+1)}$ a buffer of $u_d(k)$, both buffers of length $L+1$. $F(k) \in \mathbb{R}^{n_y \cdot (L+1)}$ is the fault vector. And matrices $H \in \mathbb{R}^{L+1 \times n_u \cdot (L+1)}$, $W \in \mathbb{R}^{n_y \cdot (L+1) \times nx}$ and $M \in \mathbb{R}^{n_y \cdot (L+1) \times n_y \cdot (L+1)}$ defined in the standard manner of the parity space approach according to [CP12].

Note that in the parity representation of the system in Eq. (6.12), all the elements for the left-side of the equality are known in real time. On the other hand, in the right side of the equality appears the system state, which may be not completely measured, and the fault vector $F(k)$ which is unknown. In order to make the fault detection independent of the system state, Eq. (6.12) can be left-multiplied by the so called parity vector V, which is defined in such a way that the following condition is fulfilled:

$$V \cdot W = 0 \tag{6.13}$$

If such a parity vector V exists for a number L of past considered data samples, then the residual signal is given by:

$$r(k) = V(Y(k) - HU(k)) \tag{6.14}$$

The interpretation of $r(k)$ is the following: since the parity vector V fulfills the condition in Eq. (6.13), left-multiplying (6.12) by V leads to:

$$r(k) = VMF(k) = VF(k) \tag{6.15}$$

where using the definition for the matrix M in [CP12] and the fault model definition (6.11) it can be observed that $M = I$, thus $r(k)$ depends only on the fault vector value. Therefore, in the considered driver error detection problem, the residual signal $r(k)$ equals zero (or almost) when the driver's action match or are close to those expected from the nominal driver. On the other hand, when the human steering differs significantly with respect the considered nominal driver it is considered as an erroneous action and the value of $r(k)$ becomes important.

6.4 $\mathcal{H}_\infty$ Lateral ADAS Controller

This section presents the main result of the chapter, namely an LPV fault-scheduling controller allowing to reconfigure the control action in the presence of driver errors. In what follows, we present first the general structure of the control scheme, then we define the scheduling parameter function of the residual, then the LPV/$\mathcal{H}_\infty$ control problem is formulated, and finally the control synthesis method is explained.

Note that contrary to the rest of the thesis, the synthesis process is carried here in Continuous-Time, using the LPVTools toolbox [HSP15] for Matlab.

6.4.1 Structure of the control system scheduled by the detected driver error

The proposed structure for the integrated fault detection/control system is presented in Fig. 6.2. In this architecture, high levels elements of the ADAS system are assumed to provide with reference signals for the desired path, mainly y_e, k_{path} and $\dot{\psi}_{ref}$. The first two signals in conjunction with measurements from the human steering δ_f are used to evaluate the driver performance as explained in Sec. 6.3, using the Parity Space approach in order to generate a residual signal $r(k)$. This indicator for the driver's performance is then transformed into an adequate design varying parameter $\rho(k)$ used for the real-time reconfiguration of the $LPV/\mathcal{H}_\infty$ controller $K(\rho)$ acting on the combined Driver-Vehicle System.

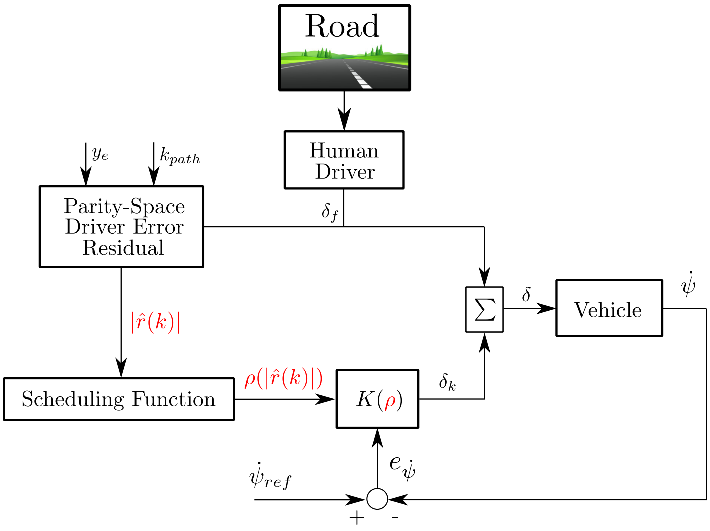

Figure 6.2: Global Lateral Driver-in-the-Loop ADAS Control Scheme

The considered control problem for the design of $K(\rho)$ is given in Fig. 6.3, which illustrates how the controller acts on the combined Driver-Vehicle System presented in Sec. 6.2 by acting on parallel to the driver and being scheduled by the signal ρ. As proposed, the objective with such a scheduled controller, is that when the levels of performance of the driver are within the accepted levels, the ADAS system will have low control authority. Meanwhile, when an important driver error is detected, the automated lateral steering assistance system will be given more freedom to act on the vehicle to help overcome critical situations.

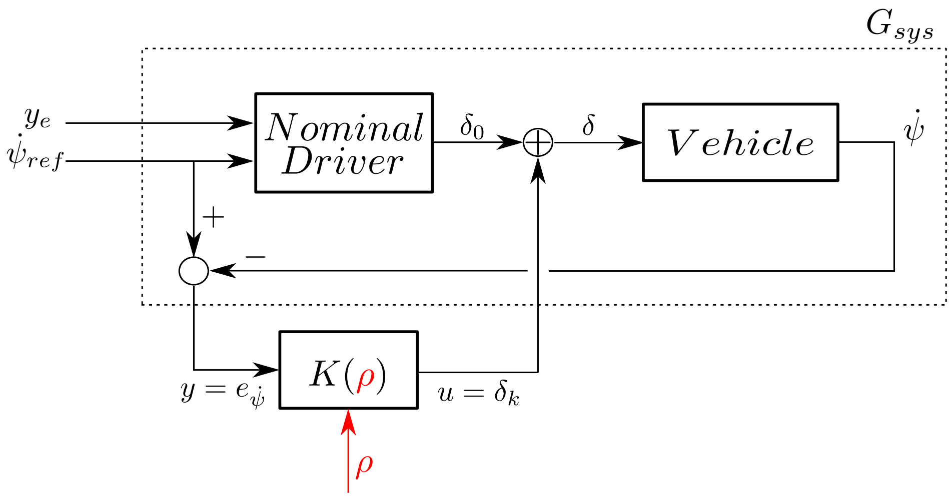

Figure 6.3: Driver plus ADAS Closed-Loop System

6.4.2 LPV/$\mathcal{H}_\infty$ Control Problem

The control problem is here formulated as an LPV/$\mathcal{H}_\infty$ problem where the objective is to minimize the induced L_2 norm of the LPV closed-loop system from exogenous inputs w to exogenous outputs z.

$$\|z\|_2 \leq \gamma_\infty \|w\|_2 \tag{6.16}$$

where the exogenous inputs w represent external references and disturbances inputs and the exogenous outputs z represent the control performance channels. The closed-loop interconnection for $\mathcal{H}_\infty$ design is shown in Fig. 6.4, and is given by the Lower Fractional Transformation [AG95] between the generalized plant $P(\rho)$ and the controller $K(\rho)$, e.g. $\Sigma_{CL}(\rho) = LFT(P(\rho), K(\rho))$. For control design, W_e and W_u are used to set performances on the closed-loop system by means of frequency shaping [ZD98]; [SP07].

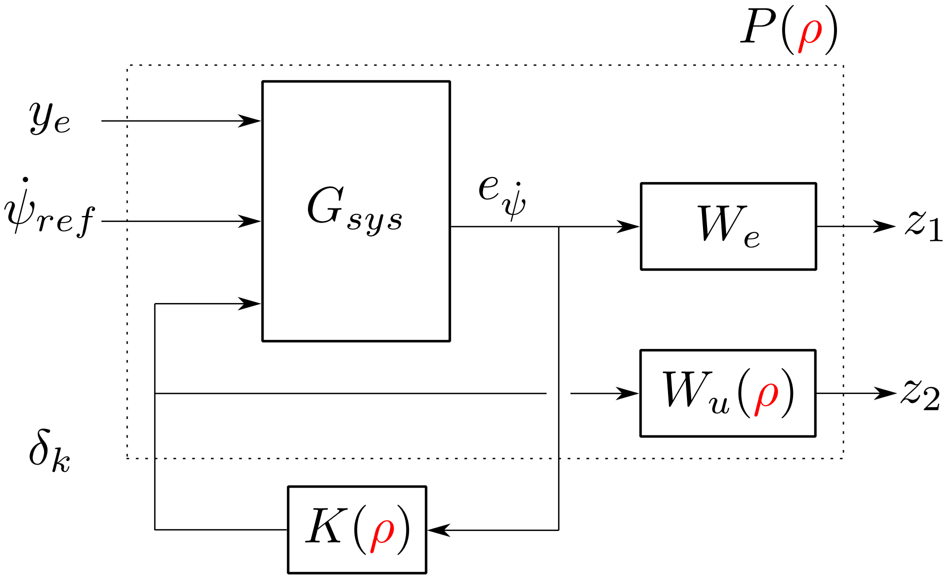

Figure 6.4: Control Loop Interconnection for LPV/H_∞ Design

The weight W_e shapes the tracking performances (through the sensitivity function S) from the reference $\dot{\psi}_{ref}$ to the tracking error $e_{\dot{\psi}}$, and is given by:

$$W_e(s) = \frac{s/M + 2\pi f_1}{s + 2\pi f_1 \varepsilon_e} \tag{6.17}$$

with $M = 2$ to ensure robustness at all frequencies, $f_1 = 3Hz$ to set the closed-loop system bandwidth and $\varepsilon_e = 0.1$ to ensure a closed-loop steady-state error less than 10%.

The weight $W_u(\rho)$ is dedicated to the control input performance (through the control sensitivity function KS from $\dot{\psi}_{ref}$ to the control output u). The weight is chosen as an LPV system of the form:

$$\begin{aligned} W_u(\rho) &= \rho \cdot G_\delta^0 \frac{(s/2\pi f_2+1)(s/2\pi f_3+1)}{(\alpha s/2\pi f_2+1)(s/\alpha 2\pi f_3 s+1)} \\ G_\delta^0 &= \frac{(\alpha\Delta_f/2\pi f_2+1)(\Delta_f/\alpha 2\pi f_3+1)}{(\Delta_f/2\pi f_2+1)(\Delta_f/2\pi f_3+1)} \\ \Delta_f &= 2\pi(f_2+f_3)/2 \end{aligned} \tag{6.18}$$

which is a band-pass filter extended from [GGK08]; [PV+11]. The objective of such a filter is to constraint the controller commands in the frequency range between $f_2 = 1Hz$ and $f_3 = 10Hz$, where it can affect the vehicle dynamics while not being felt intrusive to the driver, who is mainly sensitive to low steady-state frequencies ($\leq 1Hz$) and very high frequencies vibrations ($\geq 10Hz$) acting on the steering wheel. The constant α is used to shape the filter.

The originality is here to use a parameter dependent weight $W_u(\rho)$, where the design varying parameter ρ is obtained from the residual signal as explained previously in Eq. (6.22). Note that when $\rho = 100$, the control action is heavily penalized so the controller does not have much control authority, meanwhile with the minimum value $\rho = 0.1$ it is given extra authority in order to help the driver to overcome a critical driving situation.

6.4.3 LPV/$\mathcal{H}_\infty$ Controller Synthesis

The synthesis of the $\mathcal{H}_\infty$ dynamic output feedback controller, as represented in Fig.6.4 consists in applying the Bounded Real Lemma to the closed loop system $\Sigma_{CL}(\rho) = LFT(P(\rho), K(\rho))$. Such a problem being defined for an infinite set of parameter values, several methods do exist to reduce it to a finite dimensional problem.

We here consider the referred-to-as grid based approach considering a PDLM $X(\rho)$, and using a gridding of the parameter space to solve the optimisation problem [Wu95]. The grid-based LPV model, consists of a series of LTI models "frozen" along the trajectories of the varying parameters. For both modelling and synthesis of the grid-based LPV/$\mathcal{H}_\infty$ controller the toolbox LPVTools [HSP15] has been used. Note that since the combined driver-vehicle model is LTI, as v_x is assumed constant in this chapter, the only varying parameter is then ρ, appearing in the performance weight W_u of the generalized plant P that defines the formulated $\mathcal{H}_\infty$ control problem. The grid for the parameter is here defined by: $\rho_p = [0.1,\ 1,\ 100]$ with the parameter variation bounded by $\dot{\rho} \in [-400,\ 400]$. Finally, the basis for the parameter dependent Lyapunov function has been chosen as:

$$X(\rho) = X_0 + \rho X_1 \tag{6.19}$$

where X_0 and X_1 are constant matrices to be computed during the LMI optimization. The structure for the PDLM $X(\rho)$ according to how the design varying parameters appears in the generalized plant $P(\rho)$ used for the LPV/$\mathcal{H}_\infty$ control problem formulation. Using LPVTools the controller synthesis was proven successful with a found upper bound for the induced L_2-norm of $\gamma_\infty = 9.68$.

6.4.4 Frequency Analysis of the Controller

In Fig. 6.5 the controller sensitivity function $KS = \frac{\delta_k}{\dot{\psi}_{ref}}$ is shown together with the template $\frac{1}{W_u(\rho)}$ for the considered grid points $\rho_p = [0.1,\ 1,\ 100]$. We can see that the LPV synthesis allows to provide a varying gain for the controller sensitivity function, so to schedule the control action, from low to high, function of the design varying parameter ρ.

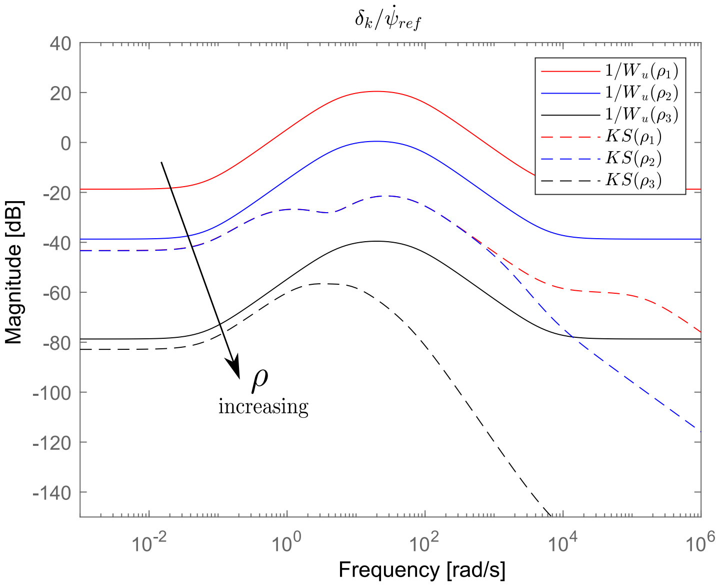

Figure 6.5: Controller Sensitivity Function $KS(\rho)$ compared with the demanded performance template $\frac{1}{W_u(\rho)}$ for the grid points $\rho_p = [0.1,\ 1,\ 100]$.

6.4.5 Residual Dependant Design Varying Parameter ρ

In order to define the scheduling function, let us first define the relative residual signal as:

$$\hat{r}(k) = \frac{r(k)}{\overline{r}_0} \tag{6.20}$$

where $r(k)$ is the residual signal as computed according to Sect. 6.3 and $\overline{r}_0$ is the threshold residual value, which is defined as the maximum value achieved by the residual when the Driver-Vehicle system, described in Sect. 6.2, is evaluated during the nominal scenario. Its determination follows a three-step procedure:

1. Simulation of an obstacle avoidance steering maneuver of the Driver-Vehicle system with a given nominal driver defined by a set of nominal parameters P_0.
2. Computation of the residual vector r_0 (of length N) using a constant sampling period T_s.

3. Definition of the threshold residual $\overline{r}_0$ as:

$$\overline{r}_0 = \sup |r_0(k)|, \quad \forall k \in [0, N] \tag{6.21}$$

Then, let us define the scheduling signal that defines the evolution of the design varying parameter ρ, as the following hyperbolic function:

$$\rho(\nu) = \frac{\overline{\rho}}{2} \cdot \frac{e^{a(\nu-\nu_0)} - e^{-b(\nu-\nu_0)}}{e^{a(\nu-\nu_0)} + e^{-b(\nu-\nu_0)}} + (\frac{\overline{\rho}}{2} + \varepsilon) \tag{6.22}$$

with $\nu := |\hat{r}(k)|$, $\overline{\rho}$ is the maximum value desired for the scheduling function $\rho(|\hat{r}(k)|)$, ε is the minimum value desired for $\rho(|\hat{r}(k)|)$, ν_0 can be used to shift the x axis of the function if desired, a and b determine the slope of the hyperbolic function.

6.5 Simulation Results

To assess the performances of the proposed control strategy, simulations have been carried out using a full vehicle model based on the real Renault Megane car Simulink model, see Chapter 2, thus performing a truthful vehicle dynamics simulation. Moreover, to increase the accuracy of the driver action for simulation, the simplified precision model used to represent the neuromuscalar behaviour in the LEDM is replaced by a more complex precision model [MK74]:

$$\frac{\delta_{fb}(s)}{y_e(s)} = K \frac{T_L s + 1}{(T_N s + 1) \cdot (\frac{s^2}{\omega_n} + \frac{2\varsigma}{\omega_n} s + 1)} e^{-\tau s} \tag{6.23}$$

Other elements of the LEDM remain as presented in Sect. 3.3.1 from Chapter 3. However, for simulation, the parameters that define a real human through a (faulty) LEDM are the following:

Parameters	Faulty
K	1/25
T_L	0.3
T_N	0.15
τ	0.18
K_v	1.7
K_{ff}	0.81
ω_n	19
ς	0.17

Moreover, to show the controller robustness faced to parameter uncertainties, the LPV controller from Sect. 6.4 is synthesized assuming a longitudinal speed of $v_x = 35$m/s whereas the simulation is performed at a speed of $v_x = 40$m/s.

The test scenarios presented to show the performance of the proposed ADAS system are the following:

1. Firstly, the Driver-Vehicle system is required to perform a double lane-change (DLC) maneuver at high speeds without ADAS assistance (case referred to as Only Driver in Fig. 6.7).

2. In a second simulation case, the Driver-Vehicle system performs the DLC maneuver at high speeds with the aid of the integrated ADAS strategy (case referred to as With ADAS in Fig. 6.7).

The collected data from the simulations are:

- in Fig. 6.6 information related to the controller reconfiguration is given: the relative residual signal (up), the scheduling function (center) and finally the controller command (down)

- in Fig. 6.7 it is shown useful information to compare the gains in performance and safety thanks to the proposed scheme, the global car trajectory (up-left), the longitudinal velocity along the simulation (up-right), the steering actions by the faulty driver δ_f together with the total combined steering applied to the car $\delta = \delta_f + \delta_k$ and the expected steering according to the nominal driver δ_0 (down-left), and the lateral acceleration (down-right)

From Fig. 6.6, it can be seen that the high speed DLC maneuver is demanding for the faulty driver. This can be quantified thanks to the value of the relative residual $\hat{r}(k)$ reaching a value on the order of 100, an important difference with respect to the nominal driver expected steering behaviour. Such a large driver error leads the scheduling function $\rho(k)$ to become small, which then schedules the LPV controller to be able to act. Bringing the system to the nominal scenario ($\hat{r}(k) \simeq 0$) with a soft and safe trajectory.

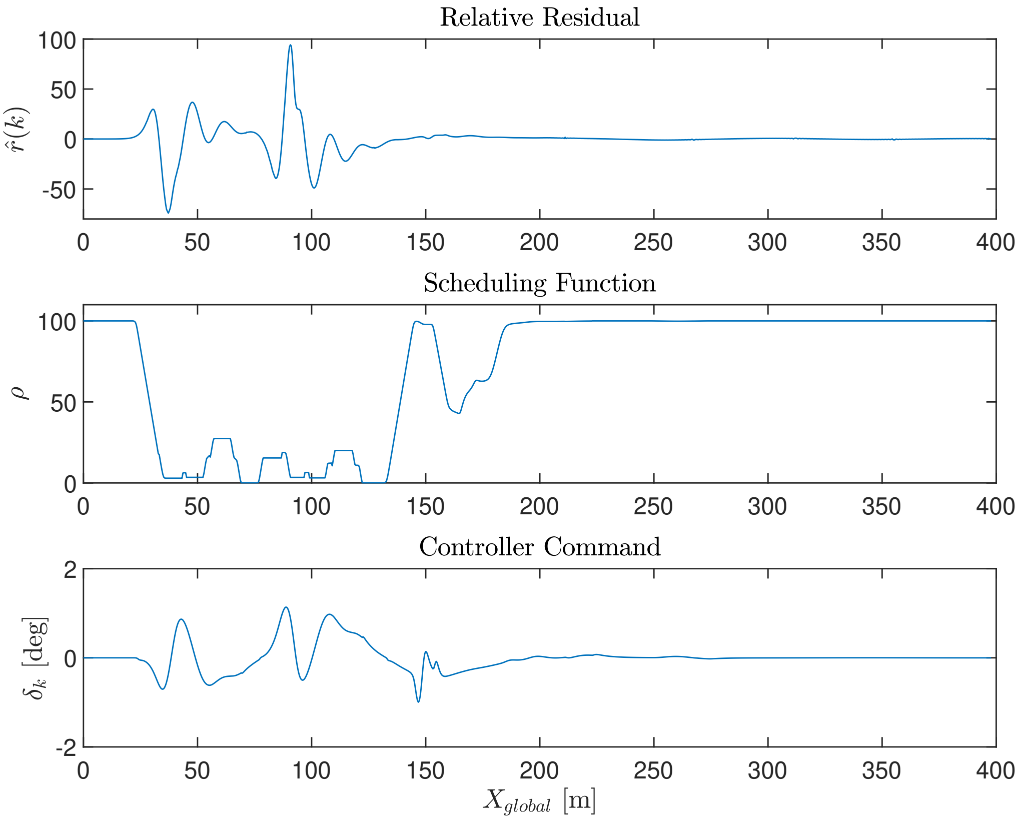

Figure 6.6: Controller Scheduling and Command **(DLC)**.

Significant differences in vehicle performance and safety between the open-loop case (without ADAS) and the case with ADAS can be observed in Fig. 6.7. In the open-loop case where only the driver is controlling the vehicle, there is a notable oscillation in the vehicle trajectory that persists for a considerable duration after the DLC maneuver is completed. Such oscillations would be deemed unsafe in a real-world scenario. However, when the ADAS is active, the steering applied by the controller results in a smoother trajectory. This improved trajectory also leads to a 50% reduction in the lateral acceleration experienced by the vehicle during the maneuver. This reduction enhances passenger comfort and, more importantly, increases vehicle safety. High lateral accelerations at high speeds have the potential to cause rollovers or over-steering, and the reduced lateral acceleration mitigates these risks.

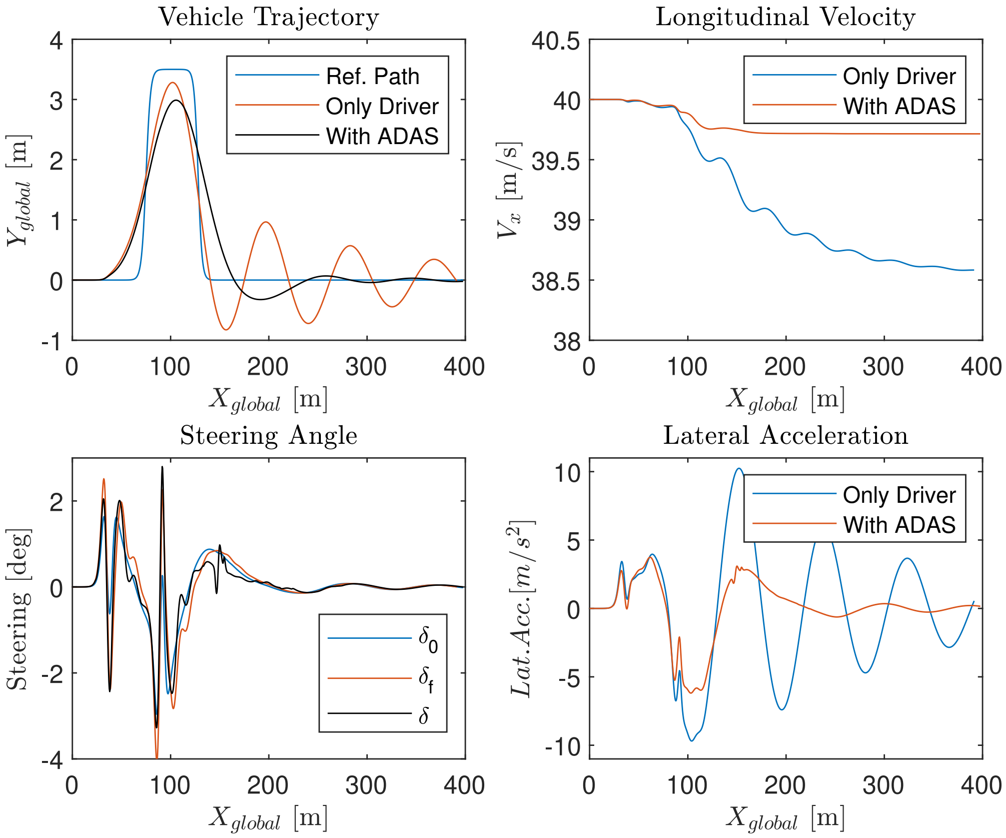

Figure 6.7: System Evaluation with/without Proposed ADAS **(DLC)**.

From the steering angle information, Fig. 6.7 bottom-left, it can be seen that the actual applied steering on the vehicle $\delta = \delta_f + \delta_k$ closely aligns with the simulated steering δ_0 of the nominal LEDM employed in the controller design. This indicates that the nominal LEDM significantly influences the controller performance by guiding the real driver steering towards the expected steering behavior of the nominal driver. Consequently, the choice of the driver model utilized in controller synthesis plays a critical role in achieving favorable ADAS performance. Therefore, it is recommended to employ idealized nominal Driver Models that exhibit desired behaviors during the synthesis stage. This selection ensures that the controller is designed to align with the anticipated responses and characteristics of the nominal driver, thereby enhancing the overall effectiveness of the ADAS system.

6.6 Conclusion

In this chapter, a novel approach to ADAS systems design for lateral vehicle steering has been introduced. The method combines the Parity Space approach to quantify the driver performance as a residual signal and a reconfigurable controller is designed using LPV/$\mathcal{H}_\infty$

control techniques. Using design varying parameters, the lateral ADAS controller was able to adapt to the driver-vehicle criticality state. When the driver performance is good the control action is penalized. However, when important driver errors are detected the controller helps in improving the vehicle yaw stability by greatly decreasing trajectory oscillations, overshoots and lowering lateral accelerations. The strategy was proven in simulation using a full vehicle dynamical model of a Renault Megane Car. Thus showing that the proposed architecture allows indeed to obtain a robust and safe ADAS controller while not being invasive to the human driver in non-critical situations.

Serving as a preliminary study on the feasibility of the proposed ADAS strategy, the results from this chapter show that it presents great potential. Following chapters will expand in these results by including the longitudinal speed as a varying parameter on the LPV design and by considering additional actuators in conjunction with the steering actuator. Furthermore, the results of following chapters will benefit from the Grid Based DT-LPV framework introduced in previous chapters, which can allow to improve synthesis performance in challenging control designs.

Chapter 7

LPV Lateral Control for ADAS Based on Driver Performance Monitoring and Using Joint Steering and Braking Actuators

Contents

7.1 Introduction

This chapter introduces advancements to the integrated ADAS strategy discussed in Chapter 6. Firstly, the presented ADAS strategy in this chapter incorporates the longitudinal vehicle speed v_x as a variable parameter in the LPV design. This modification impacts not only the design of the lateral ADAS controller but also the approach to detecting driver errors. To address the wide range of vehicle speeds, fault detection techniques capable of accommodating this variability are required. In this chapter, the driver error detection algorithm employs an LPV PI observer.

Furthermore, the ADAS strategy presented in this chapter take advantage of the presence of actuators beyond the steering wheel to modify the vehicle's dynamic response. Specifically, in this chapter it is considered the use of braking actuators to induce a moment on the yaw axis of the car through differential braking [Dou+13]. Actuator coordination is accomplished by introducing two design-related varying parameters that modulate the level of control authority for each ADAS actuator command. The online LPV scheduling policy then assumes the responsibility of selecting the appropriate actuator and determining the magnitude of its contribution.

The contents of this chapter are based on the following publication:

- Ariel M. Borrell, Olivier Sename, and Vicenç Puig. "LPV lateral control for ADAS based on driver performance monitoring". In: *IFAC-PapersOnLine* 55.6 (2022). 11th IFAC Symposium on Fault Detection, Supervision and Safety for Technical Processes SAFEPROCESS 2022, pp. 685–690

7.1.1 Integrated LPV ADAS Strategy

The proposed ADAS strategy is depicted in Fig. 7.1. The human driver steers the vehicle, but their actual driving dynamics and ability are unknown. To estimate the driver's steering performance, a PI Observer is employed, which compares the driver's actions with those of a virtual nominal driver, resulting in the estimated value $\hat{f}(k)$. This estimation serves as an input for the design-related varying parameters ρ_1 and ρ_2, which are used to schedule the ADAS controller and modulate the level of assistance. Specifically, ρ_1 influences the steering command δ_k, while ρ_2 affects the magnitude of the differential yaw moment command M_z. The LPV ADAS controller $K(v_x, \rho_1, \rho_2)$ operates in parallel with the human driver. The purpose of the scheduling signals ρ_1 and ρ_2 is to limit the influence of the ADAS controller in normal situations, while allowing for greater control authority when the driver's performance is poor.

Compared to the ADAS architecture presented in Chapter 6, the strategy depicted in Fig. 7.1 incorporates two different actuators: additive steering and direct yaw moment control. The fault detection approach for driver errors is also significantly different, utilizing an LPV PI Observer. Additionally, the scheduling strategy involves generating two distinct design-related parameters based on the estimation of driver errors. The relationship between these parameters can be used to prioritize the use of one actuator over the other.

It is important to note that the external signals y_e, k_{path}, and $\dot{\psi}_{ref}$ in the scheme are generated by a higher-level planner during the guidance stage, which falls outside the scope of this work.

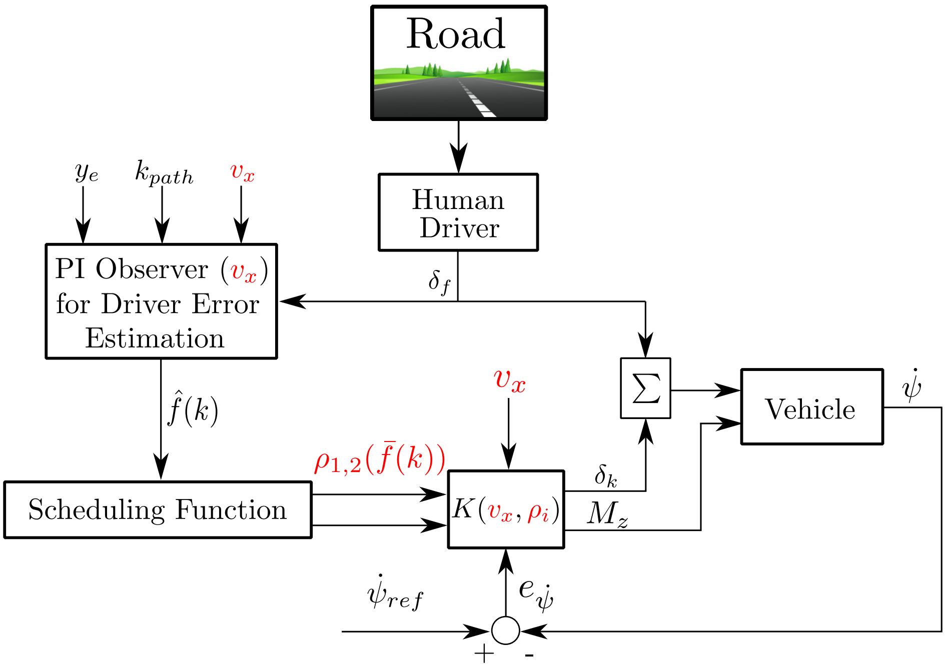

Figure 7.1: Combined Driver Error Detection / ADAS Controller Scheme

7.1.2 Chapter Structure

The structure of the rest of the chapter is the following. Section 7.2 introduces the driver model used in this chapter, whose parameters change with the vehicle speed. Section 7.3 introduces the fault detection approach for detecting driver errors based on a LPV PI observer algorithm. Sec. 7.4 presents the joint driver-vehicle model used for lateral ADAS control design. Then Sec. 7.5 explains the design and synthesis of the lateral ADAS controller as well as the scheduling strategy used for the activation/deactivation of the LPV controller. Finally, Sec. 7.6 presents simulation results validating the proposed integrated ADAS design.

7.2 An LPV Driver Model

The Driver Models (DM) explored in Chapter 3 are mostly LTI DM. However, one could expect that the driver steering behaviour needs to adapt with changes in vehicle speed. To evaluate this idea, the following simulation scenarios have been carried out to see whether the vehicle speed has any influence on the DM performance:

1. First, the Lateral Error Driver Model (LEDM), see Sect. 3.3.1 from Chapter 3, is used to provide the steering angle in order to perform a Double Lane Change (DLC) at a longitudinal speed of $v_x = 40m/s$. The vehicle model used for simulation being the full model Renault Megane Simulink model, see Chapter 2. The parameters of the LEDM

are selected to perform such a maneuver with a smooth trajectory and no overshoot, and are given in Table 7.1.

Table 7.1: DM Parameters

Parameter	Value
K	1/26
T_L	0.3
T_N	0.1
τ	0.1
K_v	1.4
K_{ff}	0.85

2. Then, the same LEDM is used to steer the Renault Megane car during the DLC maneuver considering now a vehicle speed of $v_x = 25m/s$.

The results of the simulated vehicle trajectories are given in Fig 7.2. In blue it is given the result from the first scenario, while in red it is presented the observed trajectory during the second simulation scenario. As expected, a LTI DM cannot reproduce the same vehicle behaviour over a large range of speeds. It can be seen that by employing a unique LTI DM we obtain large variations of the car trajectory from $25m/s$ compared with the test at $40m/s$.

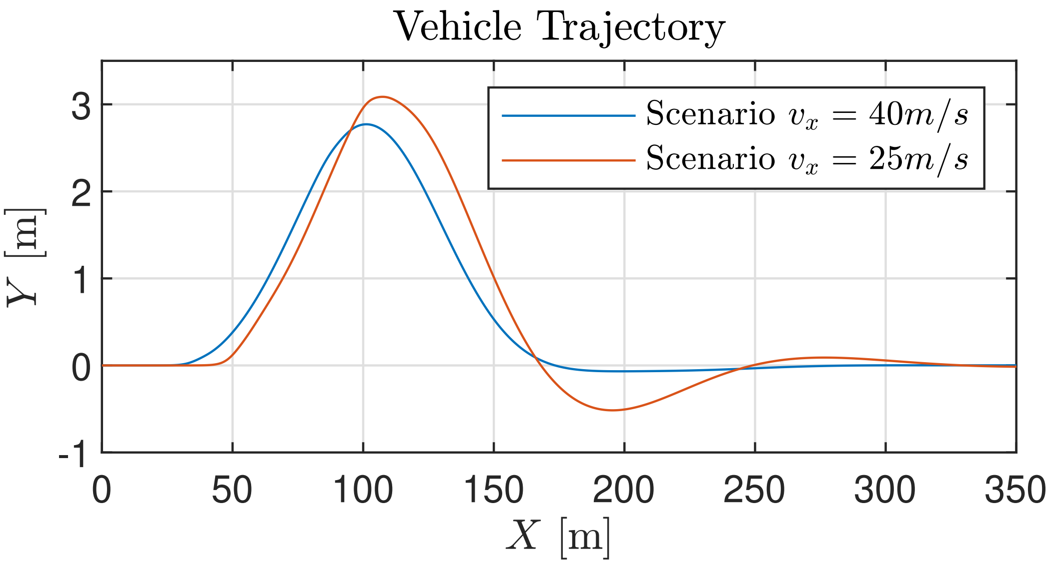

Figure 7.2: Steering test of one LTI DM at different speeds

Recall from the ADAS strategy presented in Chapter 6, that the use of a nominal DM is key both for driver error detection and for lateral ADAS controller synthesis. For this reason, it is desired to obtain a nominal DM that presents a unified performance across the whole range of speeds in terms of trajectory overshoot and reduced lateral accelerations. This can be done by modifying the LEDM incorporating some dependency on the speed velocity. The modified LPV LEDM used for the following of this chapter is given in Fig. 7.3.

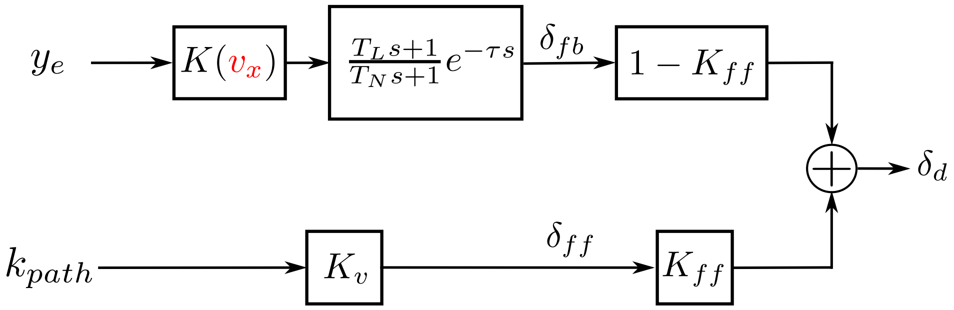

Figure 7.3: LPV Lateral Error Driver Model

Note that the gain K in the LPV-LEDM has been modified to be parameter dependent, and denoted $K(v_x)$. This modification alone allows to produce an homogeneous driver/vehicle performance in terms of vehicle trajectory for a wide range of speeds. The values for $K(v_x)$ are selected such that the driver-vehicle system could achieve a similar DLC maneuver without trajectory overshoots and gentle lateral accelerations ($a_y \leq 5m/s^2$) over the range of speeds of interest. This was done by carrying similar simulations to those described earlier in order to obtain the results presented in Fig. 7.2. The chosen values for $K(v_x)$ at different speeds are the following:

Table 7.2: Values of $K(v_x)$ for Different Speeds

v_x $[m/s]$	25	30	35	40
K	1/11	1/17.5	1/21	1/26

Remark 7.1

The information from Table 7.2 can be used to obtain a suitable value for $K(v_x)$ for any v_x within the range of 25m/s to 40m/s by interpolation or by fitting the data to some polynomial function.

Notice that the values of the parameter dependent gain $K(v_x)$ decrease with v_x. This makes physical sense, as it is to be expected that at higher speeds the amount of steering gain required will be smaller than at lower speeds.

From the LPV LEDM presented in Fig. 7.3, it can be seen that the model is characterized with the set of parameters

$$\mathcal{P} = \{K(v_x), T_L, T_N, \tau, K_v, K_{ff}\} \in \mathbb{R}^6 \tag{7.1}$$

Let us first consider a nominal LPV LEDM with parameters $P_0 \in \mathcal{P}$. The parameter values are chosen to be those from Table 7.1, except for the gain $K(v_x)$ which is chosen to be velocity dependent and with varying value based on the information from Table 7.2 and computed according to Remark 7.1.

Then, this nominal DM is represented into a discrete LPV state-space model (considering a sample time $T_s = 0.01s$) as follows:

$$\begin{cases} x_d(k+1) = A_0 \cdot x_d(k) + B_0 \cdot u_d(k) \\ \delta_d(k) = C_0(v_x) \cdot x_d(k) + D_0(v_x) \cdot u_d(k) \end{cases} \tag{7.2}$$

with

$$u_d(k) = \begin{bmatrix} y_e(k - \tau_0/T_s) \\ k_{path}(k) \end{bmatrix} \tag{7.3}$$

where $x_d \in \mathbb{R}$ is the state of the DM, $u_d \in \mathbb{R}^2$ are the inputs of the driver model and $\delta_d \in \mathbb{R}$ is the steering output of the DM. Notice that the pure delay in Fig. 7.3, is treated in Eq. (7.3) as an input delay where $\tau_0 \in P_0$. Notice also that the output matrices of the DM depend on the longitudinal velocity, as these terms are function of $K(v_x)$.

Different from the nominal DM, the steering of a real driver δ_f is modelled as the following additive fault representation:

$$\delta_f(k) = \delta_d(k) + f(k) \tag{7.4}$$

7.3 Driver Error Detection

7.3.1 PI Observer for Driver Error Estimation

The objective is now to synthesize a PI observer in order to estimate the additive fault f, which according to Eq. (7.4) can be interpreted as the human error with respect the nominal LPV LEDM. In that framework, the fault f is assumed to be such that $\dot{f} = 0$, which could be conservative since it means that the theoretical approach is valid only for a slow varying fault (even if the results will show the efficiency of the approach when f varies).

By incorporating $f(k)$ as a state variable, the extended faulty driver model is then given by:

$$\begin{cases} \begin{bmatrix} x_d^+ \\ f^+ \end{bmatrix} = \begin{bmatrix} A_0 & 0 \\ 0 & 1 \end{bmatrix} \cdot \begin{bmatrix} x_d \\ f \end{bmatrix} + \begin{bmatrix} B_0 \\ 0 \end{bmatrix} \cdot u_d \\ \delta_f = \begin{bmatrix} C_0(v_x) & 1 \end{bmatrix} \cdot \begin{bmatrix} x_d \\ f \end{bmatrix} + D_0(v_x) \cdot u_d + \bar{d} \end{cases} \tag{7.5}$$

where the disturbance input $\bar{d} \in \mathbb{R}$ represents high-frequency uncertainties to account for possible unmodeled dynamics neglected in the simplified nominal LPV LEDM as well as sensor noise.

The above driver error f can then be estimated with the aid of an LPV PI observer of the form:

$$\begin{cases} \begin{bmatrix} \hat{x}_d^+ \\ \hat{f}^+ \end{bmatrix} = \begin{bmatrix} A_0 & 0 \\ 0 & 1 \end{bmatrix} \cdot \begin{bmatrix} \hat{x}_d \\ \hat{f} \end{bmatrix} + \begin{bmatrix} B_0 \\ 0 \end{bmatrix} \cdot u_d - L(v_x) \cdot (\delta_f - \hat{\delta}_f) \\ \hat{\delta}_f = \begin{bmatrix} C_0(v_x) & 1 \end{bmatrix} \cdot \begin{bmatrix} \hat{x}_d \\ \hat{f} \end{bmatrix} + D_0(v_x) \cdot u_d \end{cases} \tag{7.6}$$

According to Eq. (7.6) and with the interconnection as shown in Fig. 7.4 the extended observer error dynamics are given by Eq. (7.7).

$$\begin{cases} x_O^+ = (A(v_x) + \tilde{L}(v_x)C(v_x)) \cdot x_O + (B_w(v_x) + \tilde{L}(v_x)D_w(v_x)) \cdot d \\ z_e = C_z(v_x) \cdot x_O \end{cases} \tag{7.7}$$

with $x_O \in \mathbb{R}^{2+n_D+n_F}$ the states of the extended error dynamics (with n_D the order of the high-pass filter W_D and n_F the order of the low-pass filter W_F) and $z_e \in \mathbb{R}$ the estimation error for the additive fault f and where

$$\tilde{L}(v_x) = \begin{bmatrix} L(v_x) \\ 0^{1\times n_D} \\ 0^{1\times n_F} \end{bmatrix} \tag{7.8}$$

In Fig. 7.4, W_D is a high-pass filter approximating the high-frequency uncertainties due to possible unmodeled dynamics and sensor noise. W_F is a low-pass filter used to ensure the observer estimation convergence performance at low-frequencies.

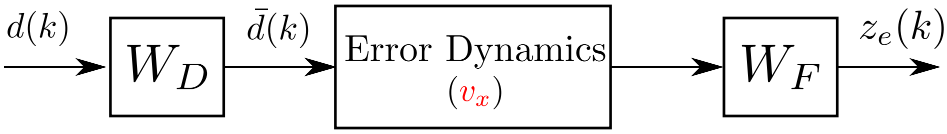

Figure 7.4: PI Observer Error Dynamics Interconnection with Filters W_D and W_F

The shaping filters have been considered as digital Butterworth filters. The low-pass filter W_F has been chosen with cut-off frequency at $2.5Hz$ and of order $n_F = 6$. Meanwhile, the high-pass filter W_D is chosen with cut-off frequency at $4Hz$ and order $n_D = 2$. In Fig. 7.5 the magnitude frequency response is presented for the used shaping filters W_F and W_D.

7.3.2 Observer Synthesis

Considering the LPV Extended Observer Error Dynamics Eq. (7.7), the objective for observer gain $L(v_x)$ synthesis is to minimize the induced L_2 norm of the LPV PI observer Eq. (7.6) estimation error from disturbance d to observer estimation error z_e.

$$\|z_e\|_2 \leq \gamma_\infty \|d\|_2 \tag{7.9}$$

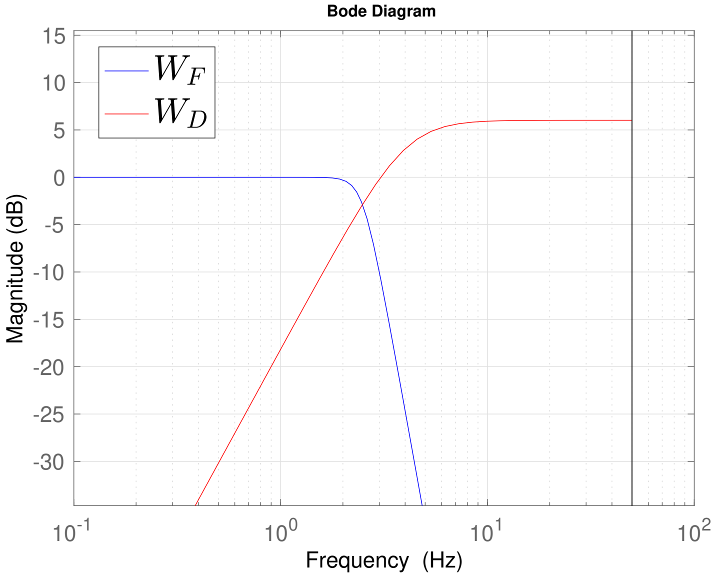

Figure 7.5: Bode magnitude plot for the DT filters W_D and W_F used to shape the $\mathcal{H}_\infty$ PI Observer.

The synthesis for the observer gain $L(v_x)$ will be carried out using the dual approach to the Parameter-Dependent State-Feedback (PDSF) synthesis seen in Chapter 4. For the two-step synthesis procedure of the LPV/$\mathcal{H}_\infty$ observer gain, the first step consists in applying the Bounded Real Lemma (BRL), as seen in Theorem 1.2, over the extended observer error dynamics in Eq. (7.7). The existence of such observer gain $L(\theta)$ can be tested according to the following proposition.

Proposition 7.1
Consider the DT-LPV observer error dynamics $\Xi(\rho)$, with parameter space $\Omega \in \mathbb{R}^m$ gridded by a grid space $\mathcal{G} \in \Omega$ and assuming bounded parameter rate of variation $\nu \in \mathbb{R}^m$ such that $\forall g_p \in \mathcal{G}$ there exists a bounding polytope $\mathcal{V}_p$ for g_p^+ with 2^m vertices $g_p^v \in \mathcal{V}_p$, and scalar $\gamma_\infty > 0$. If there exist constant matrices $\mathbf{X_0}, \dots, \mathbf{X_N}$, which form a symmetric positive-definite PDLM $X(\rho) \in \mathbb{R}^{n_x \times n_x}$ with basis function $\theta(\rho) = (1, \theta_1, \dots, \theta_N)$, with $\theta_n \in \mathbb{R}$, $n = 1, \dots, N$, and a set of matrices $\mathbf{G_p} \in \mathbb{R}^{n_x \times n_x}$ such that for all (g_p, g_p^v) pairs the following condition holds

$$\mathcal{N}_M^T(\theta_p) \begin{bmatrix} \mathbf{G_p}^T + \mathbf{G_p} - X(\theta_p^v) & \mathbf{G_p}^T A(\theta_p) & \mathbf{G_p}^T B_w(\theta_p) & 0 \\ \star & X(\theta_p) & 0 & C_z^T(\theta_p) \\ \star & \star & \gamma_\infty I & 0 \\ \star & \star & \star & \gamma_\infty I \end{bmatrix} \mathcal{N}_M(\theta_p) > 0 \qquad (7.10)$$

with

$$X(\theta_p) = \mathbf{X_0} + \sum_{n=1}^{N} \theta_{n,p} \mathbf{X_n}, \qquad (7.11)$$

$$X(\theta_p^v) = \mathbf{X_0} + \sum_{n=1}^{N} \theta_{n,p}^v \mathbf{X_n}, \qquad (7.12)$$

$$\mathcal{N}_M(\theta_p) = ker(\begin{bmatrix} 0 & C(\theta_p) & D_w(\theta_p) & 0 \end{bmatrix}), \tag{7.13}$$

then, there exists an observer gain $L(\rho)$ such that the observer error dynamics $\Xi(\rho)$ are robustly stable and γ_∞ is an upper bound on its induced L_2-norm.

Proof. This Proposition is the dual version of the more standard control problem solution, presented in Proposition 4.2. □

Concerning the synthesis of the observer gain $L(v_x)$ for the driver fault estimation observer Eq. (7.6), the following frozen grid points for the time-varying parameter v_x are chosen

$$v_{xi} = [25, 27.5, 30, 32.5, 35, 37.5, 40] \tag{7.14}$$

The maximum parameter variation rate for the longitudinal speed between sampling instances is assumed as $\nu = 3 \cdot T_s$, with sampling time $T_s = 0.01s$.

Then, considering the following structure for the PDLM $X(v_x)$ for the observer gain synthesis problem:

$$X(v_x) = X_0 + \frac{1}{v_x}X_1 + \frac{1}{v_x^2}X_2, \tag{7.15}$$

the existence of an observer gain that can render stable the Extended Observer Error Dynamics in Eq. (7.7) and minimize its induced L_2-norm can be tested solving Proposition 7.1 as a minimization problem over γ_∞. This was implemented with the parser Yalmip [Löf04] and solved employing the SDPT3 solver [TTT04] finding an upper bound on the induced L_2-norm of γ_∞=0.13. Note that the structure of the PDLM $X(v_x)$ in Eq. (7.15) is chosen with the objective of imitating the decreasing value of the LPV LEDM gain $K(v_x)$ as seen in Table 7.2.

Employing the numerical solutions from Proposition 7.1 for the values of the PDLM $X(v_x)$ and the set of slack matrices $G(v_x)$, the following proposition allows to compute a Parameter-Dependent observer gains for $L(v_x)$.

Proposition 7.2
Consider the DT-LPV observer error dynamics $\Xi(\rho)$, with parameter space $\Omega \in \mathbb{R}^m$ gridded by a grid space $\mathcal{G} \in \Omega$ and assuming bounded parameter rate of variation $\nu \in \mathbb{R}^m$ such that $\forall g_p \in \mathcal{G}$ there exists a bounding polytope $\mathcal{V}_p$ for g_p^+ with 2^m vertices $g_p^v \in \mathcal{V}_p$, and scalar γ_∞. Moreover, consider a given symmetric positive-definite PDLM $X(\rho) \in \mathbb{R}^{n_x \times n_x}$ and a set of matrices $G_p \in \mathbb{R}^{n_x \times n_x}$, both computed as the solutions to Proposition 7.1. If there exist constant matrices $\mathbf{L_0}, \ldots, \mathbf{L_N}$, which form a Parameter-Dependent observer gain $L(\rho) \in \mathbb{R}^{n_x \times n_y}$ with basis function $\theta(\rho) = (1, \theta_1, \ldots, \theta_N)$, with $\theta_n \in \mathbb{R}$, $n = 1, \ldots, N$ such that for all (g_p, g_p^v) pairs the following condition holds

$$\Psi(\theta_p, \theta_p^v) + \mathrm{He}\left(\begin{bmatrix} G_p^T \\ 0 \\ 0 \\ 0 \end{bmatrix} L(\theta_p) \begin{bmatrix} 0 & C(\theta_p) & D_w(\theta_p) & 0 \end{bmatrix}\right) > 0 \tag{7.16}$$

where

$$L(\theta_p) = \mathbf{L_0} + \sum_{n=1}^{N} \theta_{n,p}\mathbf{L_n}, \tag{7.17}$$

$$\Psi(\theta_p, \theta_p^v) = \begin{bmatrix} G_p^T + G_p - X(\theta_p^v) & G_p^T A(\theta_p) & G_p^T B_w(\theta_p) & 0 \\ \star & X(\theta_p) & 0 & C_z^T(\theta_p) \\ \star & \star & \gamma_\infty I & 0 \\ \star & \star & \star & \gamma_\infty I \end{bmatrix} \tag{7.18}$$

then, the observer error dynamics $\Xi(\rho)$ *are exponentially stable and* γ_∞ *is an upper bound on its induced* L_2*-norm.*

Proof. This proposition is the dual version of the more standard control problem solution, presented in Proposition 4.3. □

Proposition 7.2 was also implemented with the parser Yalmip [Löf04] and solved employing the SDPT3 solver [TTT04]. This was done enforcing the following parameter dependent structure on the observer gain $L(v_x)$:

$$L(v_x) = L_0 + \frac{1}{v_x}L_1 + \frac{1}{v_x^2}L_2 \tag{7.19}$$

Recall that the observer gain vector $\tilde{L}(v_x)$ in the extended observer error dynamics Eq. (7.7) is augmented with a vector of zeros. As a result, in Proposition 7.2 the observer gain vector is implemented according to Eq. (7.8) with the parameter-dependent structure $L(v_x)$ as in Eq. (7.19).

7.4 Integrated Driver-Vehicle Control Oriented Model

To tackle the design of the ADAS controller, the control-oriented model considers the joint driver-vehicle system. To incorporate the driver in the control loop, the nominal LPV LEDM from Fig. 7.3 is considered, modified according to the relationship:

$$k_{path} = \frac{\dot{\psi}_{ref}}{v_x} \tag{7.20}$$

This results in the inputs to the control-oriented LPV LEDM being:

$$u_d = \begin{bmatrix} y_e & \dot{\psi}_{ref} \end{bmatrix}^T, \tag{7.21}$$

and with feedforward gain given as K_v/v_x. As explained in Remark 3.1 from Chapter 3, this change of variable is done in order to describe the inputs of the control-oriented LPV LEDM in terms of the reference signals used for control design. Note that due to this change of variables, the longitudinal speed v_x acts as a time varying parameter for the feedback DM path due to the gain $K(v_x)$ and for the feed-forward path due to the change of variables in Eq. (7.20).

On the other hand, for modeling the lateral dynamics of the vehicle it is used the extended Bicycle Model according to Definition 2.2 with the given parameters of the Renault Megane car in Table 2.1. Recall that this extended model considers the presence of a moment of force M_z on the yaw axis as a second control input.

The generated yaw moment M_z on the Renault Megane car is assumed to be produced by means of differential braking, with braking torques T_{brl} and T_{brr} for the left and right rear wheels respectively, computed according to the following relations:

$$T_{brl} = \begin{cases} \frac{R \cdot M_z}{t_f}, & \text{if } M_z \geq 0 \\ 0, & \text{otherwise} \end{cases}, \quad T_{brr} = \begin{cases} \frac{-R \cdot M_z}{t_f}, & \text{if } M_z < 0 \\ 0, & \text{otherwise} \end{cases} \tag{7.22}$$

where R is the radius of the wheel and t_f is the distance from the wheel to the center-line of the car, see Chapter 2. Finally, the interconnection of the driver-vehicle open-loop system $G_{sys}(v_x)$ can be seen in Fig. 7.6.

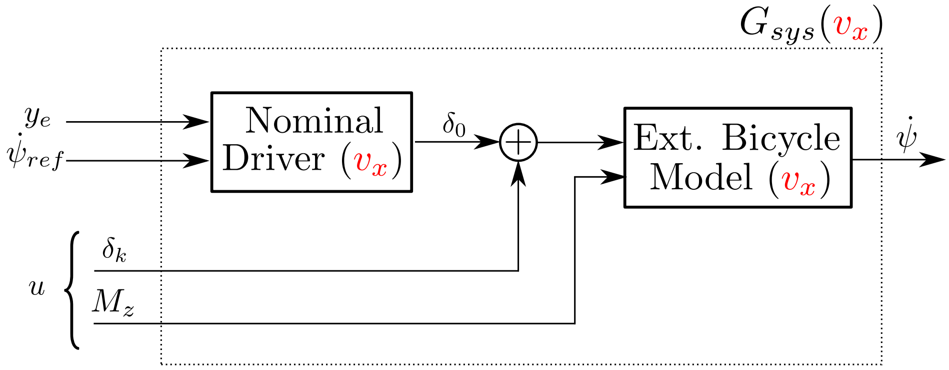

Figure 7.6: Integrated Driver-Vehicle Control Model

7.5 Robust Lateral LPV ADAS Control

7.5.1 LPV/$\mathcal{H}_\infty$ ADAS Control Design

The control problem is here formulated according to the induced L_2-norm Parameter-Dependent State-Feedback (PDSF) control problem given in Definition 4.2. The generalized plant P for the induced L_2-norm problem including the State-Feedback ADAS controller is given in Fig. 7.7.

Note that performance weights are included to tackle the different objectives. The weight W_e shapes the tracking performances (through the sensitivity function S) from the reference $\dot{\psi}_{ref}$ to the tracking error $e_{\dot{\psi}} = \dot{\psi}_{ref} - \dot{\psi}$, and is given by:

$$W_e = \mathcal{Z}_T \left(\frac{s/M + 2\pi f_1}{s + 2\pi f_1 \varepsilon_e} \right) \tag{7.23}$$

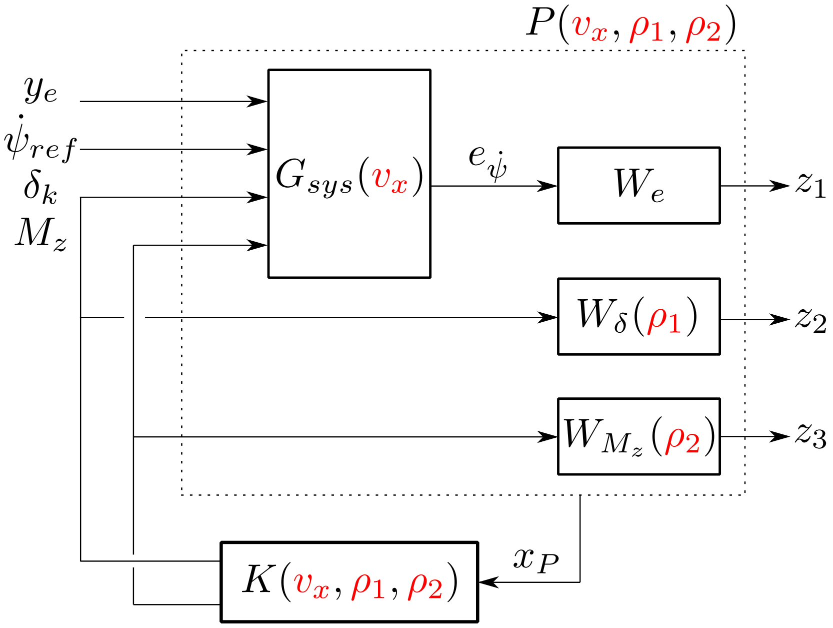

Figure 7.7: LPV / $\mathcal{H}_\infty$ Generalized Plant P for the State-Feedback Problem

with $M = 2$ to ensure robustness at all frequencies, $f_1 = 3Hz$ to set the closed-loop system bandwidth and $\varepsilon_e = 0.1$ to ensure a closed-loop steady-state error less than 10%.

The weight $W_\delta(\rho_1)$ is dedicated to the steering control performance (through the control sensitivity function KS from $\dot{\psi}_{ref}$ to the controller output δ_k). It is chosen as an LPV system of the form:

$$\begin{aligned} W_\delta(\rho_1) &= \mathscr{Z}_T\left(\rho_1 \cdot G^0 \frac{(s/2\pi f_2 + 1)(s/2\pi f_3 + 1)}{(\alpha_\delta s/2\pi f_2 + 1)(s/\alpha_\delta 2\pi f_3 s + 1)}\right) \\ G^0 &= \frac{(\alpha_\delta \Delta_f/2\pi f_2 + 1)(\Delta_f/\alpha_\delta 2\pi f_3 + 1)}{(\Delta_f/2\pi f_2 + 1)(\Delta_f/2\pi f_3 + 1)} \\ \Delta_f &= 2\pi(f_2 + f_3)/2 \end{aligned} \tag{7.24}$$

which is a band-pass filter extended from [GGK08]; [PV+11]. The objective of such a filter is to constraint the controller commands in the frequency range between $f_2 = 1Hz$ and $f_3 = 10Hz$, where it can affect the vehicle dynamics while not being felt intrusive to the driver, who is mainly sensitive to low steady-state frequencies ($\leq 1Hz$) and very high frequencies vibrations ($\geq 10Hz$) acting on the steering wheel. The constant α_δ is used to set a maximum actuator gain of less than 2° in absolute magnitude for a change in yaw rate reference $|\Delta\dot{\psi}_{ref}| = 1rad/s$.

The weight $W_{M_z}(\rho_2)$ is dedicated to the direct yaw moment control performance (through the control sensitivity function KS from $\dot{\psi}_{ref}$ to the controller output M_z). It is chosen as an

LPV system of the form:

$$\begin{aligned} W_{M_z}(\rho_2) &= \mathscr{Z}_T\left(\rho_2 \cdot G^0 \frac{(s/2\pi f_2+1)(s/2\pi f_3+1)}{(\alpha_{M_z}s/2\pi f_2+1)(s/\alpha_{M_z}2\pi f_3 s+1)}\right) \\ G^0 &= \frac{(\alpha_{M_z}\Delta_f/2\pi f_2+1)(\Delta_f/\alpha 2\pi f_3+1)}{(\Delta_f/2\pi f_2+1)(\Delta_f/2\pi f_3+1)} \\ \Delta_f &= 2\pi(f_2+f_3)/2 \end{aligned} \tag{7.25}$$

Note that the band-pass filter $W_{M_z}(\rho_2)$ cutoff frequencies f_2 and f_3 are the same as for the filter $W_\delta(\rho_1)$. That is $f_2 = 1Hz$ and $f_3 = 10Hz$. The constant α_{M_z} is used to set a maximum yaw moment gain such that the braking torque T_b according to Eq. (7.22) results in less than $1200Nm$ in absolute magnitude for a change in yaw rate reference $|\Delta\dot{\psi}_{ref}|= 1rad/s.$.

Notice that control performance weights $W_\delta(\rho_1)$ and $W_{M_z}(\rho_2)$ can be modified independently by the scheduling signals ρ_1 and ρ_2. When the scheduling functions present high values, they penalize the corresponding control action. On the other hand, when they are at values $\rho_i \approx 1$, the corresponding control command is given control authority to aid the driver. These design varying parameters can then be exploited to activate/deactivate by means of LPV scheduling the ADAS control action based on some desired objective. In the case of the presented ADAS strategy, the scheduling rules are based on the estimation of the driver performance. Details will be given in Sect. 7.5.4

7.5.2 LPV/$\mathcal{H}_\infty$ State-Feedback Synthesis

The synthesis of the LPV/$\mathcal{H}_\infty$ controller is here carried employing the Parameter-Dependant State-Feedback (PDSF) approach introduced in Chapter 4. In order to pose the control problem as a finite dimension LMI optimization problem the parameter grid and local bounds approach is used, see Sect. 4.2 from Chapter 4. The considered frozen grid values for each varying parameter are:

$$v_{x,p} = [25, 27.5, 30, 32.5, 35, 37.5, 40] \tag{7.26}$$

$$\rho_{1,p} = [1, 10, 100] \tag{7.27}$$

$$\rho_{2,p} = [1, 10, 100] \tag{7.28}$$

The vector of maximum variation rates of the varying parameters is assumed as $\nu = [3, 600, 600]\cdot T_s$, where the sampling time is $T_s = 0.01s$.

At each grid-point it is then possible to build the generalized plant for LPV/$\mathcal{H}_\infty$ design illustrated in Fig. 7.7. For each grid-point, the driver/vehicle system $G_{sys}(v_{x,p})$ is discretized using the exact zero-order-hold discretization method. The performance weights W_e, $W_\delta(\rho_{1,p})$ and $W_{M_z}(\rho_{2,p})$ are discretized at each grid-point using the Tustin discretization method. Putting all these elements together according to Fig. 7.7, define the open-loop generalized plant at a frozen grid-point $P(v_{x,p}, \rho_{1,p}, \rho_{2,p})$ as:

$$\begin{cases} x_P^+ = A(v_{x,p}, \rho_{1,p}, \rho_{2,p}) \cdot x_P + B_u(v_{x,p}, \rho_{1,p}, \rho_{2,p}) \cdot u + B_w(v_{x,p}, \rho_{1,p}, \rho_{2,p}) \cdot w \\ z = C_z(v_{x,p}, \rho_{1,p}, \rho_{2,p}) \cdot x_P + D_u(v_{x,p}, \rho_{1,p}, \rho_{2,p}) \cdot u + D_w(v_{x,p}, \rho_{1,p}, \rho_{2,p}) \cdot w \end{cases} \tag{7.29}$$

where $x_P \in \mathbb{R}^8$ are the states of the generalized plant, $u \in \mathbb{R}^2$ are the control inputs, $w \in \mathbb{R}^2$ are the exogenous inputs and $z \in \mathbb{R}^3$ are the exogenous outputs.

Then, considering the following structure for the PDLM $X(v_x, \rho_1, \rho_2)$ for the ADAS controller problem:

$$X(v_x, \rho_1, \rho_2) = X_0 + v_x X_1 + \frac{1}{v_x} X_2 + \rho_1 X_3 + \rho_2 X_4 \tag{7.30}$$

The existence of the LPV ADAS controller $K(v_x, \rho_1, \rho_2)$ can be tested using Proposition 4.2. Implemented with the parser Yalmip [Löf04] and solved employing the SDPT3 solver [TTT04]. The found bound on the induced L_2-norm had a large value, however, the frequency domain and time domain results prove that the synthesis was satisfactory.

From the solution to Proposition 4.2 we now have numerical values for the PDLM $X(v_x, \rho_1, \rho_2)$ and the set of slack matrices $G(v_x, \rho_1, \rho_2)$. Using these numerical values, we can solve the LMI optimization problem from Proposition 4.3 in order to compute the gains of a PDSF controller as seen in Definition 4.1. For this, we select a PDSF controller with the following fixed structure

$$K(v_x, \rho_1, \rho_2) = K_0 + v_x K_1 + \frac{1}{v_x} K_2 + \rho_1 K_3 + \rho_2 K_4 \tag{7.31}$$

Employing this choice of structure for the PDSF controller $K(v_x, \rho_1, \rho_2)$, Proposition 4.3 can be solved with $K_0, \ldots, K_4$ as the only decision variables to be found.

7.5.3 Frequency Analysis of the Control Design

A first validation of the controller design is carried out on the frequency domain. In Fig. 7.8 it is presented the Controller Sensitivity transfer function from yaw rate reference $\dot{\psi}_{ref}$ to the steering control output δ_k computed at frozen grid-point values of the resulting LPV closed-loop system according to the generalized plant scheme shown in Fig. 7.7. Fig. 7.8 presents the Controller Sensitivity transfer function from yaw rate reference $\dot{\psi}_{ref}$ to the direct yaw moment control output M_z.

From the frequency domain results it can be observed that for both control actions the effect of increasing the value of the related design-related parameter ρ_i, $i = 1, 2$, translates in a significant reduction in control authority for the respective actuator. On the other hand, for both Controller Sensitivity transfer functions it is seen that the resulting LPV closed-loop system does not respect the actuator constraints set at low frequencies for low values of ρ_i. This is not considered a concerning issue as the overall maximum actuator gains are respected.

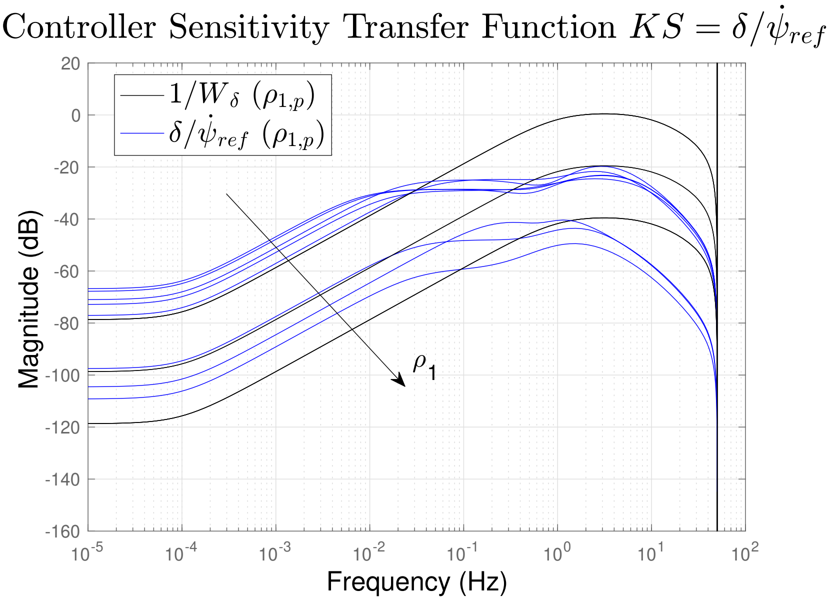

Figure 7.8: Controller Sensitivity Transfer Function $KS = \frac{\delta}{\dot{\psi}_{ref}}$ versus actuator performance template W_δ^{-1} at frozen values of the varying parameter ρ_1.

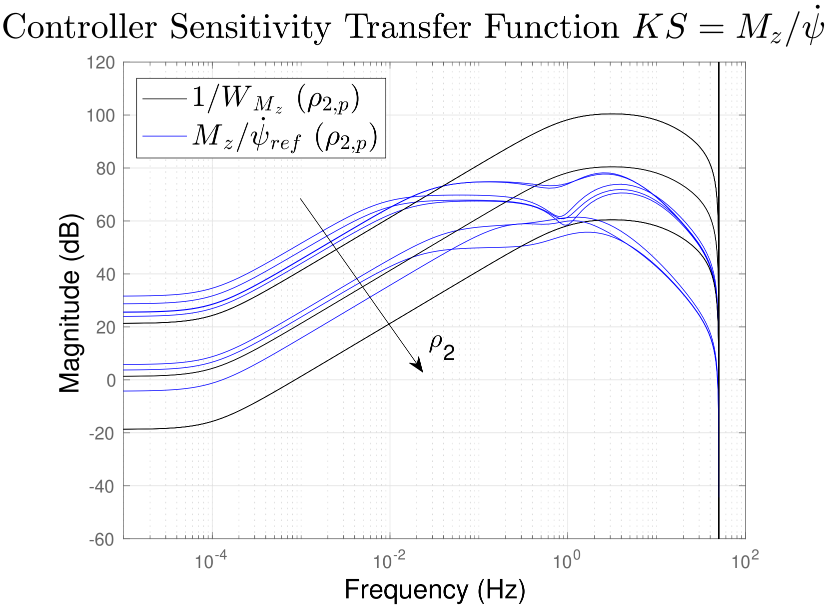

Figure 7.9: Controller Sensitivity Transfer Function $KS = \frac{M_z}{\dot{\psi}_{ref}}$ versus actuator performance template $W_{M_z}^{-1}$ at frozen values of the varying parameter ρ_2.

7.5.4 Fault Dependent Scheduling Functions

In the following, the scheduling strategy for the design varying parameters ρ_1 and ρ_2 is described. As can be seen from the integrated ADAS strategy scheme in Fig. 7.1, the ADAS controller scheduling depends on the driver fault estimation, presented in Sect. 7.3. The driver fault estimation $\hat{f}$ is not directly used, but the relative fault instead:

$$\bar{f}(k) = \frac{\hat{f}(k)}{f_0}, \tag{7.32}$$

where f_0 is a threshold value defining the maximum additive fault estimation not considered as an actual fault.

The scheduling functions for the design varying parameters ρ_1 and ρ_2 are chosen as hyperbolic functions of the absolute value of the relative fault, e.g $|\bar{f}|$. The plot of the scheduling functions $\rho_i(|\bar{f}|)$, $i = 1, 2$ given in Fig. 7.10.

According to Fig. 7.10, the ADAS controller scheduling strategy is as follows. When the estimated driver error is low, both scheduling function compute to $\rho_i \approx 100$, $i = 1, 2$. This value for the design varying parameters ρ_1 and ρ_2 represent grid-points where the control actions are heavily penalized. As a result the ADAS controller output will be null and the driver does not receive any aid in this scenario.

As the driver error grows, the varying parameter ρ_2 is scheduled to descend progressively towards $\rho_2 = 1$, activating the use of the direct yaw control action M_z. As the driver error reaches $|\bar{f}| \geq 10$ the yaw moment control action M_z is from there given full control authority, with performance constraints $W_{M_z}(\rho_2)$ in Eq. (7.25).

On the other hand, the additive steering action δ_k only gets fully activated at $|\bar{f}| \geq 45$. This represents that the additive steering actuator only receives control authority when driving errors are above the critical value set at $|\bar{f}| \geq 30$, corresponding to dangerous situations. Note that$|\bar{f}|$ according to Eq. (7.32) gives a direct quantification of how much the real driver steering is deviating from the assumed nominal behaviour.

This scheduling choice for ρ_1 and ρ_2 has the objective of prioritizing the use of the yaw moment control action M_z in the ADAS controller over additive steering δ_k. The overall goal with this decision being to attempt not to interfere with the driver steering unless it is ultimately required.

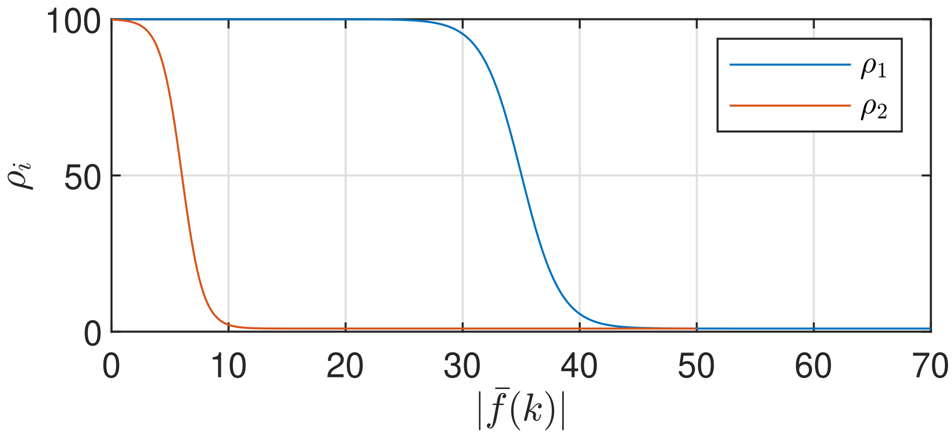

Figure 7.10: Driver Error Based Scheduling Functions

7.6 Simulation Results

The performance of the proposed integrated lateral ADAS strategy is here validated in simulation. To simulate the vehicle dynamics it is considered the full car model of a Renault Megane developed in the previous thesis work [FSD16], see Chapter 2. To simulate the human driver steering (faulty driver) it is used the LPV LEDM presented in Fig 7.3. The vehicle speed is varying throughout the simulations, with the profile of the longitudinal vehicle speed v_x given in Fig. 7.11.

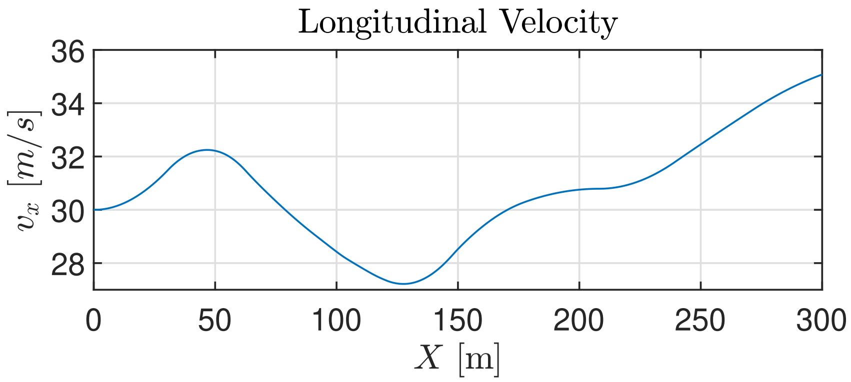

Figure 7.11: Longitudinal Speed Profile of the Vehicle During Simulations

Two simulation scenarios are tested:

1. In the first scenario the driver must perform a Double Lane Change emergency maneuver without ADAS assistance.

2. In the second scenario the same DM must perform the same maneuver, this time with ADAS assistance enabled.

The simulations were performed considering ten randomly generated drivers profiles. The range in which the randomized faulty LPV LEDM parameters can lie are given in Table 7.3. Additionally, as a reference comparison with the faulty driver parameter range used for simulation, Table 3.1 presents the values of the nominal LPV LEDM used for control and observer synthesis.

Table 7.3: DM Parameters

Parameter	Nominal	Faulty Range
T_L	0.3	[0.2, 0.3]
T_N	0.1	[0.14, 0.25]
τ	0.1	[0.15, 0.22]
K_v	1.4	[1.1, 1.5]
K_{ff}	0.85	[0.75, 0.85]

Information on the the simulation results for both scenarios are shown in Fig. 7.12. This figure presents at the top, data from the scenario without assistance. The vehicle trajectory on the X and Y global coordinate frame given at the top-left and vehicle lateral acceleration at the top-right. At the bottom of Fig. 7.12, data for the case when ADAS assistance is active is shown, the vehicle trajectory at the bottom-left and the vehicle lateral acceleration at the top-right.

From the results in Fig. 7.12 it can be seen that in the case without ADAS, the performance between generated drivers are very different. Some have very poor performances, which in a real scenario would lead to an accident if such maneuver is carried. Meanwhile, some of the simulated drivers can accomplish the DLC in a safer manner, although some oscillations are still present in their trajectory.

In the scenario where the ADAS controller is used, it can be seen that the performances are quite homogeneous in between all ten drivers, both in terms of the vehicle trajectory and lateral acceleration. More importantly, vehicle stability was achieved for all drivers when employing the ADAS controller. The trajectories during the DLC can be seen to be smoother, and once finished the DLC, oscillations in the trajectories are greatly reduced. Moreover, in the scenario with ADAS, the lateral acceleration the vehicle experiences are less than half of those in the case without ADAS. This is significant as high values of lateral acceleration at high-speeds can cause the vehicle to over-steer.

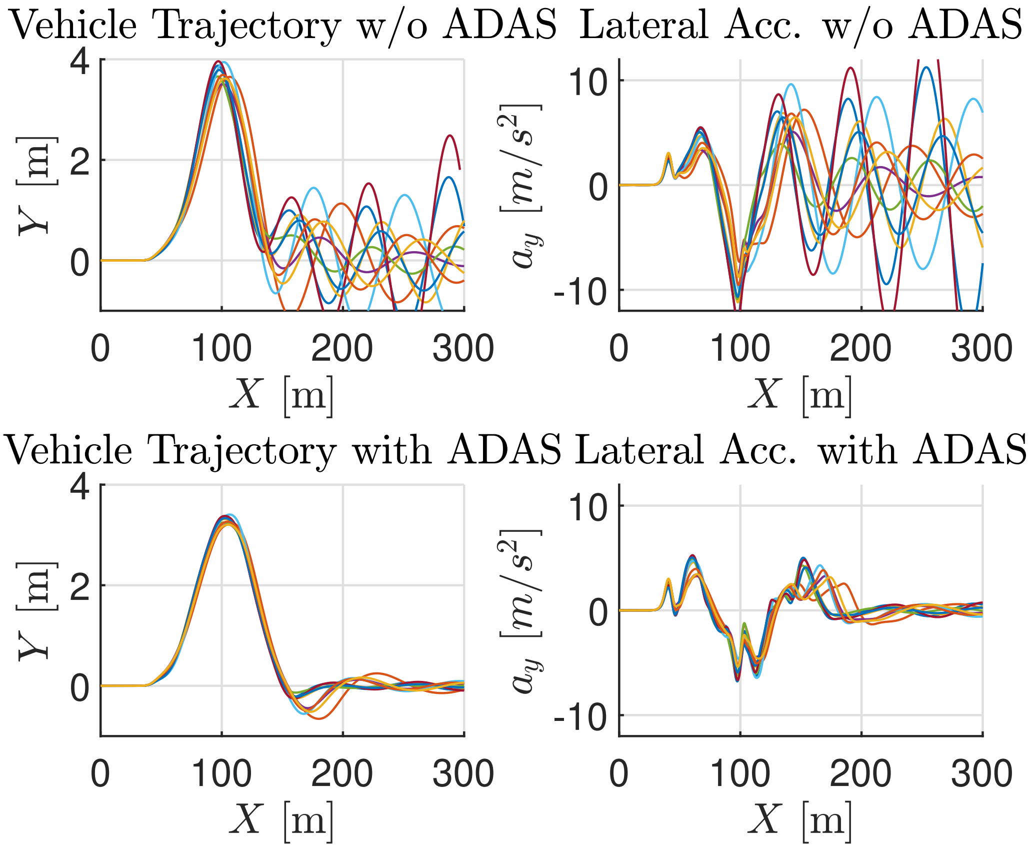

Figure 7.12: Driving Comparison with and without ADAS During DLC Maneuver

Information regarding the controller scheduling and controller commands for scenario employing the integrated ADAS strategy can be found in Fig. 7.13 and Fig. 7.14. For the sake of clarity of presentation, each figure represents data from a single driver, Fig. 7.13 and Fig. 7.14 correspond to the worst and best performers respectively out from the ten generated drivers.

Both figures present on top the scheduling signals used to modulate the magnitude of the controller actions. It is shown on the top-left ρ_1 (affects the additive steering command δ_k) and at the top-right ρ_2 (affects the differential torque M_z command). On the bottom, it is shown the control signals computed by the LPV ADAS controller. On the bottom-left it is given the additive steering command δ_k and on the bottom-right the braking torque command for the left (T_{brl}) and right (T_{brr}) rear wheels, computed according to Eq. (7.22) from the M_z output of the controller.

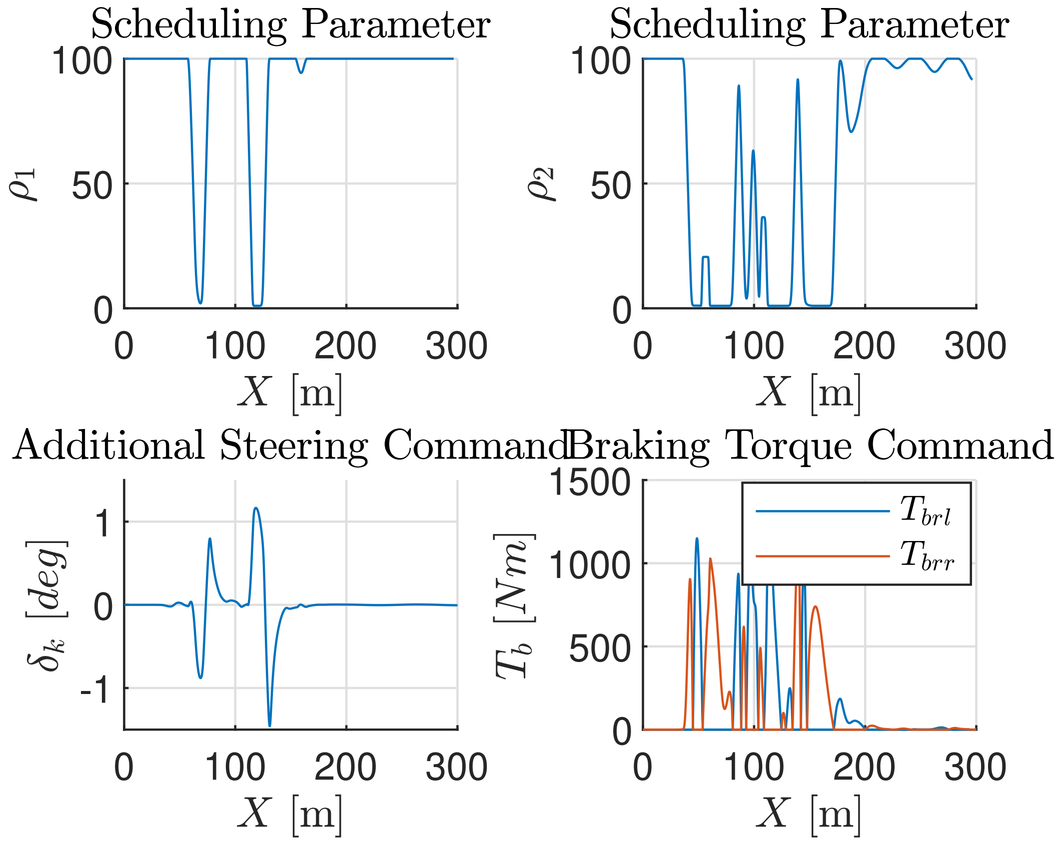

Figure 7.13: Scheduling Signals and Actuator's Commands for the Case of Worst Driver Performance

For the worst case driver, Fig 7.13, it can be seen that an important driver error is being estimated, as both scheduling functions reach low values. According to the scheduling design in Fig. 7.10, this represents and estimated driver error residual $|\bar{f}|\geq 45$. Therefore, the LPV scheduling reconfiguration needs to activate the additive steering control input to assist the driver successfully. From the scheduling signals, it can be seen that they only get activated during the critical DLC maneuver. Once this critical phase has passed, they return quickly to the deactivated status, not interfering the driver afterwards.

For the best driver case, in Fig. 7.14, the magnitude of driver error estimated is smaller. As a result, the steering command is not activated. Moreover, the commanded braking torques are half in magnitude than those of the previous case. In conclusion, the best case driver receives aid during the critical DLC but as his driving performance allow to complete the DLC in safer manner, the amount of aid is minimized when compared with a bad driver.

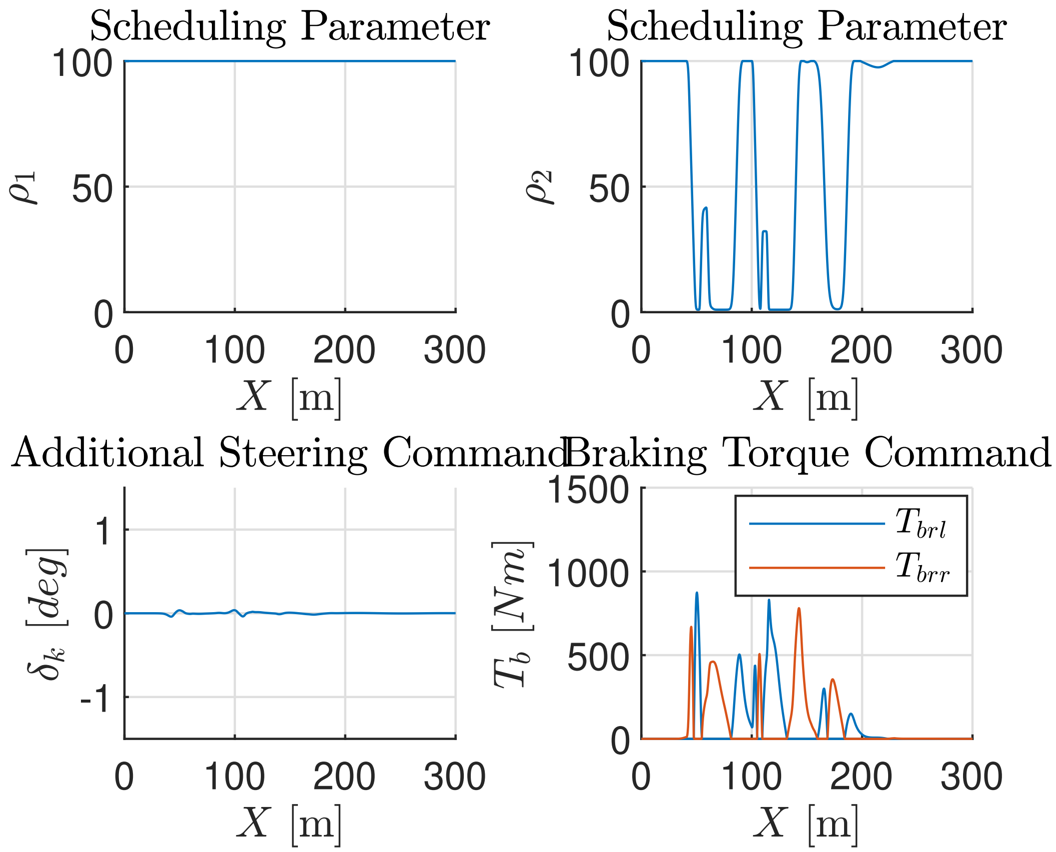

Figure 7.14: Scheduling Signals and Actuator's Commands for the Case of Best Driver Performance

7.7 Conclusion

In this chapter, a lateral control strategy for ADAS has been presented, which takes into account a wide range of vehicle speeds and the coordination of multiple actuators. Through simulation results, it was demonstrated that the proposed LPV driver error estimation and ADAS controller strategy successfully achieves the objectives of the ADAS system. These objectives include minimizing the interference of ADAS in the driver's experience without compromising safety when necessary, all while remaining robust to various driver behaviors and changes in vehicle velocity.

The effectiveness of the proposed strategy was evaluated using simulated driver models representing a diverse range of driver profiles. The results indicated that for drivers with poor performance, the ADAS strategy was able to maintain vehicle stability in critical scenarios. However, for highly skilled drivers in the same scenario, the level of assistance provided by the ADAS system was significantly reduced. This demonstrates the adaptability of the integrated

LPV ADAS strategy, which is achieved through the use of design-related varying parameters and a scheduling strategy based on driver performance estimation. Proven effective and adaptable, the next chapter will focus on the experimental validation of the ADAS strategy on the Scaled Automated Vehicle (SAV) platform with multiple Test Drivers.

Chapter 8

Integrated LPV ADAS Strategy on the SAV Platform

Contents

8.1 Introduction

This chapter presents an ADAS strategy to be tested experimentally on the SAV car. This strategy draws from the lessons learned in the LPV ADAS design discussed in Chapter 6 and 7 and from the autonomous lateral controller presented in Chapter 5. The strategy revolves around the utilization of a PI observer to detect driver errors, similar to what was introduced in Chapter 7. The detected driver error is then used to determine the amount of steering assistance provided by the ADAS system.

With regards the lateral ADAS controller, one of the novel elements introduced in this chapter is the inclusion of a Heading Error Driver Model (HEDM) in the joint driver-vehicle model utilized as the controlled system plant. Additionally, the controller design presented here incorporates recommendations from [WGP00] regarding the use of design-related varying parameters, similar to what was discussed in Chapter 5. As a result, the design-related parameter modifies both the actuator and tracking error performances on the LPV/$\mathcal{H}_\infty$ design, which differentiates it from the design approaches in Chapter 6 and Chapter 7.

However, the overall philosophy and objectives of the integrated ADAS strategy remains unchanged. An important objective of this chapter, with regards the experimental validation, is to prove whether the driver error detection based on model based fault detection techniques presents an appropriate correlation with real dangerous or anomalous driving situations. Moreover, it is of interest to validate whether the lateral LPV ADAS controller design actually provides an efficient aid without feeling invasive when tested by multiple drivers.

The contents of this chapter have been recently developed and have not yet been published at the time of writing this thesis manuscript.

8.1.1 Integrated LPV ADAS Strategy

The proposed strategy for the ADAS system is presented in Fig. 8.1. It is very similar to the strategy introduced in Chapter 6 and Chapter 7. The strategy presented in this chapter uses only the steering actuator. To control the magnitude of the steering aid it is introduced the design-related varying parameter ρ which modifies the controller by means of LPV scheduling. As in Chapter 7, the scheduling is based on the estimation of driver errors made by a PI observer which compares the vehicle-road information with the actual steering of driver.

The most important distinction is that this strategy will be validated experimentally, with the SAV platform used for this purpose. This is illustrated in Fig. 8.1 with a joystick representing the way in which the human driver inputs its steering commands. This joystick allows a person to manually drive the SAV car along a desired trajectory, providing a means to test the effectiveness of the various components of the ADAS strategy. Specifically, the experiment will assess the performance of the model-based driver error detection and the LPV/$\mathcal{H}_\infty$ ADAS controller, ensuring that they function as intended in a real-world driving scenario.

8.1.2 Chapter Structure

The structure of the rest of the chapter is the following. Sec. 8.2 introduces the fault detection approach for detecting driver errors based on a PI observer algorithm. Section 8.3 presents the joint driver-vehicle model used for lateral ADAS control design. Then Sec. 8.4 explains the design and synthesis of the lateral ADAS controller as well as the scheduling strategy used for the activation/deactivation of the LPV controller. Finally, Sec. 8.5 presents experimental

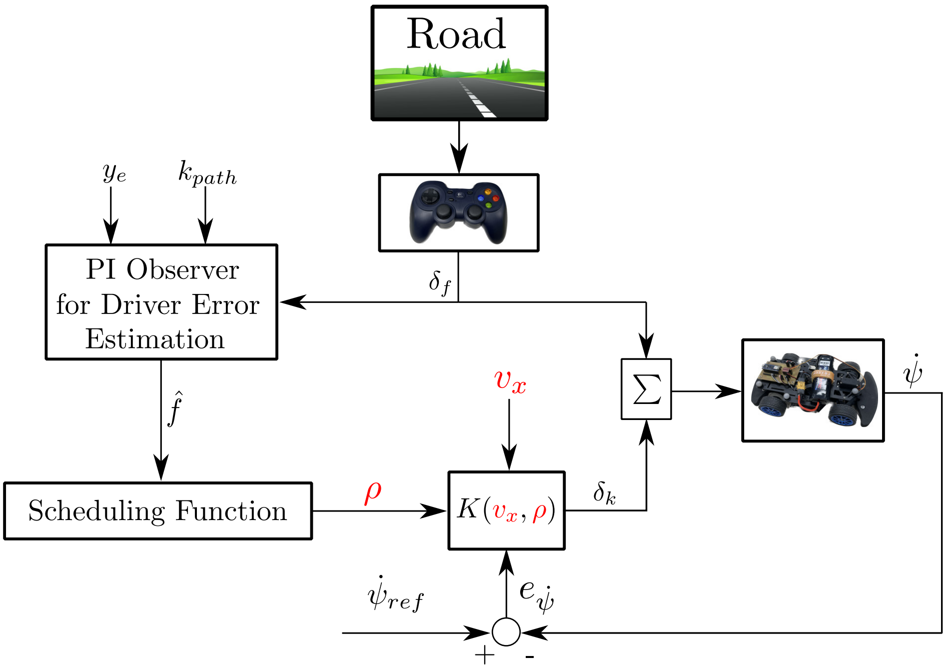

Figure 8.1: Combined Driver Error Detection / ADAS Controller Scheme on the SAV platform.

results obtained with multiple Test Drivers after driving on the SAV platform with the aid of the proposed integrated ADAS design.

8.2 Driver Error Detection

8.2.1 PI Observer for Driver Error Estimation

The strategy for the detection of driver errors is similar to that followed in Sec. 7.3 from Chapter 7. The objective is here to synthesize a PI observer in order to estimate faults in the driver steering action. As a nominal driver model behaviour it is used the Lateral Error Driver Model (LEDM), see Sec. 3.3.1 from Chapter 3, with the following set of parameters:

Table 8.1: Nominal LEDM Parameters Used for Driver Error Detection

Parameter	Value
K_0	1
T_{L0}	0.3
T_{N0}	0.1
τ_0	0.1
K_{v0}	0.26
K_{ff0}	0.80

Then, this nominal LEDM is represented into a discrete LTI state-space model (considering a sample time $T_s = 0.02s$) as follows:

$$\begin{cases} x_d^+ = A_0 \cdot x_d + B_0 \cdot u_d \\ \delta_0 = C_0 \cdot x_d + D_0 \cdot u_d \end{cases} \tag{8.1}$$

with

$$u_d(k) = \begin{bmatrix} y_e(k - \tau_0/T_s) \\ k_{path}(k) \end{bmatrix} \tag{8.2}$$

Different from the nominal LEDM, the steering of a real driver δ_f is modelled as the following additive fault representation:

$$\delta_f = \delta_0 + \bar{f} \tag{8.3}$$

A visual representation of the faulty driver model is provided in Fig. 8.2. The signal $\bar{f}$ is the filtered additive fault such that the additive fault f signal is passed through the band-pass filter W_F:

$$\begin{aligned} W_F &= \mathcal{Z}_T \left(G^0 \frac{(s/2\pi f_1 + 1)(s/2\pi f_2 + 1)}{(\alpha_f s/2\pi f_1 + 1)(s/\alpha_f 2\pi f_2 s + 1)} \right) \\ G^0 &= \frac{(\alpha_f \Delta_f/2\pi f_1 + 1)(\Delta_f/\alpha_f 2\pi f_2 + 1)}{(\Delta_f/2\pi f_1 + 1)(\Delta_f/2\pi f_2 + 1)} \\ \Delta_f &= 2\pi(f_1 + f_2)/2 \end{aligned} \tag{8.4}$$

The objective behind this filter is to limit the frequency range in which the additive fault f affects the nominal LEDM. For this, the cutoff frequencies in W_F are chosen with $f_1 = f_2 = 0.85Hz$ in Eq. (8.4). A narrow frequency band for W_F around $f = 0.85Hz$ limits the effect of constant and low frequencies discrepancies between the real driver and nominal LEDM. The objective of this decision can be better explained with the following example:

Picture an scenario were a driver is driving with a constant lateral error offset y_e with respect the center line of the road lane. This lateral error would produce a steering action δ_0 from the nominal LEDM. However, as this offset is maintained constant it cannot be concluded that this error is dangerous, it is in all likelihood a driving style preference. Consequently, this scenario should not be categorized as a *faulty* situation that requires the intervention of the ADAS system.

Thus, limiting the frequency range of the additive fault f by the the shaping filter W_F is another attempt to limit the impact that the proposed integrated ADAS strategy can cause on the driving experience. Recall that the objective behind our proposed ADAS strategies is to not feel invasive on the driver style preferences and only act when dangerous errors are detected.

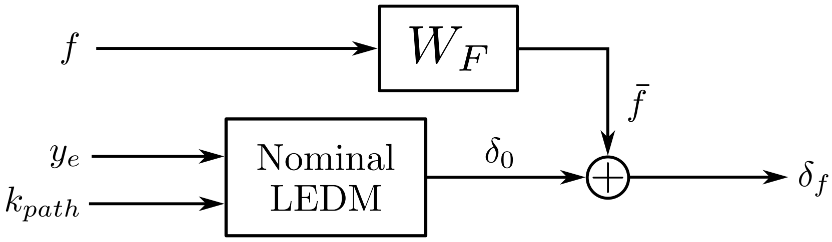

Figure 8.2: Faulty Driver Model with Filtered Fault

In the PI Observer framework, the fault f is assumed to be such that $\dot{f} = 0$, which could be conservative since it means that the theoretical approach is valid only for a slow varying fault (even if the results will show the efficiency of the approach when f varies).

By incorporating f as a state variable, the extended faulty driver model is then given by:

$$\begin{cases} \begin{bmatrix} x_d^+ \\ x_f^+ \\ f^+ \end{bmatrix} = \begin{bmatrix} A_0 & 0 & 0 \\ 0 & A_f & B_f \\ 0 & 0 & 1 \end{bmatrix} \cdot \begin{bmatrix} x_d \\ x_f \\ f \end{bmatrix} + \begin{bmatrix} B_0 \\ 0 \\ 0 \end{bmatrix} \cdot u_d \\ \delta_f = \begin{bmatrix} C_0 & C_f & D_f \end{bmatrix} \cdot \begin{bmatrix} x_d \\ x_f \\ f \end{bmatrix} + D_0 \cdot u_d + \bar{d} \end{cases} \tag{8.5}$$

where the disturbance input $\bar{d} \in \mathbb{R}$ represents high-frequency uncertainties to account for possible unmodeled dynamics neglected in the nominal LEDM as well as sensor noise and A_f, B_f, C_f, and D_f are the system matrices of the DT-SS representation of the filter W_F, which is discretized using the Tustin method.

The above driver error f can then be estimated with the aid of an LPV PI observer of the form:

$$\begin{cases} \begin{bmatrix} \hat{x}_d^+ \\ \hat{x}_f^+ \\ \hat{f}^+ \end{bmatrix} = \begin{bmatrix} A_0 & 0 & 0 \\ 0 & A_f & B_f \\ 0 & 0 & 1 \end{bmatrix} \cdot \begin{bmatrix} \hat{x}_d \\ \hat{x}_f \\ \hat{f} \end{bmatrix} + \begin{bmatrix} B_0 \\ 0 \\ 0 \end{bmatrix} \cdot u_d - L \cdot (\delta_f - \hat{\delta}_f) \\ \hat{\delta}_f = \begin{bmatrix} C_0 & C_f & D_f \end{bmatrix} \cdot \begin{bmatrix} \hat{x}_d \\ \hat{x}_f \\ \hat{f} \end{bmatrix} + D_0 \cdot u_d \end{cases} \tag{8.6}$$

with $L \in \mathbb{R}^4$ the observer gain.

According to Eq. (8.6) and with the interconnection as shown in Fig. 8.3 the extended observer error dynamics are given by Eq. (8.7). Note that in Fig. 8.3, W_D is a high-pass filter approximating the high-frequency uncertainties due to possible unmodeled dynamics. The observer error dynamics are given by

$$\begin{cases} x_O^+ = (A + \tilde{L}C) \cdot x_O + (B_w + \tilde{L}D) \cdot d \\ z_e = C_z \cdot x_O \end{cases} \tag{8.7}$$

with $x_O \in \mathbb{R}^{4+n_D}$ the estates of the extended error dynamics (with n_D the order of the high-pass filter W_D) and $z_e \in \mathbb{R}$ the estimation error for the additive fault f and where

$$\tilde{L}(v_x) = \begin{bmatrix} L(v_x) \\ 0^{1\times n_D} \end{bmatrix} \tag{8.8}$$

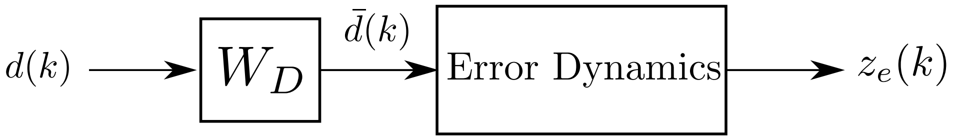

Figure 8.3: PI Observer Error Dynamics Interconnection with Shaping Filter W_D.

Concerning the driver error detection PI Observer, the shaping filter W_D has been considered as digital Butterworth filter with cut-off frequency at $2Hz$ and order $n_D = 2$. In Fig. 8.4 it is represented the magnitude frequency response for the used shaping filters W_F and W_D.

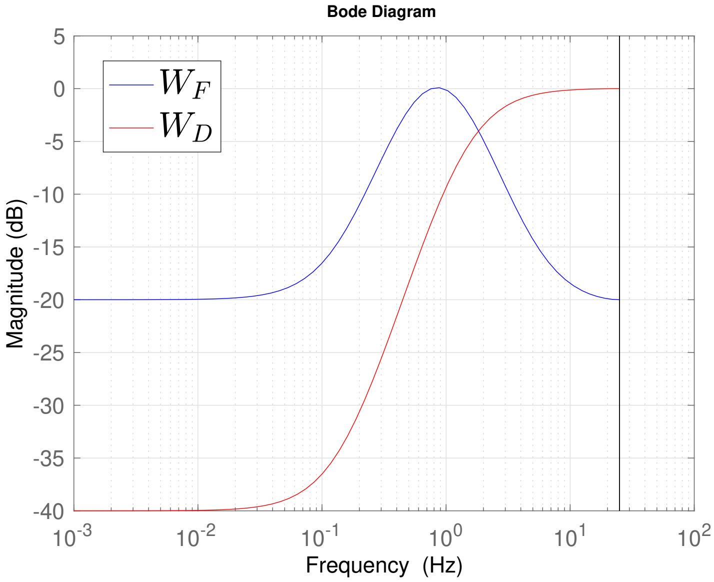

Figure 8.4: Bode magnitude plot for the DT filters W_D and W_F used to shape the $\mathcal{H}_\infty$ PI Observer.

8.2.2 Observer Synthesis

With the Extended Observer Error Dynamics Eq. (8.7), the objective of observer gain L synthesis is to minimize the induced L_2-norm of the PI observer Eq. (8.6) estimation error from disturbance d to observer estimation error z_e.

$$\|z_e\|_2 \leq \gamma_\infty \|d\|_2 \tag{8.9}$$

The synthesis of the observer gain L will be carried out using the dual approach to the Parameter-Dependent State-Feedback (PDSF) synthesis seen in Chapter 4, as was done in Sect. 7.3 from Chapter 7. For the two-step synthesis procedure of the $\mathcal{H}_\infty$ observer gain, the first step consists in applying the Bounded Real Lemma (BRL), as seen in Theorem 1.2, over the extended observer error dynamics in Eq. (8.7).

The existence of such observer gain L can be tested according to Proposition 7.1. The LMI optimization problem in Proposition 7.1 was implemented for the system Eq. (8.7) employing the parser Yalmip [Löf04] and solved with the SDPT3 solver [TTT04] as minimization over the scalar γ_∞, taking a constant Lyapunov Matrix such that:

$$X = X_0 \tag{8.10}$$

Remark 8.1
Proposition 7.1 was posed for LPV systems. However, note that the condition in Eq. 7.10 can be easily adapted for LTI systems. For this reason, to avoid unnecessary duplication, it was not considered to provide here specific theorems or propositions for the synthesis of LTI observers.

From the numerical solutions from Proposition 7.1 of the values of the Lyapunov Matrix X_0 and the set of slack matrix G_0, the computation of the observer gain L can be carried solving the LMI problem in Proposition 7.2. Recall that the observer gain vector $\tilde{L}(v_x)$ in the extended observer error dynamics Eq. (8.7) is augmented with a vector of zeros. As a result, in Proposition 7.2 the observer gain vector is implemented according to Eq. (8.8).

Note that even for LTI systems, the two-step synthesis used for LPV controller synthesis seen in Sec. 4.3 and for LPV observer synthesis in Sec. 7.3 can provide benefits. Using the more standard approach based on change of variables, it would not be straightforward to find a solution enforcing the structure of $\tilde{L}$ as in Eq. (8.8). However, with the two-steps approach, $\tilde{L}$ appears directly on the second LMI problem, as a result it is simple to apply constraints on the gain structure. On the other hand, this comes at a cost of added conservatism.

8.3 Integrated Driver-Vehicle Control Oriented Model

To tackle the design of the ADAS controller, the control-oriented plant model consists of the joint driver-vehicle system. To incorporate the driver in the control loop, a nominal Heading Error Driver Model (HEDM) is considered, see Sec. 3.3 from Chapter 3. According to Remark 3.1, the feedforward curvature input k_{path} of the HEDM is modified by considering the relationship [Raj11]:

$$k_{path} = \frac{\dot{\psi}_{ref}}{v_x} \tag{8.11}$$

Moreover, the heading error ψ_e is not assumed as an exogenous input. Instead, for ADAS controller design, the heading error ψ_e for the HEDM is modeled as:

$$\psi_e = \int (\dot{\psi}_{ref} - \dot{\psi})dt \tag{8.12}$$

Note that in previous chapters, when employing the LEDM for ADAS design, the lateral error y_e was indeed considered as an independent exogenous input, e.g. see the $\mathcal{H}_\infty$ generalized plant in Fig. 7.7.

These modifications on the original HEDM render the driver model with $\dot{\psi}_{ref}$ as the only input. This being the exogenous input used for tracking. Furthermore, the presence of an integrator on the HEDM provides it with high gain on the lower frequencies. Both of theses facts are beneficial on the ADAS design and controller synthesis. Firstly, minimizing the number of exogenous inputs reduces the number of signals for which the induced L_2-norm of the closed-loop system needs to be minimized. Secondly, as the HEDM provides high gain at lower frequencies, this complements the constraints set on the ADAS controller. Especially, as the $\mathcal{H}_\infty$ design used for the ADAS synthesis penalizes the controller actions at low frequencies, as was seen in Chapter 6 and Chapter 7. The nominal HEDM considered for ADAS design was chosen with the set of parameters given in Table 8.2.

Table 8.2: Nominal HEDM Parameters Used for ADAS Controller Design

Parameter	Value
K_0	3
T_{L0}	0.3
T_{N0}	0.1
τ_0	0.1
K_{v0}	0.1740
K_{ff0}	0.85

For the control-oriented plant, the vehicle dynamics are modeled considering the augmented SAV Bicycle Model (BM) with additional steering actuator model, see Definition 2.4 from Chapter 2. An schematic of the joint driver-vehicle model is provided in Fig. 8.5. It can be noticed that the modifications made on the HEDM make implicit the presence of the feedback loop within the driver-vehicle system.

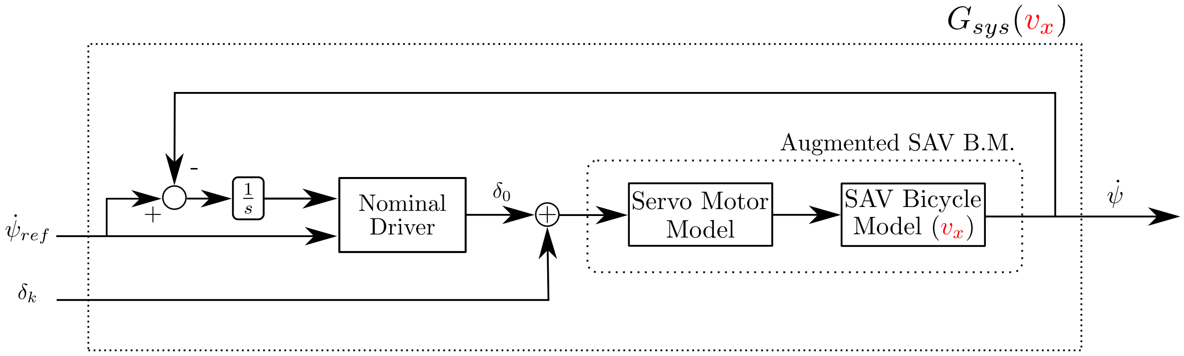

Figure 8.5: Integrated Driver-Vehicle Control Model

8.4 Robust Lateral LPV ADAS Control

8.4.1 LPV/$\mathcal{H}_\infty$ ADAS Control Design

The control problem is here formulated according to the induced L_2-norm Gain-Scheduled SF DT-LPV control problem given in Definition 5.2. The generalized plant $P(v_x, \rho)$ for the induced L_2-norm problem including the State-Feedback ADAS controller is given in Fig. 8.6. The exogenous input is $w = \dot{\psi}_{ref}$ and the vector of controlled outputs is $z = (z_1, z_2)^T$, which represents the tracking error and the controller output performances respectively. The controller action is the steering command δ_k $[rad]$ given to the SAV servomotor, the controller is a State-Feedback controller with x_P the full state vector of the generalized plant $P(v_x, \rho)$.

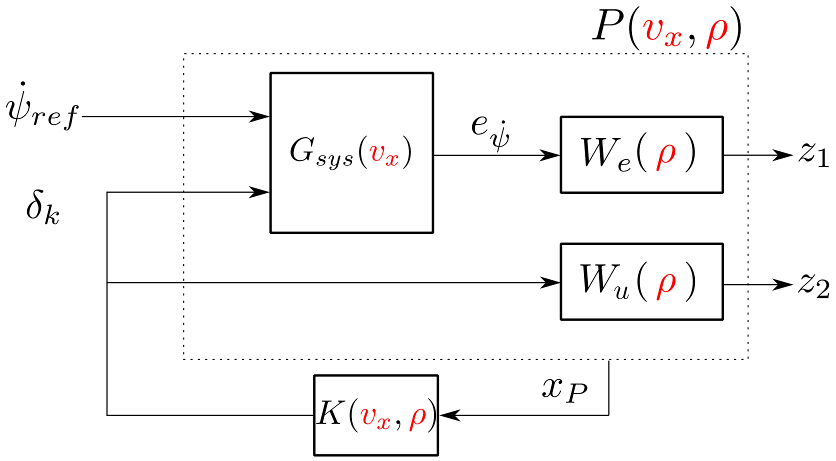

Figure 8.6: LPV/$\mathcal{H}_\infty$ Generalized Plant P for the State-Feedback Problem

Note that performance weights are included to tackle the different objectives. The weight $W_u(\rho)$ is dedicated to the steering control performance (through the control sensitivity function

KS from $\dot{\psi}_{ref}$ to the controller output δ_k). It is chosen as an LPV system of the form:

$$\begin{aligned}
W_u(\rho) &= \mathcal{Z}_T\left(\rho \cdot G^0 \frac{(s/2\pi f_3+1)(s/2\pi f_4+1)}{(\alpha_\delta s/2\pi f_3+1)(s/\alpha_\delta 2\pi f_4 s+1)}\right) \\
G^0 &= \frac{(\alpha_\delta \Delta_f/2\pi f_3+1)(\Delta_f/\alpha_\delta 2\pi f_4+1)}{(\Delta_f/2\pi f_3+1)(\Delta_f/2\pi f_4+1)} \\
\Delta_f &= 2\pi(f_3+f_4)/2
\end{aligned} \tag{8.13}$$

which is a band-pass filter extended from [GGK08]; [PV+11]. The objective of such a filter is to constraint the controller commands in the frequency range between $f_3 = 1Hz$ and $f_4 = 10Hz$, where it can affect the vehicle dynamics while not being felt intrusive to the driver, who is mainly sensitive to low steady-state frequencies ($\leq 1Hz$) and very high frequencies vibrations ($\geq 10Hz$) acting on the steering wheel. The constant α_δ is used to set a maximum actuator gain of less than $1rad$ ($\approx 57.3°$) in absolute magnitude for a change in yaw rate reference $|\Delta\dot{\psi}_{ref}| = 1rad/s$.

Remark 8.2
In comparison to the ADAS design for the Renault Megane model discussed in Chapter 6 and Chapter 7, the SAV ADAS design presented here allows for a considerably larger range of actuator movement. In the Renault Megane designs, the steering angle δ_k was limited to a maximum of $\leq 5°$ for a change in the desired yaw rate $|\Delta\dot{\psi}_{ref}| = 1rad/s$. However, for the SAV design, the steering angle δ_k is permitted to reach a maximum of $\leq 57.3°$ for the same change in the desired yaw rate. This adjustment is primarily motivated by the contrasting speeds and vehicle dynamics between the Renault Megane and the SAV car. A steering angle of $\leq 5°$ does not result in a significant rotation for the SAV as it would for the Renault Megane. Additionally, the specific application scenarios also differ. The ADAS for the Renault Megane was mainly designed for high-speed highway driving, whereas the SAV ADAS design is specifically tailored for racing circuits with sharp turns.

As can be seen from Eq. (8.13), the design-related varying parameter ρ modifies the gain of the actuator performance weight $W_u(\rho)$. When $\rho = 1$, considered as the faulty condition, the actuator is then given the most control authority according to $W_u(\rho = 1)$. On the other hand, on nominal conditions with $\rho \approx 100$ the control action is heavily penalized. More details on the scheduling strategy will be seen in Sec. 8.4.4. However, it is important to keep the scheduling behaviour in mind for the task of controller design. When heavily penalizing the control action, e.g. $\rho \approx 100$, it is not consistent to demand tight tracking performances from the closed-loop system [WGP00].

As a result, the tracking error weight $W_e(\rho)$, which shapes the tracking performances (through the sensitivity function S) from the reference $\dot{\psi}_{ref}$ to the tracking error $e_{\dot{\psi}} = \dot{\psi}_{ref} - \dot{\psi}$, has to adapt based on the design-related varying parameter value. This was done according to the following expression

$$W_e(\rho) = \begin{cases} \mathcal{Z}_T\left(\frac{s/M_s+f_b}{s+f_b\underline{\epsilon}}\right), & \text{if } \rho = 1 \\ \mathcal{Z}_T\left(\frac{s/M_s+f_b}{s+f_b\overline{\epsilon}}\right), & \text{if } \rho = 100 \end{cases} \tag{8.14}$$

Considering $M_s = 2$, $f_b = 2\pi 0.5\ rad/s$, $\underline{\epsilon} = 0.01$ and $\overline{\epsilon} = 2$. In a faulty situation, e.g. $\rho \approx 1$, $\underline{\epsilon} = 0.01$ is used to set a tracking objective of less than 1% of yaw rate error. On the other hand, $\overline{\epsilon} = 2$ is used to relax the tracking requirement by that of stability in nominal situations when the controller is heavily penalized.

8.4.2 LPV/$\mathcal{H}_\infty$ State-Feedback Synthesis

The synthesis of the LPV/$\mathcal{H}_\infty$ controller is here carried out following the Gain-Scheduled Grid-Based DT-LPV approach introduced in Chapter 5. In order to pose the control synthesis as a finite dimension LMI optimization problem, the parameter grid and local bounds approach is used, see Sect. 4.2 from Chapter 4. The considered frozen grid values for each varying parameter are:

$$v_{x,p} = [0.6, 0.9, 1.2, 1.5] \tag{8.15}$$

$$\rho_p = [1, 100] \tag{8.16}$$

All possible combinations of frozen values for the varying parameters then form the grid-space $\mathcal{G}$, with each grid-point defined as $g_p = (v_{x,p}, \rho_p)$. Taking a sampling time $T_s = 0.02$, the maximum rate of parameter variation between consecutive samples is assumed as $\nu_{v_x} = 0.02 m/s$ ($a_{max} = 1 m/s^2$) for the longitudinal velocity and $\nu_\rho = 60$ for the design-related varying parameter ρ.

As the synthesis approach is based on DT methods, it is of special importance to discuss the discretization procedure of the driver-vehicle plant given by $G_{sys}(v_x)$ in Fig. 8.5. Notice that both the nominal HEDM as the Servo Motor model from Definition 2.4 present pure input delays, see Table 8.2 and Table 2.2 for the delay time values respectively. The discretization approach then consisted in discretizing the pure delays and CT model independently.

The discretization of the pure time delay is given by

$$\mathcal{Z}(e^{-\tau s}) = \frac{1}{z^d} \tag{8.17}$$

where d is the number of sample delays with $d = \tau / T_s$. For the heading error delay on the nominal HEDM it is considered $d = 5$, meanwhile, for the steering command delay on the Servo Motor model it is considered $d = 9$.

The CT models, e.g. the integrator from Eq. (8.12), the HEDM and the Augmented SAV BM, are discretized using the exact Zero-Order Hold discretization method at all frozen grid-points of v_x. Finally, the DT driver-vehicle plant is obtained from the interconnection in Fig. 8.5 of discretized elements and with Eq. (8.17) in series with the respective delayed input. On the other hand, the performance weights $W_e(\rho)$ and $W_u(\rho)$ are discretized at all frozen values of the design-related varying parameter ρ employing a Tustin discretization approach.

With individual elements discretized, for all grid-points $g_p = (v_{x,p}, \rho_p)$ the interconnection given in Fig. 8.6 then defines the generalized plant $P(v_{x,p},\rho_p)$ used for LPV/$\mathcal{H}_\infty$ design as:

$$\begin{cases} x_P^+ = A(v_{x,p},\rho_p)\cdot x_P + B_u(v_{x,p},\rho_p)\cdot u + B_w(v_{x,p},\rho_p)\cdot w \\ z = C_z(v_{x,p},\rho_p)\cdot x_P + D_u(v_{x,p},\rho_p)\cdot u + D_w(v_{x,p},\rho_p)\cdot w \end{cases} \tag{8.18}$$

Note that the dimensions of the state vector of the generalized plant $P(v_x,\rho)$ is $x_P \in \mathbb{R}^{23}$. The system states are the following: the SAV BM adds two states $(v_y, \dot{\psi})$, the servo motor model adds states $(\delta, \dot{\delta})$, the HEDM adds the state x_d from the simplified precision model used on the feedback path plus ψ_e as the integrator state from Eq. (8.12), the performances weights $W_e(\rho)$ and $W_u(\rho)$ add three states combined, finally, accounting for the DT time delays as in Eq. (8.17) directly on the control model adds five states for the input delay present on the HEDM and nine states for the input delay present on the servomotor model.

Considering the following structure for the PDLM $X(v_x,\rho)$ in the ADAS controller synthesis problem:

$$X(v_x,\rho) = X_0 + v_x X_1 + \frac{1}{v_x} X_2 + \rho X_3 \tag{8.19}$$

the individual gains K_p of the Grid-Based DT-LPV controller $K(v_x,\rho)$ at each grid-point g_p can be computed by solving the LMI optimization problem posed in Proposition 5.1. The LMI problem was implemented making used of the parser Yalmip [Löf04] and solved using the Mosek solver [ApS19]. The synthesis resulted successful with a computed bound in the induced L_2-norm of $\gamma_\infty = 92.84$.

8.4.3 Frequency Analysis of the Control Design

A first validation of the controller design is carried out on the frequency domain. Fig. 8.7 presents the Controller Sensitivity transfer function from yaw rate reference $\dot{\psi}_{ref}$ to the steering control output δ_k computed at frozen grid-point values of the resulting LPV closed-loop system according to the generalized plant scheme shown in Fig. 8.6. The Controller Sensitivity transfer function computed at grid-points with the maximum control authority, e.g. $\rho = 1$, is given in blue color. On the other hand, the grid-points were the additive steering is *deactivated* are represented in red color. From the frequency domain result it can be observed that the effect of increasing the value of the design-related parameter ρ translates in a significant reduction in control authority of the additive steering action in fulfillment of the desired objectives.

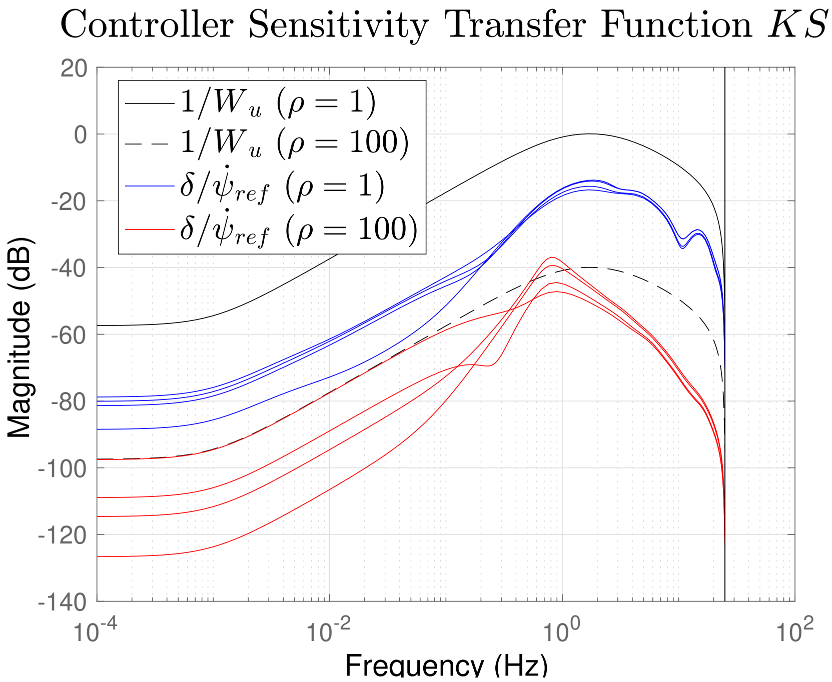

Figure 8.7: Controller Sensitivity Transfer Function $KS = \frac{\delta}{\dot{\psi}_{ref}}$ versus actuator performance template W_u^{-1} at frozen grid-points.

8.4.4 Fault Dependent Scheduling Function

In the following it is described the scheduling strategy for the design-related varying parameter ρ. As can be seen from the integrated ADAS strategy scheme in Fig. 8.1, the ADAS controller scheduling depends on the driver fault estimation, presented in Sect. 8.2. The driver fault estimation $\hat{f}$ is not directly used, instead it is used the filtered estimation fault $\bar{f}$ with band-pass filter W_F as in Eq. (8.4). See Fig. 8.2 from Sec. 8.2. Moreover, the filtered fault $\bar{f}$ is used as:

$$\tilde{f}(k) = \frac{\bar{f}(k)}{f_0}, \tag{8.20}$$

where f_0 is a threshold value defining the maximum additive fault estimation not considered as an actual fault.

The scheduling function that modifies the online value for the design-related varying parameter $\rho(k)$ is chosen as:

$$\rho(k) = \text{MAX}\left(100 \cdot (1 - |\tilde{f}(k)|), 1\right) \tag{8.21}$$

Observing this scheduling rule function, according to the filtered driver fault estimation $\bar{f}(k)$ when the driver is not committing any important fault, e.g. $|\bar{f}(k)| \approx 0$, then $\rho(k) \approx 100$. As seen in Sec. 8.4.1, this means that the ADAS steering command δ_k is heavily penalized and the driver does not receives any aid. On the other hand, as the estimated fault $\bar{f}(k)$

grows larger, $\rho(k)$ will trend towards $\rho(k) \approx 1$. In this situation, the ADAS controller will be given full control authority to aid the driver. However, notice that the full control authority is still constrained by $W_u(\rho = 1)$. Full control authority is given in the frequency range $1Hz$ to $10Hz$, as a result, even in the critical scenario the control command should not feel invasive to the human.

Remark 8.3
The band-pass filter W_F plays a crucial role in the fault estimation algorithm but also the integrated ADAS strategy as a whole. It helps in dividing faults into different frequency ranges. Low frequency faults result from driver preferences that remain constant over time, and cannot be categorized as dangerous. On the other hand, very high frequency faults will be detected due to driver dynamics that are either unknown or not accounted for in the simple HEDM model as well as due to steering angle sensor noises. The use of the filter W_F allows then to focus on a specific range of frequencies. This, in turn, enables us to establish a strong connection between the detected fault magnitude $\bar{f}$ and the criticality of the driving situation.

8.5 Experimental Results

8.5.1 Experimental Setup

In order to carry out the experimental validation of the ADAS design on the SAV platform it was used the same setup used for Data Acquisition explained in Sec. 3.4.1 from Chapter 3. For manual driving on the SAV platform, a joystick is used as the driver input device. This joystick is connected to the Remote PC, see Fig. 2.4 from Chapter 2, which then processes the driver inputs and transmits it to the SAV Car.

On the other hand, the ADAS strategy is fully programmed on the Remote PC. Both the PI Observer from Sec. 8.2 and the LPV ADAS controller from Sec. 8.4 are coded in Python on the ROS2 environment of the Remote PC. Thanks to the ROS2 topics and nodes environment, the observer and controller have access to all states and inputs required. Mainly, the car position and velocities as well as information on the driver inputs. When the lateral ADAS system is active, the steering command sent to the SAV car is the following:

$$\delta(k) = \underset{[-0.7,0.7]}{\text{SAT}} \left(\delta_f(k) + \delta_k(k)\right) \tag{8.22}$$

The steering command applied on the SAV δ is the combination of the human *faulty* steering δ_f and the ADAS controller output δ_k, saturated according to the maximum steering angle of the steering servomotor at $\pm 0.7rad$ ($\approx \pm 40^\circ$).

To test the performance and robustness of the lateral ADAS strategy the experimental validation was done with multiple individuals. Each Test Driver had to do the following tests:

1. The Test Driver carries out two laps around a closed circuit, without ADAS steering assistance.

2. The Test Driver carries out two laps around a closed circuit, with the integrated ADAS system providing steering assistance.

For the sake of brevity, in the following the completed set of captured information is given only for one of the Test Drivers. Firstly, Sec. 8.5.2 gives information from the test without ADAS assistance while Sec. 8.5.3 gives information of the second test where the ADAS strategy is enabled. Finally, Sec. 8.5.4 gives only the trajectory information of both tests from a second driver. This will show that indeed the ADAS strategy is able to adapt to multiple drivers. Results for other test participants are presented in Appendix A.

8.5.2 Test Results Without ADAS

Figure 8.8 provides the information from the longitudinal velocity of the SAV car during the first test. As it can be seen, the speed was kept constant around a comfortable to drive velocity of $0.9m/s$. A constant speed provides a consistent car steering behavior during the test. This eliminates possible distractions for the driver, who can then focus only on the steering action.

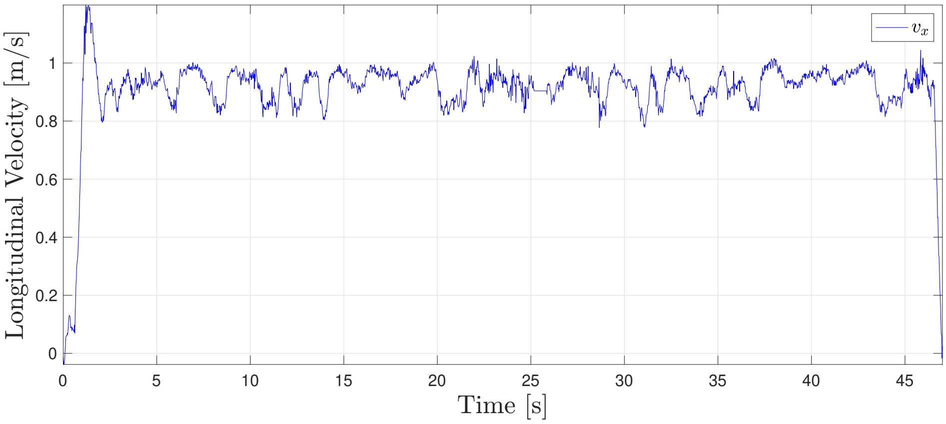

Figure 8.8: Longitudinal Velocity During the Test Without ADAS

In Fig. 8.9 it is then presented information on the SAV trajectory during the first test on X and Y global coordinate frame. On the left of the figure it is represented the reference circuit in black and the trajectory followed by the SAV during the complete test. Note that in order to better identify the multiple laps the SAV has done around the circuit, the followed trajectory is color mapped with the instantaneous longitudinal velocity, corresponding with the information given in Fig. 8.8. On the right side of the figure it is given in black the reference trajectory and with blue triangles the orientation and position of the SAV.

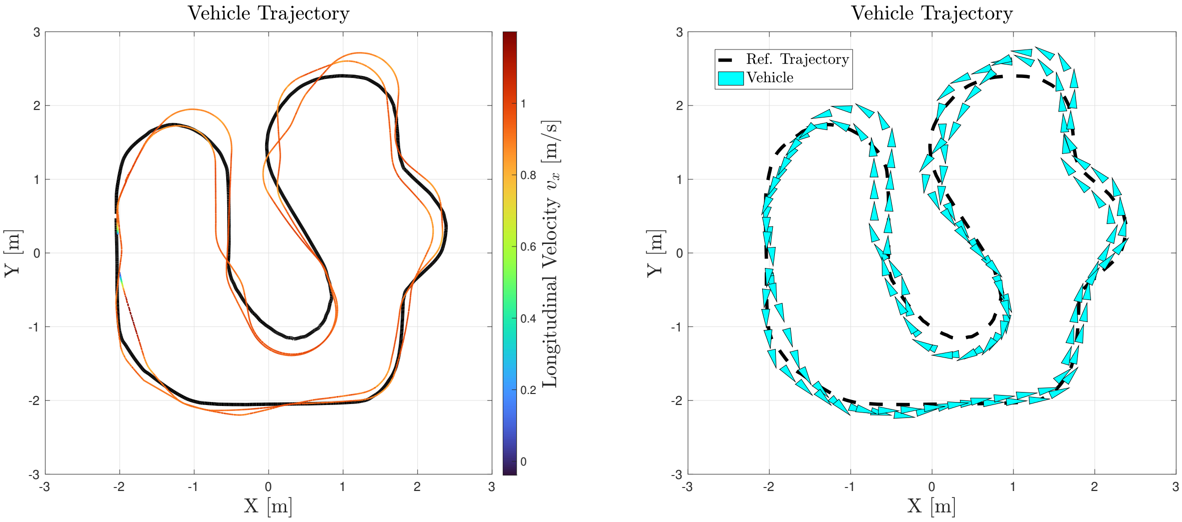

Figure 8.9: Reference trajectory and actual vehicle trajectory color coded with the instantaneous longitudinal velocity (left). Reference trajectory and position and orientation of the SAV during the test. Data from the test without ADAS assistance.

In general, the Test Driver is able to follow the desired circuit path. However, there are certain sections of the circuit where the driver encounters difficulties in closely adhering to the reference path. As mentioned in Chapter 2, specifically as given in Table 2.2, the SAV car exhibits a significant delay in its steering response. This delay makes manual control of the SAV car challenging. Additionally, as discussed in Section 3.4.1, the driving setup for the SAV is not optimal and feels unnatural. Consequently, it is expected that driver errors will occur in areas of the circuit with high curvature. In fact, the design of the circuit trajectory intentionally induces such errors.

8.5.3 Test Results With ADAS

For the sake of clarity this subsection is subdivided into three subsubsections. Sec. 8.5.3.1 provides information regarding the trajectory and speed of the SAV during the test with lateral ADAS assistance enabled. Then Sec. 8.5.3.2 presents data regarding results from the driver fault detection strategy, presented in Sec. 8.2. Finally, Sec. 8.5.3.3 presents data regarding the controller action and the LPV design-related scheduling signal, both presented in Sec. 8.4.

8.5.3.1 Trajectory Data

Figure 8.10 provides the information from the longitudinal velocity of the SAV car during the first test. In order to make a fair comparison, it can be seen that the SAV speed during the test with ADAS enabled is almost identical to that observed during the first test in Fig. 8.8.

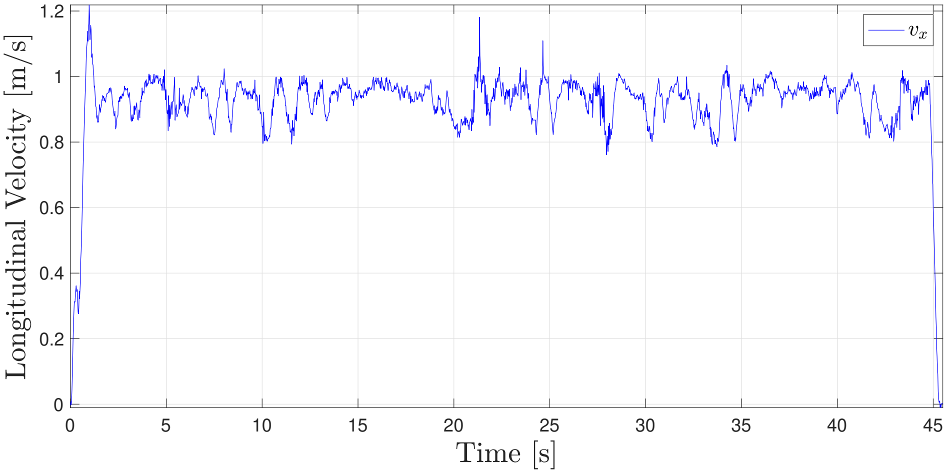

Figure 8.10: Longitudinal velocity during the test with ADAS enabled.

Figure 8.11 provide analogous information to Fig. 8.9. It is evident that in this second test with ADAS enabled, the driver errors have been practically eliminated. The lateral ADAS assistance allows the Test Driver to follow the desired path almost perfectly. As a result, during the two laps of the tests the vehicle trajectories match closely.

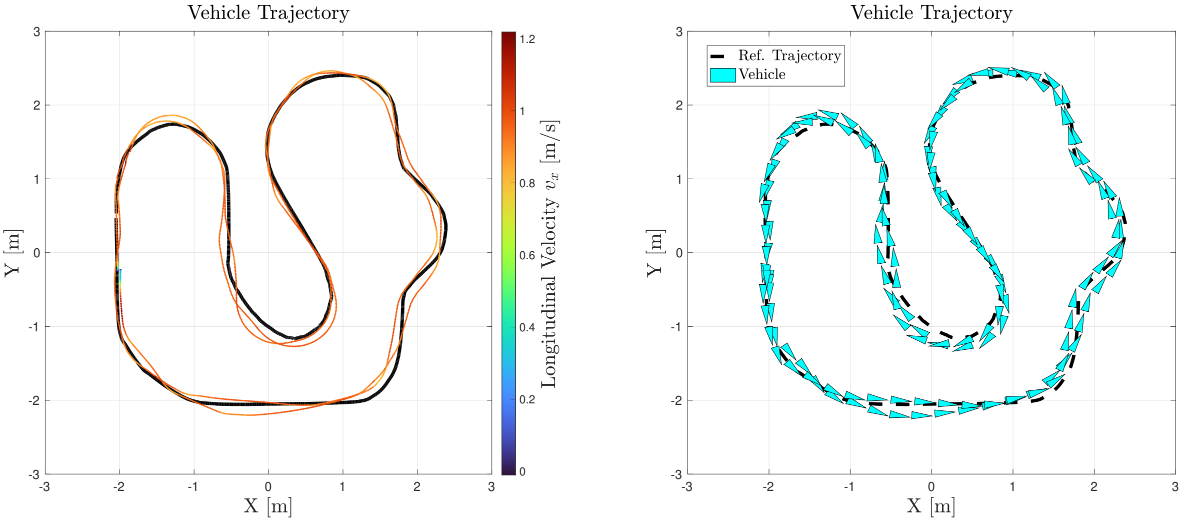

Figure 8.11: Reference trajectory and actual vehicle trajectory color coded with the instantaneous longitudinal velocity (left). Reference trajectory and position and orientation of the SAV during the test. Data from the test with ADAS assistance enabled.

8.5.3.2 Driver Fault Detection Data

Here it is presented information with regards the performance of the driver error fault estimation based on the PI observer introduced in Sec. 8.2. Figure 8.12 presents on top the driver steering input δ_f coming from the joystick signal and the estimated driver steering according $\hat{\delta}_f$ according to the PI Observer. Recall from the PI Observer equation in Eq. (8.6), the estimated steering action $\hat{\delta}_f$ is result of the nominal LEDM steering plus some additive fault.

This additive fault signal $\bar{f}$ was modeled as the output of a narrow bandpass filter W_F, see Fig. 8.2. This estimated fault is presented in the bottom figure of Fig. 8.12. Moreover, Fig. 8.13 also presents the estimated fault signal color mapped onto the trajectory followed by the car. Note that the information in Fig. 8.13 is given considering the absolute value of fault signal. Dark blue colors represent the points in the trajectory where the driver error is zero, meanwhile, in warmer colors indicates the zones where the driver error is large.

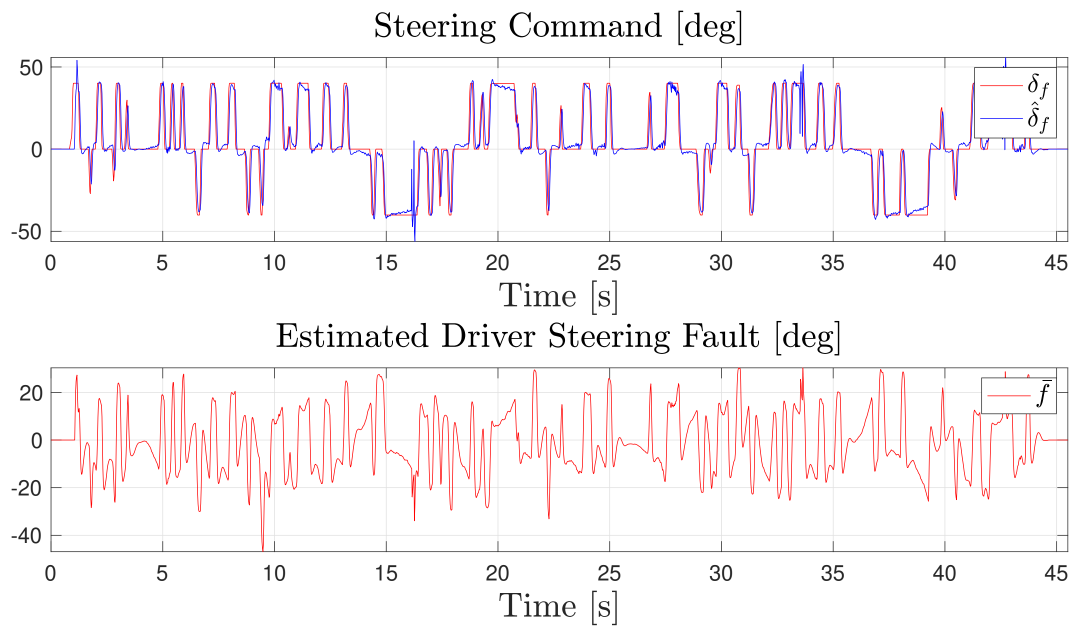

Figure 8.12: On top, Test Driver steering input δ_f (red) and estimated driver steering $\hat{\delta}_f$ (blue). In the bottom figure, estimated driver fault $\bar{f}$.

The use of a joystick as the input device for steering has a noticeable impact on the behavior of the Test Driver steering signal δ_f, as shown in Figure 8.12. The steering signal exhibits a somewhat digital or abrupt nature. Despite this unnatural behavior, the estimation $\hat{\delta}_f$ from the PI Observer closely matches the measured driver steering.

The effect of this unnatural steering response is also evident in the estimated fault $\bar{f}$ depicted in Figure 8.12. The *digital* nature of the driver steering input results in a square-like appearance of the estimated fault signal. This is expected because the sharp steering actions performed by the driver deviate significantly from what is expected based on the nominal LEDM. Consequently, the PI Observer interprets this dynamic deviation as a fault. Therefore, solely relying on Figure 8.12 does not provide a conclusive assessment of the PI Observer performance in detecting driver errors.

However, when mapping the fault signal onto the SAV trajectory, as shown in Figure 8.13, the effectiveness of the driver fault estimation becomes apparent. In sections of the circuit with straight lines, where the trajectory is relatively easy to follow, the estimated driver error is small, represented by dark blue colors. Conversely, before and after sections with pronounced curvature, the magnitude of the estimated driver error is large, indicated by warm colors. Moreover, the zones where significant errors are detected (in warm colors) align with the areas where the Test Driver struggles to closely follow the trajectory during the test without ADAS assistance, as observed previously in Figure 8.9.

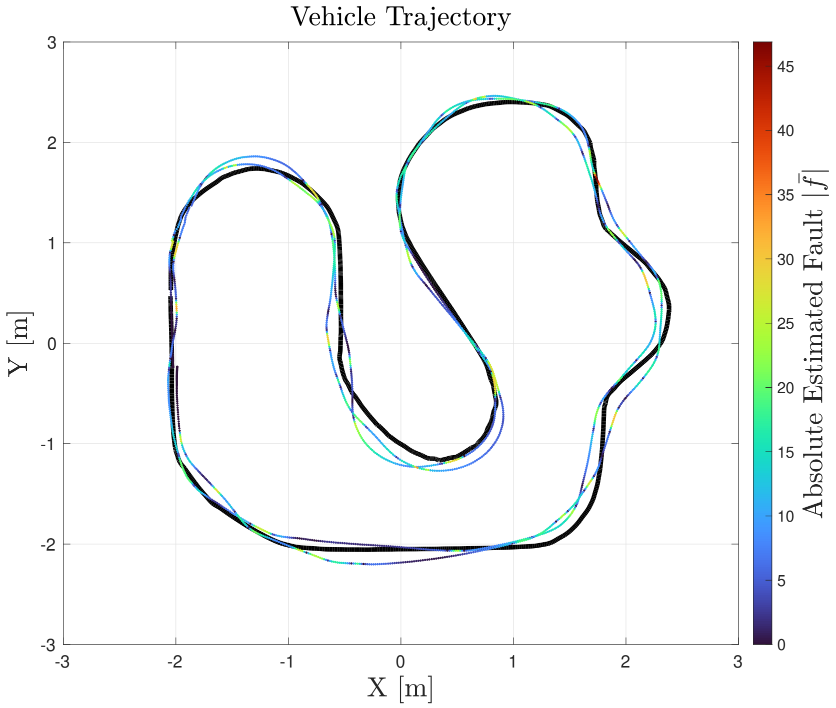

Figure 8.13: Reference trajectory and actual vehicle trajectory color coded with the instantaneous absolute value of the estimated driver fault $|\bar{f}|$. Data from the test with ADAS assistance enabled.

8.5.3.3 Controller Scheduling and Steering Action Data

In the following it is presented information on the behaviour of the controller scheduling with regards the design-related varying parameter ρ and information on the controller output. Figure 8.14 shows the scheduling signal $\rho(k)$ and the lateral ADAS controller command $\delta_k(k)$. Recall that when $\rho \approx 100$ the ADAS steering command is heavily penalized, meanwhile, the closest the scheduling parameter is to $\rho \approx 0$ the higher the ADAS control authority is.

Fig. 8.15 it shows the same information as in Fig. 8.14, projected onto the SAV trajectory. The scheduling parameter $\rho(k)$ is given on the left side and the absolute value of the controller output $|\delta_k(k)|$ is shown on the right side of Fig. 8.15 respectively. Presenting the information projected onto the trajectory allows to understand the controller behaviour related to the different sections of the reference circuit.

Finally, Fig. 8.16 provides a better understanding on the effect of the additive ADAS command on the overall steering of the SAV car. This figure presents in red the steering command δ_f given by the Test Driver through the joystick input. In blue it is then given the actual steering command $\delta(k)$ sent to the SAV servomotor from the Remote PC. Recall that this command is computed according to Eq. 8.22 as $\delta(k) = \delta_f(k) + \delta_k(k)$. As a result, Fig. 8.16 allows to visualize effect of the ADAS controller command on the driver steering. Figure 8.16 presents on top information for the whole test and, for the ease of presentation, on the middle and on the bottom it is given the same information on a reduced time frame from $[5, 10]sec$ and $[30, 40]sec$, respectively.

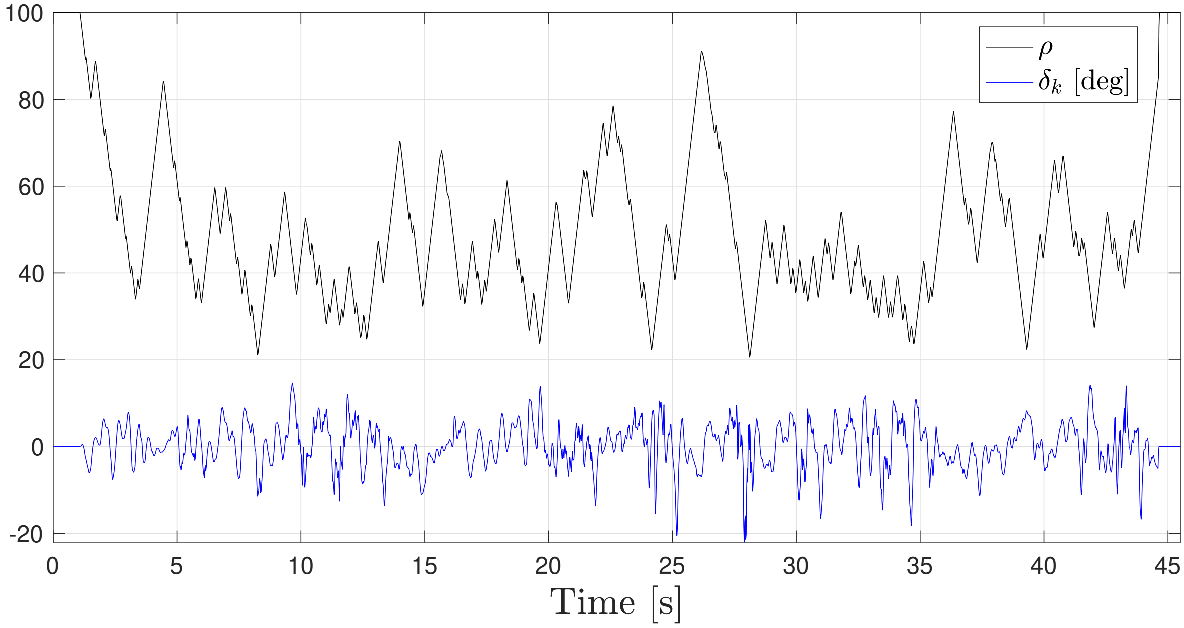

Figure 8.14: Scheduling parameter signal ρ and ADAS controller output δ_k during the test with ADAS assistance enabled.

The scheduling signal evolves constantly during the test as seen in Fig. 8.14, with an average value of $\rho = 57.57$. Recall that according to Eq. (8.21), the value of ρ is directly related to the driver fault estimation from the PI Observer. As it was seen in Sec 8.5.3.2, the unnatural *digital* steering resulting from the joystick driver input is a major origin of this estimated driver fault. Nonetheless, as in Fig. 8.13, when projecting the signal $\rho(k)$ on the SAV trajectory as in Fig. 8.15 (left), then it becomes apparent where the scheduling is used to provide more control authority to the ADAS controller.

Notice in Fig. 8.15 (left) that the warmer colors (higher values of ρ) are in sections where it is relatively easier to drive, mostly on straight lines. However, the sections with high curvature present dark blue colors (lower values of ρ). As a result, in Fig. 8.15 (left) clearly shows that the ADAS steering is primarily used in these critical sections of the circuit. For the most part, the color map of the steering command is in colder dark colors (lower values of δ_k). This is in line with the desired objectives for the integrated ADAS strategy: acting in critical situations and not affecting the driving experience for the most part.

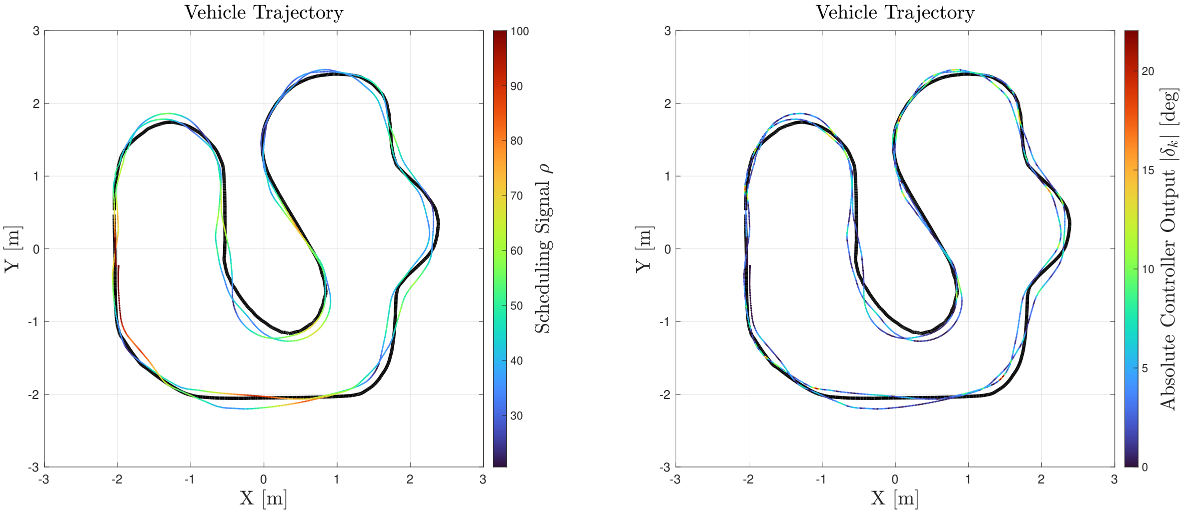

Figure 8.15: Reference trajectory and actual vehicle trajectory color coded with the scheduling parameter signal ρ (left). Reference trajectory and actual vehicle trajectory color coded with the absolute value of the ADAS controller output $|\bar{\delta}_k|$ (right). Data from the test with ADAS assistance enabled.

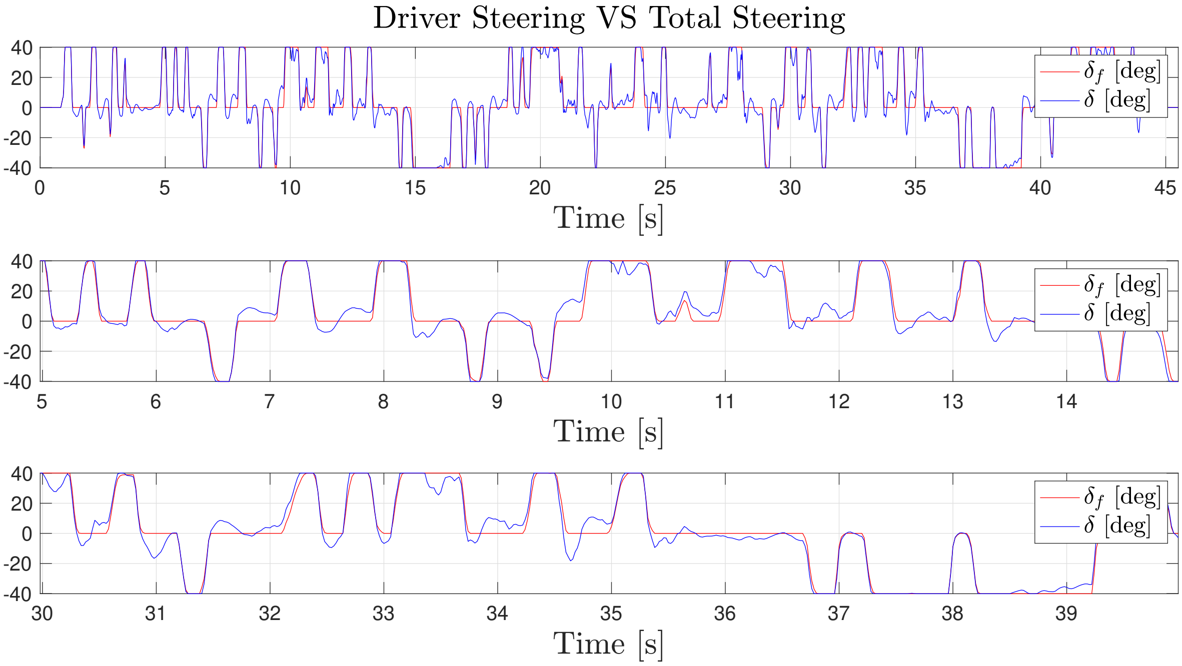

Figure 8.16: Longitudinal Velocity During the Test Without ADAS

From the information shown in Fig. 8.16, it can be seen that indeed the influence of the of the ADAS controller on the driver preference is reduced. The total steering signal $\delta(k)$ that is actually being executed matches for the most part the driver steering command δ_f. Defining driver-ADAS conflict as steering commands, δ_f for the driver and δ_k for the ADAS system respectively, in opposites directions [Oud+22]; it cannot be observed during the test high conflict between the Test Driver and the ADAS control. Instead, the ADAS steering provides anticipatory steering actions or fast corrections. From the comparison of Fig. 8.9 with Fig. 8.11, these small corrections add up to a safer and smoother trajectory.

8.5.4 Results for a Different Test Driver

In order to demonstrate that the proposed integrated ADAS strategy adapts to multiple drivers, here it is provided information on obtained results for a different Test Driver. The information provided here is complemented with the results of other four different Test Drivers in Appendix A.

For the sake of brevity, not all details from the analysis of the obtained results are repeated here. For the tests without the use of the ADAS systems the information given is the following:

- Figure 8.17 provides analogous information to Fig. 8.9, that is, the SAV trajectory color coded with the instantaneous SAV longitudinal speed (left side) and the SAV position and orientation at discrete time instances during the whole test (right side).

For the second test, when the Test Driver is being aided by the ADAS the information given here is the following:

- Fig. 8.18 is analogous to that of Fig. 8.17, the SAV trajectory color coded with the instantaneous SAV longitudinal speed (left side) and the SAV position and orientation during the whole test (right side).

- Fig. 8.19 provides information on the design-related varying parameter ρ (left side) and the absolute ADAS control signal (right side), color coded for both signals into the actual SAV trajectory during the test with ADAS assistance enabled.

This last figure is of particular interest as it shows the sections of the circuit where important driver errors are being detected, thanks to the relation given in Eq. (8.21) between estimated driver faults and scheduling parameter value. Moreover, it shows the areas of the circuit where the additive ADAS steering is more active and areas where it is barely used.

The findings for this second Test Drivers yield consistent conclusions. The Test Driver is generally able to follow the intended trajectory reasonably well by its own during the test without assistance. However, in certain sections, his tracking of the reference path is not optimal. On the other hand, the trajectory the Test Driver follows when counting with the lateral ADAS is instead close to the reference path throughout the whole test. Notably, for the test conducted with ADAS assistance enabled, the trajectory followed during both laps of the test closely correspond to each other. Figure 8.19 illustrates that even with a different Test Driver, the ADAS strategy effectively manages to identify critical sections and provides focused assistance in those areas.

Remark 8.4
It is important to emphasize that the only difference between the results from different Test Drivers is the individual person driving the SAV car. Neither the PI Observer, the LPV ADAS controller nor the scheduling rule for ρ *is tuned specifically for any individual person.*

8.5.4.1 Results Without ADAS Assistance

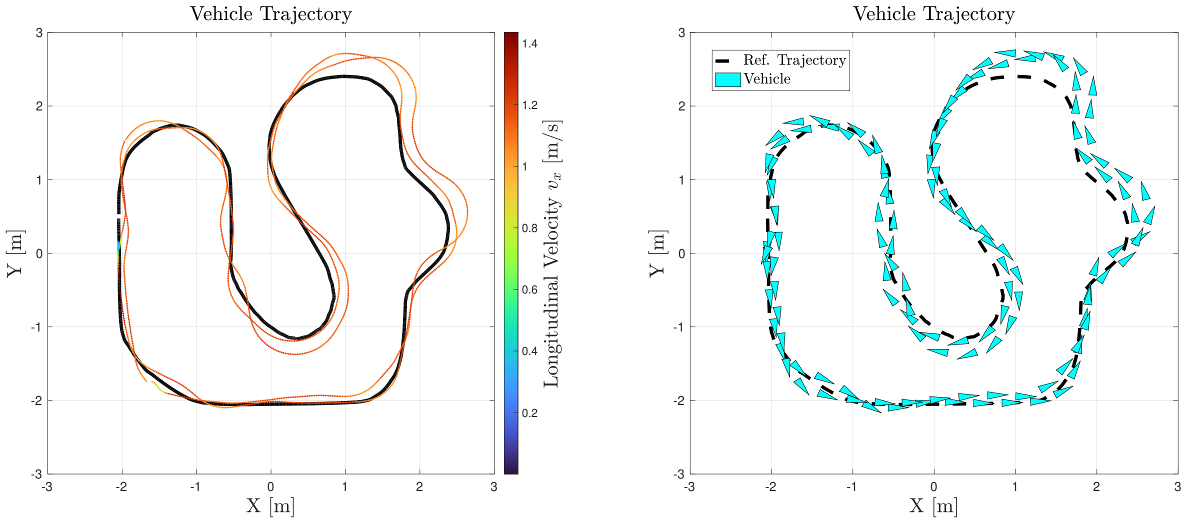

Figure 8.17: Reference trajectory and actual vehicle trajectory color coded with the instantaneous longitudinal velocity (left). Reference trajectory and position and orientation of the SAV during the test. Data from the test without ADAS assistance for a second Test Driver.

8.5.4.2 Results With ADAS Assistance

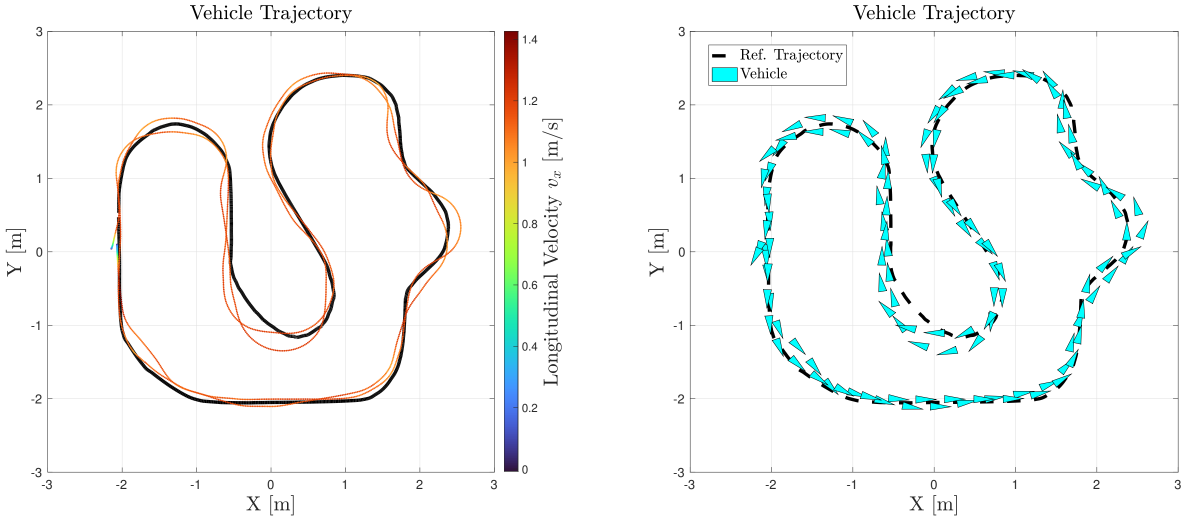

Figure 8.18: Reference trajectory and actual vehicle trajectory color coded with the instantaneous longitudinal velocity (left). Reference trajectory and position and orientation of the SAV during the test. Data from the test with ADAS assistance enabled for a second Test Driver.

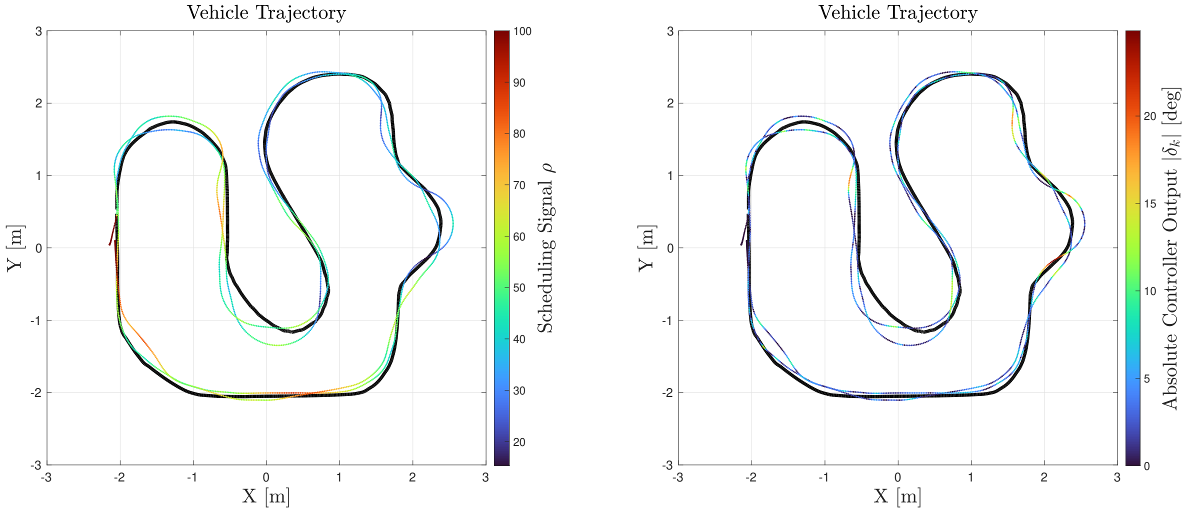

Figure 8.19: Reference trajectory and actual vehicle trajectory color coded with scheduling parameter signal ρ (left). Reference trajectory and actual vehicle trajectory color coded with the absolute value of the ADAS controller output $|\bar{\delta}_k|$ (right). Data from the test with ADAS assistance enabled for a second Test Driver.

8.6 Conclusion

In this chapter, the proposed integrated ADAS strategy was experimentally validated with multiple drivers, and the results obtained were highly satisfactory. It was observed that the ADAS assistance significantly helped the drivers in maintaining a smoother and safer trajectory without deviating from the intended path. Importantly, the ADAS control command provided only minor corrections, and there was no evidence of conflict with the drivers' steering actions. The implementation of the PI observer driver error estimation scheme demonstrated its capability in identifying the sections where the Test Drivers faced the most challenges. Consequently, the ADAS actions were primarily focused on these specific sections.

However, it is important to acknowledge the limitations of the experimental setup and the significant differences between the driving experience in the current SAV platform setup and that of a full-scale vehicle. Despite these limitations, the highly satisfactory results obtained provide confidence and support for future experimental scenarios involving the proposed ADAS strategy presented in this chapter.

Conclusions and Perspectives

Conclusions

This thesis is concerned with the study of LPV approaches for the control of automated driving, with special focus on LPV techniques that allow to adapt the performance of the control system when the system changes. This could be due to the presence of driver errors or actuator malfunctions, which may deteriorate the stability of the system if not considered. During this study it has also been developed a new framework for Grid-Based Discrete-Time LPV control. The main conclusions of the thesis are the following:

- We have presented an approach referred to as grid and local variation bound framework to reduce the infinitely constrained LMI conditions for the stability and computation of the induced L_2-norm of DT-LPV systems into finite LMI problems using a Grid Based DT-LPV approach. This framework has proved to be effective and led to two novel controller synthesis approaches: the Parameter-Dependent State Feedback (PDSF) control and Gain-Scheduled Grid-Based DT-LPV SF control.
- The PDSF and the Gain-Scheduled Grid-Based DT-LPV SF controller synthesis approaches have been experimentally validated in path tracking applications on the SAV platform. The PDSF approach showed how it greatly simplifies the implementation aspect of LPV controllers. Despite considering more than 150 grid-points on the LPV design, the PDSF controller implementation only required four constant matrix gains in the Python code and no interpolation. On the other hand, the Gain-Scheduled Grid-Based control approach proved successful even if the control design included a design-related varying parameter, used to emulate an Anti-Windup mechanism.
- The implementation of the autonomous steering using the Gain-Scheduled Grid-Based controller with LPV Anti-Windup emulation successfully improved the path tracking performance of the SAV car. This highlights the effectiveness of incorporating design-related parameters in LPV control designs to achieve complex objectives beyond stability and performance requirements. The specific case of the LPV Anti-Windup emulation demonstrated in Chapter 5 effectively prevented integrator Windup in the presence of actuator saturation.
- The design philosophy of utilizing design-related parameters to activate/deactivate a controller output was applied to the design of LPV/$\mathcal{H}_\infty$ lateral ADAS controllers. The primary objective of the proposed ADAS controller strategy is to assist the driver during critical situations while minimizing intrusiveness when not needed. This is achieved through two design features. Firstly, control action constraints are enforced using band-pass filters, focusing the control actions within a frequency range that feels transparent to the human driver. Secondly, the scheduling of the design-related parameters ensures that the ADAS control output remains inactive unless a significant driver error is detected.

- The detection of driver-errors was made possible by posing it as a fault detection problem. This is achieved by comparing the actions of a virtual nominal driver model with those from the human driver. Doing this with the aid of $\mathcal{H}_\infty$ PI Observers allowed to detect the driver errors within a specif frequency range. Focusing on a narrow specific frequency range, slightly lower than $1Hz$, allows to discard measurements noises, unmodeled dynamics on the simple nominal driver model and human driver preferences as sources of driver error estimation. The goal of the driver error detection algorithm is to estimate driving errors correlated with critical situations where the ADAS controller should assist the driver.

- The proposed integrated ADAS strategy was experimentally validated with multiple drivers, yielding highly satisfactory results. It was observed that the ADAS assistance significantly helped the drivers in maintaining a smoother and safer trajectory without deviating from the intended path.

  When the ADAS strategy was activated, driver errors were successfully detected in challenging zones where the Test Drivers faced difficulties. This correlation between the estimation algorithm and critical situations validates its effectiveness. Moreover, by having the ADAS controller scheduled by the driver error estimation, in the sections of the circuit where the Test Drivers felt confident they did not had interference. These outcomes affirm that the ADAS design objectives of minimizing intrusiveness while enhancing safety have been achieved.

Future Perspectives

This thesis has provided some contributions which could open interesting lines of works for future studies:

- **Discrete-Time synthesis LMI conditions**: It will be useful to extend the LMI conditions presented in this thesis for Parameter-Dependent structures and Grid-Based gain-scheduled LPV controllers beyond State-Feedback synthesis. Some preliminary work has been done with regard Static Output Feedback controller synthesis, however, the Dynamic Output Feedback control synthesis on the Grid-Based Discrete-Time framework remains an open challenge.

- **Optimal scheduling of design-related varying parameters**: The use of MPC based methods for scheduling online design-related varying parameters is a promising approach. The preliminaries results developed during the thesis could be extended by integrating the planning stage with this optimal scheduling problem as a joint optimal problem. This opens up the possibility of increasing the interconnection between planning and control stages, which may lead to better performances.

- **Handover/Takeover robust control with M^3D theory**: Study of stability and robustness properties of the handover/takeover transitions in automated system is well suited for the M^3D control approach. If taken as base designs the lateral autonomous and ADAS lateral controllers proposed in this thesis, this will imply the need of extending the results from M^3D control to LPV theory.

- **Further ADAS experimental validation**: The experimental validation carried out in the SAV platform of the integrated ADAS strategy showed great potential. However, it should be acknowledge the limitation of the SAV platform for the ADAS application. Future ADAS experimental validation of the proposed strategy could be done by improving the platform, e.g. by installing a front camera to give the Test Driver a *first-person* view and using a steering wheel as the driver input device. Furthermore, the strategy could be tested in dedicated ADAS simulators or even in full-scale vehicles.

Appendix A

ADAS SAV Experimental Results

This appendix complements the experimental results from Chapter 8 for the experimental validation of the integrated lateral ADAS strategy with additional experiments carried out with four Test Drivers. The objective is here to demonstrate the capabilities of the integrated ADAS strategy to adapt to multiple drivers. Note that the strategy was validated with the help of six different Test Drivers in total.

Not all details from the analysis of the results are repeated here. For each Test Driver it is given results with and without the ADAS assistance. For the tests without the use of the ADAS systems the information given is the following:

- Fig. A.1, Fig. A.4, Fig. A.7 and Fig. A.10 provide the SAV trajectory color coded with the instantaneous SAV longitudinal speed (left side) and the SAV position and orientation at instantaneous time frames during the whole test (right side).

For the test when the Test Driver is being aided by the ADAS the information given here is the following:

- Fig. A.2, Fig. A.5, Fig. A.8 and Fig. A.11 provide analogous information the SAV trajectory color with the car speed (left side) and SAV car position and orientation during the test (right side).
- Fig. A.3, Fig. A.6, Fig. A.9 and Fig. A.12 present the design-related varying parameter ρ (left side) and the absolute ADAS control signal (right side), color coded for both signals into the actual SAV trajectory during the test with ADAS assistance enabled.

  This last figure is of particular interest as it shows the sections of the circuit where important driver errors are being detected, thanks to the relation given in Eq. (8.21) between estimated driver faults and scheduling parameter value. Recall that large driver errors are mapped to small values of the varying parameter such that $\rho \approx 1$. On the other hand, negligible driver errors are mapped as $\rho \approx 100$. Moreover, this last figure shows the areas of the circuit where the additive ADAS steering is more active and areas where it is barely used.

The conclusions of the results here presented are in line with those already given in Chapter 8. Without the ADAS enabled, the Test Drivers do a good job of following the reference circuit. However, there are some clear zones where the drivers seem to struggle and their trajectory deviates away from the reference. Moreover, most drivers present a high degree of trajectory variation between laps.

On the other hand, when the ADAS strategy proposed in Chapter 8 is enabled, the presence of driver errors observable in the SAV trajectories vanishes. Most remarkable, the variation between laps almost disappears for all the Test Drivers. This can be specially confirmed with the results of the Additional Test Driver 4 in Fig. A.11, the driver actually does more than two laps, yet, through all the ADAS enabled test the laps seem to overlap with each other. Moreover, the results from Fig. A.3, Fig. A.6, Fig. A.9 and Fig. A.12 , left side, show that the driver error detection scheme recognizes effectively the zones where the Test Drivers commit mistakes, zones in dark tones of blues. As a result, the zones and degree of ADAS steering command in Fig. A.3, Fig. A.6, Fig. A.9 and Fig. A.12 , right side, focuses for the most part in sections of the circuit where the Test Driver struggles.

A.1 Additional Test Driver 1

A.1.1 Results Without ADAS Assistance

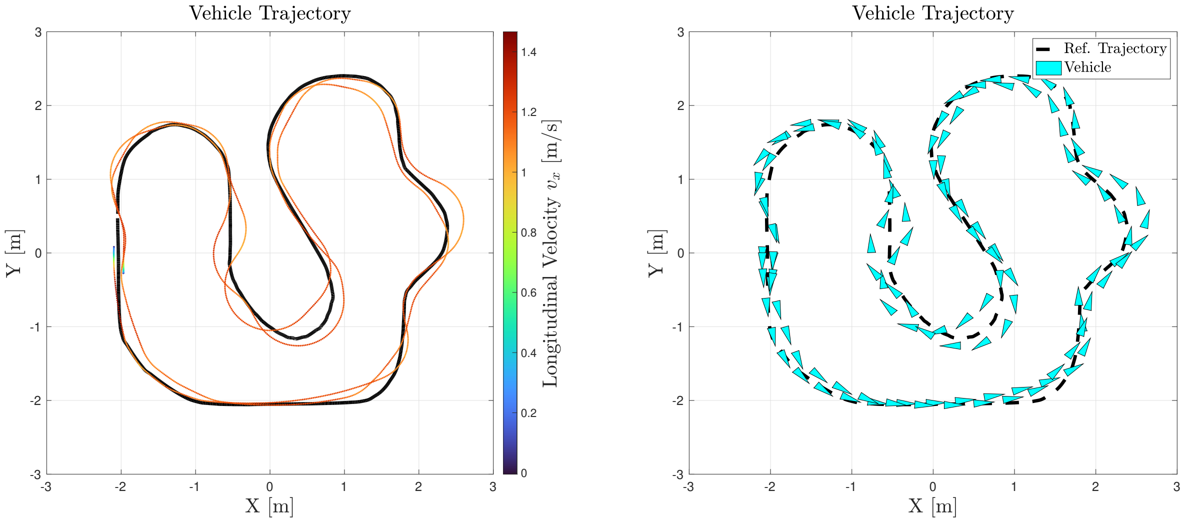

Figure A.1: Reference trajectory and actual vehicle trajectory color coded with the instantaneous longitudinal velocity (left). Reference trajectory and position and orientation of the SAV during the test. Data from the test without ADAS assistance for the Additional Test Driver 1.

A.1.2 Results With ADAS Assistance

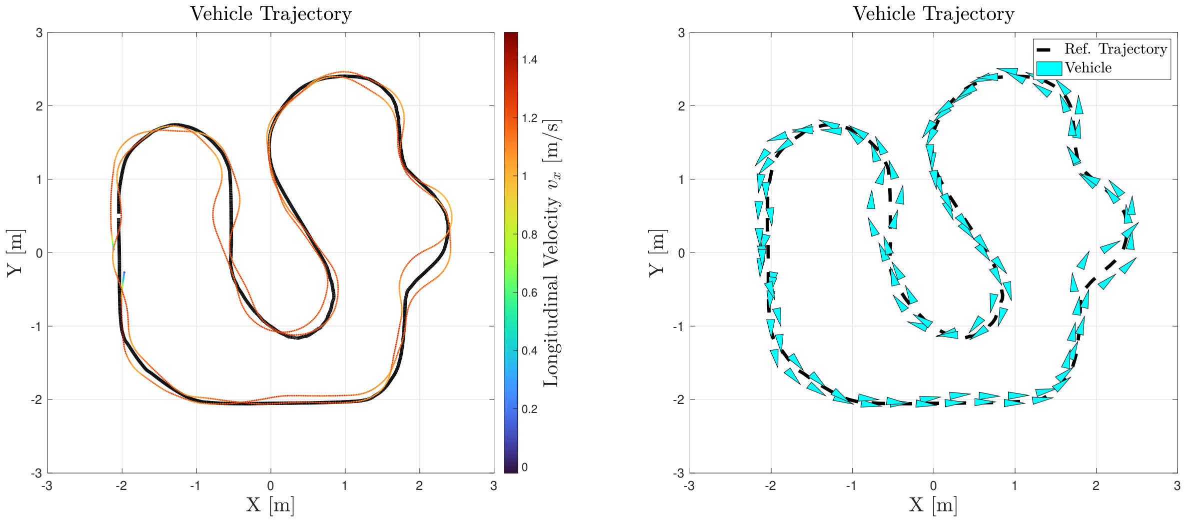

Figure A.2: Reference trajectory and actual vehicle trajectory color coded with the instantaneous longitudinal velocity (left). Reference trajectory and position and orientation of the SAV during the test. Data from the test with ADAS assistance enabled for the Additional Test Driver 1.

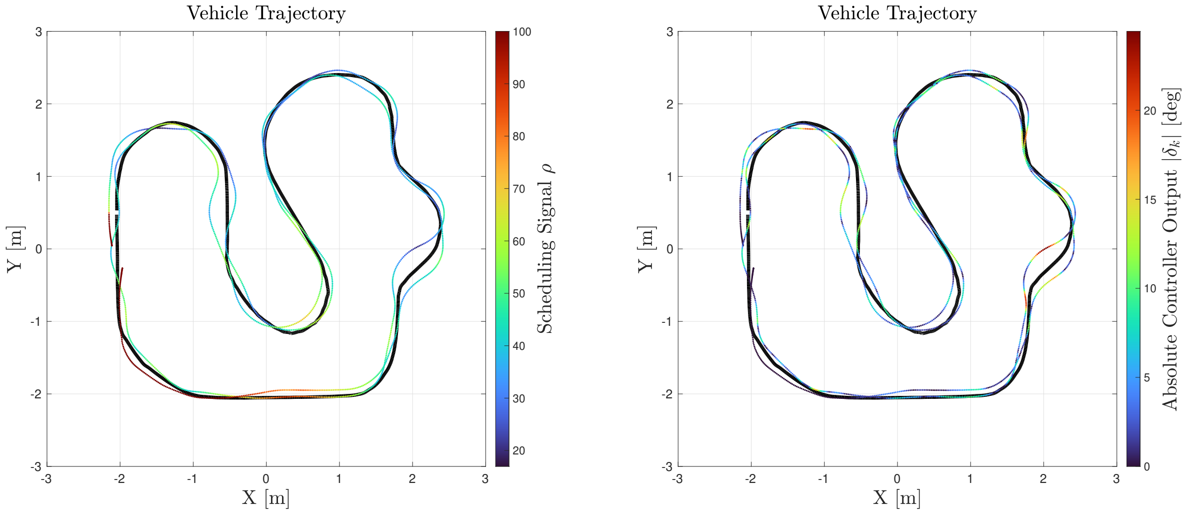

Figure A.3: Reference trajectory and actual vehicle trajectory color coded with scheduling parameter signal ρ (left). Reference trajectory and actual vehicle trajectory color coded with the absolute value of the ADAS controller output $|\bar{\delta}_k|$ (right). Data from the test with ADAS assistance enabled for the Additional Test Driver 1.

A.2 Additional Test Driver 2

A.2.1 Results Without ADAS Assistance

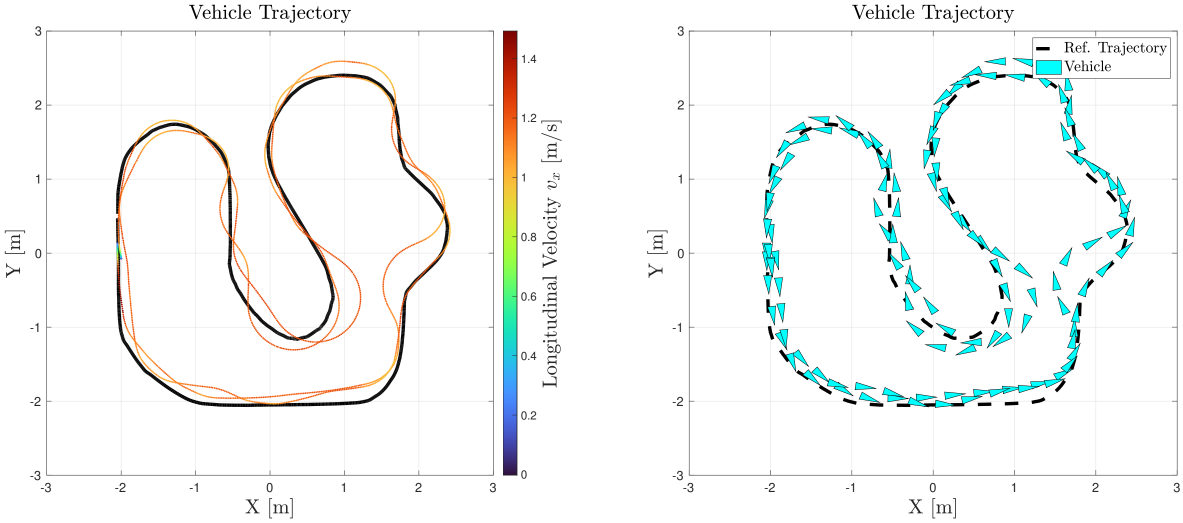

Figure A.4: Reference trajectory and actual vehicle trajectory color coded with the instantaneous longitudinal velocity (left). Reference trajectory and position and orientation of the SAV during the test. Data from the test without ADAS assistance for the Additional Test Driver 2.

A.2.2 Results With ADAS Assistance

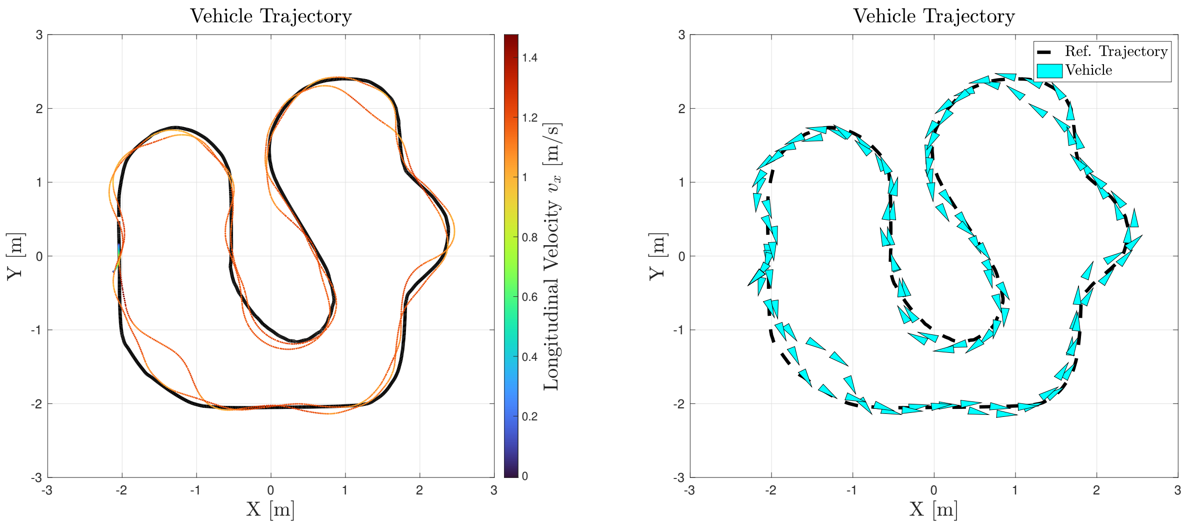

Figure A.5: Reference trajectory and actual vehicle trajectory color coded with the instantaneous longitudinal velocity (left). Reference trajectory and position and orientation of the SAV during the test. Data from the test with ADAS assistance enabled for the Additional Test Driver 2.

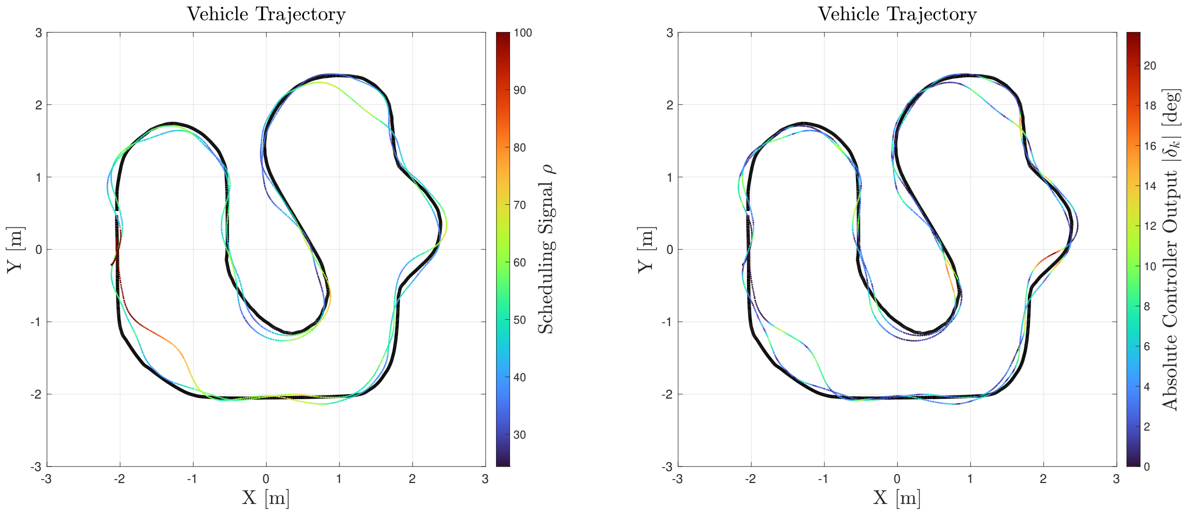

Figure A.6: Reference trajectory and actual vehicle trajectory color coded with scheduling parameter signal ρ (left). Reference trajectory and actual vehicle trajectory color coded with the absolute value of the ADAS controller output $|\bar{\delta}_k|$ (right). Data from the test with ADAS assistance enabled for the Additional Test Driver 2.

A.3 Additional Test Driver 3

A.3.1 Results Without ADAS Assistance

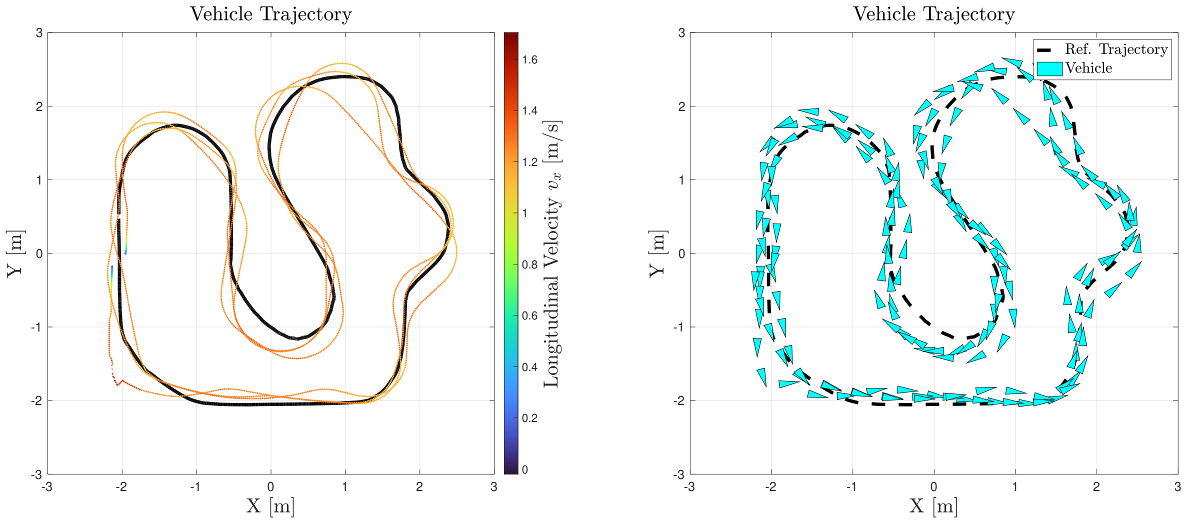

Figure A.7: Reference trajectory and actual vehicle trajectory color coded with the instantaneous longitudinal velocity (left). Reference trajectory and position and orientation of the SAV during the test. Data from the test without ADAS assistance for the Additional Test Driver 3.

A.3.2 Results With ADAS Assistance

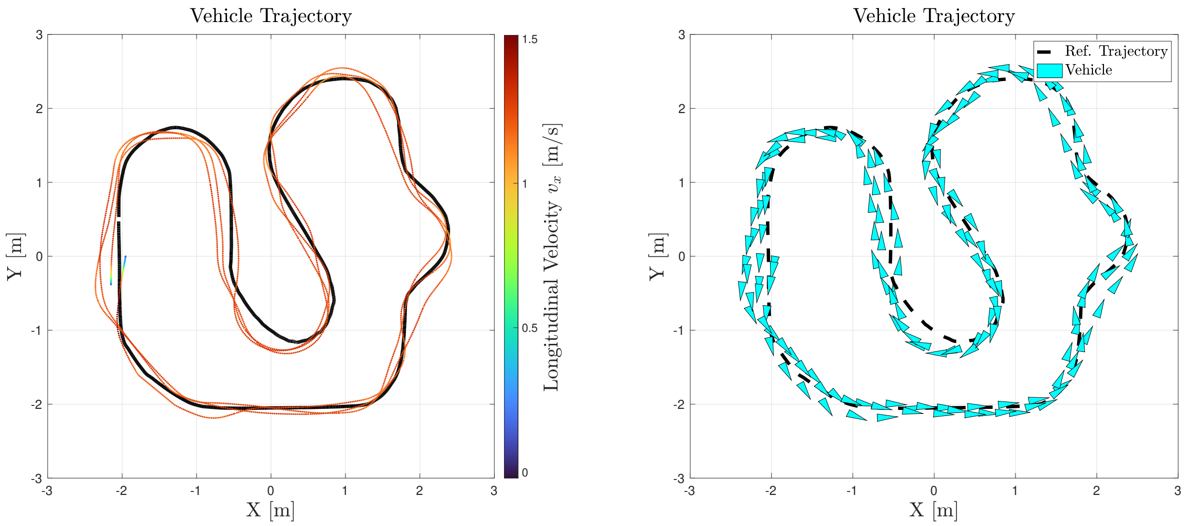

Figure A.8: Reference trajectory and actual vehicle trajectory color coded with the instantaneous longitudinal velocity (left). Reference trajectory and position and orientation of the SAV during the test. Data from the test with ADAS assistance enabled for the Additional Test Driver 3.

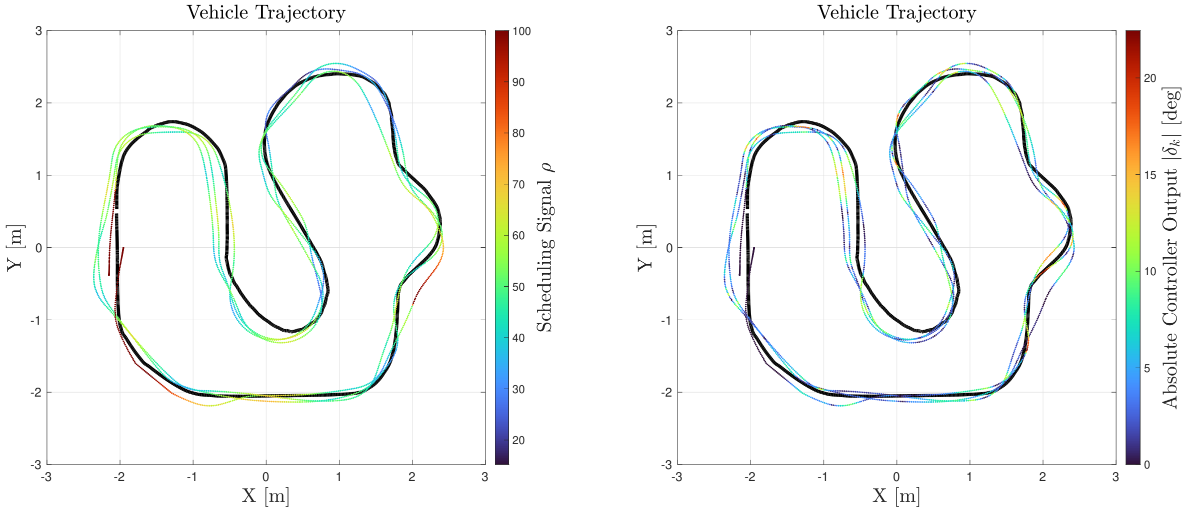

Figure A.9: Reference trajectory and actual vehicle trajectory color coded with scheduling parameter signal ρ (left). Reference trajectory and actual vehicle trajectory color coded with the absolute value of the ADAS controller output $|\bar{\delta}_k|$ (right). Data from the test with ADAS assistance enabled for the Additional Test Driver 3.

A.4 Additional Test Driver 4

A.4.1 Results Without ADAS Assistance

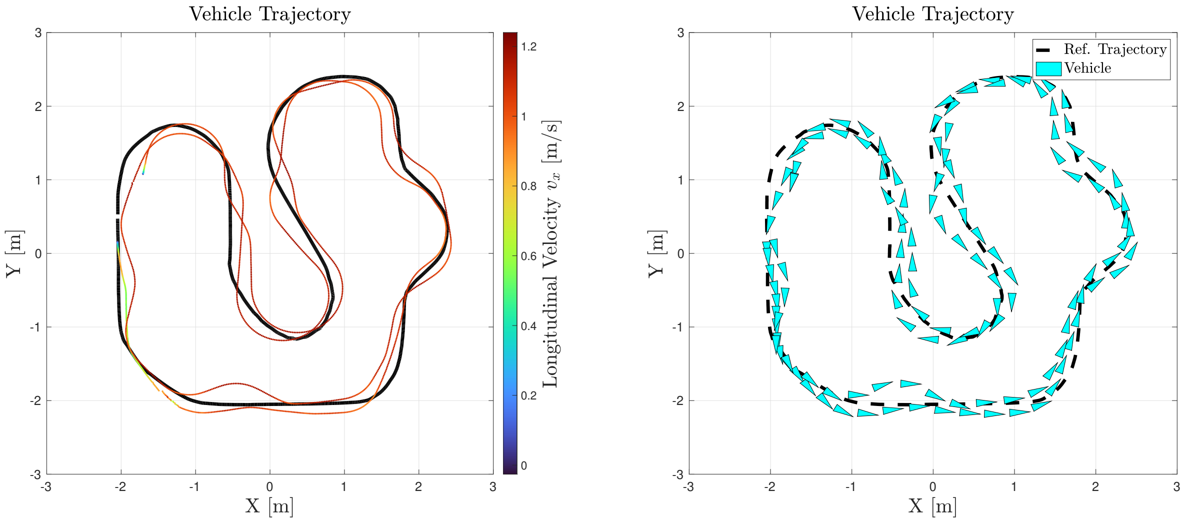

Figure A.10: Reference trajectory and actual vehicle trajectory color coded with the instantaneous longitudinal velocity (left). Reference trajectory and position and orientation of the SAV during the test. Data from the test without ADAS assistance for the Additional Test Driver 4.

A.4.2 Results With ADAS Assistance

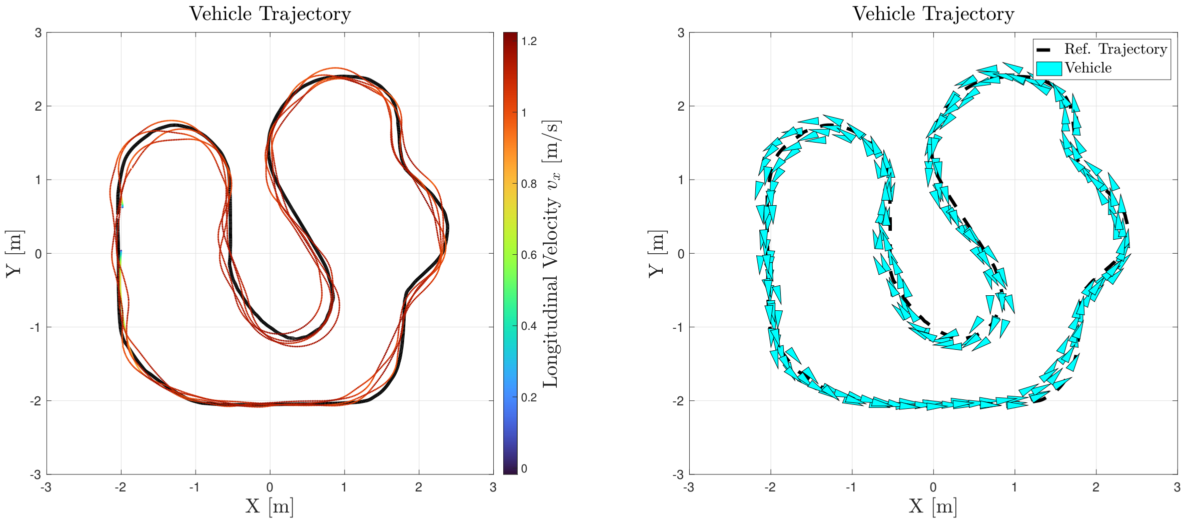

Figure A.11: Reference trajectory and actual vehicle trajectory color coded with the instantaneous longitudinal velocity (left). Reference trajectory and position and orientation of the SAV during the test. Data from the test with ADAS assistance enabled for the Additional Test Driver 4.

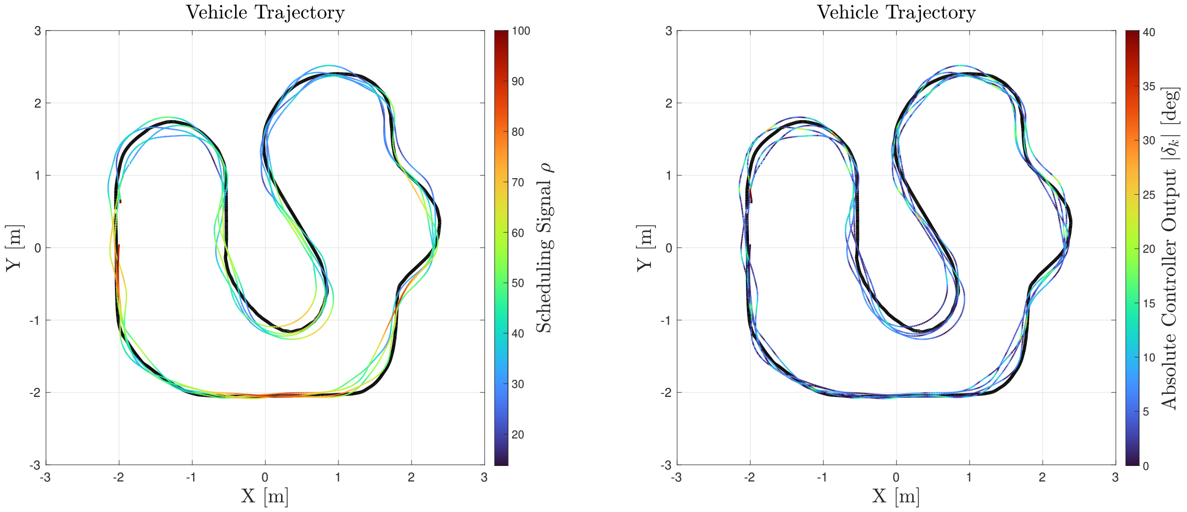

Figure A.12: Reference trajectory and actual vehicle trajectory color coded with scheduling parameter signal ρ (left). Reference trajectory and actual vehicle trajectory color coded with the absolute value of the ADAS controller output $|\bar{\delta}_k|$ (right). Data from the test with ADAS assistance enabled for the Additional Test Driver 4.

Appendix B

LMI Conditions for Stability and State-Feedback $\mathcal{H}_\infty$ Control of Discrete-Time Multi-Mode Multi-Dimensional Systems

---

This appendix presents a pre-print version of the following publication:

- Ariel M. Borrell, Olivier Sename, Vicenç Puig. “LMI Conditions for Stability and State-Feedback $\mathcal{H}_\infty$ Control of Discrete-Time Multi-Mode Multi-Dimensional Systems”. In: IEEE Control Systems Letters, vol. 6, pp. 2876-2881, 2022, doi: 10.1109/LCSYS.2022.3179941.

LMI Conditions for Stability and $\mathcal{H}_\infty$ Control of Discrete-Time Multi-Mode Multi-Dimensional Systems*

Ariel Medero[1,2], Vicenç Puig[1] and Olivier Sename[2]

***Abstract*— This paper deals with the Stability and Feedback Control of discrete-time Multi-Mode Multi-Dimensional (M^3D) LTI systems. The M^3D switch dynamics are modeled with the introduction of a state mapping, which describes the embedding or truncation of states during mode transitions. This model description of the M^3D systems and Lyapunov poly-quadratic energy storage functions are used to obtain Linear Matrix Inequalities conditions for stability check and for synthesis of state-feedback controllers under $\mathcal{H}_\infty$ performance. A numerical example is given to illustrate the benefits of the proposed method. The example consists in the feedback control of a discrete-time M^3D LTI system which can arbitrarily switch in between an open-loop stable and two open-loop unstable modes, with modes having different state dimensions.**

I. INTRODUCTION

Most works dealing with switching systems consider multi-mode systems for which all modes share the same number of states and model structure. The study in [1] by Erik I. Verriest was an innovative work that presents for the first time tools allowing the description of Multi-Mode Multi-Dimensional switching system, categorized there as M^3D systems. Since then, the generalization of switching systems to the multi-dimensional mode case have gained in popularity thanks to the problems this framework allows to tackle. In [2], the authors provide a framework for the optimal control of M^3D switching systems. As a motivating example, they derived a model of an ice-skater with four distinct modes for which the optimal control algorithm provides the optimal switching instant and the forces to be applied. An interesting application of M^3D systems was presented in [3], where it is modeled a spacecraft group formation as a state-varying switched system in which new spacecrafts can join or leave the formation. Moreover, the authors provided results to analyze the stability and fault tolerance of the formation. In [4], conditions are given for checking the stability of Multi-Dimensional switching systems with additional state jump, based on parametric Lyapunov functions, given an application to the problem of consensus in open multi-agent systems. Meanwhile, in [5], the LQ control approach is studied for multi-agent dynamic systems with increasing state dimensions, and is applied to a tracking problem in leader-following dynamics.

As emphasized, the application space of M^3D systems covers many different fields and opens up the possibility of tackling new problems with a straightforward framework. However, to the best of the Authors knowledge no work has presented yet tools for the general stabilization and feedback control of M^3D systems. This work concerns the domain of linear systems, for which many problems in control theory can be formulated using Linear Matrix Inequalities (LMI) [6]. The main contributions of this work are therefore the introduction of LMI conditions, in the context of discrete-time M^3D LTI systems, for:

- Asymptotic Stability proof,
- Computation of the $\mathcal{H}_\infty$ norm,
- Synthesis of state-feedback controllers

The paper is organized as follows: Section II presents the dynamical equations of discrete-time M^3D LTI systems. In Section III, the stability of discrete-time M^3D systems is studied. Meanwhile, in Section IV, conditions for computing the $\mathcal{H}_\infty$ norm of discrete-time M^3D systems are given, which in Section V are extended to the synthesis of state-feedback control for discrete-time M^3D systems. A numerical example is used in Section VI to explore the benefits of the proposed method. Finally, some conclusions about the present study and possible applications are discussed in Section VII.

The paper notation is the following. $\|\cdot\|_2$ represents the Euclidean norm and $\|\cdot\|_\infty$ represents the $\mathcal{H}_\infty$ norm. x^T represents the transpose of x, x^{-1} represents the inverse of x and x^+ is the left pseudo-inverse of x. Matrix $X > 0$ represents that X is positive-defined and $*$ in an LMI represents a symmetric element transposed. $x^{(i)}$ represents that x belongs to the mode i of the M^3D system, x_{ij} represents that x is an element involved in the transition from mode i to mode j.

II. M^3D SYSTEM DYNAMICS

This work is concerned with the study of discrete-time LTI systems under Multi-Mode Multi-Dimensional (M^3D) switching conditions. In the absence of M^3D switching, the dynamics of the active mode i (given m modes) are given as:

$$M^{(i)} = \begin{cases} x_{k+1}^{(i)} = \mathcal{A}^{(i)} x_k^{(i)} + \mathcal{B}^{(i)} w_k \\ z_k = \mathcal{C}^{(i)} x_k^{(i)} + \mathcal{D}^{(i)} w_k \end{cases} \tag{1}$$

---

*This work has been supported by the French National Research Agency (CNRS, “Investissements d’Avenir”, ANR-15-IDEX-02). It has also been partially funded by the Spanish State Research Agency (AEI) and the European Regional Development Fund (ERFD) through the project SCAV (ref. MINECO DPI2017-88403-R) and by FPI UPC grant 2020FPI-UPC-008.

[1] Institut de Robòtica i Informàtica Industrial (CSIC-UPC), C/. Llorens i Artigas 4-6, 08028 Barcelona, Spain (`ariel.medero@upc.edu`, `vicenc.puig@upc.edu`).

[2] Univ. Grenoble Alpes, CNRS, Grenoble INP, GIPSA-Lab, 38000 Grenoble, France (`ariel.medero@grenoble-inp.fr`, `olivier.sename@grenoble-inp.fr`).

where $x_k^{(i)} \in \mathbb{R}^{n_i}$ is the state vector, $w_k \in \mathbb{R}^{n_w}$ is the vector of exogenous inputs and $z_k \in \mathbb{R}^{n_z}$ is the vector of control performances. All along this paper, it is assumed that the switching signal is available in real-time, therefore, the active mode i is always know.

To account for the M^3D switching, we consider the framework introduced in [1], based on the notion of energy limited transitions. Such representations are of high interest when the structure and size of the system model can change accordingly to operating conditions. Let assume two modes with states $x^{(i)} \in \mathbb{R}^{n_i}$ and $x^{(j)} \in \mathbb{R}^{n_j}$ respectively. By introducing the state mapping T_{ij} at the transition from mode i to j we set:

$$x_{k+1}^{(i)} = T_{ij} x_k^{(j)}, \quad T_{ij} \in \mathbb{R}^{n_i \times n_j} \tag{2}$$

Assumption 1: T_{ij} is left pseudo-invertible.
By constraining the study to M^3D systems where states are only embedded or truncated during mode transitions, Assumption 1 is not restrictive. Now, it is worth noticing that under said constraint, given a state mapping T_{ij} for the transition from mode i to j, the mapping for the inverse transition fulfils:

$$T_{ji} = T_{ij}^{+} = T_{ij}^{T}, \quad T_{ji} \in \mathbb{R}^{n_j \times n_i} \tag{3}$$

From (1)-(2) it follows that the state dynamics of the system during switching from mode i to j are given as:

$$M^{(ij)} = \begin{cases} x_k^{(j)} = T_{ij}^T \mathcal{A}^{(i)} x_k^{(i)} + T_{ij}^T \mathcal{B}^{(i)} w_k \\ z_k = \mathcal{C}^{(i)} x_k^{(i)} + \mathcal{D}^{(i)} w_k \end{cases} \tag{4}$$

III. Stability of M^3D Systems

As stated in [1] for energy limited transitions, a energy function $V^{(i)}(x_k^{(i)})$ is associated with each mode i. By setting (2), the energy function at the switching instance must fulfill for energy dissipation:

$$V^{(j)}(x_k^{(j)}) = V^{(j)}(T_{ij}^T x_{k+1}^{(i)}) \leq V^{(i)}(x_k^{(i)}) \tag{5}$$

By considering in this work a poly-quadratic energy function of the type

$$V^{(i)}(x_k^{(i)}) = x_k^{(i)^T} X^{(i)} x_k^{(i)}, \tag{6}$$

where $X^{(i)}$ is a mode-dependent positive-defined symmetric matrix, as in [7], then the stability of a M^3D system can be proved if the following theorem holds true.

Theorem 1: A M^3D discrete-time system M, is stable if, for each mode $i = 1, ..., m$ of M there exist matrices $Q^{(i)} = Q^{(i)^T} > 0$, with $Q^{(i)} \in \mathbb{R}^{n_i \times n_i}$, and $G^{(i)} \in \mathbb{R}^{n_i \times n_i}$ such that the following conditions are satisfied:

$$\begin{bmatrix} G^{(i)^T} + G^{(i)} - Q^{(i)} & G^{(i)^T} \mathcal{A}^{(i)^T} \\ * & Q^{(i)} \end{bmatrix} > 0 \tag{7}$$

$\forall i$ mode

$$\begin{bmatrix} G^{(i)^T} + G^{(i)} - Q^{(i)} & G^{(i)^T} \mathcal{A}^{(i)^T} T_{ij} \\ * & Q^{(j)} \end{bmatrix} > 0 \tag{8}$$

$\forall (i, j)$ connected pair of modes, $i \neq j$

Proof: Let us consider the active mode (1) restricted to the autonomous dynamics:

$$M^{(i)} = \left\{ x_{k+1}^{(i)} = \mathcal{A}^{(i)} x_k^{(i)} \right. . \tag{9}$$

By considering (2), the dynamics of the autonomous mode during the M^3D transition then are:

$$M^{(ij)} = \left\{ x_k^{(j)} = T_{ij}^T \mathcal{A}^{(i)} x_k^{(i)} \right. . \tag{10}$$

From (5), considering a energy function (6), the energy limited condition during the switching instance can be written as:

$$x_k^{(j)^T} X^{(j)} x_k^{(j)^T} - x_k^{(i)^T} X^{(i)} x_k^{(i)^T} < 0, \tag{11}$$

which according to (10) is equivalent to:

$$(T_{ij}^T \mathcal{A}^{(i)} x_k^{(i)})^T X^{(j)} (T_{ij}^T \mathcal{A}^{(i)} x_k^{(i)}) - x_k^{(i)^T} X^{(i)} x_k^{(i)^T} < 0 \tag{12}$$

This can then be rearranged as:

$$x_k^{(i)^T} \left[\mathcal{A}^{(i)^T} T_{ij} X^{(j)} T_{ij}^T \mathcal{A}^{(i)} - X^{(i)} \right] x_k^{(i)} < 0 \tag{13}$$

Using Schur complement [8], (13) is then equivalent to:

$$\begin{bmatrix} X^{(j)^{-1}} & T_{ij}^T \mathcal{A}^{(i)} \\ * & X^{(i)} \end{bmatrix} > 0 \tag{14}$$

Applying basic matrix row/column manipulation and a congruence transformation with $diag([G^{(i)}, I])$, where $G^{(i)} \in \mathbb{R}^{n_i \times n_i}$ is a general matrix, leads to:

$$\begin{bmatrix} G^{(i)^T} X^{(i)} G^{(i)} & G^{(i)^T} \mathcal{A}^{(i)^T} T_{ij} \\ * & X^{(j)^{-1}} \end{bmatrix} > 0, \tag{15}$$

which thanks to Young's relation [9], [8]:

$$G^T X^{-1} G \geq G^T + G - X$$

it is equivalent to:

$$\begin{bmatrix} G^{(i)^T} + G^{(i)} - X^{(i)^{-1}} & G^{(i)^T} \mathcal{A}^{(i)^T} T_{ij} \\ * & X^{(j)^{-1}} \end{bmatrix} > 0, \tag{16}$$

Finally, by setting $X^{-1} \equiv Q$, (8) is recovered. Notice that for the non-switching case, the same steps with $X^{(i)} = X^{(j)}$ and $T_{ij} = I \in \mathbb{R}^{n_i \times n_i}$ recover (7), which is a well known result for checking the asympotic stability of systems through the use of LMI [9]. This concludes the proof. ■

Remark 1: Theorem 1 can be seen as an extension to discrete-time M^3D systems of well-know results for the stability of linear continuous-time switched systems, e.g. [10]. To note, as this work deals with discrete-time systems, the concept of dwell time is here only related to the sampling time of the system.

In the next section, the stability condition for M^3D systems is extended with conditions for $\mathcal{H}_\infty$ performance.

$$\begin{bmatrix} \mathcal{A}^{(i)^T} T_{ij} X^{(j)} T_{ij}^T \mathcal{A}^{(i)} - X^{(i)} + \frac{1}{\gamma_\infty}\mathcal{C}^{(i)^T}\mathcal{C}^{(i)} & \mathcal{A}^{(i)^T} T_{ij} X^{(j)} T_{ij}^T \mathcal{B}^{(i)} + \frac{1}{\gamma_\infty}\mathcal{C}^{(i)^T}\mathcal{D}^{(i)} \\ * & \mathcal{B}^{(i)^T} T_{ij} X^{(j)} T_{ij}^T \mathcal{B}^{(i)} + \frac{1}{\gamma_\infty}\mathcal{D}^{(i)^T}\mathcal{D}^{(i)} - \gamma_\infty I \end{bmatrix} \tag{23}$$

IV. $\mathcal{H}_\infty$ NORM FOR DISCRETE M^3D SYSTEMS

Closed-loop systems need not only to be stable with respect uncertainties and disturbances but also being able to fulfill some performance requirements. To achieve this, one of the most well known and powerful techniques in the control literature for LTI systems is the $\mathcal{H}_\infty$ robust control theory. The key concept being the $\mathcal{H}_\infty$ norm of systems, which is associated with the maximum effect γ_∞ the exogenous inputs w_k have over the system exogenous outputs z_k:

$$\frac{\|z\|_2}{\|w\|_2} \le \gamma_\infty \tag{17}$$

Nowadays, the most common way of determining γ_∞ is making use use of the very well known Bounded Real Lemma [6]. The next theorem extends the Bounded Real Lemma to the case of discrete M^3D systems to determine an upper bound of its $\mathcal{H}_\infty$ norm.

Theorem 2: Given a discrete M^3D system M and positive scalar γ_∞, if for each mode $i = 1, ..., m$ of M there exist matrices $Q^{(i)} = Q^{(i)^T} > 0$, with $Q^{(i)} \in \mathbb{R}^{n_i \times n_i}$, and $G^{(i)} \in \mathbb{R}^{n_i \times n_i}$ such that the following LMI problem is feasible:

$$Q^{(i)} > 0 \tag{18}$$

$$\begin{bmatrix} G^{(i)^T} + G^{(i)} - Q^{(i)} & G^{(i)^T}\mathcal{A}^{(i)^T} & G^{(i)^T}\mathcal{C}^{(i)^T} & 0 \\ * & Q^{(i)} & 0 & \mathcal{B} \\ * & * & \gamma_\infty I & \mathcal{D} \\ * & * & * & \gamma_\infty I \end{bmatrix} > 0 \tag{19}$$

$$\forall i \text{ mode}$$

$$\begin{bmatrix} G^{(i)^T} + G^{(i)} - Q^{(i)} & G^{(i)^T}\mathcal{A}^{(i)^T} T_{ij} & G^{(i)^T}\mathcal{C}^{(i)^T} & 0 \\ * & Q^{(j)} & 0 & T_{ij}^T\mathcal{B} \\ * & * & \gamma_\infty I & \mathcal{D} \\ * & * & * & \gamma_\infty I \end{bmatrix} > 0 \tag{20}$$

$$\forall (i, j) \text{ connected pair of modes, } i \neq j$$

The given positive scalar γ_∞ is an upper bound of the $\mathcal{H}_\infty$ norm of M, such that $\|M\|_\infty \le \gamma_\infty$. If the optimal γ_∞ is required, the LMI minimization problem for γ_∞ is still an LMI problem with variables γ_∞, Q and G.

Proof: Let us consider a poly-quadratic energy function $V^{(i)}(x_k^{(i)})$ (6) such that during the M^3D mode transition the following condition holds true

$$V(x_k^{(j)}) - V(x_k^{(i)}) + \frac{1}{\gamma_\infty} z_k^T z_k - \gamma_\infty w_k^T w_k < 0. \tag{21}$$

Expanding the quadratic energy condition according to the M^3D switching dynamics (4), it can then be rearranged in matrix form as

$$\begin{bmatrix} x_k^{(i)} \\ w_k \end{bmatrix}^T (23) \begin{bmatrix} x_k^{(i)} \\ w_k \end{bmatrix} < 0 \tag{22}$$

Applying a Schur Complement around $\frac{1}{\gamma_\infty} I$ followed by a Schur Complement around $X^{(j)}$, then (22) is equivalent to

$$\begin{bmatrix} X^{(j)^{-1}} & T_{ij}^T\mathcal{A}^{(i)} & T_{ij}^T\mathcal{B}^{(i)} & 0 \\ * & X^{(i)} & 0 & \mathcal{C}^{(i)^T} \\ * & * & \gamma_\infty I & \mathcal{D}^{(i)^T} \\ * & * & * & \gamma_\infty I \end{bmatrix} > 0 \tag{24}$$

Now, from basic row/column manipulations followed by a congruence transformation by $diag([G^{(i)}, I, I, I])$ and making use of Young's relation:

$$G^T X^{-1} G \ge G^T + G - X,$$

the LMI (20) is recovered, with $X^{-1} \equiv Q$. As in the stability case, by setting $X^{(i)} = X^{(j)}$ and $T_{ij} = I \in \mathbb{R}^{n_i \times n_i}$, the same chain of steps recover (19), which is a well known result for the computation of the $\mathcal{H}_\infty$ performance of discrete-time systems through the use of LMI [11]. This concludes the proof. ■

V. $\mathcal{H}_\infty$ STATE-FEEDBACK CONTROL FOR DISCRETE M^3D SYSTEMS

The objective of this section is to introduce the $\mathcal{H}_\infty$ control of discrete M^3D systems. Let us consider the discrete M^3D system N, where the dynamics of the active mode i are:

$$N^{(i)} = \begin{cases} x_{k+1}^{(i)} = A^{(i)} x_k^{(i)} + B_u^{(i)} u_k + B_w^{(i)} w_k \\ z_k = C_z^{(i)} x_k^{(i)} + D_u^{(i)} u_k + D_w^{(i)} w_k \end{cases} \tag{25}$$

where $x_k^{(i)} \in \mathbb{R}^{n_i}$ is the state vector, $w_k \in \mathbb{R}^{n_w}$ is the vector of exogenous inputs, $z_k \in \mathbb{R}^{n_z}$ is the vector of control performances and $u_k \in \mathbb{R}^{n_u}$ is the vector of control inputs.

By introducing the discrete-time state-feedback control law

$$u_k = K^{(i)} x_k^{(i)}, \tag{26}$$

the $\mathcal{H}_\infty$ control problem is therefore to find suitable matrices $K^{(i)} \in \mathbb{R}^{n_u \times n_i}$ that render N closed-loop stable, and minimizes the influences of the exogenous inputs w_k on the control performances z_k, according to an $\mathcal{H}_\infty$ norm criterion. This is achieved if the following theorem holds true.

Theorem 3: Given a discrete M^3D system N and positive scalar γ_∞, if for each mode $i = 1, ..., m$ of N there exist matrices $Q^{(i)} = Q^{(i)^T} > 0$, with $Q^{(i)} \in \mathbb{R}^{n_i \times n_i}$, $G^{(i)} \in \mathbb{R}^{n_i \times n_i}$ and $Y^{(i)} \in \mathbb{R}^{n_u \times n_i}$ such that the following LMI conditions are satisfied:

$$Q^{(i)} > 0 \tag{27}$$

$$\begin{bmatrix} G^{(i)^T} + G^{(i)} - Q^{(i)} & \Psi_{1,2}^{(i)} & \Psi_{1,3}^{(i)} & 0 \\ * & Q^{(i)} & 0 & B_w^{(i)} \\ * & * & \gamma_\infty I & D_w^{(i)} \\ * & * & * & \gamma_\infty I \end{bmatrix} > 0 \tag{28}$$

with

$$\Psi_{1,2}^{(i)} = G^{(i)^T} A^{(i)^T} + Y^{(i)^T} B_u^{(i)^T},$$

$$\Psi_{1,3}^{(i)} = G^{(i)^T} C_z^{(i)^T} + Y^{(i)^T} D_u^{(i)^T}$$

$$\forall i \text{ mode}$$

$$\begin{bmatrix} G^{(i)^T} + G^{(i)} - Q^{(i)} & \Psi_{1,2}^{(ij)} & \Psi_{1,3}^{(ij)} & 0 \\ * & Q^{(j)} & 0 & T_{ij}^T B_w^{(i)} \\ * & * & \gamma_\infty I & D_w^{(i)} \\ * & * & * & \gamma_\infty I \end{bmatrix} > 0 \tag{29}$$

with

$$\Psi_{1,2}^{(ij)} = G^{(i)^T} A^{(i)^T} T_{ij} + Y^{(i)^T} B_u^{(i)^T} T_{ij},$$

$$\Psi_{1,3}^{(ij)} = G^{(i)^T} C_z^{(i)^T} + Y^{(i)^T} D_u^{(i)^T}$$

$$\forall (i,j) \text{ connected pair of modes, } i \neq j$$

then there exists a state-feedback control law $u_k = K^{(i)} x_k^{(i)}$ such that $\frac{\|z\|_2}{\|w\|_2} \leq \gamma_\infty$. The state-feedback control matrices of each mode $i = 1, ..., m$ are recovered according to $K^{(i)} = Y^{(i)} G^{(i)^{-1}}$. Now, if the optimal γ_∞ is required, the LMI minimization problem for γ_∞ is still an LMI problem with variables γ_∞, Q, G and Y.

Proof: Note that $N^{(i)}$ can be rewritten as $M^{(i)}$ in (1) considering:

$$\begin{aligned} \mathcal{A}^{(i)} &= A^{(i)} + B_u^{(i)} K^{(i)} \\ \mathcal{B}^{(i)} &= B_w^{(i)} \\ \mathcal{C}^{(i)} &= C_z^{(i)} + D_u^{(i)} K^{(i)} \\ \mathcal{D}^{(i)} &= D_w^{(i)} \end{aligned} \tag{30}$$

Substitute the closed-loop system matrices $M^{(i)}$ from (19) and (20) with the system matrices of $N^{(i)}$, according to (30). Then, with the introduction of the linearizing change of variables $Y^{(i)} = K^{(i)} G^{(i)}$, the LMI conditions (28) and (29) are both recovered. This concludes the proof. ■

Remark 2: Note that, in some cases Theorem 3 may be too restrictive. Indeed, as formulated, the closed-loop $\mathcal{H}_\infty$ performance should be maintained even during a M^3D mode transition. If too conservative or unnecessary, a compromise may be to drop the strong requirement of $\mathcal{H}_\infty$ switching performance in favor of only requiring switching stability. This can be achieved by substituting the LMI condition (29) by

$$\begin{bmatrix} G^{(i)^T} + G^{(i)} - Q^{(i)} & \Psi_{1,2}^{(ij)} \\ * & Q^{(j)} \end{bmatrix} > 0, \tag{31}$$

which comes from applying the linearizing change of variables $Y^{(i)} = K^{(i)} G^{(i)}$ in (8).

Remark 3: Reduction of conservatism in Theorem 3 could also be achieved with the introduction of a new slack variable $Y^{(ij)} = K^{(ij)} G^{(i)}$ in either LMI condition (29) or (31), such that the state-feedback controller $K^{(ij)} = Y^{(ij)} G^{(i)^{-1}}$ is only active during the transition from mode i to mode j. Similar as have been proposed for control of continuous-time switching systems in [12].

VI. NUMERICAL EXAMPLE

In this section a numerical example is given to illustrate the potential of the synthesis conditions provided in this work for M^3D systems. First, the M^3D system is presented. Then, the use and interest of the provided theorems are illustrated. Finally some simulation results are carried out together with some analysis fo the obtained resultts.

A. System Description

It is considered a discrete-time M^3D system N such that the active mode i dynamics are given by:

$$N^{(i)} = \begin{cases} x_{k+1}^{(i)} = A^{(i)} x_k^{(i)} + B_u^{(i)} u_k + B_w^{(i)} w_k \\ z_k = C_z^{(i)} x_k^{(i)} \end{cases} \tag{32}$$

The system N has three modes with state dimensions $x_k^{(1)} \in \mathbb{R}^4$, $x_k^{(2)} \in \mathbb{R}^{10}$ and $x_k^{(3)} \in \mathbb{R}^6$. The system matrices are given by:

$$A^{(1)} = \begin{bmatrix} 0.25 & 0.16 & 0.44 & -0.08 \\ 0.2 & -0.07 & -0.28 & 0.06 \\ 0.48 & -0.29 & 0.18 & -0.02 \\ 0.00 & 0.06 & 0.00 & 0.60 \end{bmatrix}, \tag{33}$$

$$A^{(3)} = \begin{bmatrix} 1.5 & -0.15 & 0.06 & 0.18 & -0.10 & 0.09 \\ 0.14 & -0.02 & -0.29 & 0.42 & 0.35 & -0.13 \\ -0.08 & -0.27 & 0.21 & 0.06 & -0.27 & -0.06 \\ 0.24 & 0.34 & 0.09 & 0.15 & -0.16 & -0.16 \\ 0.10 & 0.32 & -0.28 & -0.11 & -0.12 & -0.07 \\ 0.07 & -0.07 & -0.09 & -0.15 & -0.03 & 0.46 \end{bmatrix} \tag{34}$$

and

$$A^{(2)} = \begin{bmatrix} A^{(1)} & A_{1,2}^{(2)} \\ A_{2,1}^{(2)} & A^{(3)} \end{bmatrix} \tag{35}$$

with

$$\begin{aligned} A_{1,2}^{(2)} &= \begin{bmatrix} 0.26 & -0.28 & 0.16 & -0.27 & 0.15 & -0.13 \\ -0.08 & 0.07 & -0.21 & -0.34 & 0.30 & -0.11 \\ -0.08 & 0.34 & 0.07 & -0.20 & 0.00 & 0.42 \\ 0.14 & 0.26 & 0.46 & 0.04 & 0.07 & 0.04 \end{bmatrix} \\ A_{2,1}^{(2)} &= \begin{bmatrix} 0.27 & -0.17 & -0.16 & -0.02 \\ -0.12 & 0.03 & 0.33 & 0.19 \\ 0.09 & -0.18 & 0.08 & 0.51 \\ -0.23 & -0.37 & -0.23 & -0.02 \\ 0.26 & 0.27 & -0.01 & 0.00 \\ -0.14 & -0.09 & 0.43 & 0.08 \end{bmatrix} \end{aligned} \tag{36}$$

Notice from (35) that modes 1 and 3 are subsystems of mode 2. Also, note from the first diagonal element in (34), that mode 3 (thus, mode 2 too) has unstable open-loop dynamics.

On the other hand the system N has two control inputs, with the input matrix of each mode given by:

$$B_u^{(1)} = \begin{bmatrix} -1.53 & 0 & -1.96 & 0.73 \\ -1.01 & -0.52 & 1.96 & 0 \end{bmatrix}^T, \tag{37}$$

$$B_u^{(3)} = \begin{bmatrix} 0.83 & -0.10 & 0.43 & 0.30 & 0 & -0.68 \\ 0 & 0 & 0 & 0.89 & 0 & 0.06 \end{bmatrix}^T \tag{38}$$

and

$$B_u^{(2)} = \begin{bmatrix} B_u^{(1)^T} & B_u^{(3)^T} \end{bmatrix}^T \tag{39}$$

All modes are affected by disturbance inputs, such that the disturbance input matrix of each mode is given by

$$B_w^{(i)} = 0.1 \cdot B_u^{(i)}. \tag{40}$$

The performance output matrix for each of the three modes of N are chosen as:

$$C_z^{(1)} = \begin{bmatrix} 0 & 0 & 0 & 1 \end{bmatrix}, \tag{41}$$

$$C_z^{(2)} = \begin{bmatrix} 0 & 0 & 0 & 1 & 0 & 0 & 0 & 0 & 0 & 0 \\ 0 & 0 & 0 & 0 & 0 & 0 & 0 & 0 & 0 & 1 \end{bmatrix} \quad (42)$$

and

$$C_z^{(3)} = \begin{bmatrix} 0 & 0 & 0 & 0 & 0 & 1 \end{bmatrix} \quad (43)$$

It is worth noticing that the dimension of the control performance output vector $z(k)$ is different for all modes. This has been chosen to illustrate that the proposed method can handle cases where the dimensions of $u(k)$, $w(k)$ and $z(k)$ do change during mode transitions. This can be accomplished without any modification on the results provided in previous sections. It is also important to note that the control performance output matrices $C_z^{(i)}$ indicate the signals to be minimized following the $\mathcal{H}_\infty$ criterion. Of course, for state feedback control, it is moreover assumed that all states are available.

Note also that, later on, the control performance output of the mode 1 is referred to as $z_1(k)$, while it is referred to as $z_2(k)$ for the mode 3, and, therefore, for the mode 2 the considered performance output vector is denoted $z(k) = [z_1(k),\, z_2(k)]^T$.

The M^3D system N is considered to switch with arbitrary conditions and no restrictions, such that the active mode in the next sampling instance could potentially (but not necessarily) switch to any of the other two modes. As a result, it is considered all mode pairs (i, j), $i \neq j$, are connected. The state mappings T_{ij} that describe the state embedding/truncation during the Multi-Dimensional switch from each mode are:

$$T_{12} = \begin{bmatrix} I^{4\times 4} & \mathbf{0}^{4\times 6} \end{bmatrix}, \quad (44)$$

$$T_{13} = \begin{bmatrix} \mathbf{0}^{4\times 6} \end{bmatrix}, \quad (45)$$

$$T_{32} = \begin{bmatrix} \mathbf{0}^{6\times 4} & I^{6\times 6} \end{bmatrix}, \quad (46)$$

and

$$T_{21} = T_{12}^T, \quad T_{31} = T_{13}^T, \quad T_{32} = T_{23}^T. \quad (47)$$

B. Control Design

Two different control approaches are considered in this section. In the first baseline approach, independent state-feedback controllers are designed for each mode i of N. In order to check the stability of the global system N in closed-loop, Theorem 1 is then employed. The second approach follows our proposed method, so the design of the state-feedback control law is carried out applying Theorem 3 to the global system N.

As mentioned, the synthesis of controllers for the first approach is done as an independent discrete-time LTI control synthesis problem for each mode of N. The computation of all controllers $K^{(i)}$ is performed considering the LMI condition (28) from Theorem 3 only, without accounting for the transition's effect (so actually using the method in [11]). As each controller is computed independently of the others, this results in three different LMI optimization problems where the optimal $\mathcal{H}_\infty$ norms found in each case are $\gamma_\infty^{(1)} = 0.0732$, $\gamma_\infty^{(2)} = 0.1442$ and $\gamma_\infty^{(3)} = 0.0686$. However, it is well known that stable systems can be rendered unstable under arbitrary switching conditions [13]. With the independently computed state-feedback controllers $K^{(i)}$ and relation (30), the stability of the switched M^3D closed-loop system can be tested employing Theorem 1. It was found that Theorem 1 conditions were not satisfied, meaning that, the discrete-time M^3D system N in closed-loop could not be proved to be stable in the case where controllers $K^{(i)}$ are computed independently.

Concerning the second scenario (our approach), the controllers $K^{(i)}$ are computed considering the global M^3D system N by employing Theorem 3. To tackle the design problem it is required to solve a total of nine LMI conditions, with three LMI according to (28) for the $\mathcal{H}_\infty$ control of each mode plus six LMI conditions according to (29) to account for all the possible Multi-Dimensional mode transitions. The obtained optimal upper bound on the $\mathcal{H}_\infty$ norm of the closed-loop system is $\gamma_\infty = 0.19$.

C. Simulation Analysis

Following the discussed control design approaches, two simulation scenarios are proposed. The first scenario considers the case with independent controllers for each mode, when the second scenario is the global design approach of the controllers according to Theorem 3. In both scenarios, the system N evolves under arbitrary switching conditions, where the switching sequence in the same for both cases, as shown in Fig. 1.

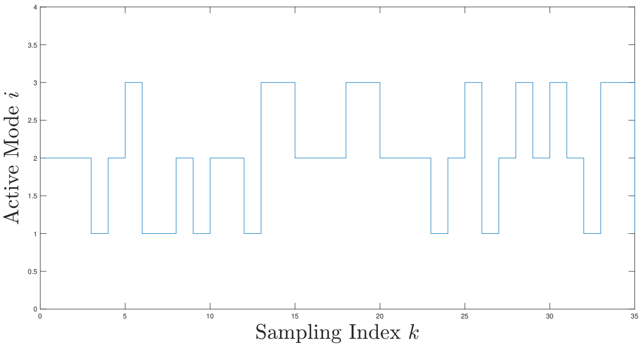

Fig. 1. Active mode i during arbitrary switching conditions

The control output performance $z(k)$ for each scenario is shown in Fig. 2. On the top figure, it is shown the control performances obtained during the first scenario with independent controllers for each mode. On the bottom, it is given the control performances output in the second scenario with state-feedback controllers computed for the system N globally according to Theorem 3.

From the simulation results given in Fig 2, it can be seen that during the first scenario, the control performances do not converge and, in fact, they increase in magnitude with time as the system N in this case is unstable. For the second scenario however, the closed-loop system is stable despite the presence of the arbitrary switch conditions and state dimension and system structure changes during mode transitions.

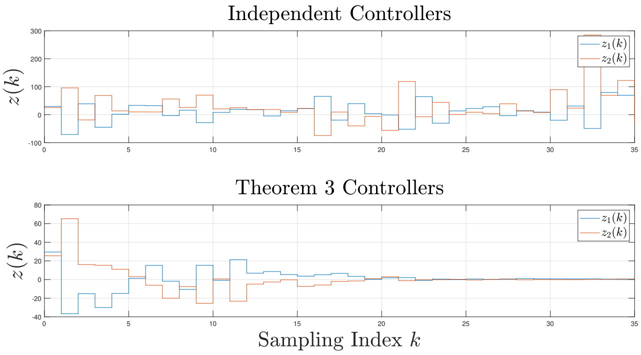

Fig. 2. Control performance output $z(k)$

The stability of the closed-loop system can also be assessed considering a quadratic storage function

$$V^{(i)}(x_k^{(i)}) = {x_k^{(i)}}^T X^{(i)} x_k^{(i)},$$

where $X \equiv Q^{-1}$, with Q being the symmetric positive defined matrix found from applying Theorem 3. Fig. 3 shows the evolution of the storage function during both simulation scenarios.

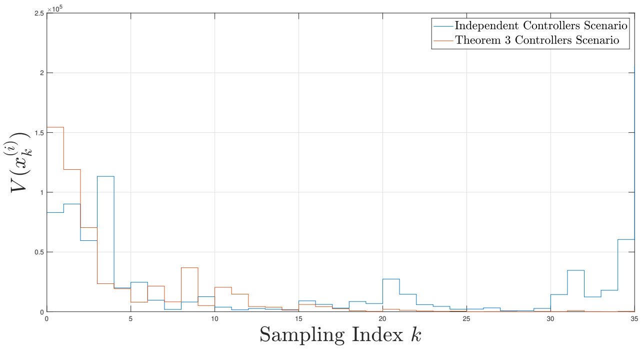

Fig. 3. Energy Storage Function $V(x_k^{(i)})$ of system N under arbitrary switching

In the first scenario (in blue), the energy in the system initially converges towards zero, however, affected by the arbitrary Multi-Dimensional transitions, the energy in the last sampling instances starts to increase dramatically indicating closed-loop instability. In the second scenario, thanks to the global approach in the M^3D controller synthesis, the energy of the system converges to zero, showing that the system has been stabilized despite the switching conditions.

VII. CONCLUSIONS

In this work new conditions using LMI formulation have been provided in order to test the stability of discrete-time M^3D LTI systems, to compute the $\mathcal{H}_\infty$ norm of such systems, as well as to design state-feedback controllers robust to Multi-Dimensional switching. Importantly, some remarks have been given that could allow to alleviate possible conservatism of the results here presented. The synthesis conditions were tested in a numerical example, allowing to stabilize a M^3D system composed of three modes, two of which are open-loop unstable, all of different dimensions and under arbitrary switching conditions. To the best of the Authors knowledge, no other work proposed in the literature allows for a global approach to the synthesis of controllers for M^3D system.

Therefore, the results here presented allow to study control problems associated with complex Multi-Dimensional systems while retaining strong stability guarantees. Some application examples could be: the control of nonlinear systems modeled as piecewise reduced linearizations of different dimensions (as commented in [14]), the control of speed and inter-vehicle distance of autonomous vehicles in a platoon highway application (where vehicles could dynamically enter or leave the platoon), or the control of MIMO systems with subsystems that could be discarded or not. Furthermore, the results presented in this study may be extended to the Linear Parameter Varying framework, allowing to study problems beyond the scope of LTI systems.

REFERENCES

[1] E. I. Verriest, “Multi-mode multi-dimensional systems,” in *Proceedings of the 17th International Symposium on Mathematical Theory of Networks and Systems*, 2006, pp. 1268–1274.

[2] T. R. Mehta, D. Yeung, E. I. Verriest, and M. Egerstedt, “Optimal control of multi-dimensional, hybrid ice-skater model,” in *2007 American Control Conference*. IEEE, 2007, pp. 2787–2792.

[3] H. Yang, B. Jiang, V. Cocquempot, and M. Chen, “Spacecraft formation stabilization and fault tolerance: A state-varying switched system approach,” *Systems & control letters*, vol. 62, no. 9, pp. 715–722, 2013.

[4] M. Xue, Y. Tang, W. Ren, and F. Qian, “Stability of multi-dimensional switched systems with an application to open multi-agent systems,” *arXiv preprint arXiv:2001.00435*, 2020.

[5] R. Galván-Guerra, V. Azhmyakov, and M. Egerstedt, “Optimization of multiagent systems with increasing state dimensions: hybrid lq approach,” in *Proceedings of the 2011 American Control Conference*. IEEE, 2011, pp. 881–887.

[6] S. Boyd, L. E. Ghaoui, E. Feron, and V. Balakrishnan, *Linear Matirx Inequalities in Systems and Control Theory*. SIAM, Studies in Applied and Numerical Mathematics, Philadelphia, 1994.

[7] J. Daafouz, G. Millerioux, and C. Iung, “A poly-quadratic stability based approach for linear switched systems,” *International journal of Control*, vol. 75, no. 16-17, pp. 1302–1310, 2002.

[8] R. J. Caverly and J. R. Forbes, “Lmi properties and applications in systems, stability, and control theory,” *arXiv preprint arXiv:1903.08599*, 2019.

[9] M. C. De Oliveira, J. Bernussou, and J. C. Geromel, “A new discrete-time robust stability condition,” *Systems & control letters*, vol. 37, no. 4, pp. 261–265, 1999.

[10] J. C. Geromel and P. Colaneri, “Stability and stabilization of continuous-time switched linear systems,” *SIAM Journal on Control and Optimization*, vol. 45, no. 5, pp. 1915–1930, 2006.

[11] M. De Oliveira, J. Geromel, and J. Bernussou, “An lmi optimization approach to multiobjective controller design for discrete-time systems,” in *Proceedings of the 38th IEEE Conference on Decision and Control (Cat. No. 99CH36304)*, vol. 4. IEEE, 1999, pp. 3611–3616.

[12] L. I. Allerhand and U. Shaked, “Robust control of linear systems via switching,” *IEEE Transactions on Automatic Control*, vol. 58, no. 2, pp. 506–512, 2012.

[13] D. Liberzon, *Switching in systems and control*. Springer, 2003, vol. 190.

[14] E. I. Verriest, “Pseudo-continuous multi-dimensional multi-mode systems,” *Discrete Event Dynamic Systems*, vol. 22, no. 1, pp. 27–59, 2012.

Bibliography

[AA98] P. Apkarian and R.J. Adams. “Advanced gain-scheduling techniques for uncertain systems”. In: *IEEE Transactions on Control Systems Technology* 6.1 (1998), pp. 21–32 (cit. on pp. 18, 77, 78).

[AG95] P. Apkarian and P. Gahinet. “A convex characterization of gain-scheduled H_∞ controllers”. In: *IEEE Transactions on Automatic Control* 40.5 (1995), pp. 853–864 (cit. on pp. 18, 78, 127).

[AGB95] Pierre Apkarian, Pascal Gahinet, and Greg Becker. “Self-scheduled H_∞ control of linear parameter-varying systems: a design example”. In: *Automatica* 31.9 (1995), pp. 1251–1261 (cit. on pp. 18, 68).

[Alc+20] Eugenio Alcalá et al. “Autonomous racing using Linear Parameter Varying-Model Predictive Control (LPV-MPC)”. In: *Control Engineering Practice* 95 (2020), p. 104270 (cit. on p. 69).

[All+02] R. Wade Allen et al. “Driver/Vehicle Modeling and Simulation”. In: *SAE Transactions* 111 (2002), pp. 1745–1766 (cit. on p. 55).

[AM97] A. Apel and M. Mitschke. “Adjusting vehicle characteristics by means of driver models”. In: *International Journal of Vehicle Design* 18.6 (1997), pp. 583–596 (cit. on p. 60).

[APQ20] Eugenio Alcalá, Vicenç Puig, and Joseba Quevedo. “LPV-MP planning for autonomous racing vehicles considering obstacles”. In: *Robotics and Autonomous Systems* 124 (2020), p. 103392 (cit. on p. 69).

[ApS19] Mosek ApS. “Mosek optimization toolbox for matlab”. In: *User’s Guide and Reference Manual, Version* 4 (2019), p. 1 (cit. on p. 168).

[Ato+21] Hussam Atoui et al. “Interpolation of multi-LPV control systems based on Youla–Kucera parameterization”. In: *Automatica* 134 (2021), p. 109963 (cit. on p. 71).

[Ato+22a] Hussam Atoui et al. “Intelligent Control Switching for Autonomous Vehicles based on Reinforcement Learning”. In: *2022 IEEE Intelligent Vehicles Symposium (IV)*. 2022, pp. 792–797 (cit. on p. 71).

[Ato+22b] Hussam Atoui et al. “LPV-Based Autonomous Vehicle Lateral Controllers: A Comparative Analysis”. In: *IEEE Transactions on Intelligent Transportation Systems* 23.8 (2022), pp. 13570–13581 (cit. on pp. 29, 68).

[Bec96] Gregory Becker. “Additional Results on Parameter-Dependent Controllers for LPV Systems”. In: *IFAC Proceedings Volumes* 29.1 (1996). 13th World Congress of IFAC, 1996, San Francisco USA, 30 June - 5 July, pp. 3222–3227 (cit. on p. 82).

[Bor+05] F. Borrelli et al. “MPC-based approach to active steering for autonomous vehicle systems”. In: *International Journal of Vehicle Autonomous Systems* 3.2-4 (2005), pp. 265–291 (cit. on p. 69).

[Boy+94] Stephen Boyd et al. *Linear Matrix Inequalities in System and Control Theory.* Society for Industrial and Applied Mathematics, 1994 (cit. on pp. 18, 19, 24).

[Bri14] Corentin Briat. "Linear Parameter-Varying and Time-Delay Systems". In: *Analysis, observation, filtering & control* 3 (2014), pp. 5–7 (cit. on pp. 18, 23).

[Cao+23] Xuanhao Cao et al. "Gain-scheduling LPV synthesis H_∞ robust lateral motion control for path following of autonomous vehicle via coordination of steering and braking". In: *Vehicle System Dynamics* 61.4 (2023), pp. 968–991 (cit. on p. 69).

[CF19] Ryan James Caverly and James Richard Forbes. "LMI Properties and Applications in Systems, Stability, and Control Theory". In: *CoRR* abs/1903.08599 (2019). arXiv: `1903.08599` (cit. on pp. 21, 23).

[Chr+07] Gauthier Christophe et al. "An $\mathcal{H}_\infty$ linear parameter-varying (LPV) controller for a diesel engine common rail injection system". In: *2007 European Control Conference (ECC).* 2007, pp. 1932–1939 (cit. on p. 95).

[Chu+18] Zhengrong Chu et al. "Active disturbance rejection control applied to automated steering for lane keeping in autonomous vehicles". In: *Control Engineering Practice* 74 (2018), pp. 13–21 (cit. on p. 67).

[Cor+21] Matteo Corno et al. "An LPV Approach to Autonomous Vehicle Path Tracking in the Presence of Steering Actuation Nonlinearities". In: *IEEE Transactions on Control Systems Technology* 29.4 (2021), pp. 1766–1774 (cit. on pp. 29, 68, 70).

[Cou92] R Craig Coulter. *Implementation of the pure pursuit path tracking algorithm.* Tech. rep. Carnegie-Mellon UNIV Pittsburgh PA Robotics INST, 1992 (cit. on p. 84).

[CP12] Jie Chen and Ron J Patton. *Robust model-based fault diagnosis for dynamic systems.* Vol. 3. Springer Science & Business Media, 2012 (cit. on p. 124).

[CZW19] Yimin Chen, Xinjie Zhang, and Junmin Wang. "Robust vehicle driver assistance control for handover scenarios considering driving performances". In: *IEEE Transactions on Systems, Man, and Cybernetics: Systems* (2019) (cit. on p. 117).

[DB01a] J. Daafouz and J. Bernussou. "Poly-quadratic stability and H_∞ performance for discrete systems with time varying uncertainties". In: *Proceedings of the 40th IEEE Conference on Decision and Control (Cat. No.01CH37228).* Vol. 1. 2001, 267–272 vol.1 (cit. on p. 25).

[DB01b] Jamal Daafouz and Jacques Bernussou. "Parameter dependent Lyapunov functions for discrete time systems with time varying parametric uncertainties". In: *Systems & Control Letters* 43.5 (2001), pp. 355–359 (cit. on pp. 23, 24).

[dBG99] M.C. de Oliveira, J. Bernussou, and J.C. Geromel. "A new discrete-time robust stability condition". In: *Systems & Control Letters* 37.4 (1999), pp. 261–265 (cit. on pp. 23, 24).

[DC+10] J. De Caigny et al. "Gain-scheduled $\mathcal{H}_2$ and $\mathcal{H}_\infty$ control of discrete-time polytopic time-varying systems". English. In: *IET Control Theory & Applications* 4 (3 2010), 362–380(18) (cit. on pp. 25, 95).

[Din08] Steven X Ding. *Model-based fault diagnosis techniques: design schemes, algorithms, and tools*. Springer Science & Business Media, 2008 (cit. on p. 119).

[DOBG99] Maurício C De Oliveira, Jacques Bernussou, and José C Geromel. "A new discrete-time robust stability condition". In: *Systems & control letters* 37.4 (1999), pp. 261–265 (cit. on p. 22).

[Don78] Dr. Edmund Donges. "A Two-Level Model of Driver Steering Behavior". In: *Human Factors* 20.6 (1978), pp. 691–707 (cit. on pp. 52, 53, 55).

[Dou+13] Moustapha Doumiati et al. "Integrated vehicle dynamics control via coordination of active front steering and rear braking". In: *European Journal of Control* 19.2 (2013), pp. 121–143 (cit. on pp. 35, 68, 70, 116, 136).

[EFG15] Stephen M Erlien, Susumu Fujita, and Joseph Christian Gerdes. "Shared steering control using safe envelopes for obstacle avoidance and vehicle stability". In: *IEEE Transactions on Intelligent Transportation Systems* 17.2 (2015), pp. 441–451 (cit. on p. 117).

[Fer14] Soheib Fergani. "Robust multivariable control for vehicle dynamics". Theses. Université de Grenoble, Oct. 2014 (cit. on pp. 18, 29, 35, 69, 116).

[FNG22] Dániel Fényes, Balázs Németh, and Péter Gáspár. "Design of LPV control for autonomous vehicles using the contributions of big data analysis". In: *International Journal of Control* 95.7 (2022), pp. 1802–1813 (cit. on p. 68).

[FSD16] Soheib Fergani, Olivier Sename, and Luc Dugard. "An LPV/$\mathcal{H}_\infty$ Integrated Vehicle Dynamic Controller". In: *IEEE Transactions on Vehicular Technology* 65.4 (2016), pp. 1880–1889 (cit. on p. 151).

[GA94] Pascal Gahinet and Pierre Apkarian. "A linear matrix inequality approach to H∞ control". In: *International Journal of Robust and Nonlinear Control* 4.4 (1994), pp. 421–448 (cit. on p. 80).

[Gao+10] *Predictive Control of Autonomous Ground Vehicles With Obstacle Avoidance on Slippery Roads*. Vol. ASME 2010 Dynamic Systems and Control Conference, Volume 1. Dynamic Systems and Control Conference. Sept. 2010, pp. 265–272 (cit. on p. 67).

[Gás+16] Péter Gáspár et al. "Robust control design for active driver assistance systems". In: *Springer, DOI* 10 (2016), pp. 978–3 (cit. on p. 69).

[GC06a] Jose C Geromel and Patrizio Colaneri. "Stability and stabilization of continuous-time switched linear systems". In: *SIAM Journal on Control and Optimization* 45.5 (2006), pp. 1915–1930 (cit. on pp. x, 5).

[GC06b] José C Geromel and Patrizio Colaneri. "Stability and stabilization of discrete time switched systems". In: *International Journal of Control* 79.07 (2006), pp. 719–728 (cit. on pp. x, 5).

[GCS21] Alex Gimondi, Matteo Corno, and Sergio Matteo Savaresi. "Linear Parameter Varying Path Tracking Control for Over-Actuated Electric Vehicles". In: *Frontiers in Control Engineering* 2 (2021) (cit. on p. 69).

[GGK08] Bilin Aksun Guvenc, Levent Guvenc, and Sertaç Karaman. “Robust yaw stability controller design and hardware-in-the-loop testing for a road vehicle”. In: *IEEE Transactions on Vehicular Technology* 58.2 (2008), pp. 555–571 (cit. on pp. 116, 128, 146, 166).

[GNB12] Péter Gáspár, Balázs Németh, and József Bokor. “Design of integrated vehicle control using driver models”. In: *IFAC Proceedings Volumes* 45.13 (2012), pp. 517–522 (cit. on p. 116).

[GSB05] P. Gaspar, I. Szaszi, and J. Bokor. “Reconfigurable control structure to prevent the rollover of heavy vehicles”. In: *Control Engineering Practice* 13.6 (2005), pp. 699–711 (cit. on p. 69).

[Gá+17] Péter Gáspár et al. *Robust Control Design for Active Driver Assistance Systems.* Jan. 2017 (cit. on p. 29).

[Hil+14] G. Hilhorst et al. “On Extended LMI Conditions for $\mathcal{H}_2/\mathcal{H}_\infty$ Control of Discrete-Time Linear Systems”. In: *IFAC Proceedings Volumes* 47.3 (2014). 19th IFAC World Congress, pp. 9307–9312 (cit. on p. 25).

[HM90] R.A. Hess and A. Modjtahedzadeh. “A control theoretic model of driver steering behavior”. In: *IEEE Control Systems Magazine* 10.5 (1990), pp. 3–8 (cit. on pp. 54, 116).

[HSP15] Arnar Hjartarson, Peter Seiler, and Andrew Packard. “LPVTools: A toolbox for modeling, analysis, and synthesis of parameter varying control systems”. In: *IFAC-PapersOnLine* 48.26 (2015), pp. 139–145 (cit. on pp. 120, 125, 128).

[Ino+16] Shintaro Inoue et al. “Cooperative lateral control between driver and ADAS by haptic shared control using steering torque assistance combined with Direct Yaw Moment Control”. In: *2016 IEEE 19th International Conference on Intelligent Transportation Systems (ITSC).* 2016, pp. 316–321 (cit. on p. 117).

[Jaz08] Reza N Jazar. *Vehicle dynamics.* Vol. 1. Springer, 2008 (cit. on pp. 30, 33).

[JHB15] Miroslav Jirgl, Marie Havlikova, and Zdenek Bradac. “The Dynamic Pilot Behavioral Models”. In: *Procedia Engineering* 100 (2015). 25th DAAAM International Symposium on Intelligent Manufacturing and Automation, 2014, pp. 1192 –1197 (cit. on p. 51).

[Ji+18] Xuewu Ji et al. “Shared steering torque control for lane change assistance: a stochastic game-theoretic approach”. In: *IEEE Transactions on Industrial Electronics* 66.4 (2018), pp. 3093–3105 (cit. on p. 117).

[Jia+11] Wenjuan Jiang et al. “A new mathematical model for car drivers with spatial preview”. In: *IFAC Proceedings Volumes* 44.1 (2011). 18th IFAC World Congress, pp. 1139–1144 (cit. on p. 54).

[KAG99] H. Kajiwara, P. Apkarian, and P. Gahinet. “LPV techniques for control of an inverted pendulum”. In: *IEEE Control Systems Magazine* 19.1 (1999), pp. 44–54 (cit. on p. 74).

[Kap+22] Dimitrios Kapsalis et al. "A reduced LPV polytopic look-ahead steering controller for autonomous vehicles". In: *Control Engineering Practice* 129 (2022), p. 105360 (cit. on pp. 39, 68).

[KN00] Uwe Kiencke and Lars Nielsen. *Automotive control systems: for engine, driveline, and vehicle*. 2000 (cit. on p. 30).

[Lef+15] Stéphanie Lefèvre et al. "Driver models for personalised driving assistance". In: *Vehicle System Dynamics* 53.12 (2015), pp. 1705–1720 (cit. on p. 54).

[Liu+17] Chang Liu et al. "Path planning for autonomous vehicles using model predictive control". In: *2017 IEEE Intelligent Vehicles Symposium (IV)*. 2017, pp. 174–179 (cit. on p. 69).

[Löf04] J. Löfberg. "YALMIP : A Toolbox for Modeling and Optimization in MATLAB". In: *In Proceedings of the CACSD Conference*. Taipei, Taiwan, 2004 (cit. on pp. 87, 102, 143, 144, 148, 163, 168).

[LW04] Bei Lu and Fen Wu. "Control design of switched LPV systems using multiple parameter-dependent Lyapunov functions". In: *Proceedings of the 2004 American Control Conference*. Vol. 4. 2004, 3875–3880 vol.4 (cit. on p. 80).

[Mac01] C. MacAdam. "Development of a driver model for near/at-limit vehicle handling". In: (Jan. 2001) (cit. on p. 53).

[Mac+22] Steven Macenski et al. "Robot Operating System 2: Design, architecture, and uses in the wild". In: *Science Robotics* 7.66 (2022), eabm6074 (cit. on p. 36).

[MC11] Chulwoo Moon and Seibum B Choi. "A driver model for vehicle lateral dynamics". In: *International journal of vehicle design* 56.1-4 (2011), pp. 49–80 (cit. on pp. 52–55).

[McR+77] Duane T. McRuer et al. "New Results in Driver Steering Control Models". In: *Human Factors* 19.4 (1977), pp. 381–397 (cit. on pp. 50–52).

[MDH14] Franck Mars, Mathieu Deroo, and Jean-Michel Hoc. "Analysis of human-machine cooperation when driving with different degrees of haptic shared control". In: *IEEE transactions on haptics* 7.3 (2014), pp. 324–333 (cit. on p. 117).

[MK74] Duane T McRuer and Ezra S Krendel. *Mathematical models of human pilot behavior*. Tech. rep. Advisory Group for Aerospace Research and Development, Neuilly-sur-Seinge, France, 1974 (cit. on pp. 51, 55, 130).

[MMM95] William F Milliken, Douglas L Milliken, and L Daniel Metz. *Race car vehicle dynamics*. Vol. 400. SAE international Warrendale, 1995 (cit. on p. 30).

[MNRS20] Marcelo M Morato, Julio E Normey-Rico, and Olivier Sename. "Model predictive control design for linear parameter varying systems: A survey". In: *Annual Reviews in Control* 49 (2020), pp. 64–80 (cit. on p. 69).

[MSN11] Riccardo Marino, Stefano Scalzi, and Mariana Netto. "Nested PID steering control for lane keeping in autonomous vehicles". In: *Control Engineering Practice* 19.12 (2011), pp. 1459–1467 (cit. on p. 67).

[NCA19] Hyunsik Nam, Wansik Choi, and Changsun Ahn. “Model predictive control for evasive steering of an autonomous vehicle”. In: *International journal of automotive technology* 20 (2019), pp. 1033–1042 (cit. on p. 69).

[Oga95] Katsuhiko Ogata. *Discrete-Time Control Systems (2nd Ed.)* USA: Prentice-Hall, Inc., 1995 (cit. on p. 18).

[OGB02] M. C. De Oliveira, J. C. Geromel, and J. Bernussou. “Extended H_2 and H_∞ norm characterizations and controller parametrizations for discrete-time systems”. In: *International Journal of Control* 75.9 (2002), pp. 666–679 (cit. on pp. 22, 23, 26).

[OT16] Kazuhide Okamoto and Panagiotis Tsiotras. “A new hybrid sensorimotor driver model with model predictive control”. In: *2016 IEEE International Conference on Systems, Man, and Cybernetics (SMC)*. 2016, pp. 001866–001871 (cit. on p. 54).

[Oud+22] Mohamed Radjeb Oudainia et al. “Dynamic Conflict Mitigation for Cooperative Driving Control of Intelligent Vehicles”. In: *2022 IEEE Intelligent Vehicles Symposium (IV)*. 2022, pp. 1445–1452 (cit. on pp. 71, 117, 178).

[Pac12] Hans B. Pacejka. *Tire and Vehicle Dynamics*. Third Edition. Oxford: Butterworth-Heinemann, 2012 (cit. on pp. 33, 35).

[Pad+16] Brian Paden et al. “A Survey of Motion Planning and Control Techniques for Self-Driving Urban Vehicles”. In: *IEEE Transactions on Intelligent Vehicles* 1.1 (2016), pp. 33–55 (cit. on p. 84).

[Pan+20] Béatrice Pano et al. “Systematic $\mathcal{H}_2/\mathcal{H}_\infty$ haptic shared control synthesis for cars, parameterized by sharing level”. In: *2020 IEEE International Conference on Systems, Man, and Cybernetics (SMC)*. 2020, pp. 4416–4423 (cit. on p. 117).

[PE07] Manfred Plöchl and Johannes Edelmann. “Driver models in automobile dynamics application”. In: *Vehicle System Dynamics* 45.7-8 (2007), pp. 699–741 (cit. on pp. 51, 54).

[PO19] Amit P. Pandey and Maurício C. de Oliveira. “Discrete-time $\mathcal{H}_\infty$ control of linear parameter-varying systems”. In: *International Journal of Control* 92.12 (2019), pp. 2750–2760 (cit. on p. 25).

[PV+08] C. Poussot-Vassal et al. “A new semi-active suspension control strategy through LPV technique”. In: *Control Engineering Practice* 16.12 (2008), pp. 1519–1534 (cit. on pp. 71, 94).

[PV08] Charles Poussot-Vassal. “Robust LPV multivariable Automotive Global Chassis Control”. Theses. Institut National Polytechnique de Grenoble - INPG, Sept. 2008 (cit. on pp. 18, 35, 69, 81).

[PV+11] Charles Poussot-Vassal et al. “Vehicle dynamic stability improvements through gain-scheduled steering and braking control”. In: *Vehicle System Dynamics* 49.10 (2011), pp. 1597–1621 (cit. on pp. 116, 128, 146, 166).

[Raj11] Rajesh Rajamani. *Vehicle dynamics and control*. Springer Science & Business Media, 2011 (cit. on pp. 29, 30, 32, 33, 56, 122, 163).

[Rei83] Lloyd D. Reid. “A survey of recent driver steering behavior models suited to accident studies”. In: *Accident Analysis & Prevention* 15.1 (1983), pp. 23 –40 (cit. on p. 50).

[Rob07] David Robert. “Contribution à l’interaction commande/ordonnancement”. Theses. Institut National Polytechnique de Grenoble - INPG, Jan. 2007 (cit. on p. 18).

[RSB81] L. D. REID, E. N. SOLOWKA, and A. M. BILLING. “A systematic study of driver steering behaviour”. In: *Ergonomics* 24.6 (1981), pp. 447–462 (cit. on pp. 51, 56).

[Sal+13] Louay Saleh et al. “Shared steering control between a driver and an automation: Stability in the presence of driver behavior uncertainty”. In: *IEEE Transactions on Intelligent Transportation Systems* 14.2 (2013), pp. 974–983 (cit. on p. 117).

[SBN06] C.E. de Souza, K.A. Barbosa, and A.T. Neto. “Robust $\mathcal{H}_\infty$ filtering for discrete-time linear systems with uncertain time-varying parameters”. In: *IEEE Transactions on Signal Processing* 54.6 (2006), pp. 2110–2118 (cit. on p. 25).

[Sch+16] Scott Schnelle et al. “A driver steering model with personalized desired path generation”. In: *IEEE Transactions on Systems, Man, and Cybernetics: Systems* 47.1 (2016), pp. 111–120 (cit. on pp. 53, 54, 61, 117).

[Sen+09] C. Sentouh et al. “A sensorimotor driver model for steering control”. In: *2009 IEEE International Conference on Systems, Man and Cybernetics*. 2009, pp. 2462–2467 (cit. on pp. 53, 54).

[Sen+19] Chouki Sentouh et al. “Driver-Automation Cooperation Oriented Approach for Shared Control of Lane Keeping Assist Systems”. In: *IEEE Transactions on Control Systems Technology* 27.5 (2019), pp. 1962–1978 (cit. on p. 117).

[SG04] Dario D Salvucci and Rob Gray. “A Two-Point Visual Control Model of Steering”. In: *Perception* 33.10 (2004), pp. 1233–1248 (cit. on pp. 52, 53).

[SGB13] Olivier Sename, Peter Gaspar, and József Bokor. *Robust control and linear parameter varying approaches: application to vehicle dynamics*. Vol. 437. Springer, 2013 (cit. on p. 69).

[Sha12] Jeff S Shamma. “An overview of LPV systems”. In: *Control of linear parameter varying systems with applications*. Springer, 2012, pp. 3–26 (cit. on p. 20).

[SP07] Sigurd Skogestad and Ian Postlethwaite. *Multivariable feedback control: analysis and design*. Vol. 2. Citeseer, 2007 (cit. on pp. 18, 127).

[THH12] Roland Tóth, Peter S. C. Heuberger, and Paul M. J. Van den Hof. “Prediction-Error Identification of LPV Systems: Present and Beyond”. In: *Control of Linear Parameter Varying Systems with Applications*. Ed. by Javad Mohammadpour and Carsten W. Scherer. Boston, MA: Springer US, 2012, pp. 27–58 (cit. on p. 39).

[Tót10] Roland Tóth. *Modeling and identification of linear parameter-varying systems*. Vol. 403. Springer, 2010 (cit. on pp. 18, 30).

[TTT04] K.C. Toh, R.H. Tutuncu, and M.J. Todd. “On the implementation of SDPT3 (version 3.1) - a MATLAB software package for semidefinite-quadratic-linear programming”. In: *2004 IEEE International Conference on Robotics and Automation (IEEE Cat. No.04CH37508).* 2004, pp. 290–296 (cit. on pp. 87, 102, 143, 144, 148, 163).

[Ver06] Erik I Verriest. “Multi-mode multi-dimensional systems”. In: *Proceedings of the 17th International Symposium on Mathematical Theory of Networks and Systems.* 2006, pp. 1268–1274 (cit. on pp. x, 4).

[WGP00] Fen Wu, Karolos M. Grigoriadis, and Andy Packard. “Anti-windup controller design using linear parameter-varying control methods”. In: *International Journal of Control* 73.12 (2000), pp. 1104–1114 (cit. on pp. 71, 94, 100, 158, 166).

[WM70] D.H. Weir and D.T. McRuer. “Dynamics of driver vehicle steering control”. In: *Automatica* 6.1 (1970), pp. 87–98 (cit. on pp. 51, 56).

[WS94] Siep Weiland and Carsten Scherer. “Linear Matrix Inequality in Control”. In: (Jan. 1994) (cit. on p. 18).

[Wu95] Fen Wu. *Control of linear parameter varying systems.* University of California, Berkeley, 1995 (cit. on p. 128).

[Wu+96] Fen Wu et al. “Induced L2-norm control for LPV systems with bounded parameter variation rates”. In: *International Journal of Robust and Nonlinear Control* 6.9-10 (1996), pp. 983–998 (cit. on pp. 18, 76, 78).

[Zan+14] Mario Zanon et al. “Model Predictive Control of Autonomous Vehicles”. In: *Optimization and Optimal Control in Automotive Systems.* Ed. by Harald Waschl et al. Cham: Springer International Publishing, 2014, pp. 41–57 (cit. on p. 69).

[ZD98] Kemin Zhou and John Comstock Doyle. *Essentials of robust control.* Vol. 104. Prentice hall Upper Saddle River, NJ, 1998 (cit. on pp. 18, 26, 85, 99, 127).

[Zin+08] A. Zin et al. “Robust LPV–$\mathcal{H}_\infty$ control for active suspensions with performance adaptation in view of global chassis control”. In: *Vehicle System Dynamics* 46.10 (2008), pp. 889–912 (cit. on p. 69).